Quantum Field Theory Approaches to Meson Structure

Dissertation

der Mathematisch–Naturwissenschaftlichen Fakultät
der Eberhard Karls Universität Tübingen
zur Erlangung des Grades eines
Doktors der Naturwissenschaften
(Dr. rer. nat.)

vorgelegt von
Tanja Branz
aus Tübingen

Tübingen
2011

Tag der mündlichen Prüfung:	24.02.2011
Dekan:	Prof. Dr. Wolfgang Rosenstiel
1. Berichterstatter:	Prof. Dr. Thomas Gutsche
2. Berichterstatter:	Prof. Dr. Werner Vogelsang
3. Berichterstatter:	Prof. Dr. Eulogio Oset

Zusammenfassung

Meson–Spektroskopie ist eines der interessantesten Themen in der Teilchenphysik. Vor allem durch die Entdeckung von zahlreichen neuen Zuständen im Charmonium Spektrum mit Eigenschaften, die nicht durch das Konstituenten Quark Modell erklärt werden können, hat das Interesse zahlreicher theoretischer Untersuchungen auf dieses Thema gelenkt.
In der vorliegenden Dissertation werden verschiedene Mesonstrukturen diskutiert, die von leichten und schweren Quark–Antiquark Mesonen bis hin zu gebundenen Zuständen von Hadronen, sogenannten Hadronischen Molekülen, im leichten und schweren Sektor reichen. Für die Untersuchung der Mesoneneigenschaften wie Massenspektrum, totale und partielle Breiten sowie Produktionsraten verwenden wir drei verschiedene theoretische Modelle.
Gebundene Zustände von Mesonen werden zunächst in einem Modell untersucht, das auf gekoppelten Meson Kanälen basiert, bei der Meson–Meson Resonanzen dynamisch generiert werden. Die Zerfallseigenschaften von Mesonmolekülen werden anschließend in einem zweiten Modell analysiert. Die Basis dieses zweiten Zugangs bilden effektive Lagrangedichten, die die Wechselwirkung zwischen den hadronisch gebundenem Zustand und dessen Konstituenten beschreibt. Neben den Mesonmolekülen betrachten wir auch die radiativen und starken Zerfallseigenschaften herkömmlicher Quark–Antiquark Mesonen in diesem phänomenologischen Modell.
Den Abschluss der drei theoretischen Methoden, die hier vorgestellt werden, wird von einem AdS/CFT Modell gebildet. Dieses holographische Modell unterscheidet sich fundamental von den beiden vorher diskutierten Ansätzen, da zusätzliche Dimensionen und Elemente aus der String Theorie enthalten sind. Wir berechnen das Massenspektrum leichter und schwerer Mesonen und deren Zerfallskonstanten im Rahmen dieses Modells.

Abstract

Meson spectroscopy became one of the most interesting topics in particle physics in the last ten years. In particular, the discovery of new unexpected states in the charmonium spectrum which cannot be simply explained by the constituent quark model attracted the interest of many theoretical efforts.
In the present thesis we discuss different meson structures ranging from light and heavy quark–antiquark states to bound states of hadrons—hadronic molecules. Here we consider the light scalar mesons $f_0(980)$ and $a_0(980)$ and the charmonium–like $Y(3940)$, $Y(4140)$ and $Z^{\pm}(4430)$ states. In the discussion of the meson properties like mass spectrum, total and partial decay widths and production rates we introduce three different theoretical methods for the treatment and description of hadronic structure.
For the study of bound states of mesons we apply a coupled channel approach which allows for the dynamical generation of meson–meson resonances. The decay properties of meson molecules are further on studied within a second model based on effective Lagrangians describing the interaction of the bound state and its constituents. Besides hadronic molecules the effective Lagrangian approach is also used to study the radiative and strong decay properties of ordinary quark–antiquark ($q\bar{q}$) states.
The AdS/QCD model forms the completion of the three theoretical methods introduced in the present thesis. This holographic model provides a completely different ansatz and is based on extra dimensions and string theory. Within this framework we calculate the mass spectrum of light and heavy mesons and their decay constants.

Contents

1. Introduction

Historically, mesons, i.e. pions, were first introduced by Yukawa [1] in 1935 as exchange bosons generating the strong interaction between nucleons. However, pions and nucleons did not remain the only hadron states but with the improvement of the accelerator facilities, which gave access to higher mass regions, numerous states of baryons and mesons have been observed, which needed to be interpreted in a systematic way. By arranging the nearly degenerate hadron states according to their quantum numbers such as total spin and parity, a specific pattern of multiplets emerged which was the starting point of the constituent quark model introduced in 1964 by Zweig and Gell–Mann. Mesons and baryons were interpreted as composite objects consisting of a valence quark–antiquark pair ($q\bar{q}$) or three quarks (qqq), respectively. Up to now the constituent quark model is one of the most important models for hadron structure and provides a first reference point for newly observed states.

The discovery of baryons with three identical quarks, as for example first the Δ^{++} (uuu) and then the Ω^{-} (sss) state, required the introduction of an additional quantum number, which is the color charge, since otherwise these states would be forbidden by the Pauli principle. The definition of the three colors and later on the experimental evidence for this color degree of freedom in deep inelastic scattering experiments provided the basis for quantum chromodynamics (QCD) which is the underlying theory of strong interaction. One of the major challenges in the application of QCD is how quarks and gluons combine to form composite particles called hadrons. In contrast to quantum electrodynamics, QCD becomes non–perturbative at large length scales and cannot be accessed by traditional methods as for instance perturbation theory. Therefore, we do not have analytical tools at hand which allow for *ab initio* calculations of hadron properties from QCD. As a consequence, one could rely on lattice calculations starting from first principles and which were thought to be a promising technique to disentangle the hadron spectrum [2]. The huge amount of computing power required by lattice calculations still poses the main problem. For this reason, the majority of lattice calculations were done in quenched QCD which means that the dynamics of the seaquarks (fermion loops of quark–antiquark pairs) is neglected. Furthermore, lattice computations are done with finite lattice spacing which requires an extrapolation to the infinite volume limit, the continuum. Finally, lattice calculations are usually carried out with unphysically large quark masses which are later extrapolated to physical quark masses. These limitations on computer performance increase of course the uncertainty and

restrict the application of lattice QCD. Despite certain success e.g. in computing the glueball spectrum [3] at present lattice QCD cannot be used to calculate the whole hadron spectrum. More precisely, while the experimental measurements of the masses of the ground states (pseudoscalar and vector mesons) are well reproduced by lattice calculations form factors and decay properties cannot be determined by lattice QCD. Therefore, up to now our knowledge in hadron physics is to a large extent based on effective or phenomenological models aimed to give a detailed description of hadron properties.

In this context one has to mention effective field theories which provide an approximate theory for the description of physical phenomena at a chosen length scale. One of the most successful effective field theories is chiral perturbation theory (ChPT) [4, 5, 6, 7] which is based on the approximate chiral symmetry of the QCD Lagrangian. Spontaneous breaking of this symmetry gives rise to the generation of massless pseudoscalar Goldstone bosons, the pions. Therefore, ChPT describes the dynamics of Goldstone bosons in the framework of an effective field theory. In particular it provides a systematic method to explore the low–energy QCD region based on non–elementary hadronic degrees of freedom which are experimentally accessible. Since ChPT can successfully describe the structure and interaction of light mesons and also nucleons this effective field theory became a very important tool for nuclear and low–energy particle physics. However, since ChPT is based on chiral symmetry this method is necessarily restricted to the low–energy region of QCD, i.e. three flavors ($N_f = 3$), where current quark masses are small.

While the light meson sector is described by ChPT the Heavy Quark Effective Theory (HQET) has become a successful and widely used tool in the heavy quark sector (for a review see [8, 9, 10, 11]). HQET is based on the expansion of QCD in inverse powers of the heavy quark mass m_Q since the mass of a heavy quark is large compared to the typical scale of the light QCD degrees of freedom. In particular, HQET works very efficiently in transitions between hadrons containing heavy quarks, e.g. in $b \to c$ semileptonic decays. For this reason, HQET played for example an important role in the determination of the CKM matrix element V_{cb}.

Despite that lattice QCD, ChPT and HQET provide three important pillars in hadron physics, up to now there is no complete and consistent method available which can cover the full range of non–perturbative QCD. Moreover, even the aforementioned methods cannot explain the complete spectrum of the light mesons. For this reason hadron spectroscopy is an essential tool to study the strongly coupled QCD regime. The decay and production patterns together with the mass spectrum observed by experiments provide valuable information on the substructure and interaction mechanisms of hadronic matter. Phenomenological approaches modeling the hadron structure are the counterpart to the experimental observations. They aim to understand and finally explain the nature of hadrons but also serve as a framework with which new experimental observations are compared to.

Another interesting question is whether there exists hadron structures besides the

well established $q\bar{q}$ and qqq hadrons. In principle, the framework of QCD allows for further color–singlet states such as multiquark, hybrid and glueball structures. From the experimental side there are numerous states that cannot be understood in the framework of the constituent quark model and might be a signal for structure beyond the standard $q\bar{q}$ picture. In summary, the understanding and interpretation of hadronic structure is still one of the major aims in modern particle physics and provides the research topic of the present thesis.

1.1. Hadronic Structure

The following section gives a compact review on hadron spectroscopy tracing back to one of the first steps in the field of hadron structure which is the constituent quark model. With the discovery of more and more hadronic resonances it became obvious that the simple quark model is not capable to explain the full meson spectrum. Therefore, we also turn to fundamental structures beyond the quark–antiquark picture like hadronic molecules. Finally, we focus on the latest progress in the heavy quark charmonium sector. Here, in the last ten years many new charmonium–like resonances have been announced which are not easily explained as quark–antiquark configurations. Recent and less recent reviews on the vast amount of phenomena related to meson spectroscopy can be found in [12, 13, 14].

1.1.1. Constituent Quark Model

Probably the must successful and complete description of hadron structure is provided by the constituent quark model which was proposed by Murray Gell–Mann and George Zweig in 1964 [15]. Within this framework quarks were introduced as algebraic entities without experimental evidence acting as elementary and fundamental constituents of matter. The basis of the constituent quark model is the ordering scheme, specific patterns of $SU(N)$ multiplets, which emerge when hadron resonances are arranged according to their quantum numbers. Considering $SU(3)$ flavor, which includes u, d and s quarks, mesons made up of a quark–antiquark pair are arranged in nonets while the lowest lying baryons, represented by three–quark states, form a decuplet and an octet. The final breakthrough of the quark model was provided by direct evidence for quarks in deep inelastic scattering experiments at SLAC in 1968 [16]. However, since quarks are confined they do not appear as free asymptotic particles but only as constituents of the color–singlet hadrons. Hence, there is only a qualitative understanding about the nature and dynamical origin of constituent quarks which occur as quasiparticles, believed to be current quarks dressed by a cloud of gluons and $q\bar{q}$–pairs. In other words, it is known that the nontrivial and nonperturbative QCD vacuum plays an important role but the possible link between the vacuum structure and the confinement property of QCD is not

J^{PC}	I=1	I=$\frac{1}{2}$	I=0		
0^{++}	$a_0(980)$	$\kappa \equiv K_0^*(800)$	$\sigma \equiv f_0(600)$	$f_0(980)$	
0^{++}	$a_0(1450)$	$K_0^*(1430)$	$f_0(1370)$	$f_0(1500)$	$f_0(1710)$

Table 1.1.: The lowest lying scalar mesons.

solved yet. Nevertheless, the simple constituent quark model works surprisingly well and is able to classify the majority of meson and baryon resonances in the hadron spectrum. Especially the masses of the low–lying pseudoscalar and vector mesons are in good agreement with experiment.

1.1.2. Beyond the Quark Model

Despite the success of the quark model, detailed observables related to spectrum, production and decay properties of observed hadrons still pose major challenges to the theoretical understanding. In particular, already in the light meson sector we have experimentally observed resonances, as for instance the low–lying scalar mesons, which cannot be simply and consistently explained by a leading order quark–antiquark structure (for a review see [12, 13, 14]). As indicated in Tab. 1.1 the scalar sector is clearly overpopulated: There exist two meson nonets instead of one, one below and one above 1 GeV. In addition, the heavier of the two nonets contains one additional state, the $f_0(1500)$. These are clear hints for 'exotic' structures in the low–lying scalar sector. Simulations in lattice gauge theory result in bound states of gluons, where the lightest scalar glueball is predicted to have a mass of about 1.5 GeV [3]. Since glueballs can mix with ordinary $q\bar{q}$ states of the same quantum numbers, the scalar mesons $f_0(1270)$, $f_0(1500)$ and $f_0(1720)$ are usually interpreted as two $q\bar{q}$ states which mix with a nearby glueball at 1.5 GeV. The situation in the light nonet below 1 GeV is even more unclear as these states are difficult to be accommodated in the constituent quark model. The scalar resonances overlap and interfere with each other since the decay widths are very broad and sometimes close to the threshold of a decay channel. The light scalars $f_0(980)$ and $a_0(980)$ were already discussed in the 1970s as possible candidates for multiquark states. The realization of this structure is a dynamical question since it is possible that multiquark states exist as bound states of color couplings, i.e. a diquark–antidiquark pair, the so–called tetraquark structures [17, 18]. However it is also possible that $(q\bar{q})(q\bar{q})$ configurations are realized in hadron–hadron potentials [19, 20, 21] leading to bound states of two mesons, hadronic molecules. Both possibilities must be taken into account when attempting to unravel the hadron spectrum.
A further indication for hadron structure beyond the constituent quark model is

given by evidence for mesons with exotic quantum numbers like $J^{PC} = 0^{--}$, 1^{+-}. They cannot be accommodated in the $q\bar{q}$ scheme since in the constituent quark model spin (S) and orbital angular momentum (L) are related to parity P and charge conjugation C by $P = (-1)^{L+1}$ and $C = (-1)^{L+S}$. States which deviate from this relation are candidates for so–called exotic states. Indeed two examples with exotic quantum numbers are the $J^{PC} = 1^{-+}$ states $\eta_1(1400)$ and $\eta_1(1600)$ [22]. They are for example candidates for hybrid structures made up of a quark–antiquark pair interacting with an excited gluon configuration.

Due to the broad range of unresolved phenomena in the meson sector it is important to understand the full picture of meson spectroscopy in order to keep a global view of the field. Therefore, investigating various structures with different models might provide a better insight than even a detailed discussion of particular issues within one specific theoretical approach. For this reason, the present dissertation covers meson spectroscopy from light to double heavy mesons, from ordinary $q\bar{q}$ mesons to bound states of mesons, so–called hadronic molecules. This structures are studied in the light of different theoretical approaches: We consider for example dynamically generated resonances from meson–meson coupled channels. Furthermore, we introduce an effective field theoretical model for hadronic bound states which is based on effective interaction Lagrangians. This method we use to study traditional $q\bar{q}$ quark model states and bound states of mesons. Besides this rather traditional methods, mesons are also discussed in the framework of a holographic model which is based on extra dimensions, or roughly speaking, on new physics. The main idea of this approach is the correspondence between string theory in Anti–de–Sitter space (AdS) and conformal field theory (CFT) describing the hadronic world.

In the following Chapter 2 we focus on selected topics which provide the subject matter of the present thesis. For example, we summarize the experimental status, previous theoretical investigations and the resulting different interpretations. The chapter is divided into two parts: The first section shortly addresses the light meson sector while section 2.2 deals with the charmonium spectrum which is rather topical through recent experimental observations.

Chapters 3–5 reflect the research work of the dissertation. Three theoretical methods are introduced to analyze binding, decay and production properties of different mesonic structures.

The range of theoretical models includes dynamically generated meson–meson resonances by coupled channels [23, 24]. From this approach we obtain information on the meson–meson interaction, for example whether the binding is strong enough to form a molecular state and which meson–meson channels yield the dominant contributions to the bound state.

Further on, we analyze meson molecules in a complementary effective field theoretical approach for hadronic bound states (Chapter 4). This method, based on effective Lagrangians, is very useful for studying decay and production properties [25, 26, 27]. Besides meson molecules we also apply this method to conventional mesons made

up of a quark–antiquark pair.
In Chapter 5 the meson properties are studied in a completely different light. The holographic model is based on the correspondence of strings living in the AdS space and conformal field theory representing hadronic matter [28].
Finally, we summarize the thesis in Chapter 6 and draw the conclusions from our findings.

2. Meson Spectroscopy

In this Chapter we give a survey on the status of meson spectroscopy looked at from two perspectives — experimental observations and theoretical interpretations. For the sake of readability we discuss mesons containing light and heavy quarks separately. We try to cover a broad range of issues in meson spectroscopy in order to give an overview of the topic. But of course the focus is put on these meson resonances which are studied in this work.

2.1. Meson Spectroscopy in the Light Sector

For decades it is known that the meson spectrum is much richer than one might expect from the simple quark model predictions. This fact was first observed and noticed in the light meson sector [12, 13, 14]. However, from the theoretical point of view this is not very surprising since QCD would allow in principle for further color singlet objects beyond the minimal $q\bar{q}$–configuration like multiquark states and hadrons containing gluonic components. In particular, the role of gluons, being well established in the high energy perturbative QCD, is still unclear in the nonperturbative limit. The non–abelian nature of QCD naturally leads to gluon self–interaction which could result in bound states of gluons. These gluonic bound states or glueballs have been intensely studied in various lattice calculations [3] and constituent glue models [29, 30]. Lattice calculations predict for the lightest glueball, which has scalar quantum numbers, a mass of about 1650 MeV with an uncertainty of about 100 MeV (see PDG [22], non–$q\bar{q}$ review). The experimental candidate for the scalar glueball was seemingly found by the Crystal Barrel Collaboration at CERN [31]. The scalar $f_0(1500)$ was later confirmed by the WA102 Collaboration [32] in glue–proton–proton reactions with the gluonic structure produced by pomeron or multigluon fusion. As a consequence, with the announcement of the $f_0(1500)$ the scalar nonet above 1 GeV is overpopulated so that a non–$q\bar{q}$ origin of the $f_0(1500)$ seems natural. Since the glueball has the same quantum numbers, the probability of mixing with the nearby scalar mesons of the quark model is rather high. In the literature the admixture of a glueball with the nearby two conventional $q\bar{q}$ states is the most common explanation for an overpopulated scalar nonet of the physical mesons $f_0(1370)$, $f_0(1500)$ and $f_0(1710)$. But also note that in some scenarios it is discussed that a dominant glueball component resides in the $f_0(1710)$.

Quark–gluon hybrids [33, 34] are a further variety of how gluon dynamics could be realized in hadron structure. Here, a $q\bar{q}$ state is bound by an excited gluon, or rather, hybrids are made up of a valence quark–antiquark pair plus an additional valence gluon.
In the present work we focus on hadronic bound states. There are two scalar mesons in the light meson sector which are most likely bound states of mesons. We therefore discuss the $f_0(980)$ and $a_0(980)$ in more detail.

2.1.1. $f_0(980)$ and $a_0(980)$

The scalars $f_0(980)$ and $a_0(980)$ are known for more than 30 years but their nature is still controversially discussed (see also the corresponding minireview in 'review of particle physics' [22]). Since the scalar nonet above 1 GeV seems established as the ${}^3P_0$ $q\bar{q}$ nonet of the quark model with an additional glueball configuration, it is not possible to further accommodate the $f_0(980)$ and $a_0(980)$. Furthermore, the properties of the isovector $a_0(980)$ and isoscalar $f_0(980)$ mesons are not in agreement with quark model predictions. For instance, the a_0 and f_0 masses lie about 100 MeV below theoretical estimates based on the constituent quark model (see e.g. [35]). Due to the very peculiar decay properties, it is difficult to precisely measure the decay widths of these states. Experimental values for the f_0 and a_0 decay widths range between 40 and 100 MeV which even deviates more from the quark model prediction of about 500 MeV [17, 35]. Finally, the near degeneracy in mass of the isosinglet and triplet states would require an ideal mixture of the states as e.g. realized in the vector nonet. Ideal mixing requires that $I = 0$ and $I = 1$ states are dominantly nonstrange as in case of ρ and ω mesons. However, ϕ production and the strong coupling to the $K\bar{K}$ channel point to a dominant strangeness content.
These large discrepancies gave evidence for a possible multiquark nature of this states. There are several distinctive signatures for the multiquark interpretation of a resonance. While tetraquarks are characterized by large decay widths due to the fall–apart mechanism (see e.g. [17]), typical features for molecules are their proximity to a threshold and the strong couplings to the constituent channel. Both criteria are fulfilled in the cases of the $f_0(980)/a_0(980)$ mesons. Both lie close to the $K\bar{K}$ threshold and the anomalously large coupling of the $f_0(980)$ to $K\bar{K}$ despite having almost no phase space is a strong hint that one possibly deals with a kaon molecule. The first analysis of the multiquark structure in the $J^{PC} = 0^{++}$ sector was performed by assuming a diquark–antidiquark structure [17]. Later it was found that the tetraquark systems, identified with the $f_0(980)$ and $a_0(980)$, are realized as weakly bound $K\bar{K}$ molecules in analogy to the deuteron [18, 19, 20]. The meson–meson potentials derived in this framework in combination with a coupled channel Schrödinger equation were used to reproduce the observed phase shifts for the a_0 and f_0 in $\pi\pi$–scattering.
The scalar mesons are experimentally well established and studied in different pro-

duction processes where the most important ones are introduced in the following.

1. **Photoproduction**

   Electromagnetic probes are ideally suited to study the hadronic substructure of a state. In particular, radiative processes are sensitive to the charge content since photons couple directly to the charged constituents of the object. In addition the QED coupling is well known and allows for a precise computation of observables as for instance two–photon production cross sections and two–photon decay widths.

   The radiative decay widths have the potential to discriminate between the various scenarios since theoretical models display a large sensitivity to different substructure assumptions. An overview on the electromagnetic decay width in the context of different f_0 scenarios is for example given in [36]. The results obtained within a tetraquark model (0.3 keV) is similar to the $K\overline{K}$ molecule prediction of 0.24 keV. In contrast, two–photon decay properties of $q\bar{q}$ states are very sensitive to the flavor content (i.e. mixing between strange and non–strange components), to the meson size and the quark masses [37]. For example, by assuming a non–strange $q\bar{q}$ state leads to the two–photon decay width of 4.5 keV [21] while a pure $s\bar{s}$ configuration results in 0.3–0.5 keV [38].

   We shortly introduce two possible photo production processes of the $f_0(980)$ and $a_0(980)$ mesons.

   - **Two–photon fusion**

     Two–photon production processes and in particular the two–photon widths extracted from them are considered to be useful to determine the structure of mesons since the photon coupling is related to the charge distribution inside the meson.

     e^+e^- colliders specifically allow for high statistics data on meson production. Meson resonances are produced by two–photon fusion in the reaction $e^+e^- \to e^+e^-H$, where the hadron H is produced by the photons radiated from the beam electron and positron. Two–photon production of mesons has further advantages over meson production in hadronic processes. For example, a single meson can be produced without 'hadronic baggage'. Furthermore, due to the fact that photons couple directly to the quarks, the photon production is sensitive to the charge distribution of the produced hadron i.e. the production rate will be proportional to the fourth power of the quark charge. As a consequence pure gluonic degrees of freedom without electric valence charge like glueballs are not expected to be produced in photon–photon collisions. Furthermore, this production mechanism profits from less unknown parameters. The production rate can be calculated from QED with the two–photon decay width as the only unknown parameter.

In the two–photon production processes we can differentiate between two ways of detection, 'tagged' and 'untagged' data samples. Provided that the scattering angle of the $e^{\pm}$ is large enough they will be detected or tagged by the detector. Since the photon propagator is proportional to the inverse of the photon momentum squared $(1/q^2)$ the virtual photons are sharply peaked in the forward direction. Therefore, in case of tagged $e^{\pm}$ the exchanged photon has a significant component of longitudinal polarization, and hence is virtual. On the contrary, if neither the electron nor the positron is tagged, the exchanged photons are 'real'. This leads to powerful selection rules on the quantum numbers of the meson formed in the collision. The quantum numbers of the final state are restricted to states with positive charge conjugation $(C = +)$.

B–factories such as BELLE and BABAR are excellent laboratories to investigate two–photon production of low lying scalar mesons with very large statistics. For example, the BELLE collaboration [39] analyses the $\gamma\gamma \to \pi^0\pi^0$ process in e^+e^- collisions. The analysis is made in the 'zero–tag' mode which means that neither the recoil electron nor the positron is detected.

- **Initial state radiation**

  A further production process from photons is initial state radiation (ISR) which is diagrammatically represented in Fig. 2.1 (a). Here, a vector meson state is produced by a virtual photon emitted by the initial electron–positron pair. The BABAR collaboration studies $f_0(980)$ production in the processes $e^+e^- \to K^+K^-(\pi^+\pi^-,\ \pi^0\pi^0,\ K^+K^-,\ \ldots)\gamma$. The signals come predominantly from the intermediate states ϕ and $f_0(980)$ with $\phi \to K^+K^-$ and $f_0 \to \pi\pi$.

  The advantage of ISR is even more apparent in the case of vector meson production since the quantum numbers of the hadron state produced by the virtual photon are necessarily determined as $J^{PC} = 1^{--}$ (see also discussion of charmonium production).

2. ϕ **production**

   f_0 and a_0 production in ϕ decays is well suited to test the flavor content of the scalars. Since the ϕ meson is a well established $s\bar{s}$ state, ϕ production is sensitive to the $s\bar{s}$ component of the $f_0(980)$ and $a_0(980)$ mesons. For instance, in the quark–antiquark picture a dominant $s\bar{s}$ component residing in f_0 or a_0 would lead to a sizable production rate while a non–strange configuration would result in a highly suppressed production.

   ϕ production of the f_0 and a_0 mesons, which subsequently decay to a $\pi\pi$ or $\pi\eta$ pair are typically studied at electron–positron colliders as for instance

SND [40], CMD–2 [41] or KLEO [42, 43]. The $e^+e^- \to \pi^+\pi^-\gamma$ and $e^+e^- \to \pi^0\eta\gamma$ transitions are fed by three different processes. The photon can either be emitted from the initial electron–positron pair (ISR), or originate from final state radiation (FSR). The ISR process is illustrated in Fig. 2.1 (a) and does not contribute to the $\phi \to f_0\gamma$ decay. In the FSR process the final photon is emitted from the final state hadrons, in this case the pions (see Fig. 2.1 (b)). Hence, FSR does also not contribute to the f_0/a_0 production. Only the third

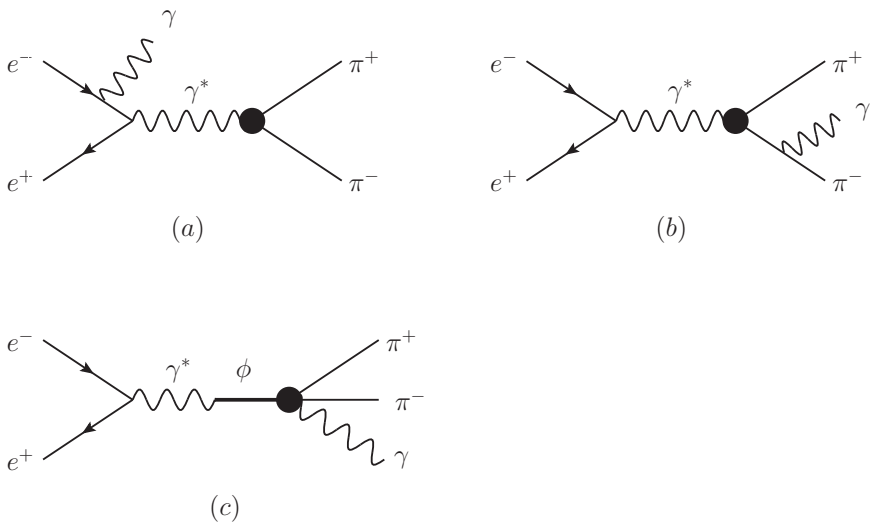

Figure 2.1.: Diagrams contributing to the $e^+e^- \to \pi^+\pi^-\gamma$ transition.

process, which is usually referred to as the structure dependent (SD) amplitude [44], can be clearly assigned to the $\phi \to f_0\gamma\,(f_0 \to \pi\pi)$ transition. Here the vector meson (ϕ meson) is produced by a virtual photon. The corresponding decay is diagrammatically represented by the graph in Fig. 2.1 (c).

In theoretical approaches the $\phi \to f_0(a_0)\gamma$ decays are found to be rather sensitive to the underlying meson structures. The different scenarios were analyzed in [45] which resulted in equal branching ratios for a_0 and f_0 of $\mathrm{Br}(\phi \to f_0(a_0)\gamma) = 4{\cdot}10^{-5}$ in the $K\bar{K}$ molecule picture while $q\bar{q}$ and tetraquark configurations lead to much smaller production rates of 10^{-6} or even less. The ϕ production rates quoted by PDG [22] are $\mathrm{Br}(\phi \to f_0\gamma) = (3.22 \pm 0.19) \cdot 10^{-4}$ and $\mathrm{Br}(\phi \to a_0\gamma) = (7.6 \pm 0.6) \cdot 10^{-5}$, respectively, clearly favoring the molecular $K\overline{K}$ interpretation.

3. **Production in semileptonic decays**

Besides the radiative production processes, weak semileptonic $D_{(s)}$ and $B_{(s)}$ decays provide a very clean environment to study the properties of the $f_0(980)$ meson. The first evidence for the scalar $f_0(980)$ in a semileptonic decay was

found in the $D_s^+ \to f_0 e^+ \nu_e$ process illustrated in Fig. 2.2, investigated by the CLEO [46, 47] and BABAR [48] collaborations.

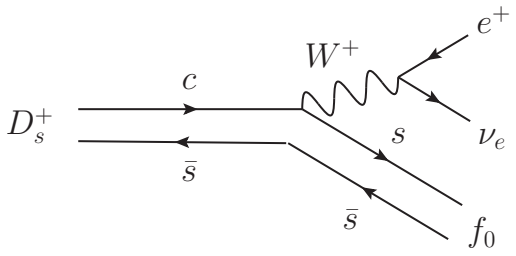

Figure 2.2.: Weak production of f_0.

Semileptonic decays are well suited to probe different structure scenarios of the f_0 quark content. For example, the D_s^+ decay is very sensitive to the strange quark component of the $f_0(980)$ as can be seen from Fig. 2.2 (see also discussion in Ref. [46, 47]). Furthermore, in Ref. [49] it was found that the ratio of f_0 production in nonleptonic and semileptonic decays is rather different in the quark–antiquark and tetraquark pictures. More precisely, the ratio $\Gamma(D_s^+ \to f_0(980) l^+ \nu_l)/\Gamma(D_s^+ \to f_0(980)\pi^+)$ is more suppressed in the $q^2\bar{q}^2$ scenario than in the standard $q\bar{q}$ model which is in favor of the multiquark interpretation for the light scalar mesons.

Since f_0 production in weak semileptonic decays is not analyzed in this thesis we do not go into further detail.

2.2. Meson Spectroscopy in the Charmonium Sector

The discussions involving a possible non–$q\bar{q}$ nature of meson resonances find their repetition in the heavy meson and especially the charmonium sector [50, 51]. Until the late 90s the charmonium spectrum was thought to be well understood. First of all, the $c\bar{c}$ mass spectrum is not overcrowded by observed extra states as is the case in the light scalar sector. Furthermore, the states below the open charm threshold are narrow since hidden–charm decay modes are OZI suppressed. The OZI–rule was suggested by Okubo, Zweig and Iizuka in the 1960s which states that processes described by disconnected quark line diagrams are strongly suppressed. As a consequence, we deal with a clear spectrum without an overlap or merger of states. On top of that, the $c\bar{c}$ mass spectrum can be well reproduced by lattice simulations and in potential models [50]. The success of theoretical approaches can be judged from Fig. 2.3. Besides some missing states potential model calculations indicated by the red lines are in good agreement with experimental measurements in blue [50].

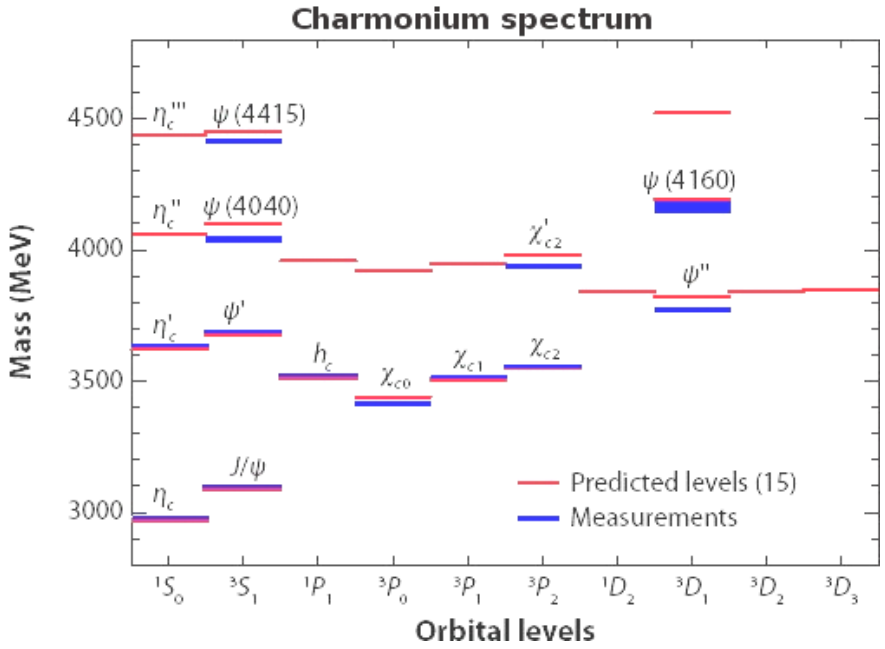

Figure 2.3.: Charmonium spectrum: experimental measurements versus theoretical predictions.

The situation changed around the turn of the millennium. Here investigations were essentially fueled by the enormous progress on the experimental side. Many new charmonium–like states were discovered by the BELLE [52, 53] and BABAR [54, 55] collaborations at the B–factories, but also in experiments by the CDF [56], D0 [57] and CLEO [58, 59] collaborations. Original built to study B physics related CP–violating processes, the B–factories turned out to be an excellent environment to study charmonium spectroscopy. Charmonium structures are produced in B meson decays, e^+e^- annihilation and photon–photon fusion as illustrated in first three diagrams of Fig. 2.4. In the latter case the very low cross sections for these processes are compensated by the very high luminosities obtained by the B–factories. Because C–parity is conserved in electromagnetic processes the final $c\bar{c}$ system can be identified as a state with positive C–parity. A further important production mechanism is provided by the initial state radiation (ISR) at electron–positron colliders as already discussed previously. Here a hard photon is emitted by the initial electron–positron pair while the vector charmonium state is produced by a second virtual photon with the quantum numbers $J^{PC} = 1^{--}$. Meson production by ISR has two important advantages. First of all, in contrast to the previous processes, ISR can definitely identify the quantum numbers $J^{PC} = 1^{--}$ of the charmonium. Second, IRS allows to measure the hadronic cross section over a wide range of energies at the same beam energy. The ISR–production became highly topical with the start of the high luminosity electron– positron colliders at B–factories.

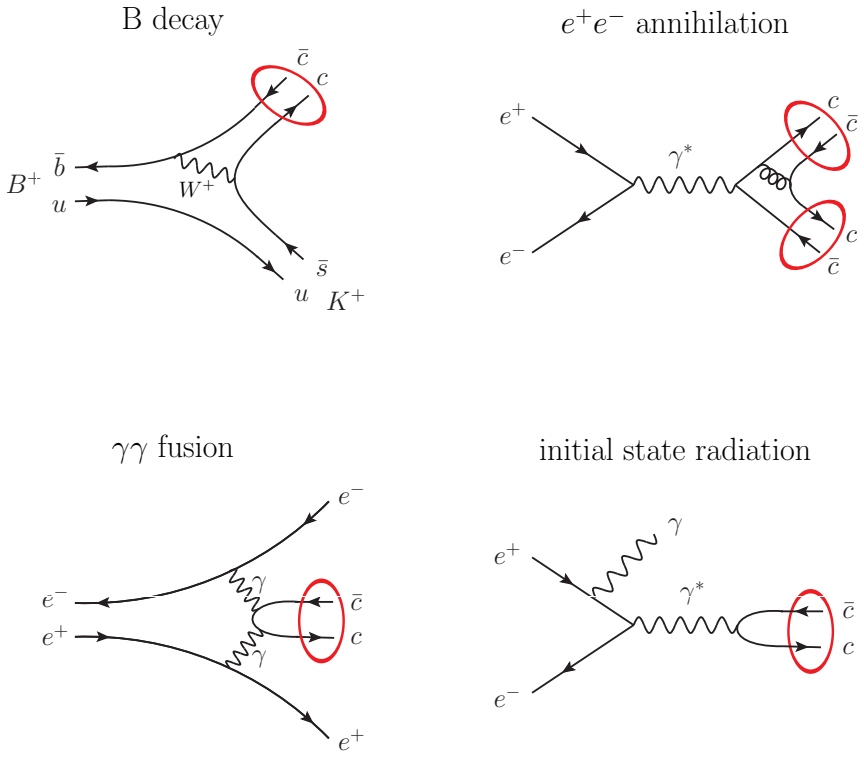

Figure 2.4.: Charmonium production processes.

In the last 10 years many charmonium–like X, Y and Z resonances have been discovered. The present status of the experimental findings is summarized in Tab. 2.1. Besides masses and widths the table also indicates the decay and production patterns and the respective experiment. In most cases the quantum numbers are only partially known. The exception are of course the vector mesons which are produced by ISR. The majority of the X, Y and Z mesons cannot be easily explained within the standard charm–anticharm ($c\bar{c}$) assignment. For instance, besides the overpopulation in the $c\bar{c}$ spectrum due to the numerous occurrence of X, Y and Z mesons, decay patterns of these mesons are in some cases in contradiction to the standard charmonium predictions. One example is the sizable $\omega\phi$ hidden charm decay width $\Gamma(Y(3940) \to \omega\phi)$ of the $Y(3940)$ [60, 61, 25] which should be significantly OZI suppressed in the charmonium picture. Some of these new charmonium–like states are considered good candidates for possessing a hadronic substructure which goes beyond the standard $c\bar{c}$ assignment ranging from quark–gluon hybrid mesons [62, 63] and tetraquark states [64] to dynamically generated states [65] or bound states of two mesons called hadronic molecules [66, 25]. A review on the experimental situation with a first overview of the present theoretical understanding is given e.g. in [50, 51, 60, 61]. From all of this newly discovered charmonium–like X, Y and Z resonances the observation of the charged $Z^{\pm}(4430)$ by the BELLE Collabora-

State	M (MeV)	Γ (MeV)	J^{PC}	Decay Modes	Production Modes	Experiments
$X(3872)$	3871.4 ± 0.6	< 2.3	1^{++}	$\pi^+\pi^- J/\psi$,$\gamma J/\psi$	$B \to KX(3872)$, $p\bar{p}$	Belle, CDF, D0, BaBar
$X(3875)$	3875.5 ± 1.5	$3.0^{+2.1}_{-1.7}$	?	$D^0\bar{D}^0\pi^0(\gamma)$	$B \to KX(3875)$	Belle, BaBar
$Z(3940)$	3929 ± 5	29 ± 10	2^{++}	$D\bar{D}$	$\gamma\gamma \to Z(3940)$	Belle
$X(3940)$	3942 ± 9	37 ± 17	J^{P+}	$D\bar{D}^*$	$e^+e^- \to J/\psi X(3940)$	Belle
$Y(3940)$	3943 ± 17	87 ± 34	J^{P+}	$\omega J/\psi$	$B \to KY(3940)$	Belle, BaBar
$Y(4008)$	4008^{+82}_{-49}	226^{+97}_{-80}	1^{--}	$\pi^+\pi^- J/\psi$	e^+e^-(ISR)	Belle
$Y(4140)$	4130 ± 4.1	$11.7^{+12.0}_{-8.7}$	J^{P+}	$J/\psi\phi$	$B^+ \to K^+Y(4140)$	CDF
$X(4160)$	4156 ± 29	139^{+113}_{-65}	J^{P+}	$D^*\bar{D}^*$	$e^+e^- \to J/\psi X(4160)$	Belle
$Y(4260)$	4264 ± 12	83 ± 22	1^{--}	$\pi^+\pi^- J/\psi$	e^+e^-(ISR)	BaBar, CLEO, Belle
$Y(4350)$	4361 ± 13	74 ± 18	1^{--}	$\pi^+\pi^-\psi'$	e^+e^-(ISR)	BaBar, Belle
$Z^{\pm}(4430)$	4433 ± 5	45^{+35}_{-18}	?	$\pi^{\pm}\psi'$	$B \to KZ^{\pm}(4430)$	Belle
$Y(4660)$	4664 ± 12	48 ± 15	1^{--}	$\pi^+\pi^-\psi'$	e^+e^-(ISR)	Belle

Table 2.1.: Charmonium–like X, Y and Z resonances.

tion [67] presents so far the culmination of the series since a $c\bar{c}$ assignment can be clearly ruled out.
In the present work three of the states in Tab. 2.1 are discussed in more detail: $Y(3940)$, $Y(4140)$ and the $Z^{\pm}(4430)$. The two Y states show similar decay and production patterns. In particular, both resonances were produced in B decays and observed in hidden–charm decay modes. Both charmonium–like objects are characterized by unusually large hidden–charm decay rates which are orders of magnitudes stronger than the predictions for conventional $c\bar{c}$ states. In general, $c\bar{c}$ states decay dominantly to open charm decay modes while the hidden–charm decay channels are OZI–suppressed which is diagrammatically represented in Fig. 2.5. Hidden–charm decays of $c\bar{c}$ mesons are typically of a few keV only [61, 60]. We will see later on that in the meson bound state assumption the OZI suppression of hidden–charm modes can be circumvented by intermediate loops of charmed mesons.

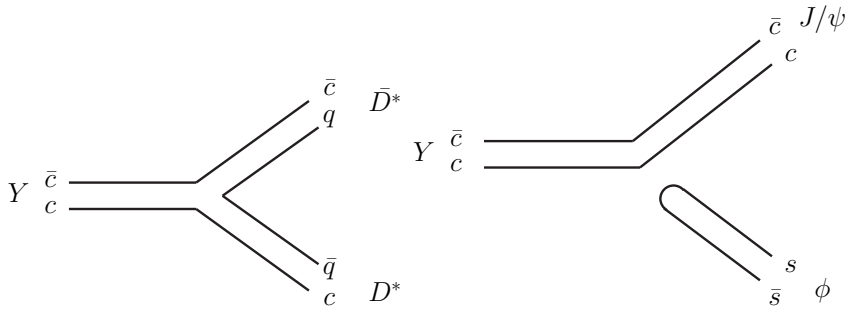

Figure 2.5.: Open– and hidden charm decays of $c\bar{c}$ states.

2.2.1. Y(3940)

The $Y(3940)$ is rather well established since it was observed by BELLE [68] in $B \to Y(3940)K$ decays with $Y(3940) \to J/\psi\omega$ and later on confirmed by BABAR [69]. The signal for the $Y(3940)$ is depicted in Fig. 2.6 (events per invariant mass of $J/\psi\omega$). Mass and widths are determined as $m_{Y(3940)} = 3914.6^{+3.8}_{-3.4}(\text{stat}) \pm 2(\text{syst})$ MeV and $\Gamma_{Y(3940)} = 34^{+12}_{-8}(\text{stat}) \pm 5(\text{syst})$ MeV by BABAR. The measurement by BELLE leads to larger values with $m_{Y(3940)} = (3943 \pm 17)$ MeV and $\Gamma_{Y(3940)} = (87 \pm 34)$ MeV.
The hidden–charm decay width can be estimated from the measured product of the branching fractions

$$\text{Br}(B \to KY(3940))\text{Br}(Y(3940) \to \omega J/\psi) = (7.1 \pm 3.4) \cdot 10^{-5} \text{ (BELLE [68])}$$
$$\text{Br}(B \to KY(3940))\text{Br}(Y(3940) \to \omega J/\psi) = (4.9 \pm 1.1) \cdot 10^{-5} \text{ (BABAR [69])}\,.$$

The upper limit for the branching fraction for B decays to a charmonium state $\text{Br}(B \to K(c\bar{c}))$ is about 10^{-3} (see also [22]) which leads to the lower limit for the

partial decay width $\Gamma(Y(3940) \to \omega J/\psi)$ of about 1 MeV. This value is several orders of magnitude larger than expected values for a charmonium state [50].
Last year the BELLE collaboration found a resonance in the process $\gamma\gamma \to J/\psi\omega$. The mass and width of the so–called $X(3915)$ state exposes this resonance as a good candidate for the $Y(3940)$. From the measured product of the two–photon decay width and branching ratio $\Gamma(X(3915) \to \gamma\gamma)\mathrm{Br}(X(3915) \to \omega J/\psi) = 61 \pm 17 \pm 8$ eV one can estimate the decay width $\Gamma(X(3915) \to \gamma\gamma) \approx 0.4$ keV.

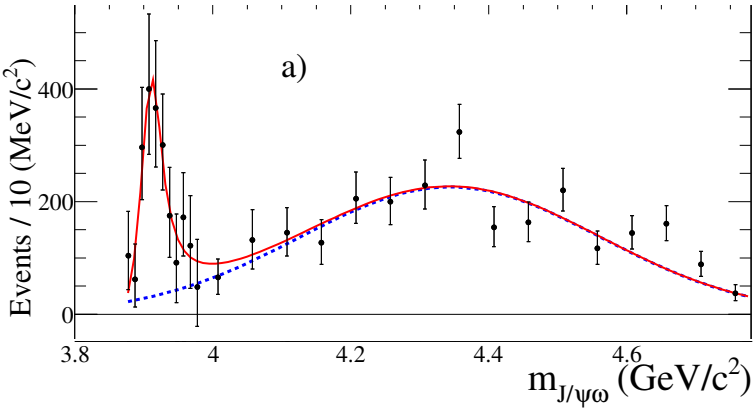

Figure 2.6.: $Y(3940)$ resonance by BABAR [69].

The $Y(3940)$ meson lies close to the $D^*\bar{D}^*$–threshold which makes a molecular bound state interpretation of D^* mesons rather natural. For this reason, the binding of the system is studied in different approaches. One of the first studies on the binding of $D^*\bar{D}^*$ systems was performed in [70]. In this work it is already predicted that one–pion exchange is sufficient to bind the $D^*\bar{D}^*$ system, many years before the discovery of the $Y(3940)$. In addition, the unitarized coupled channel model in [65] finds that the $Y(3940)$ is dominantly a $D^*\bar{D}^*$ bound state with $J^{PC} = 0^{++}$.
In chapter 4 we analyze the hidden–charm and two–photon decay properties in a theoretical approach for hadronic bound states.

2.2.2. Y(4140)

In contrast to the previously discussed $Y(3940)$ [56], the heavier charmonium–like $Y(4140)$ is only observed by the CDF Collaboration in the exclusive $B^+ \to Y(4140)K^+$ decay. The significance of the signal is smaller in comparison to the one of the $Y(3940)$ as one can see from Fig. 2.7 indicating the number of events in dependence on the invariant mass of $\phi J/\psi$. The mass and width of the new state are found to be $m_{Y(4140)}$=4130.0±2.9(stat)±1.2(syst) MeV and $\Gamma_{Y(4140)} = 11.7^{+8.3}_{-5.0}$(stat)±3.7(syst) MeV. Curiously, the $Y(4140)$ shows the same production and decay properties as the $Y(3940)$ since it is also observed in the untypically large hidden–charm decay channel $Y(4140) \to J/\psi\phi$. In analogy to the $Y(3940)$ the lower

limit for the $\Gamma(Y(4140) \to J/\psi\phi) > 100$ keV decay width can be estimated from the B decay rate $\mathrm{Br}(B^+ \to Y(4140)K^+)\mathrm{Br}(Y(4140) \to J/\psi\phi) = (9.0 \pm 3.4 \pm 2.9) \cdot 10^{-6}$ by using the estimate $\mathrm{Br}(B \to K(c\bar{c})) < 10^{-3}$.
The electromagnetic interaction of the $Y(4140)$ was studied by the BELLE collaboration [71] in the $\gamma\gamma \to \phi J/\psi$ channel, but no explicit signal for the $Y(4140)$ was deduced. The lower limit of the measured observable $\Gamma(Y(4140) \to \gamma\gamma)\,\mathrm{Br}(Y(4140) \to \phi J/\psi) < 39$ eV results in $\Gamma(Y(4140) \to \gamma\gamma) < 0.14$ keV.

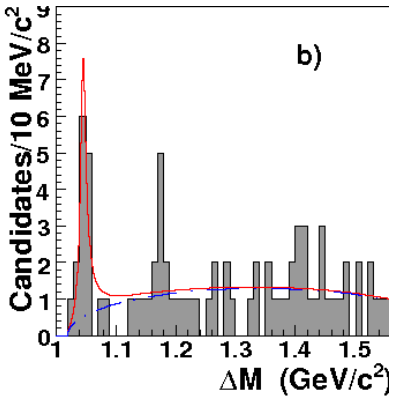

Figure 2.7.: $Y(4140)$ measured by CDF [56].

A further common feature of the $Y(3940)$ and $Y(4140)$ is the proximity to an open charm threshold. In this case the difference between the $Y(4140)$ mass and the $D_s^{*+}D_s^{*-}$ threshold is less than 100 MeV. As a consequence the $D_s^{*+}D_s^{*-}$ configuration is likely to play a dominant role. Nevertheless, the binding mechanism needs to be studied in different theoretical approaches. One of the standard methods for investigating binding is based on meson exchange potentials [72]. In this case the pion exchange potential is not sufficient to bind the system. However, when adding η and ϕ exchange mesons two $D_s^{*+}D_s^{*-}$ bound states are generated with $J^{PC} = 0^{++}$ and 2^{++}. In addition QCD sum rule studies [73] give support for a $Y(4140) = D_s^{*+}D_s^{*-}$ bound state with $J^{PC} = 0^{++}$.

2.2.3. Z(4430)

From all the X, Y and Z mesons the charged charmonium–like $Z^{\pm}(4430)$ announced by BELLE [67] is the most spectacular discovery since it is the first detection of a charged hidden–charm state. Therefore, a conventional $c\bar{c}$ as well as a hybrid configuration can be clearly ruled out. Provided that the $Z^{\pm}$ resonance becomes definitely established, this would be the proof for the existence of a multiquark state either realized as meson molecule or as compact diquark–antidiquark structure. The $Z^{\pm}$ resonance was, in analogy to the Y states, observed in $B \to Z^+(4430)K$ decays with $m_{Z^+(4430)} = 4443^{+15+19}_{-12-13}$ MeV and $\Gamma_{Z^+(4430)} = 107^{+86+74}_{-43-56}$ MeV. A remarkable property

of this state is that the $Z^+(4430)$ is only observed in the $\pi^+\psi'$ decay mode while it does not seem to decay to $\pi^+\psi$ despite that this mode is favored by phase space. Therefore, the branching fraction $\Gamma(Z^+(4430) \to \pi^+\psi')/\Gamma(Z^+(4430) \to \pi^+\psi)$ is expected to be much larger than unity. Although some arguments [74, 75, 76, 77] were put forward to understand this dynamical selection rule, a full quantitative explanation is not given yet. The $Z^\pm$ also shows a sizable coupling to the hidden–charm decay channel. Due to the product of the branching ratios $\mathrm{Br}(B \to Z^+K)\mathrm{Br}(Z^+ \to \psi'\pi^+) = (4.1 \pm 1.0 \pm 1.4) \cdot 10^{-5}$ [67] the partial decay width $\Gamma(Z^\pm \to \pi^\pm\psi')$ is expected to be of the order of several MeV [50].
The announcement of the $Z^\pm$ lead the BABAR Collaboration to search for a corresponding signal but without evidence so far. It was speculated that the resonant structure, observed by BELLE, might arise from interference effects in the $K\pi$ rather than in the $\pi\psi'$ channel. After this report the BELLE Collaboration [78] reanalyzed their data sample in a full Dalitz–plot formalism which resulted in a 6.4 σ signal for $Z^+ \to \pi^+\psi'$ with mass $m_Z = 4443^{+15+19}_{-12-13}$ MeV and width $\Gamma = 107^{+86+76}_{-43-56}$ MeV. The signal of the $Z^\pm$ resonance is depicted in Fig. 2.8 (events in dependence on the invariant $\psi'\pi$ mass squared). This reanalysis confirms and even supersedes the previous $Z^\pm(4430)$ resonance parameters of [67]. The larger errors contain e.g. the uncertainties in the spin assignment of the Z^+ ($J = 0, 1$) and in the orbital angular momentum in the B decay. The reanalysis by BELLE results in a product branching fraction $\mathrm{Br}(\bar{B}^0 \to K^- Z(4430)^+)\mathrm{Br}(Z(4430)^+ \to \pi^+\psi') = (3.2^{+1.8+5.3}_{-0.9-1.6}) \cdot 10^{-5}$ [78] which is consistent with the BABAR upper limit. The decay mode $\psi'\pi^+$, assuming standard conservation laws, leads to an identification of the Z^+ as an isotriplet state with positive G–parity. The J^P quantum numbers remain to be determined.

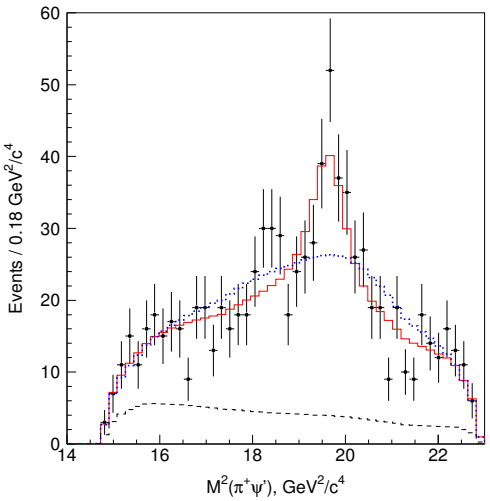

Figure 2.8.: $Z^\pm(4430)$ by BELLE [67].

After the discovery of the $Z^\pm(4430)$ the BELLE Collaboration had evidence for

further charged charmonium–like states in the $B \to K\pi^+\chi_{c1}$ decay channel called $Z_1^+(4050)$ and $Z_2^+(4250)$ [79]. The significance of the signals is much smaller than in the case of the $Z^\pm(4430)$.
Since the $Z^\pm(4430)$ cannot be explained by an ordinary $c\bar{c}$ structure it has already been discussed as either a radially excited $c\bar{c}u\bar{d}$ tetraquark [74, 64, 75, 80], a less compact hadronic meson molecule [81, 82] or as a threshold effect [77]. Further explanations for the occurrence of the $Z(4430)^+$ are a cusp in the D_1D^* channel [83], a radial excitation of a $c\bar{s}$ configuration [84], a baryon–antibaryon (baryonium) bound state [85] or even a ψ' bound state in mesonic matter [86]. However, due to the nearby $D_1\bar{D}^*$ threshold the $Z^\pm$ is regarded as a top candidate for a meson molecule. There are two D_1 mesons which are discussed as the bound state partner of the D^* meson. Both are almost degenerate in mass but their widths differ significantly. Therefore, only the $D_1(2420)$, which is fairly narrow with a total width of about 20 MeV, would principally allow the formation of a hadronic bound state. The other possibility, the $D_1' \equiv D_1(2430)$, has a rather large width of about 400 MeV which exceeds even the total width of the bound state. Meson molecules are most likely realized by s–wave bound states since they are characterized by a small binding energy, hence, the possible quantum numbers are $J^P = (0, 1, 2)^-$. The binding of the D_1D^* system is studied by standard methods like meson exchange potentials and QCD sum rule. In the one–pion exchange model of Ref. [87] it is found that the $D_1'\bar{D}^*$ can form a bound state with $J^P = 1^-$. Further inclusion of sigma meson exchange leads to s–wave binding for $D_1'\overline{D^*}$ with $J^P = 0^-,\ 1^-,\ 2^-$ [88]. However, in both approaches it is assumed that the broad D_1' is one of the constituents. Since the width of the constituent meson (D_1') becomes larger than that of the meson molecule, the formation of a bound state is disfavored. The inclusion of the sigma–exchange potential also leads to binding of the $D_1\overline{D}^*$ configuration but only for $J^P = 0^-$ and at the price of a large cutoff at the meson interaction vertex which in turn leads to an enhanced attraction of one–pion–exchange. Finally, QCD sum rule studies [89, 90] support a $D^*\bar{D}_1$ molecular structure for the $Z^\pm$ with $J^P = 0^-$. The study of the low–energy $D_1\overline{D^*}$ interaction in a quenched lattice calculation, where virtual $q\bar{q}$ fluctuations are neglected, also indicates attraction in the $J^P = 0^-$ channel, but this effect is considered probably too weak to lead to the formation of a bound state [91].
The hidden–charm decay mode $\pi\psi'$ and in particular the unexpected non–observation of the $\pi\psi$ decay is the topic of this work and we try to understand this observations in the framework of the constituent meson model in Chapter 4.

2.3. Outline of the theory part

In the following chapters we turn to the theoretical analysis of various meson properties by using different methods. The aim is to gain a broad insight into aspects

of meson spectroscopy. Therefore we discuss different resonances ranging from the established $q\bar{q}$ structures to bound states on the hadron level in the light and heavy meson sectors. In order to study the fundamental meson structures we use different theoretical approaches to illuminate the topic from different view–points.

The outline of the present work is as follows:

Chapt.	Method	Meson Structure	Details
3	Coupled Channels	**meson–meson** (dyn. generated)	$D_{s2}^*(2573)$ and flavor exotic mesons, radiative decays
4	Effective model for hadronic bound states	**meson–meson** (molecules)	light scalars: $f_0(980), a_0(980)$ hidden–charm: $Y(3940), Y(4140), Z^{\pm}(4430)$ (strong– and rad. decay properties)
		$q\bar{q}$	Dalitz–decays of η, ω, ϕ
5	Holographic (AdS/CFT)	**$q\bar{q}$**	Mass spectrum, decay constants

In the first block of the theory part (Chapters 3–4) we focus on hadronic molecules, in particular meson bound states. First, in Chapter 3, the binding and dynamical origin of hadronic molecules is studied in a unitarized coupled channel approach, from which we get information on the binding strength of meson channels and, provided the binding is strong enough, we can extract the mass and width of the meson–meson resonance. The interaction between the mesons is set up by chiral Lagrangians which provide the kernel of the Bethe–Salpeter equation used to analyze the transition amplitude with respect to resonances. Here we scan the open– and hidden–charm sectors for dynamically generated resonances resulting from meson–meson interaction. In addition, we apply this method for the first time to flavor exotic channels. In this framework we resolve the charm $D_{s2}^*(2573)$ as a K^*D^* bound state and study the radiative decays of the hidden–charm mesons $Z(3930)$, $Y(3940)$ and $X(4160)$. The $Y(3940)$ is also analyzed in an effective Lagrangian approach which will be introduced in Chapter 4.
Decay and production properties of hadronic molecules are studied in more detail in Chapter 4 by using an effective theory for hadronic bound states. In the first part we continue to study meson–meson bound state structures. In particular, this approach is used to get further information on the possible molecular structure by analyzing their decay and production properties. At the beginning we deal with

the light $f_0(980)$ and $a_0(980)$ mesons which have been discussed for many years as good candidates for bound states of kaons. Furthermore, we also study the hidden and radiative decays of the latest charmonium–like $Y(3940)$, $Y(4140)$ and $Z^{\pm}(4430)$ mesons by assuming a possible hadron molecule structure of charmed mesons. The $Y(3940)$ is especially interesting since this resonance was also studied in the framework of the dynamical approach in Chapter 3, where the $Y(3940)$ is identified as a bound state of D^* mesons.
In the second part of Chapter 4 we switch over to ordinary quark–antiquark mesons. We apply the effective Lagrangian approach, previously used to study hadronic molecules, to quark–antiquark bound states and analyze their decay and production properties in the light and heavy quark sector. This approach contains confinement which is modeled by introducing a infrared confinement scale in the quark loops. We use this model to study explicitly the electromagnetic form factors of the pion and the Dalitz decays of the η, η', ω and ϕ mesons.
In Chapter 5 we stay on the track with the conventional quark–antiquark structures. However, the method is completely different from the ones discussed previously since now we turn to a so–called holographic approach based on extra dimensions. This model is based on the correspondence of strings in the five–dimensional Anti–de–Sitter (AdS) space and conformal field theory representing the four dimensional space–time of the hadronic world. In this approach we study the mass spectrum of light and heavy mesons up to bottomia states and compute the decay constants of the ground states.
Finally, in Chapter 6, we summarize our results obtained in the different approaches which are then assembled to form a consistent picture of the mesons studied in the present thesis. Furthermore, we relate our findings to future prospects of meson spectroscopy.

3. Dynamically generated resonances

As already pointed out in the previous chapters, the introduction of meson structure besides the usual $q\bar{q}$ states seems necessary to explain certain resonances in the meson spectrum. For this reason, meson structure with gluonic components and multiquark states came into the focus of interest. The latter structure can also be realized as bound states of two mesons, which means that the meson states are made up of hadronic components rather than effective quarks. Bound states of mesons usually origin from the attractive strong interaction between mesons. This issue was already proposed in the 80s [19] and studied in various potential models [92]. One of the first systematic analyses of meson–meson bound states was performed in Ref. [70] within the framework of meson exchange potential models.
In the following we focus on meson structure composed of two other mesons. In particular, we pursue the issue of dynamically generated resonances from meson–meson interaction. In the present coupled channel approach the scattering process between different meson channels is studied with respect to resonances which give rise to poles in the transition matrix. The scattering amplitude, here contained in the Bethe–Salpeter Equation, gives information about the generation of resonances, their masses and widths and the respective contribution from the different channels. For example, if one channel clearly dominates the others, this is a strong hint for a meson molecule. For instance, the $f_0(980)$ and $a_0(980)$ are found to be dominantly kaon–antikaon bound states [93]. In the case of the $Y(3940)$ and $Z(3930)$ the $D^*\bar{D}^*$ coupling is much larger than the others which implies that the $Y(3940)$ can be considered as a $D^*\bar{D}^*$ bound state. This interpretation is in agreement with the $D^*\bar{D}^*$ molecular interpretations in Refs. [66, 25].

3.1. Coupled channels

The unitarized coupled channel approach was first applied to interacting pseudoscalar–pseudoscalar and pseudoscalar–vector meson channels [93, 94, 95]. The next step is the extension of the model to coupled channels of two vector mesons which are considered in the present case. In the previous works [94, 95] on coupled channels of pseudoscalars the interaction was set up by the lowest order chiral Lagrangian. The extension of the model to vector mesons therefore requires a method to incorporate

vector mesons in the chiral Lagrangian. Effective chiral Lagrangians for the description of low-energy hadron physics with vector mesons involved have been intensely studied in literature (for a review we refer to [96, 97]). In particular, when considering vector mesons as dynamical gauge bosons of a hidden local symmetry [96], hence the name hidden–gauge, one can derive a gauge invariant kinetic term which provides a low–energy chiral Lagrangian of vector mesons

$$\mathcal{L} = -\frac{1}{4}\langle V_{\mu\nu} V^{\mu\nu} \rangle \,, \tag{3.1}$$

where

$$V_{\mu\nu} = \partial_\mu V_\nu - \partial_\nu V_\mu - ig[V_\mu, V_\nu] \,. \tag{3.2}$$

The symbol $\langle\rangle$ indicates the trace in the flavor space and V_μ represents the extension of the vector nonet to SU(4) [95, 65]:

$$V_\mu = \begin{pmatrix} \frac{\omega_\mu + \rho^0_\mu}{\sqrt{2}} & \rho^+_\mu & K^{*+}_\mu & \overline{D}^{*0}_\mu \\ \rho^-_\mu & \frac{\omega_\mu - \rho^0_\mu}{\sqrt{2}} & K^{*0}_\mu & D^{*-}_\mu \\ K^{*-}_\mu & \overline{K}^{*0}_\mu & \phi_\mu & D^{*-}_{s\,\mu} \\ D^{*0}_\mu & D^{*+}_\mu & D^{*+}_{s\,\mu} & J/\psi_\mu \end{pmatrix}_\mu \,. \tag{3.3}$$

The Lagrangian of Eq. (3.1) provides the four–vector contact term for the $V_1 V_2 \to V_3 V_4$ transition

$$\mathcal{L}_{\rm VVVV} = \frac{1}{2} g^2 \langle [V_\mu, V_\nu] V^\mu V^\nu \rangle, \tag{3.4}$$

represented in Fig. 3.1 (a) and the three–vector meson interaction Lagrangian

$$\mathcal{L}_{VVV} \;=\; ig\langle (V^\mu \partial_\nu V_\mu - \partial_\nu V_\mu V^\mu) V^\nu) \rangle \tag{3.5}$$

which diagrammatically leads to the vector meson exchange diagrams of Fig. 3.1 (b) and (c). In general, the diagrams in the s–channel (see Fig. 3.1 (c)) lead to a repulsive p–wave interaction of the vector mesons for equal or similar masses [98] and only to a minor s–wave component in the case of different masses [99]. Since we only consider s–wave bound states we can neglect the diagrams of Fig. 3.1 (c) completely. While the interaction terms corresponding to the diagrams (a)–(b) of Fig. 3.1 are relevant for the generation of resonances, the two pseudoscalar decay modes play an important role in the generation of the decay widths. The corresponding box diagrams with intermediate pseudoscalars in Fig. 3.1 (d) are based on the interaction

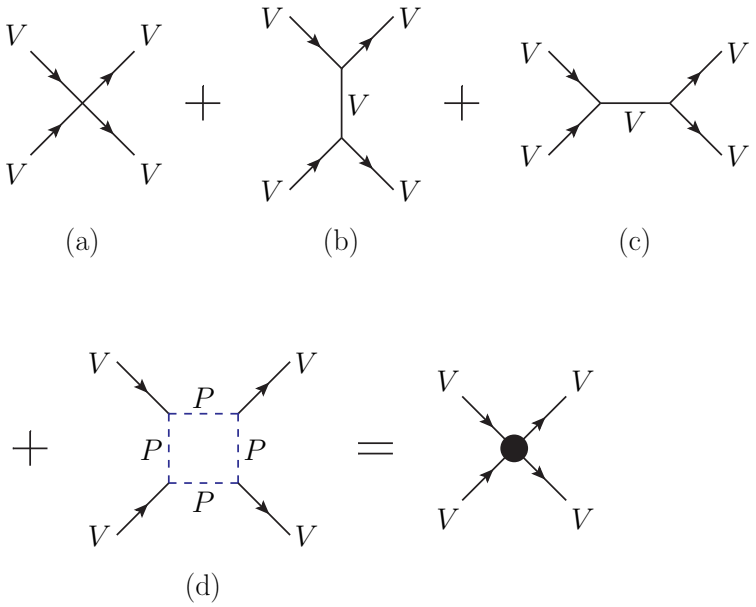

Figure 3.1.: VV–interaction diagrams.

Lagrangian

$$\mathcal{L}_{V\Phi\Phi} = -ig\langle V^\mu \big[\Phi, \partial_\mu \Phi\big]\rangle \tag{3.6}$$

taken from [95].

The resulting interaction terms characterize the potentials V_{ij} of the respective initial and final meson channels $i = V_3V_4$ and $j = V_1V_2$ which enter as a matrix type kernel in the Bethe–Salpeter Equation

$$T_{ij} = (\mathbb{1} - VG)^{-1}V_{ij}\,. \tag{3.7}$$

G represents the diagonal matrix of the respective two–meson loops given by

$$G = i\int \frac{d^4q}{(2\pi)^4}\frac{1}{q^2 - M_1^2 + i\epsilon}\frac{1}{(P-q)^2 - M_2^2 + i\epsilon}\,, \tag{3.8}$$

where M_i $(i = 1, 2)$ are the masses of the mesons in the loop and P is the total four–momentum of the two mesons. Since G is UV divergent the expression has to be regularized by either dimensional or cutoff regularization. Dimensional

regularization leads to the expression

$$G = \frac{1}{16\pi^2}\left(\alpha + \ln\frac{M_1^2}{\mu^2} + \frac{M_2^2 - M_1^2 + s}{2s}\ln\frac{M_2^2}{M_1^2} + \frac{p}{\sqrt{s}}\left(\ln\frac{s - M_2^2 + M_1^2 + 2p\sqrt{s}}{-s + M_2^2 - M_1^2 + 2p\sqrt{s}} + \ln\frac{s + M_2^2 - M_1^2 + 2p\sqrt{s}}{-s - M_2^2 + M_1^2 + 2p\sqrt{s}}\right)\right), \quad (3.9)$$

where α is the subtraction constant and μ represents the cutoff scale parameter. Both variables are not independent since they can be combined in one parameter $\widetilde{\alpha} \equiv \alpha - \ln\mu^2$. For this reason, we will later keep μ fixed and adjust α to data.

In the case of the cutoff regularization represented by

$$G = \int_0^{q_{max}} \frac{q^2 dq}{(2\pi)^2}\frac{\omega_1 + \omega_2}{\omega_1\omega_2[(P^0)^2 - (\omega_1 + \omega_2)^2 + i\epsilon]} \quad (3.10)$$

we also deal with one parameter which is the cutoff in the three–momentum q_{max}. Furthermore, $p = \left|\vec{p}\right|$ denotes the absolute value of the three—momentum of the mesons in the center–of–mass frame:

$$p = \frac{\sqrt{(s - (M_1 + M_2)^2)\,(s - (M_1 - M_2)^2)}}{2\sqrt{s}}, \quad (3.11)$$

$\omega_i = (\vec{q}_i^{\,2} + M_i^2)^{1/2}$ and $(P^0)^2 = s$ is the square of center–of–mass energy.

Dynamically generated meson–meson resonances appear as poles in the transition amplitude T_{ij}. Close to a resonance R (pole) the amplitude T_{ij} can be approximated by

$$T_{ij}^{(S)} = g_i \mathcal{P}^{(S)}(i)\frac{1}{s - M_R^2 + iM_R\Gamma_R} g_j \mathcal{P}^{(S)}(j)\,. \quad (3.12)$$

The total spin J of the resonances is equivalent to the spin S since we deal with s–wave bound states. For simplicity we consider the three–momentum of the vectors to be small, i.e. $\left|\vec{p}\right|/M_V << 1$. For this reason, the zero component of all polarization vectors $\epsilon_0 = 0$ and the spin projection operators of the respective coupled channel can be written in the simple form

$$\begin{aligned}
\mathcal{P}^{(0)} &= \frac{1}{\sqrt{3}}\epsilon_i(1)\epsilon_i(2)\,, \\
\mathcal{P}^{(1)} &= \frac{1}{2}\left[\epsilon_i(1)\epsilon_j(2) - \epsilon_j(1)\epsilon_i(2)\right], \\
\mathcal{P}^{(2)} &= \frac{1}{2}\left[\epsilon_i(1)\epsilon_j(2) + \epsilon_j(1)\epsilon_i(2)\right] - \frac{1}{3}\epsilon_m(1)\epsilon_m(2)\delta_{ij}\,.
\end{aligned} \quad (3.13)$$

The polarization vectors of the particles 1 and 2 of one particular channel are denoted

by $\epsilon(1)$ and $\epsilon(2)$. The indices i, j and m run over the spatial coordinates, i.e. i, j, m=1,2,3.
The couplings g_i and g_j of the resonance R to the respective meson–meson channels i and j can be extracted from the residues of the T–matrix at the poles because of the approximation in Eq. (3.12). The coupling strength of the resonance R to a particular channel gives a measure for the importance of its contribution to the formation of R.
The generation of resonances is primarily driven by the three and four vector meson interaction terms Eqs. (3.5) and (3.4). Already at this stage we can determine the mass of the resonance and the couplings strengths to the channels involved. However, for determining the width of the resonant state two further mechanisms have to be included. First of all, the decay width of the vector mesons involved have a certain influence on the width of the resonance. In the following section this issue is addressed by considering the mass distributions of the vector mesons.
Further on, we include the two pseudoscalar decay modes of the vector mesons, which means that initial and final vector mesons can interact via intermediate pseudoscalars corresponding to the box diagram of Fig. 3.1 (d).
Both issues are discussed in more detail in the following subsections.

Inclusion of the vector meson widths

The decay width of the vector mesons, i.e. their mass distribution, is taken into account by folding the meson loop function G in Eq. (3.8) with the spectral function

$$S(M) = -1/\pi \, \mathcal{I}m\Big(\frac{1}{M^2 - M_i^2 + iM_i\Gamma_i}\Big) \tag{3.14}$$

of the respective vector meson with mass M_i and width Γ_i. The resulting expression we refer to as convoluted function $\tilde{G}$ [100]

$$\begin{aligned}\widetilde{G}(s) =& \frac{1}{N^2} \int\limits_{(M_1-2\Gamma_1)^2}^{(M_1+2\Gamma_1)^2} \frac{d\widetilde{m}_1^2}{\pi} \mathcal{I}m\Big(\frac{-1}{\widetilde{m}_1^2 - M_1^2 + i\widetilde{\Gamma}_1\widetilde{m}_1}\Big) \\ & \times \int\limits_{(M_2-2\Gamma_2)^2}^{(M_2+2\Gamma_2)^2} \frac{d\widetilde{m}_2^2}{\pi} \mathcal{I}m\Big(\frac{-1}{\widetilde{m}_2^2 - M_2^2 + i\widetilde{\Gamma}_2\widetilde{m}_2}\Big) G(s, \widetilde{m}_1^2, \widetilde{m}_2^2)\,. \end{aligned} \tag{3.15}$$

The normalization is given by

$$N^2 = \int\limits_{(M_1-2\Gamma_1)^2}^{(M_1+2\Gamma_1)^2} \frac{d\widetilde{m}_1^2}{\pi} \mathcal{I}m\Big(\frac{-1}{\widetilde{m}_1^2 - M_1^2 + i\widetilde{\Gamma}_1\widetilde{m}_1}\Big) \cdot \int\limits_{(M_2-2\Gamma_2)^2}^{(M_2+2\Gamma_2)^2} \frac{d\widetilde{m}_2^2}{\pi} \mathcal{I}m\Big(\frac{-1}{\widetilde{m}_2^2 - M_2^2 + i\widetilde{\Gamma}_2\widetilde{m}_2}\Big)\,,$$

and $\widetilde{\Gamma}_i$ is determined as

$$\widetilde{\Gamma}_i = \Gamma_0 \frac{q_{\rm off}^3}{q_{\rm on}^3} \Theta(\widetilde{m}_i - m_1 - m_2) \,. \tag{3.16}$$

where m_1 and m_2 are the masses of the pseudoscalar decay products. The on and off–shell momenta of the respective vector meson are defined by

$$q_{\rm off} = \frac{\lambda^{1/2}(\widetilde{m}_i^2, m_1^2, m_2^2)}{2\widetilde{m}_i}, \quad q_{\rm on} = \frac{\lambda^{1/2}(M_{1(2)}^2, m_1^2, m_2^2)}{2M_{1(2)}} \,, \tag{3.17}$$

where $\lambda(a,b,c) = a^2+b^2+c^2-2ab-2ac-2bc$ is the Källen function. The convolution of the meson loop expression leads to an imaginary part of the potential which finally contributes to the width of the resonance.

Box diagrams

Besides the contact and vector meson exchange terms, the vector–vector meson interaction can also proceed via the dominant two pseudoscalar decay channels, where the vertices are provided by the hidden gauge formalism (3.1) leading to the Lagrangian

$$\mathcal{L}_{V\Phi\Phi} = -ig\langle V^\mu [\Phi, \partial_\mu \Phi] \rangle \,. \tag{3.18}$$

This issue we take into account by including box diagrams (see Fig. 3.2) with intermediate states of two pseudoscalar mesons. The real part of the box diagrams, which contribute to the mass of the resonances, was previously found to be negligible compared to the contributions of the three– and four–vector meson interaction terms [65]. In contrast, the imaginary part of the box diagrams is large which generates the width of the resonances.

The general structure of the box diagram reads

$$\begin{aligned} V \;\sim\; & \int \frac{d^4q}{(2\pi)^4} \epsilon_1 \cdot (2q-k_1) \epsilon_2 \cdot (2q-k_3) \\ & \times \epsilon_3 \cdot (2q-k_3-P) \epsilon_4 \cdot (2q-k_1-P) \\ & \times \frac{1}{(q-k_1)^2 - m_1^2 + i\epsilon} \frac{1}{q^2 - m_2^2 + i\epsilon} \\ & \times \frac{1}{(q-k_3)^2 - m_3^2 + i\epsilon} \frac{1}{(q-P)^2 - m_4^2 + i\epsilon} \,, \end{aligned} \tag{3.19}$$

where the approximation of neglecting the three–momenta of the external particles

leads to a simplified expression for V

$$\begin{aligned} V \;\sim\; & \int \frac{d^4q}{(2\pi)^4} \epsilon_1^i \epsilon_2^j \epsilon_3^m \epsilon_4^n q^i q^j q^m q^n \\ & \times \frac{1}{(q-k_1^0)^2 - m_1^2 + i\epsilon} \frac{1}{q^2 - m_2^2 + i\epsilon} \\ & \times \frac{1}{(q-k_3^0)^2 - m_3^2 + i\epsilon} \frac{1}{(q-P^0)^2 - m_4^2 + i\epsilon}. \end{aligned} \tag{3.20}$$

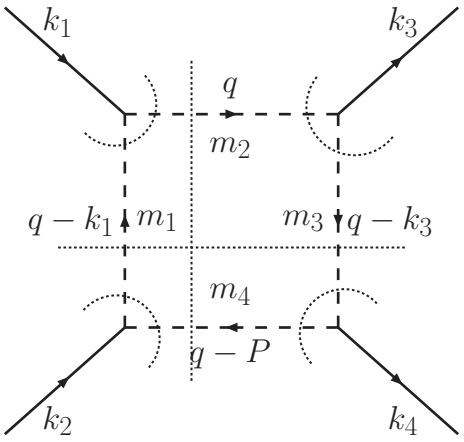

Figure 3.2.: Box diagram containing four pseudoscalar mesons. The cuts in the diagram provide the sources of the imaginary part of the potential.

Since the integral is logarithmically divergent we regularize it with a three dimensional cutoff. For this purpose we first perform the q^0 integration by means of the residue theorem and subsequently carry out the three–dimensional integration with the cutoff $q_{\max} = 1.2$ GeV [98, 65]. Since we only consider meson–meson systems in a relative s–wave we deal with resonances of positive parity. As a consequence, the intermediate pseudoscalar mesons in the box diagrams are also forced to form a $P = +$ state. This constraint is only fulfilled for the relative orbital momenta $L = 0$ and 2, which leads to total quantum numbers of $J^P = 0^+$ and 2^+. For this reason, box diagrams only contribute to resonances with quantum numbers $J^P = 0^+, 2^+$ while the 1^+ states generally appear as relatively narrow states.

Finally, we also include form factors in the box diagrams [65], where we use two different models

- Model A: We introduce form factors inspired by the empirical form used in the decay of vector mesons [101]. We therefore multiply the vertices in the

diagram of Fig. 3.2 by:

$$F_1(q^2) = \frac{\Lambda_b^2 - m_1^2}{\Lambda_b^2 - (k_1^0 - q^0)^2 + |\vec{q}|^2}, \tag{3.21}$$

$$F_3(q^2) = \frac{\Lambda_b^2 - m_3^2}{\Lambda_b^2 - (k_3^0 - q^0)^2 + |\vec{q}|^2}, \tag{3.22}$$

where $q^0 = \frac{s+m_2^2-m_4^2}{2\sqrt{s}}$. The cutoff parameter Λ_b is varied between 1.4 and 1.5 GeV to display the sensitivity of the model on this value.

- Model B: Here we introduce Gaussian form factors for off–shell pions and kaons as e.g. used in the QCD sum rule approach in [102],

$$F(q^2) = e^{((q^0)^2 - |\vec{q}|^2)/\Lambda^2}\ , \tag{3.23}$$

with $\Lambda = 1 - 1.2$ GeV.

3.2. Coupled channels including charmed mesons

We use the formalism introduced in the previous section to study coupled channels of open– and hidden–charm vector mesons [103]. In this work we pursue two main objectives: First we study charm–strange and hidden–charm meson systems since here the heavy meson sector is fueled by the enormous progress on the experimental side. We also focus on 'flavor exotic' resonances which might provide an interesting research topic in upcoming experiments. Mesons carrying flavor exotic quantum numbers would be a natural consequence of the existence of tetraquark or molecular meson structures. The observation of a flavor exotic state containing e.g. two charmed quarks, would be the proof for the existence of such kind of multiquark hadron substructure.

In the present coupled–channel approach we find a resonance in the charm–strange spectrum coupling strongly to the D^*K^* channel which is a good candidate for the $D_{s2}^*(2573)$ meson [103].

The $D_{s2}^*(2573)$ was first observed by the CLEO Collaboration in 1994 [104]. Its accommodation in the simple quark model was found to be difficult—a property which is also known from other charm–strange mesons. In the following we shortly discuss the charm–strange mesons before we study this sector with the coupled channel approach. Within the heavy quark symmetry framework (HQS) the spin of the heavy quark and the total angular momentum of the light quark are separately conserved. As a consequence, the heavy–light systems can be grouped in one doublet with $j_l = 3/2$ and $J^P = 1^+, 2^+$ and a second doublet with $j_l = 1/2$ and $J^P = 0^+, 1^+$, where j_l denotes the total spin of the light quark. While the $j_l = 3/2$ states are relatively narrow, the states of the $j_l = 1/2$ doublet are expected to be very

broad [105]. After the detection of the $D_{s2}^*(2573)$ it was first considered as the possible $j_l = 3/2$–doublet partner of the $D_{s1}^*(2536)$. The $D_{s0}^*(2317)$ and $D_{s1}(2460)$ mesons announced by the CLEO [106] and BABAR [107] collaborations in 2003 might be candidates for the $j_l = 1/2$ doublet. Unfortunately, the masses of both states are in contradiction with typical quark model predictions since experimental measurements lie around 100 MeV below the potential model estimates. In addition, the $D_{s0}^*(2317)$ and $D_{s1}(2460)$ are very narrow states with widths of about 4 MeV while in the $q\bar{q}$ picture the $j_l = 1/2$ doublet is expected to be very broad.

Since the standard $c\bar{s}$ scenario is in disagreement with experimental observations, alternative structure interpretations have been made (for a review see [59]). The proximity of the $D_{s0}^*(2317)$, $D_{s1}(2460)$ and $D_{s2}^*(2573)$ to the DK, D^*K and D^*K^* thresholds gives strong evidence for bound states of mesons.

The charmed–strange meson sector has already been in the focus of interest in earlier studies in the framework of coupled channels of two pseudoscalar mesons and pseudoscalar–vector mesons. In Refs. [95] and [94] it was argued that the $D_{s0}^*(2317)$ and $D_{s1}^*(2460)$ are possibly dynamically generated resonances with dominant DK and D^*K molecular structures.

In the present work we study charm–strange meson systems in the context of vector–vector meson coupled channels.

An overview on the coupled channels including quantum numbers of possibly generated resonances is given in Tab. 3.1. The quantum numbers C and S indicate the open–charm and strange flavors, I and J refer to the isospin and total spin of the resonances. The first three rows are related to the open– and hidden–charm sectors while the second part of the table refers to flavor exotic channels. Up to now, there is no experimental evidence for exotic states, however, they are predicted in several theoretical models ranging from QCD sum rules [108] to potential models [109, 110].

When studying the coupled channels of Tab. 3.1 we first set up the appropriate isospin states of the meson–meson channels involved. We thereby use the phase convention $(K^{*\,0}, K^{*\,+})$, $(-K^{*\,-}, \overline{K}^{*\,0})$, $(-D^{*\,0}, D^{*\,+})$, $(D^{*\,-}, \overline{D}^{*\,0})$ and $(-\rho^+, \rho^0, \rho^-)$ for the respective isospin doublets and triplet. In the next step we set up the contact interaction and the vector meson exchange terms including the projections in the respective spin basis. The formalism is demonstrated by means of the coupled channels of D_s^* and ϕ mesons since we deal with the least to the simplest expression of the Lagrangian in Eq. 3.4 with only four interaction terms

$$\begin{aligned} \mathcal{L}^{(4V)} &= \frac{g^2}{2}\big([D_{s\,\mu}^{*\,-}, D_{s\,\nu}^{*\,+}]\phi^\mu\phi^\nu + [\phi_\mu, D_{s\,\nu}^{*\,-}]D_s^{*\,+\mu}\phi^\nu \\ &+ [\phi_\mu, \phi_\nu]D_s^{*\,-\mu}D_s^{*\,+\nu} + [D_{s\,\mu}^{*\,+}, \phi_\nu]\phi^\mu D_s^{*\,-\nu}\big)\,. \end{aligned} \tag{3.24}$$

We define the polarization vectors of the initial $D_s^{*\,+}$ and ϕ mesons by $\epsilon(1)$ and $\epsilon(2)$, respectively. By analogy we denote the polarizations of the final $D_s^{*\,+}$ and ϕ mesons

Sectors	quantum numbers				channels involved		
	C	S	I	J			
open-strange (hidden–charm)	0	1	1/2		$D_s^*\bar{D}^*$	$J/\psi K^*$	
charm–strange	1	1	0	0,1,2	D^*K^*	$D_s^*\omega$	$D_s^*\phi$
charm–strange	1	1	1	0,1,2	D^*K^*	$D_s^*\rho$	
flavor exotic	1	-1	0,1	0,1,2	$D^*\bar{K}^*$		
	1	2	1/2		$D_s^*K^*$		
	2	0	0	1	D^*D^*		
	2	1	1/2		$D_s^*D^*$		
	2	2	0		$D_s^*D_s^*$		

Table 3.1.: Channels analyzed in this work: quantum numbers and contributing meson–meson channels.

by $\epsilon(3)$ and $\epsilon(4)$. Above Lagrangian can therefore be cast in the form

$$\begin{aligned}\mathcal{L}^{(4V)} &= \frac{g^2}{2}\big(-2\epsilon^\mu(1)\epsilon_\mu(2)\epsilon^\nu(3)\epsilon_\nu(4)+4\epsilon_\mu(1)\epsilon_\nu(2)\epsilon^\mu(3)\epsilon^\nu(4)\\ &- 2\epsilon_\mu(1)\epsilon_\nu(2)\epsilon^\nu(3)\epsilon^\mu(4)\big)\,. \end{aligned} \tag{3.25}$$

By using the spin projection operators of Eq. (3.13) we can determine the contributions of the respective spins $S=0,1,2$

$$\mathcal{L}^{(4V)} = g^2\big(-2\mathcal{P}^0+3\mathcal{P}^1+\mathcal{P}^2\big)\,. \tag{3.26}$$

From above expression we obtain the four vector contact potentials

$$\begin{aligned} V^{(4V)} &= -2g^2 \qquad (S=0),\\ V^{(4V)} &= 3g^2 \qquad (S=1),\\ V^{(4V)} &= g^2 \qquad (S=2). \end{aligned} \tag{3.27}$$

We consider chiral symmetry breaking by adapting the value of the coupling g to the respective mesons involved in the coupled channels. For example we use $g = M_\rho/2\,f_\pi$ when dealing with light vector mesons, where $f_\pi = 93$ MeV is the pion decay constant. If there are heavy vectors involved we either plug in the experimental value in case of charmed mesons $g_D = g^{\rm exp}_{D^*D\pi} = 8.95$ [111, 112, 113]

or use $g_{D_s} = M_{D_s^*}/2\,f_{D_s} = 5.47$ with $f_{D_s} = 273/\sqrt{2}$ MeV [22] for charm–strange vectors.

In the case of the vector meson exchange terms we proceed in complete analogy. The three–vector interaction Lagrangian (3.5)

$$\begin{aligned}\mathcal{L}^{(3V)} =& -ig\big(\phi_\mu\partial_\nu\phi^\mu\phi^\nu + D_{s\mu}^{*-}\partial_\nu D_s^{*+\mu}\phi^\nu \\ &+ \phi_\mu\partial_\nu D_s^{*-\mu}D_s^{*+\nu} + D_{s\,\mu}^{*+}\partial_\nu\phi^\mu D_s^{*-\nu}\big)\end{aligned} \tag{3.28}$$

provides the basis for the vector exchange transition matrix element (see diagram in Fig. 3.1 (b))

$$\begin{aligned}V^{(3V)} &= g^2\phi_\mu\partial_\nu D_s^{*-\mu}D_s^{*+\nu}D_s^{*-\nu'}D_s^{*-\mu'}\partial_{\nu'}\phi_{\mu'} \\ &= \frac{g^2}{m_{D_s^*}^2}(k_1+k_4)(k_2+k_3)\epsilon(1)^\mu\epsilon(2)^\nu\epsilon(3)_\nu\epsilon(4)_\mu \\ &= \frac{g^2}{m_{D_s^*}^2}(k_1+k_4)(k_2+k_3)(\mathcal{P}^2-\mathcal{P}^1+\mathcal{P}^0)\,.\end{aligned} \tag{3.29}$$

The corresponding expression for the u–channel, which is zero in the present case, would be proportional to $(k_1+k_3)\cdot(k_2+k_4)\;\epsilon(1)^\mu\epsilon(2)^\nu\epsilon(3)_\mu\epsilon(4)_\nu$. The momentum dependence can be evaluated by using

$$\begin{aligned}k_1\cdot k_2 &= \frac{s-M_1^2-M_2^2}{2} \\ k_1\cdot k_3 &= \frac{(s+M_1^2-M_2^2)(s+M_3^2-M_4^2)}{4s}\,,\end{aligned}$$

where $k_1=(k_1^0,\vec{p})$, $k_2=(k_2^0,-\vec{p})$, $k_3=(k_3^0,\vec{q})$, $k_4=(k_4^0,-\vec{q})$ and M_i $(i=1-4)$ are the masses of the external particles.

In the next step we need to consider the two–pseudoscalar decay channels of the vector mesons which diagrammatically leads to box diagrams with intermediate pseudoscalar mesons. In our calculations we consider the four boxes of Fig. 3.3 which make the dominant contribution to the transition amplitude.

It is well–known that the real part of the potential and therefore of the transition amplitude represents the mass while the imaginary part defines the width of the resonance. The real part only comes from the four and three vector meson interaction terms while the real part of the box diagrams is negligible as illustrated by the example of the $D^*K^*\to D^*K^*$ and $D^*K^*\to D_s^*\phi$ channels in Figs. 3.4 and 3.5.

In contrast, box diagrams lead to a sizable imaginary part of the potentials as depicted in Figs. 3.6 and 3.7. In summary, the inclusion of box diagrams does not influence the real part of the poles in the scattering matrix T, i.e. does not modify the mass of the resonance, but only contributes an imaginary part which characterizes the width. In Figs. 3.6 and 3.7 we compare the two types of form factors of the box

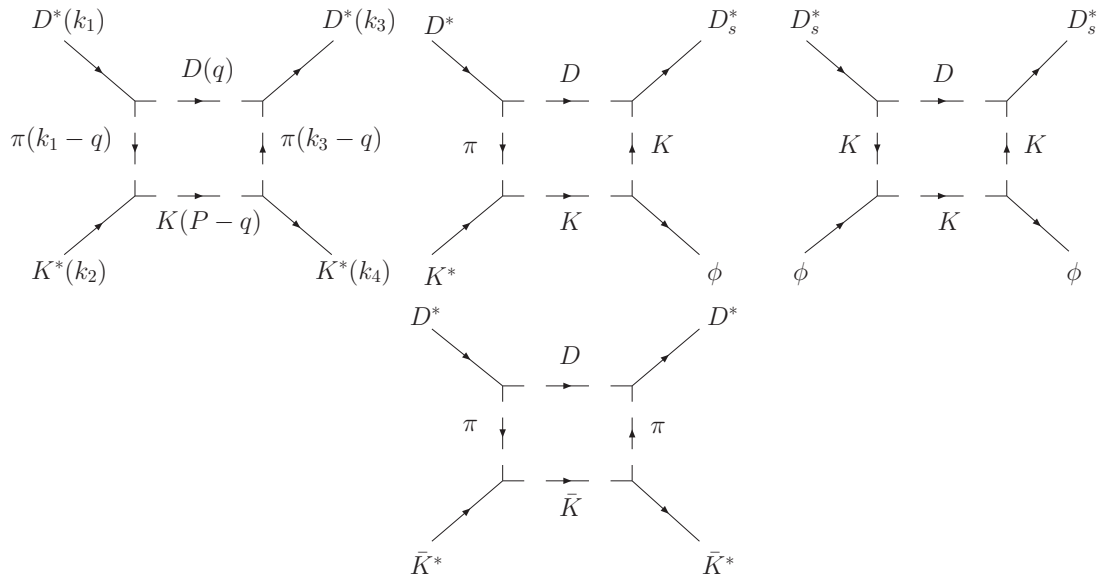

Figure 3.3.: Box diagrams.

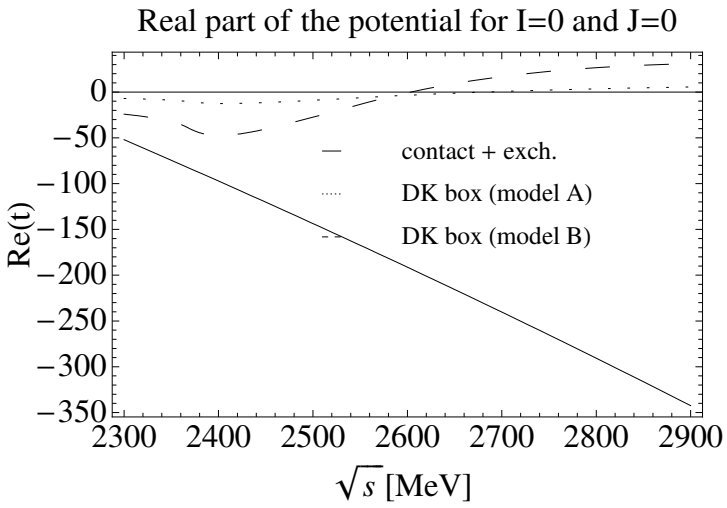

Figure 3.4.: Real parts of the contact, vector exchange and box diagrams for the $D^*K^* \to D^*K^*$ amplitude with quantum numbers $I = 0$, $J = 0$.

diagrams previously introduced as models A and B. In our numerical results we vary the cutoffs of the Gaussian and monopole form factors. However, in Fig. 3.6 we set $\Lambda = 1400$ MeV for the monopole form factor in model A while we put $\Lambda = 1200$ MeV when dealing with the Gaussian of model B in Fig. 3.7. Clearly, the Gaussian form factor (version B) (3.23) provides a larger imaginary part compared to Model A which results in a larger width of the resonance.

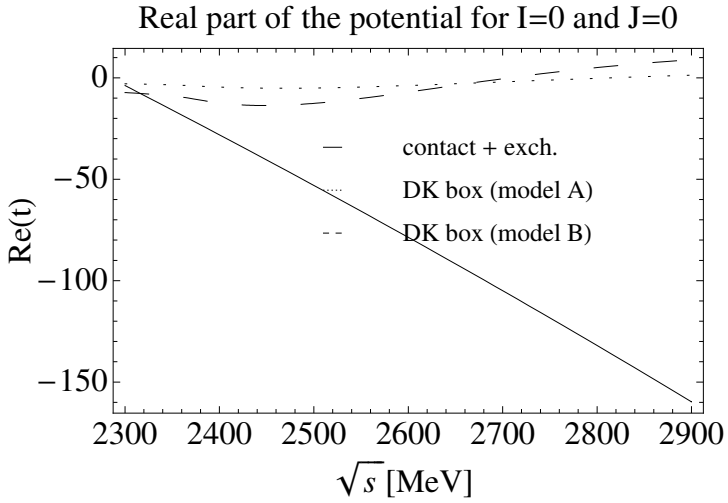

Figure 3.5.: Comparison of the real part of the box diagram with the contact term plus vector–exchange term for the $D^*K^* \to D_s^*\phi$ transitions and $I = 0$, $J = 0$.

To generate an imaginary part besides the box diagrams we also include the explicit decay widths of the vector mesons. Except for the decay widths of the ρ and K^* mesons, all widths are relatively small and can be neglected. For this reason, we only need to replace the two–meson loop function by the convoluted expression (Eq. (3.15)) when ρ or K^* mesons are involved. In the first case we use $\Gamma_\rho = 146.2$ MeV, and $m_1 = m_2 = m_\pi$ while for the K^* meson we insert $\Gamma_{K^*} = 50.55$ MeV and $m_1 = m_K$, $m_2 = m_\pi$ (see also diagrams of Fig. 3.3).

At this stage we are ready to analyze the transition matrix T for the various sets of quantum numbers. In particular, we insert the potentials including contact, vector exchange and box contributions into the Bethe Salpeter Equation (3.7). The generation of resonances with dynamical origin depends sensitively on the attraction of the resulting potential. Dynamically generated resonances appear as poles in the T matrix. In the case of a less attractive interaction we also obtain threshold cusps, which arise due to the opening of a meson–meson channel. Provided that the interaction is strong enough to generate a resonance we approximate the transition matrix by Eq. (3.12). From this representation we obtain the pole position, i.e. mass and width, and the coupling strength of the resonance to a particular channel by evaluating the residues of T.

The present coupled channel model is based on a few parameters. These are the cutoffs of the form factors entering in the box diagrams and the coupling constants g, g_D and g_{D_s} in the hidden–gauge Lagrangian (3.1) which have already been discussed above. In addition, the regularization of the meson loop G requires further parameters: Since μ and α depend on each other (see discussion after Eq. (3.9)) we

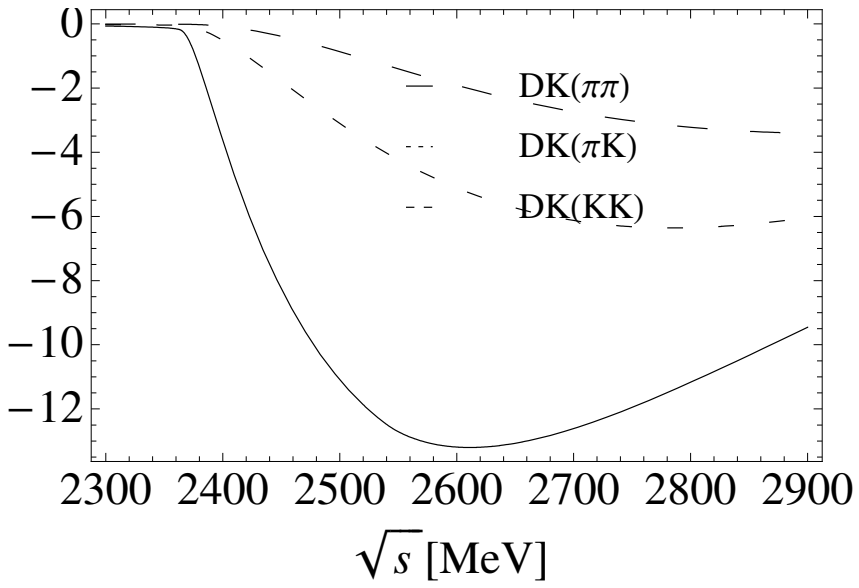

Figure 3.6.: Imaginary part of the box diagrams (Model A) for $I = 0$, $J = 0$.

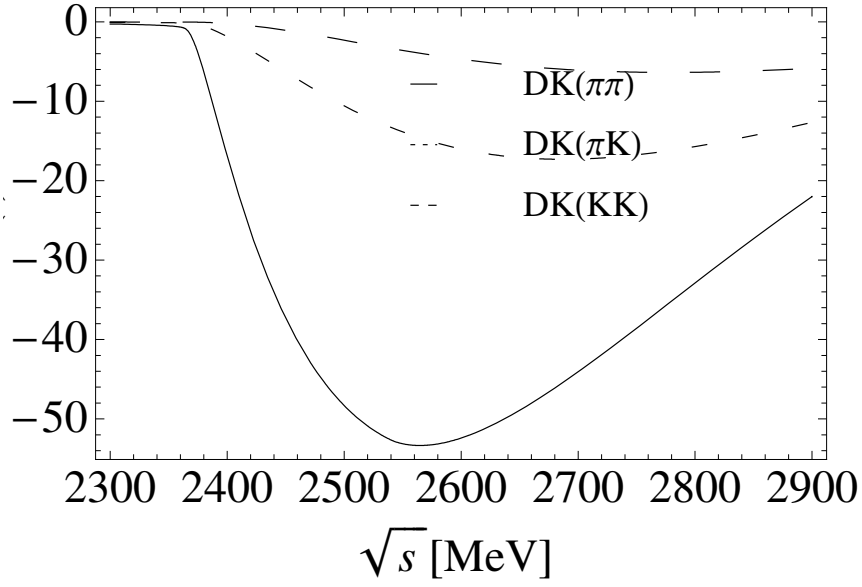

Figure 3.7.: Imaginary part of the box diagrams (Model B) for $I = 0$, $J = 0$.

use a unique scale parameter $\mu = 1500$ MeV of natural size and adjust α to one particular resonance which is e.g. experimentally well studied. For the open charm channels $C = 1; S = -1$, $C = 1; S = 1$ and $C = 1; S = 2$ we set $\alpha = -1.6$ while we choose a slightly smaller value $\alpha = -1.4$ for the heavy hidden–charm and flavor exotic sectors in order to reproduce the $Z(3930)$, $Y(3940)$ and $X(4160)$ states as done in Ref. [65]. The values of the parameter sets α and μ are close to those in earlier works where α ranges between -1.55 [94] and -1.74 [114].
In the following sections we present our results, where we discuss each flavor sector, indicated by the quantum numbers C (charm) and S (strange), separately and also differentiate between the respective isospin states denoted by I.
For the sake of readability, in the following sections we discuss the results for each flavor sector separately.

3.2.1. Hidden–charm, open–strange sector (C=0; S=1; I=1/2)

In the hidden–charm sector the potentials from the different contributing channels are repulsive except for the $D_s^* \overline{D}^* \to J/\psi K^*$ $(J = 1)$ and $D_s^* \overline{D}^* \to D_s^* \overline{D}^*$ $(J = 2)$ coupled channels as noted in Tab. 3.2. In order to estimate the absolute value and sign of the potential we indicate in the last column of Tab. 3.2 the potential for on–shell particles i.e. we replace the momenta by the masses of the mesons. Of course, we use the fully momentum dependent potentials for our calculations. However, in total the attraction is too small to bind the system. Therefore, the T–matrix is free of poles which is equivalent to the absence of resonances.

3.2.2. Charm–strange resonances (C=1; S=1; I=0, 1)

Isosinglet states

In the isosinglet channels the strong attractive interaction comes mainly from the $D^*K^* \to D^*K^*$ channel which leads to potentials of the order of $-18\, g^2$ to $-26\, g^2$ as evident from the estimate by using on–shell particles (see Tab. 3.3). The attraction is sufficient to bind the D^* and K^* system which leads to three poles with masses $M =$ 2683 MeV, 2707 MeV and 2572 MeV with total spin $J = 0$, 1 and 2, respectively, (see Tab. 3.4). When considering the K^* width neither the mass changes significantly (only of about 2 MeV) nor the total width is affected by this modification. In fact, the effect of the convolution is so small that it does not need to be considered. Only the inclusion of the box diagrams leads to a width of several MeV, where we again vary the monopole cutoff $\Lambda_A = 1.4 - 1.5$ GeV and the Gaussian cutoff from 1.0–1.2 GeV (Model B). In Figs. 3.8 and 3.9 the squared amplitude $|T|^2$ is plotted after the inclusion of the box diagrams for the two models A and B. We observe that these diagrams provide some width for the states with $J = 0$ and 2 (possible

J	Amplitude	Contact	V–exchange	$\sim$ Total
0	$D_s^*\overline{D}^* \to D_s^*\overline{D}^*$	$2g^2$	$-\frac{g^2(p_1+p_3).(p_2+p_4)}{m^2_{J/\psi}}$	$0.23g^2$
0	$D_s^*\overline{D}^* \to J/\psi K^*$	$-4g^2$	$\frac{g^2(p_1+p_4).(p_2+p_3)}{m^2_{D^*}} + \frac{g^2(p_1+p_3).(p_2+p_4)}{m^2_{D_s^*}}$	$3.6g^2$
0	$J/\psi K^* \to J/\psi K^*$	0	0	0
1	$D_s^*\overline{D}^* \to D_s^*\overline{D}^*$	$3g^2$	$-\frac{g^2(p_1+p_3).(p_2+p_4)}{m^2_{J/\psi}}$	$1.2g^2$
1	$D_s^*\overline{D}^* \to J/\psi K^*$	0	$-\frac{g^2(p_1+p_4).(p_2+p_3)}{m^2_{D^*}} + \frac{g^2(p_1+p_3).(p_2+p_4)}{m^2_{D_s^*}}$	$-0.43g^2$
1	$J/\psi K^* \to J/\psi K^*$	0	0	0
2	$D_s^*\overline{D}^* \to D_s^*\overline{D}^*$	$-g^2$	$-\frac{g^2(p_1+p_3).(p_2+p_4)}{m^2_{J/\psi}}$	$-2.8g^2$
2	$D_s^*\overline{D}^* \to J/\psi K^*$	$2g^2$	$\frac{g^2(p_1+p_4).(p_2+p_3)}{m^2_{D^*}} + \frac{g^2(p_1+p_3).(p_2+p_4)}{m^2_{D_s^*}}$	$9.6g^2$
2	$J/\psi K^* \to J/\psi K^*$	0	0	0

Table 3.2.: Amplitudes for $C = 0$, $S = 1$ and $I = 1/2$.

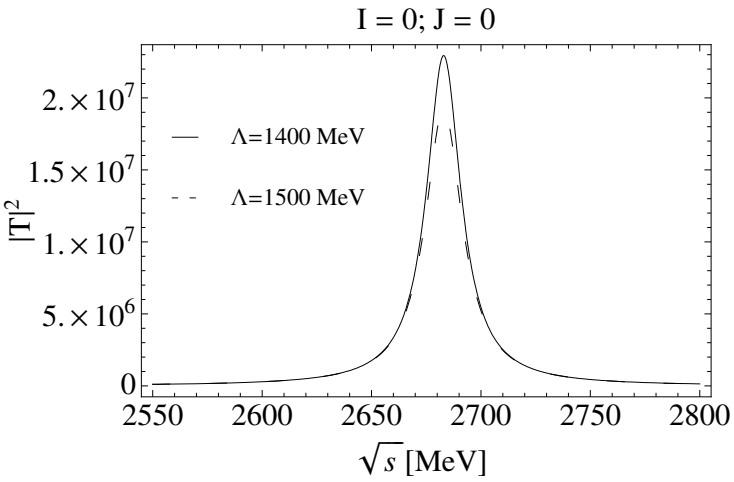

Figure 3.8.: Squared amplitude in the D^*K^* channel for $I = 0$, $J = 0$ (Model A).

quantum numbers of box diagrams), although the width provided by the model B is much bigger than that by model A. Since box diagrams do not contribute to $J = 1$ states, resonances with total spin 1 only gain their width from the convolution of G and hence are much narrower than scalar and tensor states.

J	Amplitude	Contact	V-exchange	$\sim$ Total
0	$D^*K^* \to D^*K^*$	$4g^2$	$-\frac{g^2}{2}(\frac{3}{m_\rho^2}+\frac{1}{m_\omega^2})(p_1+p_3).(p_2+p_4)$	$-19.8g^2$
0	$D^*K^* \to D_s^*\omega$	$-4g^2$	$\frac{g^2(p_1+p_4).(p_2+p_3)}{m_{D_s^*}^2}+\frac{g^2(p_1+p_3).(p_2+p_4)}{m_{K^*}^2}$	$6.8g^2$
0	$D^*K^* \to D_s^*\phi$	$2\sqrt{2}g^2$	$-\frac{\sqrt{2}g^2(p_1+p_3).(p_2+p_4)}{m_{K^*}^2}$	$-9.2g^2$
0	$D_s^*\omega \to D_s^*\omega$	0	0	0
0	$D_s^*\omega \to D_s^*\phi$	0	0	0
0	$D_s^*\phi \to D_s^*\phi$	$-2g^2$	$\frac{g^2(p_1+p_4).(p_2+p_3)}{m_{D_s^*}^2}$	$0.20g^2$
1	$D^*K^* \to D^*K^*$	$6g^2$	$-\frac{g^2}{2}(\frac{3}{m_\rho^2}+\frac{1}{m_\omega^2})(p_1+p_3).(p_2+p_4)$	$-17.7g^2$
1	$D^*K^* \to D_s^*\omega$	0	$-\frac{g^2(p_1+p_4).(p_2+p_3)}{m_{D_s^*}^2}+\frac{g^2(p_1+p_3).(p_2+p_4)}{m_{K^*}^2}$	$6.6g^2$
1	$D^*K^* \to D_s^*\phi$	$3\sqrt{2}g^2$	$-\frac{\sqrt{2}g^2(p_1+p_3).(p_2+p_4)}{m_{K^*}^2}$	$-7.8g^2$
1	$D_s^*\omega \to D_s^*\omega$	0	0	0
1	$D_s^*\omega \to D_s^*\phi$	0	0	0
1	$D_s^*\phi \to D_s^*\phi$	$3g^2$	$-\frac{g^2(p_1+p_4).(p_2+p_3)}{m_{D_s^*}^2}$	$0.8g^2$
2	$D^*K^* \to D^*K^*$	$-2g^2$	$-\frac{g^2}{2}(\frac{3}{m_\rho^2}+\frac{1}{m_\omega^2})(p_1+p_3).(p_2+p_4)$	$-25.8g^2$
2	$D^*K^* \to D_s^*\omega$	$2g^2$	$\frac{g^2(p_1+p_4).(p_2+p_3)}{m_{D_s^*}^2}+\frac{g^2(p_1+p_3).(p_2+p_4)}{m_{K^*}^2}$	$12.8g^2$
2	$D^*K^* \to D_s^*\phi$	$-\sqrt{2}g^2$	$-\frac{\sqrt{2}g^2(p_1+p_3).(p_2+p_4)}{m_{K^*}^2}$	$-13.5g^2$
2	$D_s^*\omega \to D_s^*\omega$	0	0	0
2	$D_s^*\omega \to D_s^*\phi$	0	0	0
2	$D_s^*\phi \to D_s^*\phi$	g^2	$\frac{g^2(p_1+p_4).(p_2+p_3)}{m_{D_s^*}^2}$	$3.2g^2$

Table 3.3.: Amplitudes for $C = 1$, $S = 1$ and $I = 0$.

When comparing the results with data it is immediately obvious that the $J = 2$ state with mass 2572 MeV and width 20 ± 5 MeV matches rather well the properties of the observed $D_2^*(2573)$ meson [22]. Here, the D^*K^* channel is dominant

$I[J^P]$	Mass	Width [MeV]		couplings			Data [22]
	$(\sqrt{s}_{\rm pole})$	Model A	Model B	$g_{D^*K^*}$	$g_{D_s^*\omega}$	$g_{D_s^*\phi}$	-
$0[0^+]$	2683	20 - 25	44 - 71	15635	−4035	6074	-
$0[1^+]$	2707	Convolution: $4 \cdot 10^{-3}$		14902	−5047	4788	-
$0[2^+]$	2572	7 - 8	18 - 23	18252	−7597	7257	$\Gamma = 20 \pm 5$ MeV

Table 3.4.: $C = 1; S = 1; I = 0$: Masses, widths and couplings in MeV.

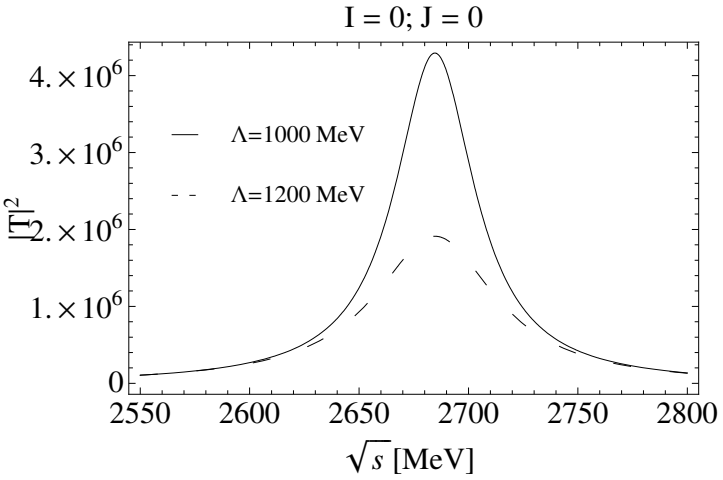

Figure 3.9.: Squared amplitude in the D^*K^* channel for $I = 0$, $J = 0$ (Model B).

which suggests the conclusion that the $D_2^*(2573)$ meson is probably a dynamically generated resonance with dominant D^*K^* component.

Isovector states

The isovector channels with charm–strange flavor quantum numbers are attractive in case of the $D^*K^* \to D_s^*\rho$ transition as one can see from Tab. 3.5. For $J = 0$ and 1 this potential is around $-7\,g^2$ while in case of $J = 2$ it is by a factor two bigger. In fact, the attraction is only sufficiently large to form a resonance for $J = 2$. In the case of $J = 0$ and 1 we only observe a cusp at the $D_s^*\rho$ threshold. In Tab. 3.6 we show the pole position and couplings of the resonance to the different channels. Both channels, D^*K^* and $D_s^*\rho$, are equally important as one can deduce from the corresponding couplings. The broad width of the ρ meson has to be taken into account by means of Eq. (3.15) which results in a width of 8 MeV for the $J = 2$ resonance. In this case the box diagrams only have a small contribution to the width of the resonance (see Fig. 3.10). In contrast to the previous situations, the width of the resonance mainly comes from the convolution of the ρ mass. Since up to now

J	Amplitude	Contact	V–exchange	$\sim$ Total
0	$D^*K^* \to D^*K^*$	0	$\frac{g^2}{2}(\frac{1}{m_\rho^2} - \frac{1}{m_\omega^2})(p_1+p_3).(p_2+p_4)$	$0.11g^2$
0	$D^*K^* \to D_s^*\rho$	$4g^2$	$-\frac{g^2(p_1+p_4)(p_2+p_3)}{m_{D^*}^2} - \frac{g^2(p_1+p_3).(p_2+p_4)}{m_{K^*}^2}$	$-6.8g^2$
0	$D_s^*\rho \to D_s^*\rho$	0	0	0
1	$D^*K^* \to D^*K^*$	0	$\frac{g^2}{2}(\frac{1}{m_\rho^2} - \frac{1}{m_\omega^2})(p_1+p_3).(p_2+p_4)$	$0.11g^2$
1	$D^*K^* \to D_s^*\rho$	0	$\frac{g^2(p_1+p_4)(p_2+p_3)}{m_{D^*}^2} - \frac{g^2(p_1+p_3).(p_2+p_4)}{m_{K^*}^2}$	$-6.6g^2$
1	$D_s^*\rho \to D_s^*\rho$	0	0	0
2	$D^*K^* \to D^*K^*$	0	$\frac{g^2}{2}(\frac{1}{m_\rho^2} - \frac{1}{m_\omega^2})(p_1+p_3).(p_2+p_4)$	$0.11g^2$
2	$D^*K^* \to D_s^*\rho$	$-2g^2$	$-\frac{g^2(p_1+p_4)(p_2+p_3)}{m_{D^*}^2} - \frac{g^2(p_1+p_3).(p_2+p_4)}{m_{K^*}^2}$	$-12.8g^2$
2	$D_s^*\rho \to D_s^*\rho$	0	0	0

Table 3.5.: Amplitudes for $C = 1$, $S = 1$ and $I = 1$.

there is no experimental evidence for a state with appropriate quantum numbers, mass and width, this resonance is a prediction of the model.

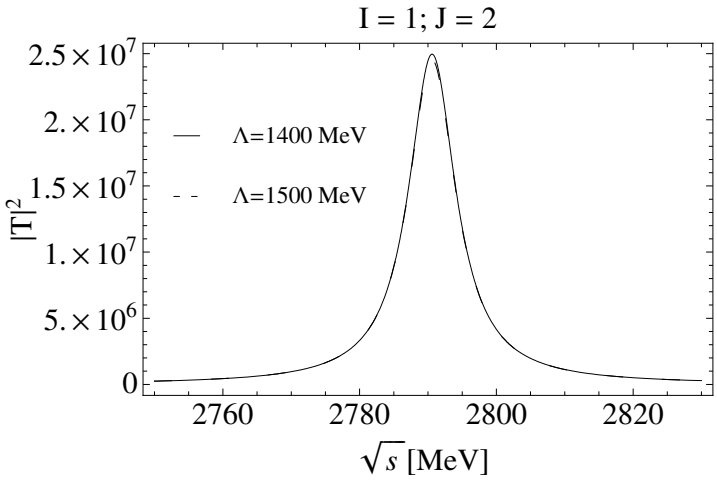

Figure 3.10.: Squared amplitude in the D^*K^* channel for $I = 1$, $J = 2$ (Model A).

$I[J^P]$	Mass [MeV]	Width [MeV]		couplings	
	$(\sqrt{s}_{\rm pole})$	Model A	Model B	$g_{D^*K^*}$	$g_{D_s^*\rho}$
$1[2^+]$	2786	8 - 9	9 - 11	11041	11092

Table 3.6.: $C = 1; S = 1; I = 1$: Masses, widths and couplings in MeV.

3.2.3. Flavor exotic resonances

Flavor exotics with C=1; S=-1; I=0 and 1

The isosinglet (I=0) channels are very attractive. For $J = 0$ and 1 the potential is around $-10\,g^2$ and it is even more attractive $\approx -16\,g^2$ for $J = 2$ which leads to three resonances with total spin J =0, 1 and 2 as indicated in Tab. 3.7.

J	Contact	V–exchange	$\sim$ Total
0	$4g^2$	$-\frac{g^2(p_1+p_4).(p_2+p_3)}{m^2_{D_s^*}} + \frac{1}{2}g^2(\frac{1}{m^2_\omega} - \frac{3}{m^2_\rho})(p_1+p_3).(p_2+p_4)$	$-9.9g^2$
1	0	$\frac{g^2(p_1+p_4).(p_2+p_3)}{m^2_{D_s^*}} + \frac{1}{2}g^2(\frac{1}{m^2_\omega} - \frac{3}{m^2_\rho})(p_1+p_3).(p_2+p_4)$	$-10.2g^2$
2	$-2g^2$	$-\frac{g^2(p_1+p_4).(p_2+p_3)}{m^2_{D_s^*}} + \frac{1}{2}g^2(\frac{1}{m^2_\omega} - \frac{3}{m^2_\rho})(p_1+p_3).(p_2+p_4)$	$-15.9g^2$

Table 3.7.: Amplitudes for $C = 1$, $S = -1$ and $I = 0$ ($D^*\overline{K}^* \to D^*\overline{K}^*$).

$I[J^P]$	Mass [MeV]	Width [MeV]		coupling
	$(\sqrt{s}_{\rm pole})$	Model A	Model B	$g_{D^*\overline{K}^*}$
$0[0^+]$	2848	23 - 30	25 - 59	12227
$0[1^+]$	2839	Convolution: 3		13184
$0[2^+]$	2733	11 - 24	22 - 36	17379

Table 3.8.: $C = 1; S = -1; I = 0$. Masses, widths and couplings in MeV.

The corresponding pole positions, characterizing the masses and widths of the resonances, and the couplings to the vector–vector channels are given in Tab. 3.8. The decay widths arise due to the inclusion of the box diagrams. The uncertainty in the widths in Tab. 3.8 indicates the parameter dependence of this approach and arises because of the variation of the cutoff from Λ_A=1.4 to 1.5 GeV (monopole, model A) and Λ_B =1.0–1.2 GeV in case of the Gaussian form factor of model B.

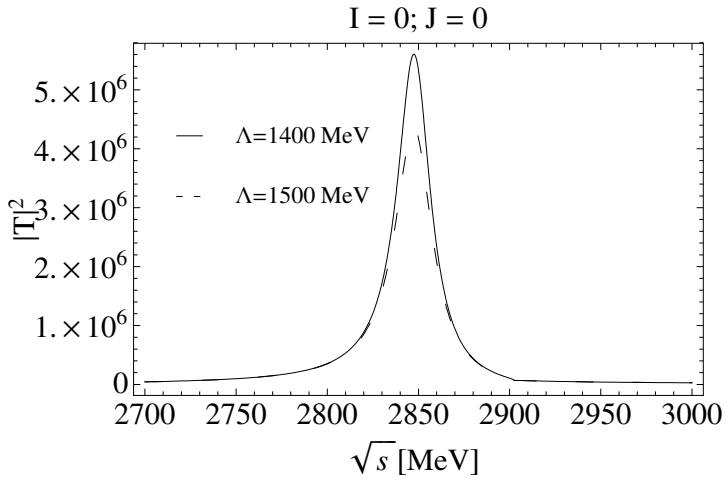

Figure 3.11.: Squared amplitude in the $D^*\overline{K}^*$ channel for $I = 0$, $J = 0$ (Model A).

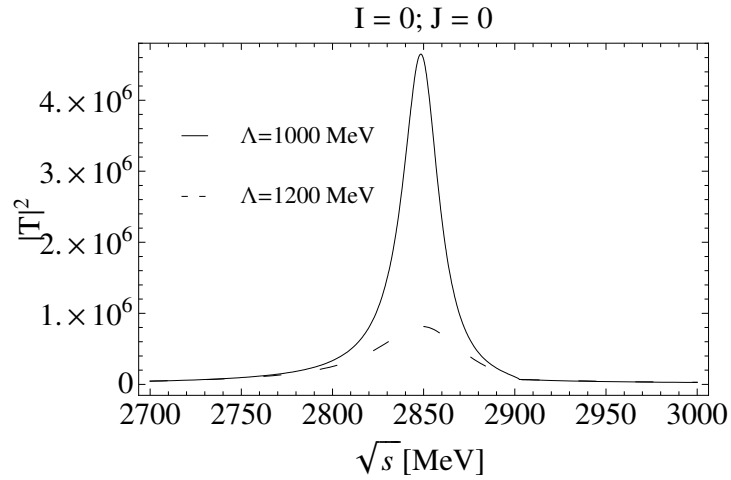

Figure 3.12.: Squared amplitude in the $D^*\overline{K}^*$ channel for $I = 0$, $J = 0$ (Model B).

Since box diagrams are only allowed for $J = 0$ and 2 (see discussion about box diagrams in Section 3.1) the spin 1 state appears to be very narrow. The width of 3 MeV arises due to the inclusion of the K^* width. Here, the two models lead to similar results except for the Model B with $\Lambda = 1200$ MeV.

The convolution of the G function by including the K^* width leads to a minor shift in the pole positions (only 3 MeV for $J = 2$) and around 3 MeV in the widths for the three states. This is a minor effect compared to the contribution of the box diagrams. The transition amplitude squared $|T|^2$ is depicted in Figs. 3.11 (Model A) and 3.12 (Model B) for $J = 0$. In analogy the tensor states with $J = 2$ are shown in Figs. 3.13 and 3.14 for the Models A and B. In general Model B is more sensitive to variations of the cutoff parameter Λ_B and leads to broader resonances which is

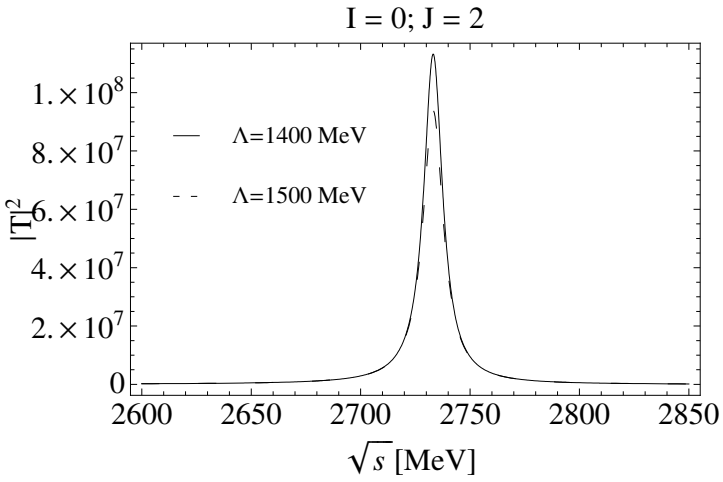

Figure 3.13.: Squared amplitude in the $D^*\overline{K}^*$ channel for $I = 0$, $J = 2$ (Model A).

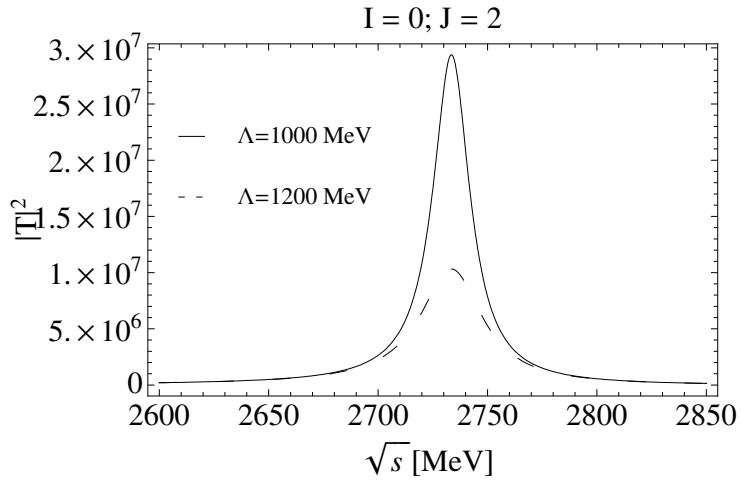

Figure 3.14.: Squared amplitude in the $D^*\overline{K}^*$ channel for $I = 0$, $J = 2$ (Model B).

also confirmed by the numerical results in Tab. 3.8.
Since we deal with exotic states we cannot compare our findings to any experimental counterpart. In contrast to the previously discussed isosinglet states, the interaction is very repulsive in the isovector coupled channels. Therefore, we have no evidence for dynamically generated resonances with $I = 1$.

Double strange sector (C=1; S=2; I=1/2)

The following section deals with coupled channels with exotic flavor quantum numbers as for instance double strange and double charmed mesons. Again, this flavor quantum numbers cannot be reached by the constituent quark model. The detection

of such states would therefore be a clear evidence for a non–$q\overline{q}$ structure. However, in the present sector the potentials are repulsive as one can see from Tab. 3.9 and therefore we do not expect dynamically generated states.

J	Amplitude	Contact	V–exchange	$\sim$ Total
0	$D_s^*K^* \to D_s^*K^*$	$-4g^2$	$\frac{g^2(p_1+p_4)(p_2+p_3)}{m_{D^*}^2} + \frac{g^2(p_1+p_3).(p_2+p_4)}{m_\phi^2}$	$5.5g^2$
1	$D_s^*K^* \to D_s^*K^*$	0	$-\frac{g^2(p_1+p_4)(p_2+p_3)}{m_{D^*}^2} + \frac{g^2(p_1+p_3).(p_2+p_4)}{m_\phi^2}$	$5.0g^2$
2	$D_s^*K^* \to D_s^*K^*$	$2g^2$	$\frac{g^2(p_1+p_4)(p_2+p_3)}{m_{D^*}^2} + \frac{g^2(p_1+p_3).(p_2+p_4)}{m_\phi^2}$	$11.5g^2$

Table 3.9.: Amplitudes for $C = 1$, $S = 2$ and $I = 1/2$.

Double–charmed coupled channels (C=2; S=0; I=0, 1)

In this case we study double charmed states by coupled D^*D^* channels. The amplitudes are given in Tab. 3.10, where the potential is zero for $J = 0$ and 2. This can be explained by the fact that the D^*D^* state is antisymmetric for $I = 0$. Therefore, the only possibility to obtain a fully symmetric wave function is provided for $J = 1$. For $J = 1$ the interaction is strongly attractive which leads to a pole in the scatter-

J	Amplitude	Contact	V–exchange	$\sim$ Total
0	$D^*D^* \to D^*D^*$	0	0	0
1	$D^*D^* \to D^*D^*$	0	$\frac{1}{4}g^2(\frac{2}{m_{J/\psi}^2} + \frac{1}{m_\omega^2} - \frac{3}{m_\rho^2})\{(p_1+p_4).(p_2+p_3)$ $+(p_1+p_3).(p_2+p_4)\}$	$-25.4g^2$
2	$D^*D^* \to D^*D^*$	0	0	0

Table 3.10.: Amplitudes for $C = 2$, $S = 0$ and $I = 0$.

ing matrix as one can see from Tab. 3.11. Since the width of the D^* meson is very small ($\sim$ 100 keV or less in the case of the neutral charmed meson) we presently do not perform the convolution of the G function. In addition, in the case of $J = 1$ states the inclusion of the box diagrams can be ruled out. Therefore, we obtain a very narrow state. Since we deal with an extremely narrow double–charmed meson we presently do not have any experimental evidence.

$I[J^P]$	Mass [MeV]	Width [MeV]	coupling
	$(\sqrt{s}_{\rm pole})$	$g_{D^*D^*}$	
$0[1^+]$	3969	≈ 0	16825

Table 3.11.: $C = 2; S = 0; I = 0$. Masses, widths and couplings in MeV.

The corresponding isovector coupled channels lead to a repulsive potential and we therefore do not obtain resonances.

Double–charmed sector with C=2; S=1; I=1/2

This sector is also exotic. The amplitudes from the four–vector contact terms plus vector–exchange diagrams lead to a repulsive potential for $J = 0$ and 2 while it is attractive for $J = 1$ as indicated in Tab. 3.12. The pole lies almost at the $D_s^* D^*$

J	Amplitude	Contact	V–exchange	$\sim$ Total
0	$D_s^* D^* \to D_s^* D^*$	$-4g^2$	$\frac{g^2(p_1+p_4).(p_2+p_3)}{m^2_{K^*}} + \frac{g^2(p_1+p_3).(p_2+p_4)}{m_{J/\psi^2}}$	$19.0g^2$
1	$D_s^* D^* \to D_s^* D^*$	0	$-\frac{g^2(p_1+p_4).(p_2+p_3)}{m^2_{K^*}} + \frac{g^2(p_1+p_3).(p_2+p_4)}{m_{J/\psi^2}}$	$-19.5g^2$
2	$D_s^* D^* \to D_s^* D^*$	$2g^2$	$\frac{g^2(p_1+p_4).(p_2+p_3)}{m^2_{K^*}} + \frac{g^2(p_1+p_3).(p_2+p_4)}{m_{J/\psi^2}}$	$25.0g^2$

Table 3.12.: Amplitudes for $C = 2$, $S = 1$ and $I = 1/2$.

threshold (4121 MeV), where the pole position and the coupling is given in Tab. 3.13. This state comes with zero width since we deal with a similar situation as in the previous case. The box diagrams are not possible for $J = 1$ states and any possible convolution of the G function would only lead to a very small width. This state is also a prediction of the model and needs to be ultimately confirmed by experiment.

$I[J^P]$	Mass [MeV]	Width [MeV]	coupling
	$(\sqrt{s}_{\rm pole})$	$g_{D_s^*D^*}$	
$1/2[1^+]$	4101	≈ 0	13429

Table 3.13.: $C = 2; S = 1; I = 1/2$. Masses, widths and couplings in MeV.

Double–charmed, double–strange (C=2; S=2; I=0)

The $D_s^* D_s^*$ channel allows us to study double–charm double–strange objects. Since we deal with two identical particles with isospin zero, the isospin $D_s^* D_s^*$–state is symmetric and hence we get interaction for $J = 0$ and 2 while the potential is zero for $J = 1$. Since the potential is strongly repulsive for $J = 0$ and 2 we do not obtain any resonant state in this sector.

3.2.4. Summary

We studied dynamically generated resonances from vector–vector interaction in the charm–strange and hidden–charm sectors and for the first time extended the formalism to flavor exotic resonances. The hidden gauge Lagrangians provide a consistent method to include vector meson interaction in the coupled channel unitarity formalism. The interaction between the vector meson channels is driven by four meson contact and vector meson exchange diagrams. At this stage we can already see if the attraction is strong enough to generate a resonance. However, in this limit the states come with zero decay width. There are two effects which are relevant for the generation of the width of the resonance. First, the widths of the vector mesons involved need to be considered by the convolution of the two–meson loop function. This effect is in particular important for the $D_s^* \rho$ channel. Second, the PP decay modes of the vector mesons play an important role. In the present coupled channel approach this issue is taken into account by the insertion of box diagrams with pseudoscalar mesons in the intermediate state.

Our analysis of the T matrix resulted in nine bound states which are summarized in Tab. 3.14. In the charm–strange sector ($C = 1, S = 1$) we obtain four resonances, where we can assign one resonance to an experimental counterpart. The $J = 2$ resonance matches the mass, width and quantum numbers of the $D_{s2}^*(2573)$ meson which suggests a new interpretation of the $D_{s2}^*(2573)$ meson as a $D^* K^*$ molecular state. This structure assumption would be in line with previous studies predicting a DK nature for the $D_{s0}^*(2317)$ [95] and a possible $D^* K$ molecular structure of the $D_{s1}^*(2460)$ [94].

We obtain two further isosinglets with $J^P = 0^+$ and 1^+ around 2700 MeV and one isovector 2^+ state around 2786 MeV. All of them are relatively narrow ($\Gamma < 8$ MeV) and are predictions of the model without experimental evidence for these states so far.

Within this framework we also studied flavor–exotic meson–meson systems. Mesons with flavor exotic quantum numbers would be a corollary of meson molecules or tetraquarks and have been mainly considered in tetraquark models [109, 108]. Up to now there is no experimental evidence for double flavored mesons. However, their observation would be a clear signal for the existence of meson structure beyond $q\overline{q}$ states.

Flavor	$I[J^P]$	Mass [MeV]	Width [MeV]		Data		
C, S		$\sqrt{s}$	$\Gamma_{\rm A}$	$\Gamma_{\rm B}$	Meson	Mass [MeV]	Width [MeV]
$1, 1$	$0[0^+]$	2683	20	44			
	$0[1^+]$	2707	4×10^{-3}	4×10^{-3}			
	$0[2^+]$	2572	7	18	$D_{s2}(2573)$	2572.6 ± 0.9	20 ± 5
	$1[2^+]$	2786	8	9			
$1, -1$	$0[0^+]$	2848	23	25			
	$0[1^+]$	2839	3	3			
	$0[2^+]$	2733	11	22			
$2, 0,$	$0[1^+]$	3969	0	0			
$2, 1$	$1/2[1^+]$	4101	0	0			

Table 3.14.: Overview of the dynamically generated resonances ($\Lambda_A = 1.4$ GeV, $\Lambda_B = 1.0$ GeV).

In the sector $C = 1; S = -1; I = 0$ we obtain three new exotic states with masses around 2.8 GeV and widths between 3 MeV for the $J = 1$ state and 25 MeV for the scalar resonance.

In the case of the double–charm vector meson systems $C = 2; S = 0; I = 0$ and $C = 2; S = 1; I = 1/2$ we obtain in both sectors one resonance with quantum numbers $J^P = 1^+$. Since the box diagrams do not contribute in this case and the D^* decay width is small, the potential has a very small imaginary part and therefore we deal with two very narrow states. The masses lie around 4.0–4.1 GeV which is close to the D^*D^* and $D_s^*D^*$ thresholds, respectively. Earlier investigations in double charmed tetraquarks found a broad isosinglet $cc(\overline{qq})$ system with $J = 1$ and mass around 4.0 GeV [108] which is similar to our result.

In summary, we found nine dynamically generated resonances, where four of them can be assigned to the charm–strange sector. One resonance, being dominantly a D^*K^* bound state, is found to be a good candidate for the $D_{s2}^*(2573)$. Furthermore, we analyzed coupled channels with exotic flavor leading to five resonances which can be interpreted as D^*K^*, $D^*\bar{K}^*$, D^*D^* and $D_s^*D^*$ molecular states. There is

no experimental counterpart to these exotic structures, nevertheless the mass of the double–charmed resonance is close to the QCD sum–rule and potential model predictions for double–charmed tetraquarks. Finally, our findings might be useful to get further insight in the flavor exotic sectors and to encourage the search for flavor–exotic mesons with e.g. double charm or double charm–strangeness in future experiments.

3.3. Radiative decays of dynamically generated states

In the following section we will have a closer look at the dynamically generated states by studying its radiative decay properties. In the hidden gauge formalism the electromagnetic interaction can easily be included by using the vector meson dominance (VMD) formalism. The VMD model was originally developed by J.J. Sakurai [115] in the 1960s to describe the interaction between hadrons and photons. The VMD formalism describes the transition of vector mesons to photons and vice versa by the current–field identity (CFI) [115]. The CFI implies the interaction of photons with vector fields by identifying the electromagnetic current with a linear combination of vector meson fields V^μ: $j_\mu^{\rm em} = -\frac{M_V^2}{g} V_\mu$, where M_V and g denote the vector meson mass and the coupling. The matrix element describing the coupling between photon and vector meson with mass M_V therefore reads

$$t_{V\gamma} = -e\frac{M_V^2}{g} A_\mu \left\langle V^\mu Q \right\rangle , \tag{3.30}$$

where A_μ is the electromagnetic field, and $\left\langle V^\mu Q \right\rangle$ denotes the trace over the vector meson matrix (3.3) and the matrix of the quark charges given by

$$Q = \mathrm{diag}(q_u = 2/3, q_d = -1/3, q_s = -1/3, q_c = 2/3) .$$

Therefore we can write

$$t_{V\gamma} = \mathcal{C}_{V\gamma}\, \frac{e}{g}\, M_V^2\, \epsilon^\mu(\gamma) \ , \text{ where } \ \mathcal{C}_{V\gamma} = \begin{cases} \frac{1}{\sqrt{2}} & \text{for } \rho^0 \\ \frac{1}{3\sqrt{2}} & \text{for } \omega \\ -\frac{1}{3} & \text{for } \phi \\ \frac{2}{3} & \text{for } J/\psi \end{cases} \tag{3.31}$$

is the flavor factor. The coupling constant $g = \frac{m_\rho}{2f_\pi}$ is determined by the pion decay constant $f_\pi = 93$ MeV. We consider $SU(4)$ breaking effects by changing the coupling g; in case of J/ψ we have $g \equiv g_{\eta_c} = M_{J/\psi}/(2f_{\eta_c})$ where $f_{\eta_c} = 420/\sqrt{2}$ MeV is taken from [116].

Therefore, in the coupled channel approach one– and two–photon decays of dynamically generated resonances can be easily studied by coupling the photon to the ρ, ω, ϕ or J/ψ vector mesons in the respective coupled channels [117, 118, 100, 24] which is depicted in Fig. 3.15. The calculation is greatly simplified and does not induce further loop calculations. The issue of gauge invariance of this prescription is addressed in Refs. [100, 119].

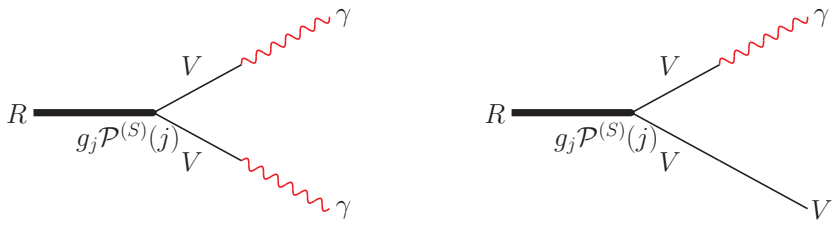

Figure 3.15.: Photon coupling via VMD.

The transition amplitude for one– and two–photon decays is set up by combining the coupling between the resonance and the appropriate vector meson channels $g_{V_1V_2}$ and the VMD amplitude (3.31)

$$T^{(R)}(\gamma\gamma) \propto \sum_{V_1,V_2} g^{(R)}_{V_1V_2}\, \mathcal{P}^{(S)}_{V_1V_2} \left(\frac{1}{-M^2_{V_1}}\right) t_{V_1\gamma} \left(\frac{1}{-M^2_{V_2}}\right) t_{V_2\gamma} \cdot F_I \,, \tag{3.32}$$

$$T^{(R)}(V_1\gamma) \propto \sum_{V_2} g^{(R)}_{V_1V_2}\, \mathcal{P}^{(S)}_{V_1V_2} \left(\frac{1}{-M^2_{V_2}}\right) t_{V_2\gamma} \cdot F_I \,. \tag{3.33}$$

F_I represents the respective isospin Clebsch Gordan coefficients of the V_1V_2 component for a certain isospin state.

After summing over the intermediate vector polarizations in Eqs. (3.32) and (3.33), the amplitudes for the $R \to \gamma\gamma$ and $R \to V\gamma$ decays are finally given by

$$T^{(R)}_{V_1\gamma} = \frac{e}{g} \sum_{V_2=\rho^0,\omega,\phi,J/\psi} g^{(R)}_{V_1V_2} \mathcal{P}^{(S)}_{V_1\gamma} \mathcal{C}_{V_2\gamma} F_I F_{V\gamma} \,, \tag{3.34}$$

$$T^{(R)}_{\gamma\gamma} = \frac{e^2}{g^2} \sum_{V_1,V_2=\rho^0,\omega,\phi,J/\psi} g^{(R)}_{V_1V_2} \mathcal{P}^{(S)}_{\gamma\gamma} \mathcal{C}_{V_1\gamma} \mathcal{C}_{V_2\gamma} F_I F_{\gamma\gamma} \,, \tag{3.35}$$

where $\mathcal{P}^{(S)}_{V_1\gamma}$ and $\mathcal{P}^{(S)}_{\gamma\gamma}$ are the spin projection operators which have been defined in (3.13).

The use of the unitarity renormalization leads to an extra factor $\frac{1}{\sqrt{2}}$ in the cases of channels with identical particles (e.g. $\rho^0\rho^0$). The unitarity normalization and the

symmetry factors are combined in $F_{\gamma\gamma}$ and $F_{V\gamma}$ with

$$F_{\gamma\gamma} = \begin{cases} \sqrt{2} & \text{for a pair of identical particles, e.g } \rho^0\rho^0 \\ 2 & \text{for a pair of different particles, e.g } \rho^0\omega\,, \end{cases} \tag{3.36}$$

$$F_{V\gamma} = \begin{cases} \sqrt{2} & \text{for a pair of identical particles, e.g } \rho^0\rho^0 \\ 1 & \text{for a pair of different particles, e.g } \rho^0\omega\,. \end{cases} \tag{3.37}$$

The radiative decay widths $\Gamma_{\gamma\gamma}$ and $\Gamma_{V\gamma}$ can be easily calculated from the transition amplitudes T by the relations

$$\Gamma_{\gamma\gamma} = \frac{1}{2S+1}\frac{1}{16\pi M_R}\frac{1}{2}\cdot\sum_{spins}\left|T^{(R)}_{\gamma\gamma}\right|^2, \tag{3.38}$$

$$\Gamma_{V\gamma} = \frac{1}{2S+1}\frac{1}{8\pi M_R}\frac{|\vec{p}_\gamma|}{M_R}\cdot\sum_{spins}\left|T^{(R)}_{V\gamma}\right|^2, \tag{3.39}$$

where the summation over all spin states contributes the factors

$$\sum_{spins}\mathcal{P}^{(S)}_{\gamma\gamma}\mathcal{P}^{*(S)}_{\gamma\gamma} = \begin{cases} \frac{2}{3} & S=0 \\ 1 & S=1 \\ \frac{7}{3} & S=2\,, \end{cases} \tag{3.40}$$

$$\sum_{spins}\mathcal{P}^{(S)}_{V\gamma}\mathcal{P}^{*(S)}_{V\gamma} = \begin{cases} \frac{2}{3} & S=0 \\ 2 & S=1 \\ \frac{10}{3} & S=2\,. \end{cases} \tag{3.41}$$

In the following we analyze the radiative decay properties of mesons which have been generated dynamically by coupled meson channels [99, 65]. As a first application we study in Section 3.3.1 the one– and two–photon decays of the dynamically generated resonances which were analyzed in the framework of SU(3) coupled channels [99, 24]. The coupled channels analysis of [99] lead to 11 dynamically generated resonances around 1.5 GeV, where five of them have been assigned to the scalar $f_0(1370)$ and $f_0(1710)$ mesons and the tensor states $f_2(1270)$, $f_2'(1525)$ and $K_2^*(1430)$. One problem of the coupled channels is that one does not obtain the full meson nonets. In both cases, the scalars and tensors, the isovector states a_0 and a_2 are heavier than data. We are aware of the fact that these mesons are in general assigned to $q\bar{q}$ states of the constituent quark model. However, the present coupled channel approach was used to see which kind of resonances one obtains in the region between one and two GeV and e.g. it is interesting if the dynamically generated states agree with the $q\bar{q}$ states. The coupled channel approach leads to a $\rho\rho$ and $K^*\overline{K}^*$ interpretation of

the f_0 and f_2 mesons which provides an alternative viewpoint and eventually gives evidence for a relevant meson–meson component in addition to the underlying $q\bar{q}$ structure of these mesons.
Besides the light mesons, in Section 3.3.2 we concentrate on the hidden–charm resonances around 4 GeV analyzed in [65, 23]. The $Z(3930)$, $Y(3940)$ and $X(4160)$ are members of the charmonium–like mesons which are not easily explained by the standard interpretation provided by the constituent quark model. The computation of the two–photon and photon–vector meson decay properties might lead to further insights concerning their possible molecular meson substructure.

3.3.1. Radiative decays of light mesons

The eleven dynamically generated resonances of Ref. [99] are summarized in Tab. 3.15. The comparison with data shows that five of them can be identified with scalar and tensor mesons. In the following we compute the radiative decay widths of all resonances to allow for a more detailed analysis. Because of C–parity conservation the

	pole position	PDG		
$I^G(J^{PC})$	$(m,\Gamma/2)$	meson	mass	width
$0^+(0^{++})$	(1512,51)	$f_0(1370)$	1200–1500	200-500
$0^+(0^{++})$	(1726,28)	$f_0(1710)$	1724 ± 7	137 ± 8
$0^-(1^{+-})$	(1802,78)	h_1		
$0^+(2^{++})$	(1275,2)	$f_2(1270)$	1275.1 ± 1.2	$185.0^{+2.9}_{-2.4}$
$0^+(2^{++})$	(1525,6)	$f_2'(1525)$	1525 ± 5	73^{+6}_{-5}
$1^-(0^{++})$	(1780,133)	a_0		
$1^+(1^{+-})$	(1679,235)	b_1		
$1^-(2^{++})$	(1569,32)	$a_2(1700)$??		
$1/2(0^+)$	(1643,47)	K_0^*		
$1/2(1^+)$	(1737,165)	$K_1(1650)$??		
$1/2(2^+)$	(1431,1)	$K_2^*(1430)$	1429 ± 1.4	104 ± 4

Table 3.15.: Dynamically generated resonances based on SU(3) coupled channels.

h_1 and b_1 mesons ($J^{PC} = 1^{+-}$) do not decay to two photons or one photon and a

vector meson. The strange mesons K_0^*, K_1 and $K_2^*(1430)$ of course only decay into $K^*\gamma$ but not into $\gamma\gamma$.
In the following we shall have a closer look at the radiative decay widths of the resonances which might be associated with the experimentally observed $f_2(1270)$, $f_2'(1525)$, $f_0(1370)$, $f_0(1710)$ and $K_2^*(1430)$ mesons [24]. In addition, we compare our results to other theoretical investigations.

Radiative decay widths of $f_2(1270)$ and $f_2'(1525)$

The decay properties of the tensor mesons are experimentally very well known because precise data are available. The dynamically generated resonance corresponding to the $f_2(1270)$ meson arises mainly from the $\rho\rho$ interaction. Our results for the radiative decay widths of the tensor mesons $f_2(1270)$ and $f_2'(1525)$ can be found in Tab. 3.16. Despite that the $f_2(1270)$ is a strong candidate for a quark–antiquark

(Mass,Width) in MeV	Meson	$\Gamma_{\rho^0\gamma}$	$\Gamma_{\omega\gamma}$	$\Gamma_{\phi\gamma}$	$\Gamma_{\gamma\gamma}$	$\Gamma_{\gamma\gamma}$ (Exp.)
$(1276, 97)$	$f_2(1270)$	1367	5.6	5.0	2.25	3.03 ± 0.35 [22]
						$2.27 \pm 0.47 \pm 0.11$ [120]
						2.35 ± 0.65 [121]
$(1525, 45)$	$f_2'(1525)$	72	224	286	0.05	0.081 ± 0.009 [22]
$(1567, 47)$	a_2	327	358	477	1.60	

Table 3.16.: Pole positions and radiative decay widths in the strangeness=0 and isospin=0 channel. The radiative decay widths are in units of keV.

structure, the present method, assuming a dynamical origin, leads to a surprisingly good agreement with data.
The two-photon decay width for the $f_2'(1525)$ is slightly smaller than the experimental value quoted in the PDG review. This is quite acceptable since 1) we can assume an inherent theoretical uncertainty of $\sim 20\%$ and 2) there might be other relevant coupled channels that have not been taken into account in the model of Ref. [99]. This can be inferred from the fact that the total decay width of the $f_2'(1525)$ in that model ~ 50 MeV is smaller than the experimental value ~ 70 MeV.
Note that the significantly small value of the widths of the $f_2'(1525)$ (and $f_0(1710)$, see below) compared to that of the $f_2(1270)$, for example, has a natural interpretation in our theoretical framework since the former two resonances are mostly $K^*\bar{K}^*$ molecules. Therefore, the couplings to $\rho\rho$, $\omega\omega$, $\omega\phi$, $\phi\phi$, which lead to the final $\gamma\gamma$

decay, are very small. The advantages of working with coupled channels become obvious in case of this radiative decays. While a pure $K^*\bar{K}^*$ assignment would lead to $\Gamma_{\gamma\gamma}$=0 keV, our coupled channel analysis gives the right strength for the couplings to the weakly coupled channels.
Unfortunately, there is no data available for the various $V\gamma$ decays, which could provide a further test for the meson–meson structure component of these mesons.
In Tab. 3.17 we compare our results for the radiative decay widths of the $f_2(1270)$ meson with those obtained in other approaches based on a $q\bar{q}$ interpretation. These

Decay	COQM [122]	TMD [123][1]	AdS/QCD [125]	TMD&VMD [126]	NRQM [127]	Present work [24]
$\gamma\gamma$	-	3.15 ± 0.43	2.71	8.8	-	2.25
$\rho^0\gamma$	254	630 ± 86	-	1364	644	1367
$\omega\gamma$	27	-	-	167.6 ± 25		5.6
$\phi\gamma$	1.3	-	-	-	-	5.0

Table 3.17.: Results for the radiative decay widths of the $f_2(1270)$ obtained in different approaches.

include the covariant oscillator quark model (COQM) [122], the tensor-meson dominance (TMD) model [123], the AdS/QCD calculation in [125], the model assuming both tensor-meson dominance and vector-meson dominance (TMD&VMD) [126], and the nonrelativistic quark-model (NRQM) [127]. From this comparison, one can see that the AdS/QCD calculation and our present study provide a two-photon decay width consistent with data. The TMD model result is also consistent with the data (it can use either $\Gamma(f_2(1270) \to \gamma\gamma)$ or $\Gamma(f_2(1270) \to \pi^+\pi^-)$ as an input to fix its single parameter), while the TMD&VMD model prediction is off by a factor of 3. Particularly interesting is the fact that although the TMD&VMD model predicts $\Gamma(f_2(1270) \to \rho\gamma)$ similar to our prediction, but in contrast their result for $\Gamma(f_2(1270) \to \omega\gamma)$ is much larger than ours, almost by a factor of 30. Therefore, an experimental measurement of the ratio of $\Gamma(f_2(1270) \to \rho\gamma)/\Gamma(f_2(1270) \to \omega\gamma)$ will be very useful to disentangle these two pictures of the $f_2(1270)$. Furthermore, one notices that all theoretical approaches predict $\Gamma_{\rho^0\gamma}$ to be of the order of a few 100 keV.
In Tab. 3.18 we compare the radiative decay widths of the $f_2'(1525)$ predicted in the present work with those obtained in the COQM [122]. We notice that the COQM predicts $\Gamma_{\phi\gamma}/\Gamma_{\rho^0\gamma} \approx 22$ while our model gives an estimate of $\Gamma_{\phi\gamma}/\Gamma_{\rho^0\gamma} \approx 4$, which is quite different even when taking into account model uncertainties. Furthermore,

	COQM [122]	Present work [24]
$f_2'(1525) \to \gamma\gamma$		0.05
$f_2'(1525) \to \rho^0\gamma$	4.8	72
$f_2'(1525) \to \omega\gamma$	0	224
$f_2'(1525) \to \phi\gamma$	104	286

Table 3.18.: Radiative decay widths of the $f_2'(1525)$ obtained in the present work in comparison with those obtained in the covariant oscillator quark model (COQM) [122].

$\Gamma_{\omega\gamma}$ in the COQM is almost zero while it is comparable to $\Gamma_{\phi\gamma}$ in our approach. An experimental measurement of any two of the three decay widths could be able to distinguish between the COQM or the dynamical picture or even rule out both scenarios.
An interesting quantity in this context is the ratio $\Gamma(f_2'(1525) \to \gamma\gamma)/\Gamma(f_2(1270) \to \gamma\gamma)$, since the ratio of rates suffers from less systematic uncertainties within a model. In Tab. 3.19 we compare our result with available data and predictions of other

	EF [128]	TMS [129]	PDG [22]	Present work [24]
$\frac{\Gamma(f_2'(1525)\to\gamma\gamma)}{\Gamma(f_2(1270)\to\gamma\gamma)}$	0.046	0.034	0.027 ± 0.006	0.023

Table 3.19.: Our results for the ratio $\Gamma(f_2'(1525) \to \gamma\gamma)/\Gamma(f_2(1270) \to \gamma\gamma)$ in comparison with other approaches and data.

theoretical approaches. It is clear that our result lies within the experimental bounds while those of the effective field approach (EF) [128] and the two-state mixing scheme (TMS) [129] are slightly larger than the experimental upper limit, with the latter being almost at the upper limit. Given the fact that we have no free parameters in this calculation such an agreement is reasonable.

Radiative decay widths of the $f_0(1370)$ and $f_0(1710)$

Now let us turn our attention to the $f_0(1370)$ and $f_0(1710)$ mesons. In Tab. 3.20 we compare our results for the radiative decay widths of the $f_0(1370)$ and $f_0(1710)$ with available data. Similar to the tensor mesons the lighter $f_0(1370)$ is dominantly a $\rho\rho$ state while the $f_0(1710)$ is generated from the $K^*\overline{K}^*$ component. For this reason the $\rho^0\gamma$ and $\gamma\gamma$ decay widths of the $f_0(1370)$ are much larger than that of

Pole position [MeV]	Meson	$\Gamma_{\rho^0\gamma}$	$\Gamma_{\omega\gamma}$	$\Gamma_{\phi\gamma}$	$\Gamma_{\gamma\gamma}$	$\Gamma_{\gamma\gamma}$ (Exp.)
$(1523, 257)$	$f_0(1370)$	726	0.04	0.01	1.31	-
$(1721, 133)$	$f_0(1710)$	24	82	94	0.05	< 0.289 [22][2]
$(1777, 148)$	a_0	247	290	376	1.61	

Table 3.20.: Pole positions and radiative decay widths of the scalar mesons in units of keV.

the $f_0(1710)$. Despite that no precise data is available, at least in the case of the $f_0(1710)$ our result is consistent with the experimental upper limit.
In Tab. 3.21 we compare our results for the radiative decay widths of the $f_0(1370)$ and $f_0(1710)$ obtained by the coupled channel model with the predictions of other theoretical approaches, including the nonrelativistic quark model (NRQM) [127], the light-front quark model (LFQM) [130], and the calculation of Nagahiro et al. [131]. In the NRQM and LFQM calculations, based on two $q\bar{q}$ states and an admixed glueball (see discussion in Sec. 2.1), two numbers are given for each decay channel depending on whether the glueball mass used in the calculation is smaller than the $n\bar{n}$ mass (Light) or larger than the $s\bar{s}$ mass (Heavy) [127, 130].
First we note that for the $f_0(1370)$ our predicted two-photon decay width is more consistent with the LFQM result in the light glueball scenario, while the $\rho\gamma$ decay width lies closer to the LFQM result in the heavy glueball scenario. Furthermore, the $\omega\gamma$ decay width in our model is an order of magnitude smaller than that in the LFQM.
For the $f_0(1710)$, the LFQM two-photon decay width is larger than the current experimental limit (see Tab. 3.20). On the other hand, our $\rho^0\gamma$ decay width is more consistent with the LFQM in the light glueball scenario while the $\phi\gamma$ decay width is more consistent with the heavy glueball scenario. Similar to the $f_0(1370)$ case, here further experimental data are needed to clarify the situation.
Furthermore, we notice that the NRQM and the LFQM in the light glueball mass scenarios and our present study all predict that $\Gamma_{\rho\gamma} \gg \Gamma_{\phi\gamma}$ for the $f_0(1370)$ while $\Gamma_{\rho\gamma} \ll \Gamma_{\phi\gamma}$ for the $f_0(1710)$. On the other hand, the NRQM and LFQM in the heavy glueball scenario predict $\Gamma_{\rho\gamma} \gg \Gamma_{\phi\gamma}$ for the $f_0(1710)$. Therefore, an experimental measurement of the ratio of $\Gamma_{f_0(1710)\to\rho\gamma}/\Gamma_{f_0(1710)\to\phi\gamma}$ not only will distinguish between the quark-model picture and the dynamical picture, but can also put a constraint on the mass of a possible glueball in this mass region.
The chiral approach in [132] delivers smaller absolute results for the two-photon decays of the $f_0(1370)$ and $f_0(1710)$. However, the ratio $\Gamma(f_0(1370) \to \gamma\gamma)/\Gamma(f_0(1710) \to \gamma\gamma) = 18.4$ lies much closer to our prediction $\Gamma(f_0(1370) \to \gamma\gamma)/\Gamma(f_0(1710) \to \gamma\gamma) \approx 26$ than the LFQM results which lies in a range between 1.7-3.0.

	NRQM [127][3]		LFQM [130][a]		[131]		[132]	Present
	Light	Heavy	Light	Heavy	$K\bar{K}$ loop	$\pi\pi$ loop		work
$f_0(1370)$								
$\to \gamma\gamma$	–	–	1.6	$5.6^{+1.4}_{-1.3}$	–	–	0.35	1.31
$\to \rho^0\gamma$	443	1540	150	530^{+120}_{-110}	79 ± 40	125 ± 80	–	726
$\to \omega\gamma$	–	–	–	–	7 ± 3	128 ± 80	–	0.04
$\to \phi\gamma$	8	32	0.98	$4.5^{+4.5}_{-3.0}$	11 ± 6	–	–	0.01
$f_0(1710)$								
$\to \gamma\gamma$	–	–	0.92	$3.0^{+1.4}_{-1.2}$	-		0.019	0.05
$\to \rho^0\gamma$	42	705	24	410^{+200}_{-160}	100 ± 40		–	24
$\to \omega\gamma$	–	–	–	–	3.3 ± 1.2		–	82
$\to \phi\gamma$	800	78	450	36^{+17}_{-14}	15 ± 5		–	94

Table 3.21.: Radiative decay widths of the $f_0(1370)$ and $f_0(1710)$ obtained in the present work and in comparison with other approaches. All decay widths are given in keV.

Nagahiro et al. [131] evaluate the contributions from $K\bar{K}$ and $\pi\pi$ loops by using a phenomenological scalar coupling of the $f_0(1710)$ and $f_0(1370)$ mesons to the $K\overline{K}$ and $\pi\pi$ channels. From the new analysis of these states within the framework of coupled channels [99] the scalar couplings may not be justified anymore. One rather has the $f_0(1710)$ coupling to $K^*\bar{K}^*$ while the coupling to the $K\bar{K}$ channel only occurs indirectly through the decay $K^* \to K\pi$. Here, the pions correspond to virtual internal propagators. As found in Ref. [98], loops containing these π propagators only lead to small contributions compared to leading terms including vector mesons (four-vector contact and t(u)-channel vector exchange).

Experimentally, there is a further piece of information on the $f_0(1710)$ that is relevant to the present study. From the J/ψ decay branching ratios to $\gamma\omega\omega$ and $\gamma K\bar{K}$, one can deduce [22]

$$\begin{aligned} \frac{\Gamma(f_0(1710) \to \omega\omega)}{\Gamma(f_0(1710) \to K\bar{K})} &= \frac{Br(J/\psi \to \gamma f_0(1710) \to \gamma\omega\omega)}{Br(J/\psi \to \gamma f_0(1710) \to \gamma K\bar{K})} = \frac{(3.1 \pm 1.0) \times 10^{-4}}{(8.5^{+1.2}_{-0.9}) \times 10^{-4}} \\ &= 0.365^{+0.156}_{-0.169}\,. \end{aligned} \tag{3.42}$$

In the same way as we obtain the two-photon decay widths, we can also calculate the two-vector-meson decay width of the dynamically generated resonances. For the

$f_0(1710)$ its decay width to $\omega\omega$ is found to be

$$\Gamma(f_0(1710) \to \omega\omega) = 15.2 \text{ MeV}.$$

Using $\Gamma_{\text{total}}(f_0(1710)) = 133$ MeV, already derived in Ref. [133], and the ratio $\frac{\Gamma(K\bar{K})}{\Gamma_{\text{total}}(f_0(1710))} \approx 55$ % also given in Ref. [133], one obtains following ratio

$$\frac{\Gamma(f_0(1710) \to \omega\omega)}{\Gamma(f_0(1710) \to K\bar{K})} = 0.21 \tag{3.43}$$

which lies within the experimental bounds although close to the lower limit.

Radiative decay widths of the $K_2^*(1430)$

The decay widths for the strange resonances are indicated in Tab. 3.22. Unfortunately, there is no data available. However, the radiative decay widths of the

Pole position [MeV]	Meson	$\Gamma_{K^{*+}\gamma}$ [keV]	$\Gamma_{K^{*0}\gamma}$ [keV]
$(1639, 139)$	K_0^*	187	520
$(1743, 126)$	K_1	143	571
$(1431, 56)$	$K_2^*(1430)$	261	1056

Table 3.22.: Radiative decay widths of the strange mesons.

	COQM [122]	Present work
$K_2^{*+}(1430) \to K^{*+}\gamma$	38	261
$K_2^{*0}(1430) \to K^{*0}\gamma$	109	1056

Table 3.23.: Radiative decay widths of the $K_2^*(1430)$ (in keV) obtained in the present work in comparison with the results of the covariant oscillator quark model (COQM) [122].

$K_2^*(1430)$ calculated in the present work are compared to those calculated in the covariant oscillator quark model (COQM) [122] in Tab. 3.23. We notice that the results from these two approaches differ by a factor of 10. However, there is one thing in common, i.e., both predict a much larger $\Gamma_{K^{*0}\gamma}$ than $\Gamma_{K^{*+}\gamma}$. More specifically, in the COQM $\Gamma_{K^{*0}\gamma}/\Gamma_{K^{*+}\gamma} \approx 3$, while in our model this ratio is ≈ 4.

As already mentioned, at present there exists no experimental measurement of these decay modes. On the other hand, the $K_2^*(1430) \to K^+\gamma$ and $K_2^*(1430) \to K^0\gamma$ decay rates have been measured. According to PDG [22], $\Gamma_{K^+\gamma} = 241 \pm 50$ keV and $\Gamma_{K^0\gamma} < 5.4$ keV. Comparing these decay rates with those shown in Tab. 3.23, one immediately notices that in the dynamical model the $\Gamma_{K^{*+}\gamma}$ is of similar order as the $\Gamma_{K^+\gamma}$ despite the reduced phase space in the former decay. This is of course closely related to the fact that the $K_2^*(1430)$ is built out of the coupled channel interaction between the ρK^*, ωK^*, and ϕK^* components in the dynamical model. Furthermore, both the COQM and our dynamical model predict $\Gamma_{K^{*0}\gamma} \gg \Gamma_{K^{*+}\gamma}$, which is opposite to the decays into a kaon plus a photon where $\Gamma_{K^+\gamma} \gg \Gamma_{K^0\gamma}$. An experimental measurement of those decays would be very interesting and will certainly help to clarify the present situation.

3.3.2. Radiative decays of hidden–charm mesons

In order to compute the radiative decay widths of the $Y(3940)$, $Z(3930)$, $X(4160)$ and the so far not observed $'Y_p(3912)'$ [23] we take the couplings between resonances and the VV channels from [65]. In the case of the $'Y_p(3912)'$ state with quantum numbers $I^G(J^{PC}) = 0^-(1^{+-})$ all couplings to vector mesons with hidden flavor are zero due to C–parity violation. Therefore, radiative decays via VMD are forbidden in this case.

In the context of the radiative decays of the X, Y and Z mesons it is important to consider the three–momenta of the vector mesons which couple to the final photons. In previous analyses the three momenta of the particles were neglected with respect to the vector meson mass, $|\vec{p}|/M_{D^*} \simeq 0$. This is indeed the case for massive states but not if we deal with two photons in the final state since $|\vec{p}_\gamma| \simeq M_{D^*}$. For simplicity we do not consider a fully relativistic approach but it turns out that in particular the vector meson exchange vertex depends sensitively on the three–momenta of the vector mesons.

Hence, improvements on the present results are necessary. For this purpose we re-analyze the couplings of [65] by considering the final momenta of the light vectors which finally couple to the photons. We therefore modify the corresponding expressions in [65] in the following way, suitable for the photon field in the Coulomb gauge.

1) For $J = 0$, we include the three–momenta by doing the following replacement:

$$(k_1^0 + k_3^0)(k_2^0 + k_4^0) \to (k_1^0 + k_3^0)(k_2^0 + k_4^0) + 5\vec{k}_3^2 + \frac{\vec{k}_3^4}{M_{\rm exc}^2} \tag{3.44}$$

2) By analogy we change in the case of $J = 2$:

$$(k_1^0 + k_3^0)(k_2^0 + k_4^0) \to \sqrt{a^2 + \frac{32}{5}\vec{k}_3^2} \tag{3.45}$$

with

$$a = (k_1^0 + k_3^0)(k_2^0 + k_4^0) + \vec{k}_3^2 + \frac{\vec{k}_3^4}{M_{\rm exc}^2} \ , \tag{3.46}$$

where $\vec{k}_3$ is the photon momentum and $M_{\rm exc}$ is the mass of the exchanged vector meson, M_{D^*} or $M_{D_s^*}$.

With this prescription we solve the coupled channels Bethe–Salpeter equations and obtain new couplings of the resonances to pairs of vectors, which, via the VMD, provide the appropriate couplings of the resonances to the photons. The couplings to $D^*\overline{D}^*$ and $D_s^*\overline{D}_s^*$ are practically unchanged as well as the masses of the resonances. We obtain new effective couplings to the light vectors which characterize the $\gamma\gamma$ decay rates.
The results for the radiative decay widths are summarized in Tab. 3.24. The decay widths of the $Y(3940)$ are in general smaller when compared to the other resonances. A further common feature is that the $\rho\gamma$ and $\gamma\gamma$ decay modes are suppressed in comparison to the $\omega\gamma$ and $\phi\gamma$ decays except for the predicted $Y_p(3912)$ resonance, which shows a rather strong coupling to the $\rho\gamma$ decay channel. The two-photon

pole [MeV]	$(3943, +i7.4)$	$(3922, +i26)$	$(4169, +i66)$	$(3919, +i74)$
$I^G\ J^{PC}$	$0^+\ (0^{++})$	$0^+\ (2^{++})$	$0^+\ (2^{++})$	$1^-\ (2^{++})$
meson	$Y(3940)$	$Z(3930)$	$X(4160)$	$'Y_p(3912)'$
$\Gamma_{\rho\gamma}$[keV]	0.015	0.040	0.029	201.458
$\Gamma_{\omega\gamma}$[keV]	0.989		15.15510.659	114.561
$\Gamma_{\phi\gamma}$[keV]	13.629	95.647	268.854	62.091
$\Gamma_{J/\psi\gamma}$[keV]	0.722	13.952	125.529	135.479
$\Gamma_{\gamma\gamma}$[keV]	0.085	0.074	0.54	1.11

Table 3.24.: Pole positions and radiative decay widths.

decay of the $Y(3940)$ is of the same order of magnitude as in Ref. [25] which is

also based on a $D^*\overline{D}^*$ molecular structure interpretation of the $Y(3940)$. The two photon width obtained within the coupled channel formalism is still by a factor three smaller than the result of the effective Lagrangian approach of [25] but this discrepancy lies within the theoretical uncertainties of this small rate.

For the two–photon width of the $X(4160)$ we obtain $\Gamma(X(4160) \to \gamma\gamma) = 0.54$ keV. In the present coupled channel approach the $X(4160)$ is found to be dominantly a $D_s^{*+}D_s^{*-}$ state. This is the same underlying structure as the $D_s^*\overline{D}_s^*$ bound state studied in [25]. In reference [25] the $D_s^*\overline{D}_s^*$ molecular state was associated with the narrow $Y(4140)$ discovered by the CDF [56] because it was possible to explain the sizable observed $J/\psi\phi$ decay width of this state. Our association with the broader $X(4160)$ is suggested by the large total theoretical width which was not evaluated in [25]. Since the nature of the resonances is the same in both approaches it is less surprising that the present result for $\Gamma(X(4160) \to \gamma\gamma) = 0.54$ keV agrees with $\Gamma(Y(4140) \to \gamma\gamma) = 0.5$ keV evaluated in [25].

Experimental observations concerning the radiative decays are rare. However, the BELLE Collaboration searched for charmonium–like resonances in the $\gamma\gamma \to \omega J/\psi$ process [134] which resulted in an enhancement of the cross section around M = $3915 \pm 3 \pm 2$ MeV. The peak was associated with a resonance denoted by $X(3915)$. But it is thought that it could be the $Y(3940)$ resonance or even the $Z(3930)$ which we have associated to our $J^P = 2^+$ resonance at 3922 MeV. In [134] the $X(3915)$ has unknown spin and parity, but 0^+ or 2^+ are preferred. In the following we compare the experimental observations [134]

$$\Gamma_{\gamma\gamma}(X(3915))\mathcal{B}(X(3915) \to \omega J/\psi) = \begin{cases} (61 \pm 17 \pm 8) \text{ eV} & \text{for } J^P = 0^+ \\ (18 \pm 5 \pm 2) \text{ eV} & \text{for } J^P = 2^+ \end{cases} \tag{3.47}$$

with the results of the present approach. Let us evaluate Eq. (3.47) for the two theoretical states with $J^P = 0^+$ and mass 3943 MeV ($Y(3940)$) and 2^+ at 3922 MeV ($Z(3930)$) in Tab. 3.24. From the respective couplings $g_{\omega J/\psi}$ of the $Y(3940)$ and $Z(3930)$ resonances to the $\omega J/\psi$ channel we can estimate the partial decay width by

$$\Gamma(Y(Z) \to \omega J/\psi) = \frac{1}{8\pi}\frac{k g^2_{\omega J/\psi}}{M_R^2} \,, \tag{3.48}$$

where k is the momentum of the final meson. We obtain

$$\begin{aligned} \Gamma(Y(3940) \to \omega J/\psi) &= 1.52 \text{ MeV} \\ \Gamma(Z(3930) \to \omega J/\psi) &= 8.66 \text{ MeV} \,. \end{aligned} \tag{3.49}$$

Together with the two photon decay widths of Tab. 3.24 we find

$$\begin{aligned}\Gamma(Y(3940)\to\gamma\gamma)\,Br(Y(3940)\to\omega J/\psi) &= 7.6\text{ eV}\\ \Gamma(Z(3930)\to\gamma\gamma)\,Br(Z(3930)\to\omega J/\psi) &= 11.8\text{ eV}\,.\end{aligned}\tag{3.50}$$

If we compare these results with the experimental observations in Eq. (3.47) we immediately see that the $J^P = 2^+$ state $Z(3930)$ matches the experimental observation of the BELLE collaboration (3.47) of about 18 eV. On the contrary, our result for the $Y(3940)$ meson with quantum numbers $J^P = 0^+$ underestimates the experimental observations by an order of magnitude. Our study thus favors the association of the $Z(3930)$ resonance with the $X(3915)$ in [134].

3.3.3. Summary

We studied the two–photon and photon–vector meson decay properties of dynamically generated resonances from vector–vector coupled channels in an unitarity hidden gauge formalism. In the present work the focus was set on radiative decays of the scalar and tensor mesons between one and two GeV and the hidden–charm mesons around 4 GeV analyzed in [65]. The results are compared with available data and other theoretical models in order to test the dynamical picture of the mesons versus the ordinary $q\bar{q}$ predictions.

First we have calculated the radiative decay widths of the $f_2(1270)$, $f_0(1370)$, $f_2'(1525)$, $f_0(1710)$, $K_2^*(1430)$, and four other states that appear dynamically from vector meson-vector meson interaction in an unitary approach. In particular, we have identified the relevant pattern of decay rates predicted by different theoretical models and found them to be quite distinct. For instance, the $\Gamma(f_2(1270)\to\rho\gamma)/\Gamma(f_2(1270)\to\omega\gamma)$ ratio is quite different in the dynamical model from those in the TMD&VMD model and the COQM model. By analogy, the $\Gamma(f_2'(1525)\to\phi\gamma)/\Gamma(f_2'(1525)\to\rho\gamma)$ ratio in the COQM model is orders of magnitude larger than in the dynamical picture.

A measurement of the $f_0(1370)/f_0(1710)$ decay rates into $\rho\gamma$ and $\phi\gamma$ is possible which not only could be used to distinguish between the quark model (NRQM and LFQM) picture and the dynamical picture but also to put a constraint on the mass of a possible glueball (in the $q\bar{q}$-g mixing scheme of the NRQM and LFQM). For the $K_2^*(1430)$, as we have discussed, a measurement of its $K^{*+}(K^{*0})\gamma$ decay mode will definitely be able to determine to what extent the dynamical picture is correct.

Besides the light unflavored mesons we also studied the radiative decays of the hidden–charm mesons around 4 GeV [65]. According to their masses and widths three of them are good candidates for the $Y(3940)$, $Z(3930)$ and $X(4160)$ mesons discovered by BELLE and BABAR. Furthermore, the $Z(3930)$ possibly corresponds to the recently observed $X(3915)$. The two–photon decay width of the $Y(3940)$ in the hidden gauge formalism, assumed to be 0^+, is more uncertain due to large can-

cellations and could be compatible with the larger width of the prediction obtained in the pure $D^*\overline{D}^*$ molecule interpretation in [25]. In the case of the $X(4160)$, which we assume to be the 2^+ state at 4169 MeV, the $\gamma\gamma$ decay width agrees with the results of [25] for a ${D_s^*}^+{D_s^*}^-$ molecule with a chosen mass of 4140 MeV.
The information on the $\Gamma_{\gamma\gamma}$ decay rate of the $X(3915)$ favors the association of this resonance with the (2^+, 3922) resonance that we obtain. Here, the quantum numbers 0^+ are clearly disfavored.
Unfortunately, there is not much data on radiative decays of the X, Y and Z mesons. The large variety of results obtained by us concerning the different decays and different resonances indicates that these measurements are very useful to shed light on the structure of these resonances. In particular, the vector meson–photon decay modes could be addressed in future facilities like PANDA and BESIII, and undoubtedly these measurements would be very valuable to help to disentangle different aspects of the nature of these charmonium like states.
Finally, we would like to stress that QCD dynamics is much richer than the present theoretical scenario described by dynamically generated resonances. It is therefore not very surprising that sometimes agreement with data is not perfect but the model delivers at least an qualitative insight in the decay pattern. Because of the distinct pattern in different theoretical models, an experimental measurement of some of the decay modes are very sensitive to the nature of these resonances.

4. Effective Model for Hadronic Bound States

In the following chapter we introduce a further theoretical approach for the investigation of hadron structure. The present relativistic quantum field theoretical method is based on effective interaction Lagrangians in order to describe any kind of hadronic bound states. In contrast to the previously discussed coupled channel approach, the present model is therefore not restricted to a particular hadron substructure but can be applied to a wide range of structure issues from conventional mesons [135, 136] and baryons [137, 138], composed of a quark-antiquark pair and three quarks, to bound states on the hadron level [26] — hadronic molecules. In addition, the method is universally applicable to study decay and production properties of all kind of hadron bound states which can either consist of quarks or hadrons. Further prominent features of the method are the manifest gauge invariance when including electroweak interactions and the consideration of the extended structure of the hadronic bound state.

We will use the effective Lagrangian approach to continue the study of mesonic bound states but also consider conventional $q\bar{q}$ mesons within this framework. We calculate radiative, strong and weak decay and production properties which we compare with other theoretical approaches and, if available, experimental observations. In the following Section 4.1 the method is introduced by the example of meson molecules. In the first part of this chapter we stay with the topic of bound states of mesons. Candidates for hadronic molecule structure are resonances which cannot be fully understood in the $q\bar{q}$ picture and which typically lie close to a two–meson threshold. Of course, the nearby threshold is necessary but not sufficient to identify a meson molecule, but binding of the system has to be guaranteed as well. This issue can e.g. be studied by coupled channel methods, meson exchange models or QCD sum rule approaches (see discussion in Chapter 3).

As a first application of the model we consider the light scalars $f_0(980)$ and $a_0(980)$ as hadronic molecules built of kaons. We study the radiative and strong decay properties and additionally also consider weak transitions between hadronic molecules, i.e. f_0 production from charmed and bottom meson bound states. Since the light scalars are well studied from the experimental side, this mesons can be also considered as a test case of our model. We find that the kaon molecule picture studied within the framework of the present method can reproduce experimental observation rather well.

We then turn to the more topical hidden–charm mesons $Y(3940)$, $Y(4140)$ and $Z^{\pm}(4430)$ which have attracted much interest in recent years. For the examples discussed here it is difficult and in the case of the $Z^{\pm}$ impossible to explain these resonances as $c\bar{c}$ states. The meson molecule interpretation of these mesons allows to explain the unusual features which are in contradiction to the charmonium interpretation.

More details on the experimental situation of the mesons discussed within the framework of hadronic molecules can be found in Chapter 3.

4.1. Formalism

In the coupled channel formalism discussed in the previous chapter we deal with several meson–meson channels which can contribute to the formation of a resonance. In contrast, the present effective Lagrangian approach is based on a structure assumption for a meson as a pure bound state of e.g. two mesons. However, this assumption is justified since we only treat mesons which show clear properties of hadron bound states. For example all mesons discussed within this formalism lie close to a two–meson threshold which is a strong hint for the possible binding of the corresponding meson–meson system. Therefore, we deal primarily with one dominant meson–meson component while other contributions can be neglected. This is also in agreement with the previously mentioned coupled channel approach. Here, resonances which lie close to a threshold also show a strong affinity to this particular channel while couplings to other meson–meson channels are much smaller. Therefore, we also end up with a molecular picture in the coupled channel approach which is consistent with the present hadronic molecule picture.

This framework technically also allows for the inclusion of different hadron substructures, e.g. a meson–meson component and a compact $q\bar{q}$ structure as it was done in [139]. However, this is at the cost of further parameters related to the amplitude of each component.

In the following we introduce the effective Lagrangian approach by means of a meson molecule H with mass m and momentum p which is considered as a bound state of two mesons M_1 and M_2. The masses of the constituent mesons we refer to as m_1 and m_2. In the first step we set up the bound state

$$\big|H\big\rangle = \big|M_1 M_2\big\rangle \tag{4.1}$$

from which we can define the effective Lagrangian describing the interaction between the hadronic bound state and its constituents

$$\mathcal{L}_{HM_1M_2} = g_{HM_1M_2} H(x) \int dx_1 \int dx_2 \Phi(x, x_1, x_2)\, J_{M_1M_2}(x_1, x_2)\,, \tag{4.2}$$

where $J_{M_1M_2}(x_1, x_2)$ represents the appropriate current of the constituent mesons M_1 and M_2 carrying the quantum numbers of H. The explicit structure of the Lagrangian and meson currents are discussed for each hadronic bound state in the following sections.

Since we consider the spatially extended structure of the molecular state, we introduce the center of mass and relative coordinates $x_1 = x + \omega_{12}y$ and $x_2 = x - \omega_{21}y$, where $\omega_{ij} = m_j/(m_i + m_j)$. Therefore, we deal with a nonlocal interaction Lagrangian (4.2). In particular, we consider the extended structure of the bound state i.e. the distribution of the constituents by the vertex function Φ. Its Fourier transform enters as a form factor in our calculations. A basic requirement for the choice of an explicit form of the correlation function Φ is that its Fourier transform vanishes at a sufficient rate in the ultraviolet region of Euclidean space to render the Feynman diagrams ultraviolet finite. In earlier analyses [140, 141] it was shown that the influence of the shape of the form factor plays a minor role for processes where the external momenta are relatively small. This criterion is fulfilled since in the present work we deal dominantly with observables characterizing decay and production processes. In the present analyses we use a Gaussian cutoff

$$\widetilde{\Phi}(k_E^2) = \exp(-k_E^2/\Lambda^2) \tag{4.3}$$

with the four-dimensional size parameter Λ. The index E in the argument of $\widetilde{\Phi}$ is chosen to emphasize that we are working in Euclidean space.

The composite structure of the bound state is set up by the compositeness or Weinberg condition [142], where a bound state is realized by setting its field renormalization constant Z to zero. Since the field renormalization constant represents the matrix element between bare and dressed fields the bound state exists as a pure composite object without any further genuine component. The renormalization constant of the composite field is defined by

$$Z_H = 1 - \Pi'(p^2)\big|_{p^2=M^2} = 1 - g_H^2\Sigma'(p^2)\big|_{p^2=M^2}\,, \tag{4.4}$$

where $\Pi(p^2)$ denotes the mass operator

$$\Pi(p^2) = g_H^2\Sigma(p^2) = \frac{g_H^2}{(4\pi)^2}\int\frac{d^4k}{\pi^2 i}\,\widetilde{\Phi}(-k^2)\Gamma S_{M_1}(k+\omega_{21}p)\Gamma^\dagger S_{M_2}(k-\omega_{12}p) \tag{4.5}$$

which is depicted in Fig. 4.1. Γ represent the appropriate vertex structures and $S_M(k)$ is the free propagator of the meson field M (for details see following sections). The Weinberg condition [142] was originally applied to the deuteron as a proton–

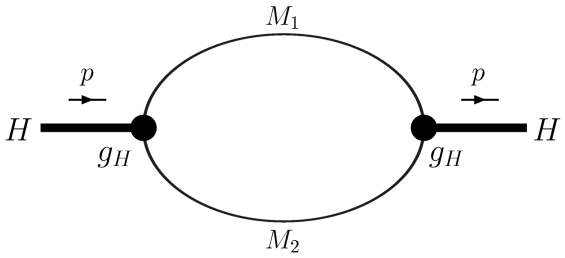

Figure 4.1.: Mass operator of the hadronic molecule H.

neutron bound state relating the coupling g_H^W and binding energy ϵ_H as

$$g_H^W = \sqrt{32\pi}\, M^{3/4}\, \epsilon_H^{1/4}\,. \tag{4.6}$$

This formula represents the leading term of an expansion in powers of the binding energy ϵ_H. Note that this expression is obtained in the local limit (i.e. the vertex function approaches the limit $\Phi(y^2) \to \delta^4(y)$).

Meson loop diagrams are evaluated by using the free meson propagators, which in momentum space read as

$$S(k) \;=\; \frac{1}{M^2 - k^2 - i\epsilon} \tag{4.7}$$

in case of pseudoscalar and scalar mesons, and

$$S^{\mu\nu}(k) \;=\; \frac{-g^{\mu\nu} + k^\mu k^\nu/M^2}{M^2 - k^2 - i\epsilon} \tag{4.8}$$

for vector mesons. Here, we do not include the finite widths of constituent mesons in the propagators since, in general, the total width of the molecular state should be bigger than the widths of the constituent mesons.

The aim of this approach is the evaluation of decay processes which in the molecular picture are usually driven by an intermediate loop containing the constituent mesons as depicted in Fig. 4.2. The final decay products couple via the constituent mesons to the hadronic molecule, where the interaction is again determined by effective Lagrangians. The most general form of the loop integral is given by

$$\begin{aligned} I(M^2, M_A^2, M_B^2) \;=\; & \int \frac{d^4k}{\pi^2 i}\, \Phi_1\big(-k^2\big)\, \Phi_2\big(-(k + \omega_{31} p - \omega_{21} p_1)^2\big) \\ & \times\; \Phi_3\big(-(k - \omega_{13} p + \omega_{23} p_2)^2\big) \\ & \times\; \Gamma_1\, S_3(k - \omega_{13} p)\, \Gamma_3\, S_2(k - \omega_{13} p + p_2)\, \Gamma_2\, S_1(k + \omega_{31} p)\,, \end{aligned} \tag{4.9}$$

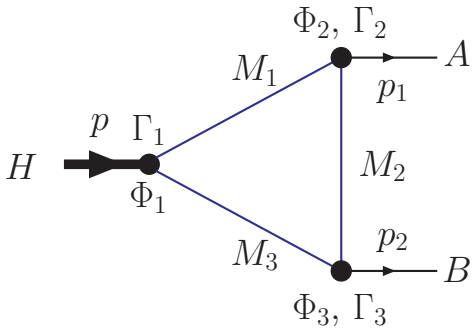

Figure 4.2.: Decay of a hadronic molecule via a meson loop.

where the indices $1, 2, 3$ refer to the respective particle and vertex structure in the loop of Fig. 4.2. In most cases the form factors Φ_2 and Φ_3 are equal to one since in comparison to the extended structure of the hadronic molecule finite size effects of the other hadrons involved are neglected.

4.1.1. Inclusion of the electromagnetic interaction

Radiative decay and production processes of mesons are an important aspect of meson structure since electromagnetic transitions are in general more precisely determined by theory and experiment than strong decays. The reason is the precise theoretical knowledge how to include the electromagnetic coupling while on the experimental side clean events can be obtained without overwhelming hadron production. The basic requirement for including the electromagnetic interaction is gauge invariance which means that the Lagrangian has to be invariant under local $U(1)$ transformations. The standard procedure to include the electromagnetic interaction is provided by minimal substitution of the free meson Lagrangians. In order to guarantee invariance of the Lagrangian with respect to the local field transformation $\Phi(x) \to e^{ie\alpha(x)}\Phi(x)$, where e is the charge and $\alpha(x)$ a local real phase, one has to include an external gauge field $A_\mu(x)$, which transforms as $A_\mu(x) \to A_\mu(x) + \partial_\mu\alpha(x)$. To compensate the field transformation in the free meson Lagrangian the four–derivative needs to be complemented by an additional term leading to the covariant derivative

$$D_\mu = \partial_\mu - ieA_\mu\,. \tag{4.10}$$

The additional term leads to one– and two–photon couplings of the charged mesons $M^\pm$ (see Fig. 4.3).
In the present approach we also deal with a nonlocal Lagrangian in Eq. (4.2) due to the spatially extended structure of the bound state. The corresponding expression in Eq. (4.2) is not gauge invariant with respect to the transformations of the meson

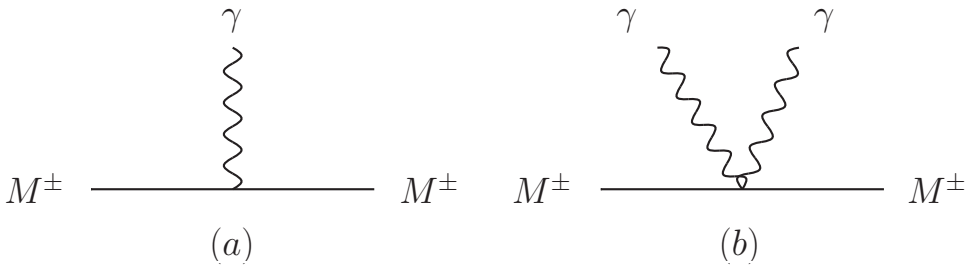

Figure 4.3.: One– and two–photon couplings from minimal substitution.

field with $M^{\pm} \to e^{\pm ie\alpha(x)} M^{\pm}$ and the gauge field $A^{\mu}(x) \to A^{\mu}(x) + \partial^{\mu}\alpha(x)$. In order to restore gauge invariance of nonlocal Lagrangians we use the method introduced in [143], where each charged meson field is multiplied by an exponential containing the gauge field

$$M^{\pm} \to e^{\mp ieI(x,y)} M^{\pm} \,, \tag{4.11}$$

with

$$I(x,y,P) = \int_x^y dz_{\mu} A^{\mu}(z) \,. \tag{4.12}$$

Superficially the results appear to depend on the path P which connects the end–points in the path integral in Eq (4.12). However, one only needs to know derivatives of the path integrals when doing the perturbative expansion. One can make use of the formalism developed in [143] which is based on the path–independent definition of the derivative of $I(x,y,P)$:

$$\lim_{dx^{\mu}\to 0} dx^{\mu} \frac{\partial}{\partial x^{\mu}} I(x,y,P) \;=\; \lim_{dx^{\mu}\to 0} [I(x+dx,y,P') - I(x,y,P)] \tag{4.13}$$

where the path P' is obtained from P by shifting the end–point x by dx. Use of the definition (4.13) leads to the key rule

$$\frac{\partial}{\partial x^{\mu}} I(x,y,P) = A_{\mu}(x) \tag{4.14}$$

which states that the derivative of the path integral $I(x,y,P)$ does not depend on the path P originally used in the definition. The non–minimal substitution (4.11) is therefore completely equivalent to the minimal prescription $\partial_{\mu} M^{\pm} \to (\partial_{\mu} \mp ieA_{\mu}) M^{\pm}$ as is evident from the identities (4.13) or (4.14).
The gauging of the nonlocal Lagrangian leads diagrammatically to new vertex structures which are illustrated in Fig. 4.4. In summary, the nonlocality of the present

approach leads to additional diagrams contributing to the respective decay which are required to guarantee full gauge invariance of the method. It is important to

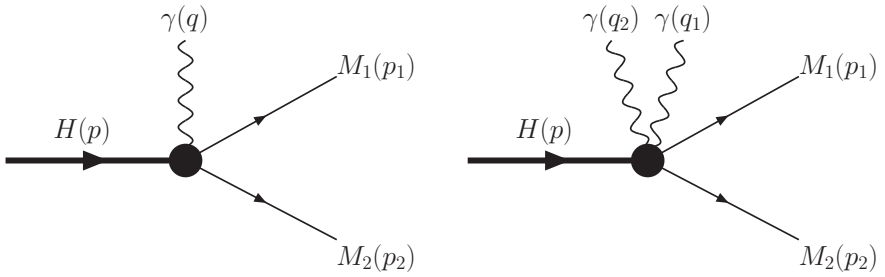

Figure 4.4.: Contact vertices arising due to the nonlocality of the interaction between bound state and constituents.

note that not necessarily each graph separately but only the sum of all diagrams leads to a gauge invariant structure of the matrix element. However, we will see later on that the inclusion of the contact vertices only leads to a negligible contribution to the transition amplitude.
Gauge invariance not only requires an invariant form of the Lagrangian but also leads to a certain structure of the transition amplitudes for processes with gauge fields involved. In the following we demonstrate this issue by means of the two–photon decay of a scalar or pseudoscalar particle M. We denote the momenta of the two photons by q_1 and q_2. The most general structure of the transition amplitude contains five form factors F_i

$$\mathcal{M}^{\mu\nu}_{H\to\gamma\gamma} = F_1 g^{\mu\nu} + F_2 q_2^\mu q_1^\nu + F_3 q_1^\mu q_2^\nu + F_4 q_1^\mu q_1^\nu + F_5 q_2^\mu q_2^\nu \,. \tag{4.15}$$

Since above matrix element is finally contracted with the photon polarizations ϵ_1^μ and ϵ_2^ν, the last three terms of $\mathcal{M}^{\mu\nu}_{H\to\gamma\gamma}$ are zero since four–momentum and polarization are perpendicular in the Lorentz gauge $\epsilon_\mu(q)q^\mu = 0$. Furthermore, it is also required that, in the case of real photons, the matrix element is perpendicular to the photon momenta, i.e. $\mathcal{M}^{\mu\nu}_{H\to\gamma\gamma} q_{1\,\mu} q_{2\,\nu} = 0$. The second condition leads to

$$F_1 = -F_2\, q_1 q_2 \,, \tag{4.16}$$

hence, the two–photon transition is characterized by only one form factor

$$\mathcal{M}^{\mu\nu}_{H\to\gamma\gamma} = F_1\big(g^{\mu\nu} - \frac{q_2^\mu q_1^\nu}{q_1 q_2}\big) = F_{H\gamma\gamma} b^{\mu\nu} \,, \tag{4.17}$$

when dealing with on-shell photons as is the case of decay and production processes. The structure $b^{\mu\nu}$reads

$$b^{\mu\nu} = g^{\mu\nu} q_1 q_2 - q_1^\nu q_2^\mu \,. \tag{4.18}$$

Off-shell photons, which differ by an additional longitudinal component of the polarization vector ϵ^μ from real photons, lead to a second form factor $G_{H\gamma\gamma}$

$$\mathcal{M}^{\mu\nu}_{H\to\gamma\gamma} = F_{H\gamma\gamma} b^{\mu\nu} + G_{H\gamma\gamma} c^{\mu\nu} \,, \tag{4.19}$$

which needs to be considered in case of radiative form factors where at least one photon is considered off–shell with

$$c^{\mu\nu} = g^{\mu\nu} q_1^2 q_2^2 + q_1^\mu q_2^\nu q_1 q_2 - q_1^\mu q_1^\nu q_2^2 - q_2^\mu q_2^\nu q_1^2 \,. \tag{4.20}$$

4.2. Light meson bound states

Before we study the interesting hadronic molecule candidates recently discovered in the heavy meson sector we focus on the light scalar mesons $f_0(980)$ and $a_0(980)$. The advantage is that the f_0 and a_0 mesons are known for a long time and experimentally well studied. Therefore, many data are available on the strong and radiative decay pattern of these states. In contrast, when dealing with the hidden–charm X, Y and Z mesons the experimental knowledge is restricted. In particular, only a few decay modes are experimentally observed and precise data are not available and often not confirmed by a second experiment. For these reasons, the f_0 and a_0 mesons provide an excellent test case for the present Lagrangian approach applied to hadronic molecules.

4.2.1. $a_0(980)$ and $f_0(980)$

The $a_0(980)$ and $f_0(980)$ were controversially discussed in different structure interpretations ranging from $q\bar{q}$ [144], $q^2\bar{q}^2$ [17, 19] to $(q\bar{q})(q\bar{q})$ [20, 26, 145] meson bound state assignments (for an overview see [13]). However, the proximity of the f_0 and a_0 to the nearby $K\overline{K}$ threshold and their mass degeneracy strongly suggest a molecular substructure assignment (see discussion in Section 2.1). In the following we study both mesons by assuming pure bound states of kaons. In this framework we analyze their radiative decays, including two-photon and photon-vector meson decay processes, and the strong two-pion and $\pi\eta$ decays. Furthermore, we also compute the f_0/a_0 production in ϕ decays, which are sensitive to the strange-quark component of the mesons. Besides the extended structure of the scalar mesons we also include a possible isospin violating mixture of the $f_0(980)$ and $a_0(980)$ mesons, originally discussed in [146]. $f_0 - a_0$ mixing is motivated by their near degenerate masses but also by the mass gap between the nearby charged K^+K^- and neutral $K^0\bar{K}^0$ thresholds (see e.g. [147, 148]). Further isospin violating processes like photon exchange and isospin-violating vertices are found to play a minor role compared to the $f_0 - a_0$ transition induced by kaon loops [149]. For this reason, in the following we restrict

to the kaon loop mixing mechanism. By considering $f_0 - a_0$ mixing we also get access to the isospin violating decays $f_0 \to \pi\eta$ and $a_0 \to \pi\pi$.
In the first step we express the f_0 and its isovector partner a_0 by the corresponding isosinglet and triplet states of the kaon–antikaon systems

$$\left|f_0^0\right\rangle = \frac{1}{\sqrt{2}}\left(\left|K^+K^-\right\rangle + \left|K^0\bar{K}^0\right\rangle\right), \tag{4.21}$$

$$\left|a_0^0\right\rangle = \frac{1}{\sqrt{2}}\left(\left|K^+K^-\right\rangle - \left|K^0\bar{K}^0\right\rangle\right), \tag{4.22}$$

where the upper index 0 refers to the unmixed states. The interaction between the hadronic molecules a_0^0 and f_0^0 is described by the phenomenological Lagrangians (see also (4.2))

$$\begin{aligned}\mathcal{L}_{f_0^0K\overline{K}} =& \frac{g_{f_0^0K\overline{K}}}{\sqrt{2}} f_0^0(x) \int dy\, \Phi(y^2)\overline{K}\Big(x-\frac{y}{2}\Big)K\Big(x+\frac{y}{2}\Big),\\ \mathcal{L}_{a_0^0K\overline{K}} =& \frac{g_{a_0^0K\overline{K}}}{\sqrt{2}} \vec{a}_0^0(x) \int dy\, \Phi(y^2)\overline{K}\Big(x-\frac{y}{2}\Big)\vec{\tau}K\Big(x+\frac{y}{2}\Big),\end{aligned} \tag{4.23}$$

where the kaon and scalar fields are collected in the kaon isospin doublets and the scalar meson triplet

$$K = \begin{pmatrix} K^+ \\ K^0 \end{pmatrix}, \quad \overline{K} = \begin{pmatrix} K^- \\ \bar{K}^0 \end{pmatrix} \quad \text{and} \quad \vec{a}_0 = (a_0^+,\, a_0^0,\, a_0^-)\,. \tag{4.24}$$

The different sign of the couplings between a_0 and the charged and neutral kaon components together with the mass gap leads to a non–vanishing $a_0 - f_0$ transition in Fig. 4.5 driven by kaon loops. We can therefore express the physical f_0 and a_0

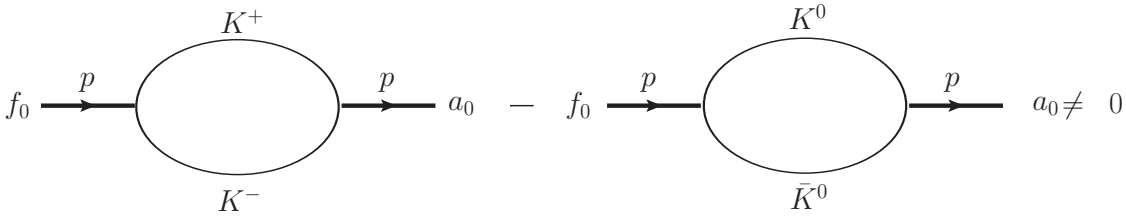

Figure 4.5.: $f_0 - a_0$ mixing due to the mass gap between K^+K^- and $K^0\bar{K}^0$ thresholds.

mesons by the unmixed states f_0^0 and a_0^0

$$\begin{aligned}\left|f_0\right\rangle &= \left|f_0^0\right\rangle\cos\theta - \left|a_0^0\right\rangle\sin\theta\\ \left|a_0\right\rangle &= \left|f_0^0\right\rangle\sin\theta + \left|a_0^0\right\rangle\cos\theta\,.\end{aligned} \tag{4.25}$$

The coupling constants $g_{f_0K\overline{K}}$ and $g_{a_0K\overline{K}}$ to the constituents are determined by the compositeness condition (4.4) which is based on the mass operator of the physical states f_0 and a_0 (see Fig. 4.1). By using the mixing matrix of Eq. (4.25) we can rewrite the mass operator of the physical particle (here the f_0) by the unmixed states f_0^0 and a_0^0

$$\begin{aligned}\Pi_{f_0f_0}(p^2) &= \cos^2\theta\,\frac{g^2_{f_0^0K\overline{K}}}{2}\,\Sigma_{f_0^0f_0^0}(p^2) - \cos\theta\sin\theta\,g_{f_0^0K\overline{K}}g_{a_0^0K\overline{K}}\,\Sigma_{f_0a_0}(p^2)\\ &\quad + \sin^2\theta\frac{g^2_{a_0^0K\overline{K}}}{2}\Sigma_{a_0^0a_0^0}(p^2)\,,\end{aligned} \tag{4.26}$$

which leads to the compositeness condition

$$\begin{aligned}1 = \Pi'_{f_0f_0}(p^2)\big|_{p^2=m^2_{f_0}} =\Big[&\cos^2\theta\frac{g^2_{f_0^0K\overline{K}}}{2}\Sigma'_{f_0^0f_0^0}(p^2) - \sin\theta\cos\theta g_{f_0^0K\overline{K}}g_{a_0^0K\overline{K}}\Sigma'_{a_0^0f_0^0}(p^2)\\ &+\sin^2\theta\frac{g^2_{a_0^0K\overline{K}}}{2}\Sigma'_{a_0^0a_0^0}(p^2)\Big]\Big|_{p^2=m^2_{f_0}}\,.\end{aligned} \tag{4.27}$$

In order to determine the couplings to the charged and neutral kaons $g_{SK^+K^-}$ and $g_{SK^0\bar{K}^0}$ ($S = f_0,\, a_0$) we substitute

$$\begin{aligned}\Sigma_{f_0^0f_0^0}(p^2) = \Sigma_{a_0^0a_0^0}(p^2) &= \Sigma_{K^+K^-} + \Sigma_{K^0\bar{K}^0}\\ \Sigma_{a_0^0f_0^0}(p^2) = \Sigma_{f_0^0a_0^0}(p^2) &= \Sigma_{K^+K^-} - \Sigma_{K^0\bar{K}^0}\end{aligned} \tag{4.28}$$

and obtain

$$\begin{aligned}1 = \Pi'_{f_0f_0}(p^2)\big|_{p^2=m^2_{f_0}} =\Big[&\underbrace{\Big(\frac{g_{f_0^0K\overline{K}}}{\sqrt{2}}\cos\theta - \frac{g_{a_0^0K\overline{K}}}{\sqrt{2}}\sin\theta\Big)}_{\equiv\, g_{f_0K^+K^-}}{}^2\Sigma'_{K^+K^-}(p^2)\\ &+\underbrace{\Big(\frac{g_{f_0^0K\overline{K}}}{\sqrt{2}}\cos\theta + \frac{g_{a_0^0K\overline{K}}}{\sqrt{2}}\sin\theta\Big)}_{\equiv\, g_{f_0K^0\bar{K}^0}}{}^2\Sigma'_{K^0\bar{K}^0}(p^2)\Big]\Big|_{p^2=m^2_{f_0}}\,.\end{aligned} \tag{4.29}$$

By analogy we evaluate the compositeness condition for the physical $a_0(980)$ meson

$$\begin{aligned}1 = \Pi'_{a_0a_0}(p^2)\big|_{p^2=m^2_{a_0}} =\Big[&\underbrace{\Big(\frac{g_{a_0K\overline{K}}}{\sqrt{2}}\cos\theta + \frac{g_{f_0^0K\overline{K}}}{\sqrt{2}}\sin\theta\Big)}_{\equiv\, g_{a_0^0K^+K^-}}{}^2\Sigma'_{K^+K^-}(p^2)\\ &+\underbrace{\Big(\frac{g_{a_0K\overline{K}}}{\sqrt{2}}\cos\theta - \frac{g_{f_0K\overline{K}}}{\sqrt{2}}\sin\theta\Big)}_{\equiv\, g_{a_0K^0\bar{K}^0}}{}^2\Sigma'_{K^0\bar{K}^0}(p^2)\Big]\Big|_{p^2=m^2_{a_0}}\,.\end{aligned} \tag{4.30}$$

In the following we pursue two ways of considering the $f_0 - a_0$ mixing in our model. In the first version referred to as Model A we treat the mixing angle as free parameter and, hence, determine the couplings to the charged and neutral kaon pairs in dependence on θ. From experiment it is known that isospin mixing effects are small. In Model B we therefore approximate the couplings to the constituents for small mixing angles θ.

1. **Model A:** First we compute the decay properties in dependence on θ by inserting $g_{SK^+K^-}$ and $g_{SK^0\bar{K}^0}$ for the coupling to the charged and neutral kaons in the loops. The dependence of the nonlocal coupling constants $g_{SK^+K^-}$ and $g_{SK^0\bar{K}^0}$ between the scalars and the charged or neutral constituent kaon pairs on the $a_0 - f_0$ mixing is demonstrated in Fig. 4.6. We plot the coupling constants for the size parameter $\Lambda = 1$ GeV as functions of the mixing angle θ. Without the inclusion of mixing effects, i.e. $\theta = 0$ we reproduce the couplings

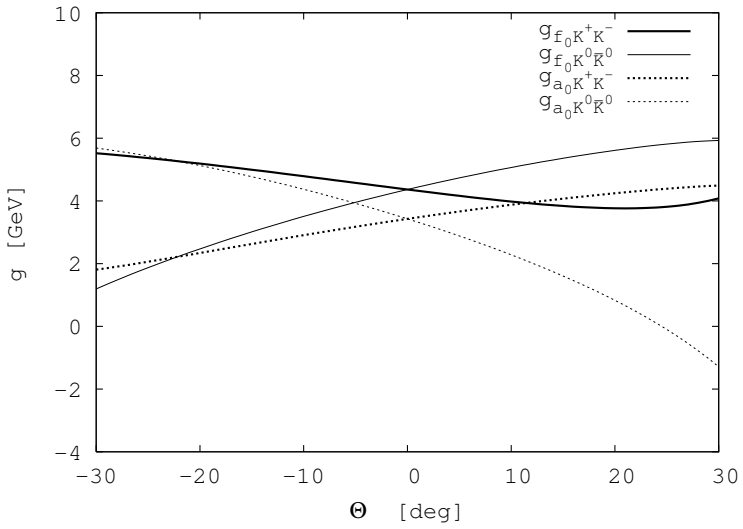

Figure 4.6.: Influence of mixing effects on the couplings $g_{SK^+K^-}$ and $g_{SK^0\bar{K}^0}$ at $\Lambda = 1$ GeV.

$g_{f_0K\overline{K}} \equiv g_{f_0K^+K^-} = g_{f_0K^0\bar{K}^0}$ and $g_{a_0K\overline{K}} \equiv g_{a_0K^+K^-} = g_{a_0K^0\bar{K}^0}$ of our previous work [26]

$$\begin{aligned} \frac{g_{f_0K\overline{K};L}}{\sqrt{2}} &= 2.90 \text{ GeV (local)}, \quad & \frac{g_{f_0K\overline{K}}}{\sqrt{2}} &= 3.09 \text{ GeV } (\Lambda = 1 \text{ GeV}), \\ \frac{g_{a_0K\overline{K};L}}{\sqrt{2}} &= 2.32 \text{ GeV (local)}, \quad & \frac{g_{a_0K\overline{K}}}{\sqrt{2}} &= 2.42 \text{ GeV } (\Lambda = 1 \text{ GeV}), \end{aligned} \tag{4.31}$$

where the index L refers to the local limit ($\Lambda \to \infty$).

2. **Model B:** In the second version we approximate the couplings to the con-

stituents by the modified couplings $G_{f_0K\overline{K}}$ and $G_{a_0K\overline{K}}$ which include one–loop corrections due to $a_0 - f_0$ mixing as depicted in Fig. 4.7 (a) and 4.7 (b). Here we use the couplings $g_{f_0K\overline{K}}$ and $g_{a_0K\overline{K}}$ of (4.31) derived in [26]. For the

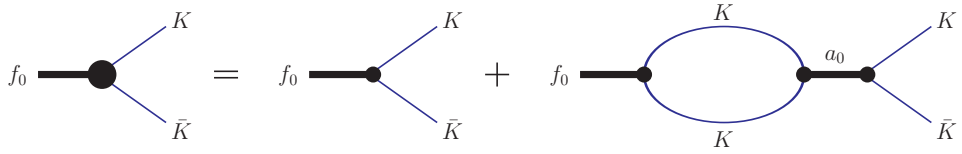

(a)

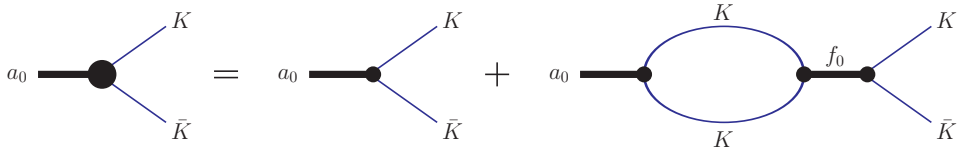

(b)

Figure 4.7.: Renormalization of the $g_{f_0K\bar{K}}$ and $g_{a_0K\bar{K}}$ couplings due to $f_0 - a_0$ mixing.

intermediate scalar propagator we use the Breit–Wigner form:

$$D_S(p^2) = \frac{1}{M_S^2 - p^2 + iM_S\Gamma_S} \tag{4.32}$$

where $\Gamma_S = \Gamma(M_S^2)$ is the total width of the $S = f_0(a_0)$ meson.

For the coupling constants between the hadronic molecules and the constituent kaons we obtain

$$\frac{G_{f_0K\overline{K};L}}{\sqrt{2}} = 2.87 \text{ GeV (local)}, \quad \frac{G_{f_0K\overline{K}}}{\sqrt{2}} = 3.06 \text{ GeV } (\Lambda = 1 \text{ GeV})\,, \tag{4.33}$$

$$\frac{G_{a_0K\overline{K};L}}{\sqrt{2}} = 2.44 \text{ GeV (local)}, \quad \frac{G_{a_0K\overline{K}}}{\sqrt{2}} = 2.55 \text{ GeV } (\Lambda = 1 \text{ GeV})\,. \tag{4.34}$$

In model B mixing effects result in slight modifications of the couplings and therefore only play a minor role with respect to decay and production properties as we will compute in the following. We will see later on that the second variant corresponds to a mixing angle θ of about 1° used in model A.

Radiative Decays

As a first application we study the radiative two–photon and photon–vector meson decays of the $f_0(980)$ and $a_0(980)$ mesons as well as their production in ϕ decays.

As already discussed in the introduction of this chapter electromagnetic interaction is included by minimal substitution in the free meson Lagrangian of the kaons

$$\mathcal{L}_K = \partial_\mu K^+ \partial^\mu K^- - M_K^2 K^+ K^- + ie\big(M^- \partial_\mu M^+ - M^+ \partial_\mu M^-\big) A^\mu + e^2 A^\mu A_\mu M^+ M^- \,.$$

The resulting one– and two–photon interaction vertices are contained in the decay diagrams (a) and (b) of Figs. 4.8 and 4.9, and (a) to (c) of Fig. 4.10. The interaction of the intermediate kaons and the final vector mesons is given by the effective Lagrangian

$$\mathcal{L}_{VK\overline{K}} = g_{\rho K\overline{K}} \vec{\rho}^{\,\mu} (\overline{K} \vec{\tau}\, i\overleftrightarrow{\partial}_\mu K) + (g_{\omega K\overline{K}} \omega^\mu + g_{\phi K\overline{K}} \phi^\mu)(\overline{K}\, i\partial_\mu K - K\, i\partial_\mu \overline{K}) \,. \quad (4.35)$$

where the respective $g_{VK\overline{K}}$ and $g_{\omega K\overline{K}}$ couplings are fixed using the $SU(3)$ symmetry constraint:

$$g_{\rho K\overline{K}} = g_{\omega K\overline{K}} = \frac{g_{\phi K\overline{K}}}{\sqrt{2}} = \frac{g_{\rho\pi\pi}}{2} = 3 \quad (4.36)$$

with $g_{\rho K\overline{K}} = 6$ extracted from the $\rho \to \pi^+\pi^-$ decay data. Note, that the $SU(3)$ value for the $g_{\phi K\overline{K}}$ coupling (4.24) is close to the one predicted by data on the $\phi \to K^+K^-$ decay. In particular, using the formula for the $\phi \to K^+K^-$ decay width

$$\Gamma(\phi \to K^+K^-) = \frac{g^2_{\phi K\overline{K}}}{48\pi} M_\phi \Big(1 - \frac{4M_K^2}{M_\phi^2}\Big)^{3/2} \quad (4.37)$$

and the central value for $\Gamma(\phi \to K^+K^-)$=2.10 MeV we deduce $g_{\phi K\overline{K}}$=4.48.

In the local limit the decay amplitude would be completely described by the sum of these Feynman diagrams. However, the nonlocal strong interaction Lagrangians require special care in establishing gauge invariance. In doing so the charged fields are multiplied by exponentials [143] containing the electromagnetic field

$$K^\pm(y) \to e^{\mp ieI(y,x,P)} K^\pm(y) \quad (4.38)$$

with $I(y,x,P) = \int\limits_x^y dz_\mu A^\mu(z)$. This gives rise to the electromagnetic gauge invariant Lagrangian

$$\mathcal{L}^{GI}_{f_0K\overline{K}} = \frac{g_{f_0K\overline{K}}}{\sqrt{2}} f_0(x) \int dy \Phi(y^2) \big[e^{-ieI(x_+,x_-,P)} K^+(x_+) K^-(x_-) + K^0(x_+) \overline{K}^0(x_-)\big] \,,$$

with $x_\pm = x \pm \frac{y}{2}$ and a corresponding expression for the a_0 meson. The interaction terms up to second order in A^μ are obtained by expanding $\mathcal{L}^{GI}_{SK\overline{K}}$ in terms of $I(y,x,P)$. Diagrammatically, the higher order terms give rise to nonlocal vertices with additional photon lines attached. Altogether, we obtain further graphs (Fig. 4.8

(c), (d) and (e)) governing the two-photon decay and the diagrams of Figs. 4.9 (c) and 4.10 (d) when massive vector mesons are involved. Quantitatively, the de-

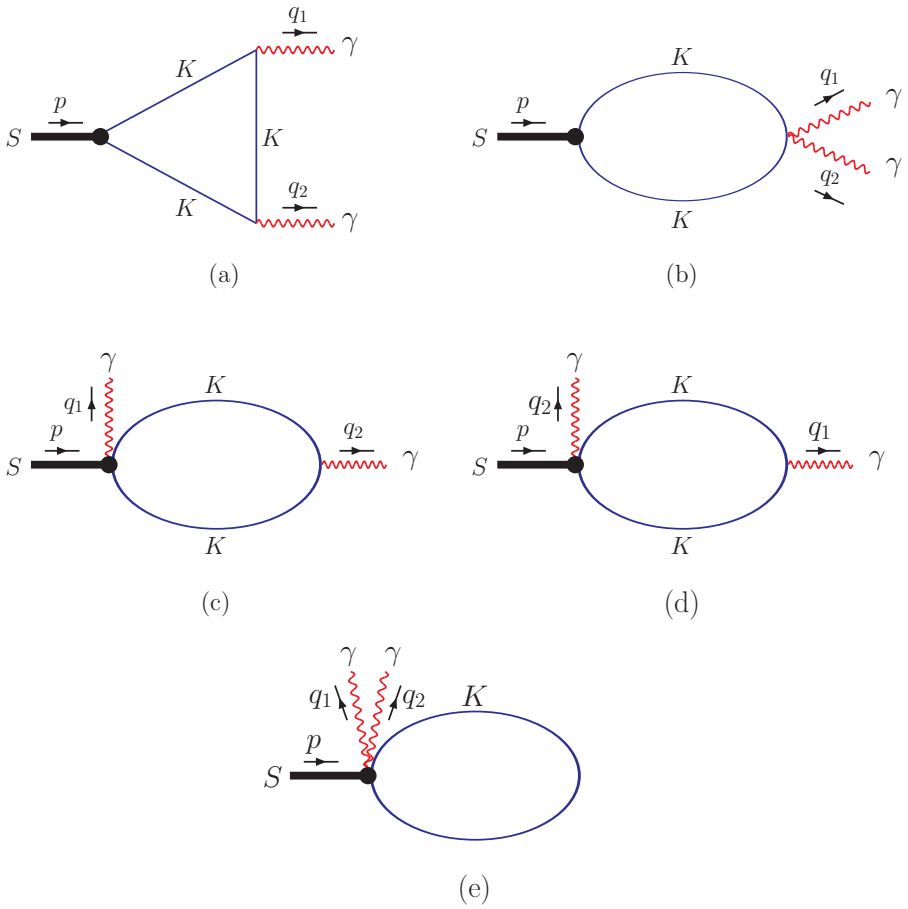

Figure 4.8.: Diagrams contributing to the electromagnetic $f_0 \to \gamma\gamma$ and $a_0 \to \gamma\gamma$ decays.

cay amplitude is dominantly characterized by the triangle diagram. The Feynman graphs containing contact vertices arising due to the non-locality only give a minor contribution to the transition amplitude but are required in order to fully restore gauge invariance.

The diagrams are evaluated by separating each Feynman integral into a part obeying gauge invariance and a remainder term. Details of this procedure can be found in Ref. [135, 26] in case of two–photon decays and in the present Appendix A.2 for the $S \to V\gamma$ transitions. The remainder terms of each graph cancel each other in total and only the gauge invariant structure of the decay matrix element is left. According to Eq. (4.19) the matrix element can be written by a linear combination

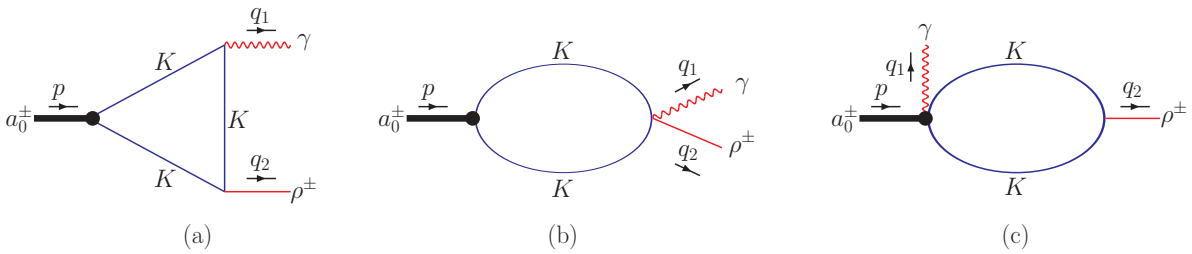

Figure 4.9.: Diagrams contributing to the charged $a_0^\pm \to \gamma\rho^\pm$ decay.

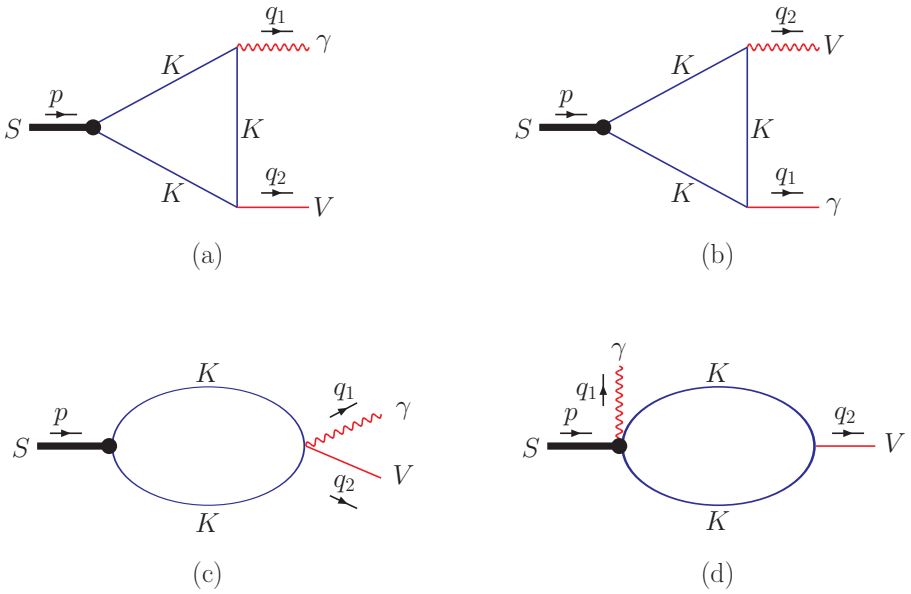

Figure 4.10.: Diagrams describing the neutral $S \to \gamma V$ decays ($V = \rho^0, \omega^0$).

of the form factors $F(p^2, q_1^2, q_2^2)$ and $G(p^2, q_1^2, q_2^2)$ of the respective decay

$$\mathcal{M}^{\mu\nu} = e^2\Big(F(p^2, q_1^2, q_2^2)b^{\mu\nu} + G(p^2, q_1^2, q_2^2)c^{\mu\nu}\Big)\,, \tag{4.39}$$

where the tensor structures are given by Eqs. (4.18) and (4.20). Here, p and q_1 denote the four-momenta of the scalar meson and photon, q_2 is the momentum of the vector meson or second photon depending on the respective decay.

Since we deal with real photons in the transition processes discussed here, the second part of $\mathcal{M}^{\mu\nu}$, proportional to $c^{\mu\nu}$, vanishes. The decay constant is therefore characterized by the form factor F which is obtained by evaluating the Feynman integrals for on-shell initial and final states, where $V = \rho, \omega, \phi, \gamma$ represents the vector particle appropriate for the respective decay.

The issue of $f_0 - a_0$–mixing we study within the two above mentioned frameworks A and B. In the first version A we use the mixing angle dependent couplings

$$g_{f_0K^+K^-} = g_{f_0^0K\overline{K}}\cos\theta - g_{a_0^0K\overline{K}}\sin\theta \tag{4.40}$$

$$g_{a_0K^+K^-} = g_{a_0^0K\overline{K}}\cos\theta + g_{f_0^0K\overline{K}}\sin\theta \tag{4.41}$$

of Eqs. (4.29) and (4.30) to compute the couplings characterizing the electromagnetic decays

$$\begin{aligned}
g_{S\gamma\gamma} &\equiv F_{S\gamma\gamma}(M_S^2, 0, 0) = \frac{2}{(4\pi)^2}\cdot\frac{g_{SK^+K^-}}{\sqrt{2}}I_{S\gamma\gamma}(M_S^2, 0, 0)\\
g_{S\gamma V} &\equiv F_{S\gamma V}(M_S^2, 0, M_V^2) = \frac{2}{(4\pi)^2}g_{VK\overline{K}}\frac{g_{SK^+K^-}}{\sqrt{2}}I_{S\gamma V}(M_S^2, 0, M_V^2)\\
g_{\phi S\gamma} &\equiv F_{\phi S\gamma}(M_\phi^2, M_S^2, 0) = \frac{2}{(4\pi)^2}g_{\phi K\overline{K}}\frac{g_{SK^+K^-}}{\sqrt{2}}I_{\phi S\gamma}(M_\phi^2, M_S^2, 0)\,,
\end{aligned} \tag{4.42}$$

where I denotes the loop integrals. The explicit expressions for the loop integrals I are given in Appendix A.1.

In the second approach B we simply replace the couplings $g_{SK^+K^-}$ by the modified dressed couplings $G_{SK\overline{K}}$ due to $f_0 - a_0$ mixing (see Eqs. (4.34) and (4.33)) which are based on the approximation of small mixing angles.

The expressions for the electromagnetic decay widths are given by

$$\begin{aligned}
\Gamma_{S\gamma\gamma} &= \frac{\alpha^2\pi}{4}M_S^3 g_{S\gamma\gamma}^2\,,\\
\Gamma_{S\gamma\rho/\omega} &= \frac{\alpha}{8}\frac{(M_S^2 - M_\rho^2)^3}{M_S^3}g_{S\gamma\rho/\omega}^2\,,\\
\Gamma_{\phi S\gamma} &= \frac{\alpha}{24}\frac{(M_\phi^2 - M_S^2)^3}{M_S^3}g_{\phi S\gamma}^2\,,
\end{aligned} \tag{4.43}$$

where the coupling constants describing the radiative decays are related to the form factors F as described in (4.42).

Two–photon decays

The results for the two–photon decay widths obtained by using the mixing angle dependent couplings of model A are summarized in Tab. 4.1. Here we vary the mixing angle θ from $-3°$ to $3°$ since data suggests small mixing angles which will also be confirmed by the results of model B. For completeness, we also indicate the decay properties for a larger mixing angle. The mixing angle $\theta = 45°$ corresponds to the configurations $\left|f_0\right\rangle = \left|K^0\bar{K}^0\right\rangle$ and $\left|a_0\right\rangle = \left|K^+K^-\right\rangle$ which leads to a zero radiative decay width for the f_0 and a maximal one for the $a_0 \to \gamma\gamma$ width since photons only couple to charged kaons.

θ	$g_{f_0\gamma\gamma}$ [TeV^{-1}]		$\Gamma_{f_0\gamma\gamma}$ [keV]		$g_{a_0\gamma\gamma}$ [TeV^{-1}]		$\Gamma_{a_0\gamma\gamma}$ [keV]	
-3°	82.6	90.2	0.27	0.32	65.0	71.5	0.17	0.20
-2°	81.4	88.9	0.26	0.31	66.3	73.0	0.18	0.21
-1°	80.3	87.6	0.25	0.30	67.7	74.6	0.18	0.22
0°	79.1	86.3	0.25	0.29	69.1	76.1	0.19	0.23
1°	77.9	85.0	0.24	0.28	70.5	77.6	0.20	0.24
2°	76.6	83.6	0.23	0.28	71.9	79.1	0.21	0.25
3°	75.3	82.2	0.22	0.27	73.2	80.6	0.21	0.26
5°	72.7	79.3	0.21	0.25	75.9	83.5	0.23	0.28
10°	65.6	71.5	0.17	0.20	82.3	90.4	0.27	0.33
20°	49.3	53.7	0.10	0.11	93.5	102.6	0.35	0.42
45°	00.0	0.00	0.00	0.00	106.6	116.7	0.45	0.54

Table 4.1.: Two–photon decay properties for different mixing angles (first value of each column nonlocal with $\Lambda = 1$ GeV, second local).

The use of the dressed couplings of model B leads to decay widths which are rather close to the unmixed results. In fact the results of variant B correspond to a mixing angle $\theta \approx 1°$

$$\begin{aligned} \Gamma(f_0 \to \gamma\gamma) &= 0.29\ (0.29)\ \text{keV}\ (\text{local})\,, \\ \Gamma(f_0 \to \gamma\gamma) &= 0.24\ (0.25)\ \text{keV}\ (\Lambda = 1\ \text{GeV})\,. \end{aligned} \tag{4.44}$$

The value in brackets refers to the corresponding value when neglecting $f_0 - a_0$ mixing effects (see also Tab. 4.1). The sensitivity of the $f_0 \to \gamma\gamma$ decay properties on finite size effects has been intensely studied in [26], even in case of virtual photons, and leads to a variation of $\Gamma(f_0 \to \gamma\gamma)$ with the result

$$\Gamma(f_0 \to \gamma\gamma) = 0.21 \text{ keV } (\Lambda = 0.7 \text{ GeV}) - \ 0.26 \text{ keV } (\Lambda = 1.3 \text{ GeV}) \,. \tag{4.45}$$

In Tables 4.2 and 4.3 we draw the comparison with data and other approaches, respectively. The $f_0 \to \gamma\gamma$ width predicted by our model matches the range of values currently deduced in experiment.

Experiment	[22]	[150]	[151]	[124]
$\Gamma_{f_0\to\gamma\gamma}$ [keV]	$0.29^{+0.07}_{-0.09}$	$0.205^{+0.095\,+0.147}_{-0.083\,-0.117}$	$0.31 \pm 0.14 \pm 0.09$	$0.29 \pm 0.07 \pm 0.12$

Table 4.2.: Electromagnetic decay width $f_0(980) \to \gamma\gamma$: experimental data.

Reference	[152]	[37]	[153]	[154]	[155]	[156]	[145]
Meson structure	$(q\bar{q})$	$(q\bar{q})$	$(q\bar{q})$	$(q\bar{q})$	$(q^2\bar{q}^2)$	(hadronic)	(hadronic)
$\Gamma_{f_0\to\gamma\gamma}$ [keV]	0.24	$0.28^{+0.09}_{-0.13}$	0.31	0.33	0.27	0.20	0.22 ± 0.07

Table 4.3.: Electromagnetic decay width $f_0(980) \to \gamma\gamma$: theoretical approaches.

For the two-photon decay of the a_0 meson our results lie between

$$\begin{aligned} &\Gamma(a_0 \to \gamma\gamma) = 0.26 \ (0.23) \text{ keV (local)} \,, \\ &\Gamma(a_0 \to \gamma\gamma) = 0.21 \ (0.19) \text{ keV } (\Lambda = 1 \text{ GeV}) \,, \end{aligned} \tag{4.46}$$

where again results without mixing are put in parentheses. By considering in addition the $f_0 - a_0$ mixing contributions our estimates are in good agreement with the experimental result 0.3 ± 0.1 keV of Crystal Barrel [12]. Finite size effects play a comparable role as $f_0 - a_0$ mixing since the variation of Λ from 0.7 GeV to 1.3 GeV changes $\Gamma(a_0 \to \gamma\gamma)$ by

$$\Gamma(a_0 \to \gamma\gamma) = 0.16 \text{ keV } (\Lambda = 0.7 \text{ GeV}) \text{ - } 0.21 \text{ keV } (\Lambda = 1.3 \text{ GeV}) \,. \tag{4.47}$$

The decay widths obtained in other approaches are combined in Tab. 4.4 and show a large discrepancy even for models with the same structure assumptions.

Reference	[37]	[21]	[155]	[156]
Meson structure	$(q\bar{q})$	$(q\bar{q})$	$(q^2\bar{q}^2)$	(hadronic)
$\Gamma(a_0 \to \gamma\gamma)$ [keV]	$0.3^{+0.11}_{-0.10}$	1.5	0.27	0.78

Table 4.4.: Electromagnetic decay width $a_0(980) \to \gamma\gamma$: theoretical approaches.

One–photon decays

In analogy to the two–photon decays we first evaluate the $\rho\gamma$ and $\omega\gamma$ decay widths of the $f_0(980)$ and $a_0(980)$ in dependence on the mixing angle θ (model A). Our results are given in Tab. 4.5, where we concentrate on small mixing angles between $-3°$ and $3°$ but for completeness we also indicate the results for maximal mixing at $\theta = 45°$. From our results it is obvious that with increasing θ the K^+K^- component decreases in case of the f_0 which leads to smaller radiative decay widths while the charged component increases for the a_0.

θ	$\Gamma_{f_0\rho\gamma}$		$\Gamma_{f_0\omega\gamma}$		$\Gamma_{a_0\rho\gamma}$		$\Gamma_{a_0\omega\gamma}$	
-3°	8.37	8.85	7.86	8.29	5.89	6.37	5.56	6.00
-2°	8.13	8.60	7.64	8.05	6.13	6.64	5.79	6.25
-1°	7.90	8.34	7.42	7.81	6.39	6.91	6.03	6.50
0°	7.65	8.09	7.19	7.57	6.64	7.18	6.27	6.76
1°	7.41	7.83	6.96	7.33	6.90	7.46	6.51	7.02
2°	7.17	7.57	6.73	7.09	7.16	7.73	6.76	7.28
3°	6.92	7.31	6.50	6.84	7.43	8.01	7.01	7.54
5°	6.44	6.79	6.04	6.84	7.95	8.58	7.50	7.54
10°	5.21	5.49	4.90	5.14	9.29	10.0	8.77	9.41
20°	2.92	3.07	2.74	2.87	11.86	12.7	11.18	12.0
45°	0.00	0.00	0.00	0.00	15.20	16.2	14.32	15.2

Table 4.5.: $f_0(a_0) \to V\gamma$ decay widths in keV for different mixing angles (first value of each column nonlocal with $\Lambda = 1$ GeV, second local).

As in the case of the two–photon decays model B leads to minor mixing effects for

the decays involving ρ and ω mesons

$$\Gamma(f_0 \to \rho\gamma) = 7.93\ (8.09)\ \text{keV (local)}, \quad 7.44\ (7.58)\ \text{keV}\ \ (\Lambda = 1\ \text{GeV})\,, \tag{4.48}$$
$$\Gamma(f_0 \to \omega\gamma) = 7.43\ (7.57)\ \text{keV (local)}, \quad 6.99\ (7.12)\ \text{keV}\ \ (\Lambda = 1\ \text{GeV})\,, \tag{4.49}$$
$$\Gamma(a_0 \to \rho\gamma) = 7.94\ (7.18)\ \text{keV (local)}, \quad 7.29\ (6.59)\ \text{keV}\ \ (\Lambda = 1\ \text{GeV})\,, \tag{4.50}$$
$$\Gamma(a_0 \to \omega\gamma) = 7.47\ (6.76)\ \text{keV (local)}, \quad 6.88\ (6.22)\ \text{keV}\ \ (\Lambda = 1\ \text{GeV})\,. \tag{4.51}$$

The deviations from the predicted widths of Ref. [36] for the $a_0/f_0 \to \gamma\rho/\omega$ decays arise because of different assumptions for the scalar masses and couplings. In [157] the decay width $a_0 \to \gamma\rho/\omega$ calculated within the framework of a Chiral Unitarity Approach is larger than our result because of the additional inclusion of vector mesons in the loop diagrams.

ϕ decays

We first study the mixing angle dependence of the decay properties within model A. As in the one- and two photon decays the ϕ production rate depends sensitively on the K^+K^- constituents of the scalar mesons which leads again to a decrease of the $\phi \to a_0\gamma$ width while the a_0 production in ϕ decays increases with larger values of θ. Physically reasonable results are found for small mixing angles.

θ	$g_{\phi f_0\gamma}$ [GeV^{-1}]	$\Gamma_{\phi f_0\gamma}$ [keV]	$g_{\phi a_0\gamma}$ [GeV^{-1}]	$\Gamma_{\phi a_0\gamma}$ [keV]
-3°	2.06	0.70	1.71	0.33
-2°	2.03	0.68	1.75	0.34
-1°	2.00	0.66	1.78	0.36
0°	1.97	0.64	1.82	0.37
1°	1.94	0.62	1.85	0.39
2°	1.91	0.60	1.88	0.40
3°	1.87	0.58	1.92	0.42
5°	1.81	0.54	1.98	0.44
10°	1.62	0.44	2.14	0.52
20°	1.21	0.24	2.41	0.66
45°	0.00	0.00	2.73	0.84

Table 4.6.: $\phi \to f_0(a_0)\gamma$ decay properties for different mixing angles.

The radiative ϕ decay widths calculated in the local limit within the framework of model B are given by

$$\Gamma(\phi \to f_0\gamma) = 0.63 \text{ keV}\,,$$
$$\Gamma(\phi \to a_0\gamma) = 0.41 \text{ keV}\,,$$

where without mixing we obtain $\Gamma(\phi \to f_0\gamma)$=0.64 keV and $\Gamma(\phi \to a_0\gamma)$=0.37 keV. Our result for the $\phi \to f_0\gamma$ decay overestimates the value quoted by PDG (2010) [158], where the branching ratio $\Gamma(\phi \to f_0\gamma)/\Gamma_{total} = (1.11 \pm 0.07) \cdot 10^{-4}$ yields $\Gamma(\phi \to f_0\gamma)$=0.44-0.51 keV. In the 2010 edition of PDG [22] the ratio is increased $\Gamma(\phi \to f_0\gamma)/\Gamma_{total} = (3.22 \pm 0.19) \cdot 10^{-4}$ which gives 1.28-1.47 keV for the $\phi \to a_0\gamma$ decay width. However our results lie within the error bars of the CMD2 data [41] $\Gamma(\phi \to f_0\gamma) = 0.48 - 2.00$ keV.
The decay width for the $\phi \to a_0\gamma$ decay slightly overestimates the PDG (2008) average value 0.3-0.35 keV ($\Gamma(\phi \to a_0\gamma)/\Gamma_{total} = (0.76 \pm 0.06) \cdot 10^{-4}$) but is in agreement with the experimental data of [159] predicting 0.30-0.45 keV for $\Gamma(\phi \to a_0\gamma)$.
Due to the self-consistent determination of the $g_{a_0K\overline{K}}$ coupling constant our result in case of the a_0 production is smaller than the width $\Gamma(\phi \to a_0\gamma)$ quoted in [45, 36], but we have quite good agreement with the predictions for the ϕ-production of the f_0.

Strong Decays

To calculate the strong decays of the f_0 and a_0 mesons we proceed in analogy to the computation of the $f_0 \to \pi\pi$ decay in [26]. Here we extend the formalism by including the $a_0 \to \pi\eta$ decay and, additionally, by considering mixing between both scalars.
According to the interaction Lagrangians

$$\begin{aligned}\mathcal{L}_{K^*K\pi} &= \frac{g_{K^*K\pi}}{\sqrt{2}} K^{*\dagger}_\mu \vec{\pi}\vec{\tau}\, i\overset{\leftrightarrow}{\partial}{}^{\mu} K + h.c.\,,\\ \mathcal{L}_{K^*K\eta} &= \frac{g_{K^*K\eta}}{\sqrt{2}} K^{*\dagger}_\mu \eta\, i\overset{\leftrightarrow}{\partial}{}^{\mu} K + h.c.\,,\end{aligned} \tag{4.52}$$

the final-state interaction effect in the t-channel proceeds via K^* exchange (see Fig. 4.11 (a)), where the massive vector meson is described by an antisymmetric tensor field [4, 160, 161]. The K^* propagators in vector representation $S^V_{K^*;\mu\nu,\alpha\beta}(x)$ and tensorial description $S^W_{K^*;\mu\nu,\alpha\beta}(x)$ differ by a term which is reflected in a second diagram containing an explicit four meson vertex (see Fig. 4.11 (b))

$$S^W_{K^*;\mu\nu,\alpha\beta}(x) = S^V_{K^*;\mu\nu,\alpha\beta}(x) + \frac{i}{M^2_{K^*}}[g_{\mu\alpha}g_{\nu\beta} - g_{\mu\beta}g_{\nu\alpha}]\delta^4(x)\,. \tag{4.53}$$

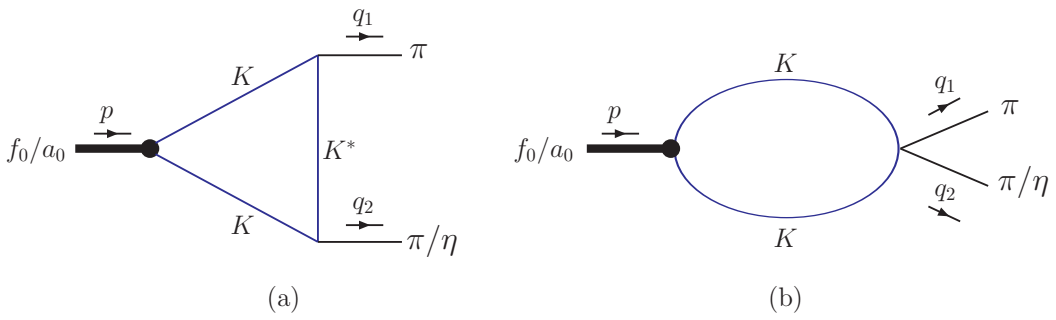

Figure 4.11.: Diagrams contributing to the strong decays.

Note that we include the interaction of four pseudoscalar mesons at leading $O(p^2)$ order in the chiral expansion given by chiral perturbation theory (ChPT) [4, 6]:

$$\mathcal{L}_U(x) = \frac{F^2}{4}\langle\, D_\mu U(x) D^\mu U^\dagger(x) + \chi U^\dagger(x) + \chi^\dagger U(x)\,\rangle\,, \tag{4.54}$$

which leads to the four meson $\pi\pi K\overline{K}$ interaction vertex. Inclusion of e.g. scalar resonances in the s-channel is of higher order, $O(p^4)$. In the t-channel we include the important vector meson exchange which also is of higher order, $O(p^4)$, but is important for the inclusion of final-state interactions. Here we use the standard notations of ChPT. The fields of pseudoscalar mesons are collected in the chiral matrix $U = u^2 = \exp(i\sum_i \phi_i\lambda_i/F)$ with $F = 92.4$ MeV being the leptonic decay constant and D_μ is the covariant derivative acting on the chiral field. Furthermore, $\chi = 2B\mathcal{M} + \cdots$, where B is the quark vacuum condensate parameter $B = -\langle 0|\bar{u}u|0\rangle/F^2 = -\langle 0|\bar{d}d|0\rangle/F^2$ and $\mathcal{M} = \mathrm{diag}\{m, m, m_S\}$ is the mass matrix of current quarks with $m = (m_u + m_d)/2$. In the leading order of the chiral expansion the masses of pions and kaons are given by $M_\pi^2 = 2mB$, $M_K^2 = (m + m_S)B$. In summary, second order ChPT gives rise to a second diagram being of the same structure as graph b) but opposite in sign. Therefore, the triangle diagram a) gives the dominant contribution to the decay amplitude.
The couplings for the strong decays are defined by

$$g_{f_0\pi\pi} = g_{f_0\pi^+\pi^-} = 2g_{f_0\pi^0\pi^0} = G(M_{f_0}^2, M_\pi^2, M_\pi^2) \tag{4.55}$$

$$g_{a_0\pi\eta} = G(M_{a_0}^2, M_\pi^2, M_\eta^2)\,, \tag{4.56}$$

where, in the case of the two-pion decay, we have to consider the ratio between the charged and neutral decay modes. Here, $G(p^2, q_1^2, q_2^2)$ is the structure integral of the $f_0 \to \pi\pi$ and $a_0 \to \pi\eta$ transitions which are conventionally split into the two terms $G^{(a)}(p^2, q_1^2, q_2^2)$ and $G^{(b)}(p^2, q_1^2, q_2^2)$. They refer to the contributions of the diagrams

of Figs. 4.11 (a) and 4.11 (b), respectively, with

$$G(p^2, q_1^2, q_2^2) = G^{(a)}(p^2, q_1^2, q_2^2) + G^{(b)}(p^2, q_1^2, q_2^2)\,. \tag{4.57}$$

The expressions for the structure integrals G can be found in Appendix A.1.2.

The strong two–pion and $\pi\eta$ decay modes are studied within model A considering the mixing angle dependence of the couplings to the charged and neutral kaon pairs. Therefore, the kaon loop integrals need to be expressed in terms of the charged and neutral couplings $g_{SK^+K^-}$ and $g_{SK^0\bar{K}^0}$

$$G(p^2, q_1^2, q_2^2) = \frac{g_{SK^+K^-}}{\sqrt{2}} \cdot I(M_{K^\pm}^2, p^2, q_1^2, q_2^2) + \frac{g_{SK^0\bar{K}^0}}{\sqrt{2}} \cdot I(M_{K^0}^2, p^2, q_1^2, q_2^2)\,, \tag{4.58}$$

where $I(M_K^2, p^2, q_1^2, q_2^2)$ denote the contributions from the intermediate charged and neutral kaons which are explicitly indicated in Appendix A.1.2.

In the second approach (method B), which restricts to small mixing angles, we use

$$G(p^2, q_1^2, q_2^2) = \frac{G_{SK\overline{K}}}{\sqrt{2}} \cdot \left(I(M_{K^\pm}^2, p^2, q_1^2, q_2^2) + I(M_{K^0}^2, p^2, q_1^2, q_2^2)\right), \tag{4.59}$$

The expressions for the decay widths are finally given by

$$\Gamma(f_0 \to \pi\pi) = \Gamma_{f_0\pi^+\pi^-} + \Gamma_{f_0\pi^0\pi^0} = \frac{3}{2}\Gamma_{f_0\pi^+\pi^-} = \frac{3}{32\pi}\frac{g_{f_0\pi\pi}^2}{M_{f_0}}\sqrt{1 - \frac{4M_\pi^2}{M_{f_0}^2}}\,, \tag{4.60}$$

$$\Gamma(a_0 \to \pi\eta) = \frac{1}{16\pi}\frac{g_{a_0\pi\eta}^2}{M_{a_0}}\frac{\lambda^{1/2}(M_{a_0}^2, M_\pi^2, M_\eta^2)}{M_{a_0}^2}\,, \tag{4.61}$$

with the Källen-function $\lambda(x, y, z) = x^2 + y^2 + z^2 - 2xy - 2xz - 2yz$.

In the numerical computations of the strong $f_0 \to \pi\pi$ and $a_0 \to \pi\eta$ decays we restrict to the charged pion mass ($M_\pi \equiv M_{\pi^\pm} 139.57$ MeV) but consider explicit kaon masses $M_{K^0} \neq M_{K^\pm}$. The influence of mixing effects can be studied in Tab. 4.7 by means of the decay properties $f_0(a_0) \to \pi\pi(\eta)$ obtained within method A for $\Lambda = 1$ GeV. The size parameter dependence can be found in [26]. From the radiative decay properties it is known that isospin–violating mixing can be considered small. Hence, by assuming a mixing angle between -3° and 3°, the strong $f_0 \to \pi\pi$ and $a_0 \to \pi\eta$ widths lie in the range of values

$$\begin{aligned} \Gamma(f_0 \to \pi\pi) &= 55.7 - 58.9 \text{ MeV}\,, \\ \Gamma(a_0 \to \pi\eta) &= 58.9 - 63.4 \text{ MeV}\,. \end{aligned} \tag{4.62}$$

As expected the results of model B are rather close to the decay widths when

θ	-3°	-2°	-1°	0°	1°	2°	3°	5°	10°	20°	45°
$g_{f_0\pi\pi}$ [GeV]	1.46	1.44	1.42	1.40	1.38	1.36	1.34	1.29	1.17	0.89	0.00
$\Gamma_{f_0\pi\pi}$ [MeV]	62.3	60.7	59.0	57.4	55.7	54.0	52.3	48.9	40.1	23.0	0.0
$g_{a_0\pi\eta}$[GeV]	2.02	2.07	2.11	2.16	2.20	2.25	2.29	2.38	2.59	2.97	3.43
$\Gamma_{a_0\pi\eta}$ [MeV]	53.8	56.2	58.8	61.3	63.9	66.5	69.2	74.6	88.7	116.5	154.6

Table 4.7.: Strong a_0 and f_0 decay properties in dependence on θ ($\Lambda = 1$ GeV).

neglecting mixing effects (see $\theta = 0$ in Tab. 4.7)

$$\begin{aligned} \Gamma(f_0 \to \pi\pi) &= 57.4 \text{ MeV}\,, \\ \Gamma(a_0 \to \pi\eta) &= 61.0 \text{ MeV}\,. \end{aligned} \tag{4.63}$$

Since experimental uncertainties are quite large in case of the strong decay properties, our results obtained within method A and B are consistent with the data listed in Tabs. 4.8 and 4.9.

Data	PDG [22]	BELLE [150]	WA102 [162]
$\Gamma(f_0 \to \pi\pi)$ [MeV]	$40 - 100$	$51.3^{+20.8\,+13.2}_{-17.7\,-3.8}$	80 ± 10

Table 4.8.: Strong decay width $f_0(980) \to \pi\pi$: experimental data.

Reference	[22]	[163]	[164]	[21]	[153]
	experimental data			$q\bar{q}$	$q\bar{q}$
$\Gamma(a_0 \to \pi\eta)$ [MeV]	50-100	$50 \pm 13 \pm 4$	61 ± 19	225	138

Table 4.9.: Strong decay width $a_0(980) \to \pi\eta$: data and theoretical approaches.

We compare our result obtained within the hadronic molecule picture to other theoretical predictions which are indicated in Tab. 4.9 for the a_0 decays and in Tab. 4.10 in case of the f_0. The theoretical results for the $f_0 \to \pi\pi$ decay in Tab. 4.10, unfortunately, cover a large range of values, even within the same structure assumption. Again, the present situation for $\Gamma(f_0 \to \pi\pi)$ does not allow for a clear statement concerning the f_0 structure. In contrast, in the case of the $a_0 \to \pi\eta$ decay the quarkonium models of [21] and [153] deliver much larger results compared to the one of the molecular interpretation and data. The strong $a_0(980)$ decay properties clearly favor the present meson molecule picture.

Reference	[152]	[165]	[166]	[153]	[167]	[168]
Meson structure	$q\bar{q}$	$q\bar{q}$	$q\bar{q}$	$q\bar{q}$	$q\bar{q}$	hadronic
$\Gamma(f_0 \to \pi\pi)$ [MeV]	20	28	52-58	53	56	18.2

Table 4.10.: Strong decay width $f_0(980) \to \pi\pi$: theoretical approaches.

In the strong decay sector $f_0 - a_0$ mixing also generates the isospin violating decays $f_0 \to \pi\eta$ and $a_0 \to \pi\pi$. In the context of our approach we obtain the results

$$\Gamma(f_0 \to \pi\eta) = 0.57 \text{ MeV}, \tag{4.64}$$
$$\Gamma(a_0 \to \pi\pi) = 1.59 \text{ MeV}, \tag{4.65}$$

which, since the processes are forbidden by isospin symmetry, are strongly suppressed compared to the dominant strong decays discussed above.

Summary

In summary, our results for the electromagnetic f_0 and a_0 decay properties are in quite good agreement with present experimental data. Therefore, the hadronic molecule approach is suitable to describe radiative f_0 and a_0 decays. However, other subleading structure components besides the $K\overline{K}$ configuration can possibly be realized. For this reason, current data do not allow any definite and final conclusion concerning the substructure of the scalar mesons since calculations based on other approaches give similar results and even overlap with each other as demonstrated in Tables 4.3 and 4.4.

A further step forward would be a more precise experimental determination of the decay properties but also of the $f_0 - a_0$ mixing strength to shed light on the isospin violating mixing mechanisms. A possible access to mixing is given by the ratio between charged and neutral a_0 meson decays since the coupling to the charged $a_0^{\pm}$ mesons is not affected by mixing.

The present framework, assuming f_0 and a_0 to be hadronic $K\overline{K}$ molecules, provides a straightforward and consistent determination of the decay properties, in particular the coupling constants and decay widths. The radiative decay properties of the a_0 and f_0 mesons have been studied comprehensively within a clear and consistent model for hadronic bound states. At the same time essential criteria such as covariance and full gauge invariance with respect to the electromagnetic interaction are satisfied.

Despite that we deal with a rather simple model, it allows to study the influence of the spatial extension of the meson molecule and isospin violating mixing. The coupling of the hadronic bound state to the constituent kaons, including $f_0 - a_0$

mixing effects, has been determined by the compositeness condition which reduces the number of free parameters to only one, the size parameter Λ.
Our results for the electromagnetic decays ($a_0/f_0 \to \gamma\gamma$ and $\phi \to \gamma a_0/f_0$) and, in addition, the strong decay widths ($f_0 \to \pi\pi$ and $a_0 \to \pi\eta$) are analyzed with respect to $f_0 - a_0$ mixing and finite size effects.
We come to the conclusion that the hadronic molecule interpretation is sufficient to describe both the electromagnetic and strong a_0/f_0 decays, based on the current status of experimental data. Furthermore, the $f_0 - a_0$ mixing strength could be determined by a precise measurement of the ratio of the charged and neutral a_0 meson decays. The $f_0 - a_0$ mixing strength could deliver new insights into the contributions being responsible for isospin-violating mixing and the meson structure issue.

4.2.2. Weak non–leptonic decays of hadron molecules

After the study of radiative and strong decay and production modes of the light scalar mesons $f_0(980)$ and $a_0(980)$ we now turn to the weak production properties. In the present section we especially deal with weak hadronic transitions of initial and final hadronic molecules involving the $f_0(980)$. In particular, we concentrate on transitions including the scalar $D_{s0}^*(2317)$ and its bottom-strange counterpart $B_{s0}^*(5725)$ as well as the weak non–leptonic decay processes of the axial-vector mesons $D_{s1}(2460)$ and $B_{s1}(5778)$. The masses of the two charmed mesons are located slightly below the DK and D^*K thresholds and are candidates for hadronic molecules with the configurations $D_{s0}^*(2317) = DK$ and $D_{s1}(2460) = D^*K$. In addition, these considerations can be extended to the bottom sector, where we treat the scalar and axial-vector mesons $B_{s0}^*(5725)$ and $B_{s1}(5778)$ as the equivalents of the charm-strange mesons $D_{s0}^*(2317)$ and $D_{s1}(2460)$. The bottom-strange counterparts $B_{s0}^*(5725)$ and $B_{s1}(5778)$ are consequently also described as bound states $B_{s0}^*(5725) = B\bar{K}$ and $B_{s1}(5778) = D^*K$. The properties of all those hadronic molecules are hence studied within the same effective Lagrangian approach [26, 27, 169, 170, 171], where the following dominant composite structure has been used

$$\left|D_{s0}^{*+}\right\rangle = \frac{1}{\sqrt{2}}\left(\left|D^+K^0\right\rangle + \left|D^0K^+\right\rangle\right), \tag{4.66}$$

$$\left|D_{s1}^{+}\right\rangle = \frac{1}{\sqrt{2}}\left(\left|D^{*+}K^0\right\rangle + \left|D^{*0}K^+\right\rangle\right), \tag{4.67}$$

$$\left|B_{s0}^{*0}\right\rangle = \frac{1}{\sqrt{2}}\left(\left|B^+K^-\right\rangle + \left|B^0\bar{K}^0\right\rangle\right), \tag{4.68}$$

$$\left|B_{s1}^{0}\right\rangle = \frac{1}{\sqrt{2}}\left(\left|B^{*+}K^-\right\rangle + \left|B^{*0}\bar{K}^0\right\rangle\right). \tag{4.69}$$

Since in the following we deal with transition processes involving the $f_0(980)$ in the

final state, the decay properties involve twice the effect of meson bound states: On the one hand by the initial heavy meson system, on the other hand by the final scalar f_0. For this reason the results might provide a sensitive observable to test the issue of hadronic molecule structure accessible in future experiments.

The charmed and bottom hadronic molecules are set up by the same nonlocal Lagrangian (4.2) which is also used for the f_0 and a_0 mesons

$$\mathcal{L}_{HM_1M_2} = \quad g_H H(x) \int dy\, \Phi_H(y^2)\, M_1^T(x + w_{21}y)\, M_2(x + w_{12}y) + \text{h.c.}\,, \tag{4.70}$$

where we refer to the hadronic molecules $H = f_0,\ D_{s0}^{*-},\ D_{s1}^{-\mu},\ \bar{B}_{s0}^{*0}$ and $\bar{B}_{s1}^{0\mu}$ the corresponding constituent meson pairs $M_1M_2 = K\bar{K},\ DK,\ D_\mu^* K,\ B\bar{K},\ B_\mu^*\bar{K}$. The constituent mesons are combined in the isospin doublets

$$\begin{aligned} K &= \begin{pmatrix} K^+ \\ K^0 \end{pmatrix}, \qquad \overline{K} = \begin{pmatrix} K^- \\ \bar{K}^0 \end{pmatrix}, \qquad D = \begin{pmatrix} D^0 \\ D^+ \end{pmatrix}, \\ D_\mu^* &= \begin{pmatrix} D^{*0} \\ D^{*+} \end{pmatrix}_\mu, \qquad B = \begin{pmatrix} B^+ \\ B^0 \end{pmatrix}, \qquad B_\mu^* = \begin{pmatrix} B^{*+} \\ B^{*0} \end{pmatrix}_\mu . \end{aligned} \tag{4.71}$$

Details and further definitions of the Lagrangian can be found in the discussion of Eq. (4.2). For each hadronic molecule we consider the correlation function Φ which is expressed by a Gaussian form factor

$$\widetilde{\Phi}(k_E^2) = \exp(-k_E^2/\Lambda^2) \tag{4.72}$$

in Euclidean momentum space. The size parameters of the scalar f_0 and the heavy mesons – Λ_{f_0} and $\Lambda_{D/B}$ – are the only adjustable parameters in our approach.

As discussed in the beginning of this chapter, the coupling constants between the hadronic molecules and its building blocks, the constituent mesons, are fixed self-consistently by the compositeness condition [142]. Below we list our predictions for the couplings g_H obtained for the respective molecular states. The coupling constants of the f_0, D_{s0}^* and D_{s1} mesons have already been calculated in [26, 27, 169, 171]:

$$g_{D_{s0}^*} = 11.26 \text{ GeV } (\Lambda_D = 1 \text{ GeV}) \qquad g_{D_{s0}^*} = 9.9 \text{ GeV } (\Lambda_D = 2 \text{ GeV}) \tag{4.73}$$

$$g_{D_{s1}} = 11.62 \text{ GeV } \quad (\Lambda_D = 1 \text{ GeV}) \quad g_{D_{s1}} = 10.17 \text{ GeV } \quad (\Lambda_D = 2 \text{ GeV})\,. \tag{4.74}$$

The results for the couplings of the B_{s0}^* and B_{s1} mesons to their constituents for

different size parameters Λ_D are [172]:

$$g_{B^*_{s0}} = 27.17 \text{ GeV } (\Lambda_B = 1 \text{ GeV}) \qquad g_{B^*_{s0}} = 23.21 \text{ GeV } (\Lambda_B = 2 \text{ GeV}) \tag{4.75}$$

$$g_{B_{s1}} = 25.64 \text{ GeV } (\Lambda_B = 1 \text{ GeV}) \qquad g_{B_{s1}} = 22.14 \text{ GeV } (\Lambda_B = 2 \text{ GeV}) \,. \tag{4.76}$$

In the mesonic molecule picture all decays proceed via intermediate states which are the composite mesons of the hadronic bound states.

$\mathbf{D^*_{s0}(2317) \to f_0 X}$ and $\mathbf{B^*_{s0}(5725) \to f_0 X}$ decays

In the following we deal with the f_0-production properties in weak hadronic decays of the heavy scalar mesons $D^*_{s_0}(2317)$ and $B^*_{s_0}(5725)$. Since both heavy quark systems are assumed to be of molecular structure the decays proceed via intermediate kaons and D or B mesons as indicated in the diagrams of Figs. 4.12 and 4.13.

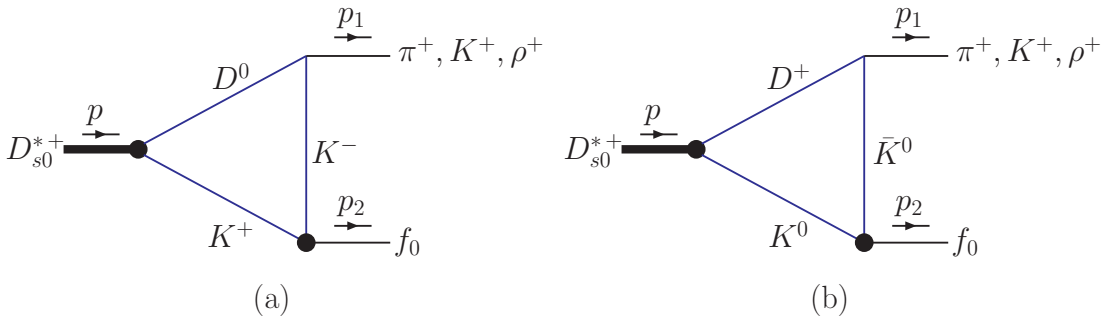

Figure 4.12.: Diagrams contributing to the $D^{*+}_{s0} \to f_0 X$ decays with $X = \pi^+$, K^+ and ρ^+.

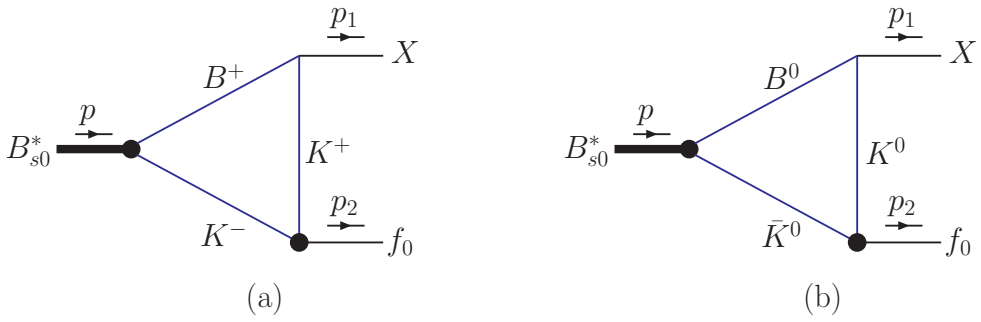

Figure 4.13.: Diagrams contributing to the $B^*_{s0} \to f_0 X$ decays with $X = \pi$, K, ρ, ω, η and η'.

While the couplings of the constituent mesons to the hadronic molecules in the loop are fixed by the compositeness condition, the coupling constants between the

intermediate K, D and B mesons and the final decay products $\pi, K, \rho, \omega\,\eta$ and η' are determined by the D and B meson decay widths:

$$g^{c,n}_{MKP} = \sqrt{\frac{16\pi\,\Gamma(M \to K\,P)\,m_M^3}{\lambda^{\frac{1}{2}}(m_M^2, m_K^2, m_P^2)}}\,, \quad (P = K, \pi, \eta, \eta', \quad M = D, B)\,, \tag{4.77}$$

$$g^{c,n}_{MKV} = \sqrt{\frac{64\pi\,\Gamma(M \to K\,V)\,m_M^3\,m_V^2}{\lambda^{\frac{3}{2}}(m_M^2, m_K^2, m_V^2)}}\,, \quad (V = \rho, \omega, \quad M = D, B)\,. \tag{4.78}$$

The superscript c (n) denotes the decays of the charged (neutral) D and B mesons. In Appendix A.3 we summarize the branching ratios as taken from [173, 174] and the resulting couplings $g_X^{c,n}$ (via Eqs. (4.77) and (4.78)) involving charged (c) and neutral (n) B and D mesons.

We first consider the D^*_{s0} (B^*_{s0}) decays to f_0 and a pseudoscalar P. The corresponding coupling constants we calculate from the expressions

$$g_{D^*_{s0} f_0\,P} = \frac{g_{D^*_{s0}}\,g_{f_0}}{(4\pi)^2}\left[g^c_{HKP} I(m^2_{D^+}, m^2_{K^0}) + g^n_{HKP} I(m^2_{D^0}, m^2_{K^+})\right], \tag{4.79}$$

$$g_{B^*_{s0} f_0\,P} = 2\frac{g_{B^*_{s0}}\,g_{f_0}}{(4\pi)^2}\left[g^c_{HKP} I(m^2_{D^+}, m^2_{K^+}) + g^n_{HKP} I(m^2_{D^0}, m^2_{K^0})\right]. \tag{4.80}$$

$I(m_H^2, m_K^2)$ denotes the loop integral over the intermediate particles

$$\begin{aligned} I(m_H^2, m_K^2) = \int \frac{d^4k}{\pi^2 i}\,\widetilde{\Phi}_f(-k^2)\widetilde{\Phi}_{H^*_{s0}}\big(-(k - \frac{p}{2} + \omega p_{H^*_{s0}})^2\big)\times \\ \times\; S_M\big(k - \frac{p}{2} + p_{H^*_{s0}}\big) S_K\big(k - \frac{p}{2}\big) S_K\big(k + \frac{p}{2}\big)\,, \end{aligned} \tag{4.81}$$

with the hadronic molecules $H^*_{s0} = B^*_{s0}, D^{*+}_{s0}$ and the constituent mesons $M = D,\, B$. The decay widths are finally obtained from

$$\Gamma(H^*_{s_0} \to f_0\,P) \;=\; \frac{\lambda^{\frac{1}{2}}(m^2_{H^*_{s0}}, m^2_{f_0}, m^2_P)}{16\pi m^3_{H^*_{s0}}} \cdot g^2_{H^*_{s0} f_0\,P}\,. \tag{4.82}$$

When dealing with the decays $D^*_{s0}/B^*_{s0} \to f_0 V$ ($V = \rho,\, \omega$) we proceed in complete analogy. For simplicity, we restrict in the following to the $D^{*+}_{s0} \to f_0 \rho^+$ decay since the corresponding expressions for the bottom B^*_{s0} decays only differ in the masses and couplings while the structure remains the same.

The starting point is the Feynman integral of Fig. 4.12 which reads

$$I^\mu(m_D^2, m_K^2) = \int \frac{d^4k}{\pi^2 i}\,\frac{\widetilde{\Phi}_f(-k^2)\,\widetilde{\Phi}_{D^*_{s_0}}\big(-(k - \frac{p}{2} + \omega p_{D^*_{s_0}})^2\big)\,(2k + p_{D^*_{s0}})^\mu}{S_D^{-1}\big(k - \frac{p}{2} + p_{D^*_{s_0}}\big) S_K^{-1}\big(k - \frac{p}{2}\big) S_K^{-1}\big(k + \frac{p}{2}\big)} \tag{4.83}$$

and defines the transition matrix element $\mathcal{M}^\mu$ which is given by

$$\mathcal{M}^\mu(m^2_{D^*_{s0}}, m^2_{f_0}, m^2_\rho) = \frac{g_{D^*_{s0}} g_f}{(4\pi)^2}\left[g^c_{HK\rho} I^\mu(m^2_{D^+}, m^2_{K^0}) + g^n_{HK\rho} I^\mu(m^2_{D^0}, m^2_{K^+})\right] \quad (4.84)$$

$$= F_1(m^2_{D^*_{s0}}, m^2_{f_0}, m^2_\rho)\, p^\mu_f + F_2(m^2_{D^*_{s0}}, m^2_{f_0}, m^2_\rho)\, p^\mu_\rho \,. \quad (4.85)$$

In the second line $\mathcal{M}^\mu$ is expressed in terms of the form factors F_1 and F_2 by writing the matrix element as a linear combination of the f_0 and ρ meson momenta p_f and p_ρ. We perform this decomposition since the form factor F_1 defines the coupling constant of the decay

$$F_1(m^2_{D_{s0}}, m^2_{f_0}, m^2_\rho) \equiv g_{D^*_{s0} f_0 \rho} \quad (4.86)$$

and therefore characterizes the decay width

$$\Gamma(D^*_{s_0} \to f_0 \rho^+) = \frac{\lambda^{\frac{3}{2}}(m^2_{D^*_{s0}}, m^2_{f_0}, m^2_\rho)}{64\pi m^3_{D^*_{s_0}} m^2_\rho}\, g^2_{D^*_{s0} f_0 \rho} \,. \quad (4.87)$$

The results for the weak $D^*_{s0} \to f_0 X$ and $B^*_{s0} \to f_0 X$ decay properties are summarized in Tab. 4.11, where we also indicate the dependence of the results for different sets of size parameters $\Lambda_{D/B}$ and Λ_{f_0}. Compared to the local case (LC) finite size effects induce a reduction of the decay widths by up to 50%. For the D^{*+}_{s0} decays we

Channel	local limit, $\Lambda_{D,B} = \Lambda_f = \infty$	$\Lambda_{D,B} = 2$ GeV, $\Lambda_f = 1$ GeV	$\Lambda_{D,B} = 1$ GeV, $\Lambda_f = 1$ GeV
$D^{*+}_{s0} \to f_0 \pi^+$	$2.35 \cdot 10^{-5}$	$1.26 \cdot 10^{-5}$	$1.14 \cdot 10^{-5}$
$D^{*+}_{s0} \to f_0 K^+$	$2.75 \cdot 10^{-6}$	$1.53 \cdot 10^{-6}$	$1.42 \cdot 10^{-6}$
$D^{*+}_{s0} \to f_0 \rho^+$	$1.60 \cdot 10^{-4}$	$1.08 \cdot 10^{-4}$	$1.11 \cdot 10^{-4}$
$B^*_{s0} \to f_0 \pi^0$	$5.66 \cdot 10^{-10}$	$9.93 \cdot 10^{-11}$	$5.03 \cdot 10^{-11}$
$B^*_{s0} \to f_0 \eta'$	$3.67 \cdot 10^{-9}$	$6.69 \cdot 10^{-10}$	$3.49 \cdot 10^{-10}$
$B^*_{s0} \to f_0 \eta$	$< 1.16 \cdot 10^{-10}$	$< 2.05 \cdot 10^{-11}$	$< 1.05 \cdot 10^{-11}$
$B^*_{s0} \to f_0 K^0$	$5.88 \cdot 10^{-11}$ GeV	$1.04 \cdot 10^{-11}$	$5.32 \cdot 10^{-12}$
$B^*_{s0} \to f_0 \rho^0$	$4.64 \cdot 10^{-10}$	$9.22 \cdot 10^{-11}$	$5.75 \cdot 10^{-11}$
$B^*_{s0} \to f_0 \omega$	$5.86 \cdot 10^{-10}$	$1.17 \cdot 10^{-10}$	$7.31 \cdot 10^{-11}$

Table 4.11.: Widths of the $D^{*+}_{s0} \to f_0 X$ and $B^{*+}_{s0} \to f_0 X$ decays in eV.

predict a decay pattern with $\Gamma(D^{*+}_{s0} \to f_0 \rho^+) > \Gamma(D^{*+}_{s0} \to f_0 \pi) > \Gamma(D^{*+}_{s0} \to f_0 K^+)$.

In the case of B_{s0}^* the weak decay mode $B_{s0}^* \to f_0\eta'$ dominates the transition pattern.

$\mathbf{D_s^+ \to f_0\pi^+}$ decay

For the calculation of the $D_{s1} \to f_0\pi$ decay width, which we will discuss in the next section, we need to derive a value for the $D^*K\pi$ coupling constant g_π. For this purpose we analyze the $D_s^+ \to f_0\pi^+$ transition of Fig. 4.14 from which we obtain the decay width $\Gamma(D^* \to K\pi)$ as an additional result. The expression for the

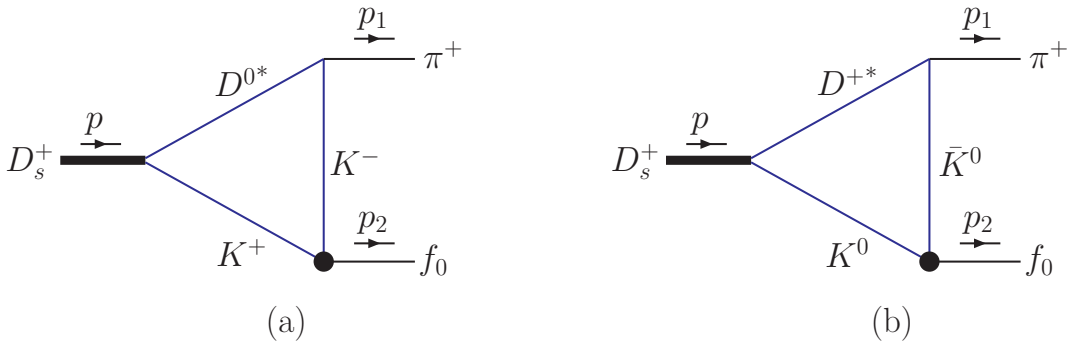

Figure 4.14.: D_s^+-decay.

$D_s^+ \to f_0\pi^+$ reads

$$\Gamma(D_s^+ \to f_0\pi^+) = \frac{\lambda^{\frac{1}{2}}(m_{D_s}^2, m_{f_0}^2, m_\pi^2)}{16\,\pi\, m_{D_s}^3} \cdot g_{D_s f_0 \pi}^2\,, \tag{4.88}$$

where we determine the coupling $g_{D_s f_0\pi}$ from the structure integral of Fig. 4.14

$$g_{D_s f_0\pi} \;=\; \frac{g_f g_{D_s} g_\pi}{(4\pi)^2}\left[I(m_{D^{*+}}^2, m_{K^0}^2) + I(m_{D^{*0}}^2, m_{K^+}^2)\right]. \tag{4.89}$$

The loop integral $I(m_{D^*}^2, m_K^2)$ is given by

$$\begin{aligned} I(m_{D^*}^2, m_K^2) = \int \frac{d^4k}{\pi^2 i}\,\widetilde{\Phi}_f(-k^2)\,\big(p_\pi - k - \frac{p}{2}\big)_\mu \big(k - \frac{p}{2} - p_{D_s}\big)_\nu \times \\ \times\; S_D^{\mu\nu}\big(k - \frac{p}{2} + p_{D_s}\big) S_K\big(k - \frac{p}{2}\big) S_K\big(k + \frac{p}{2}\big)\,. \end{aligned} \tag{4.90}$$

The coupling constant g_{D_s} of the $D_s D^* K$ interaction vertex has been estimated in two different QCD sum rule approaches [175, 176], where both results do not vary significantly from each other. Here we use the result of [175] with $g_{D_s} = 2.02$. By using the branching ratio $BR(D_S \to f_0\pi^+) = (6.0 \pm 2.4)\cdot 10^{-3}$ [174], corresponding to $\Gamma(D_S \to f_0\pi^+) = 7.9 \cdot 10^{-15}$ GeV, g_π can be easily derived by combining Eqs. (4.88)

and (4.89):

$$g_\pi = 6.41 \cdot 10^{-5}\,. \tag{4.91}$$

From above coupling we can determine the $D^* \to K\pi$ decay width given by

$$\Gamma(D^* \to K\pi) = g_\pi^2 \frac{\lambda^{\frac{3}{2}}(m_{D^*}^2, m_K^2, m_\pi^2)}{48\pi m_{D^*}^5} = 4.45 \cdot 10^{-11}\ \text{GeV}\,. \tag{4.92}$$

$\mathbf{D_{s1}(2460)}$ and $\mathbf{B_{s1}(5778)}$ decays

As a final task we study the properties of the weak transitions between the axial vector hadronic molecules $D_{s1}(2460)$ and $B_{s1}(5778)$ and the scalar $f_0(980)$ which are represented by the diagrams in Fig. 4.15. The determination of g_π in the last section enables us to compute the decay $D_{s1}^+(2460) \to f_0\pi^+$ within the $K\ D^*$ bound state framework. In the first step we define the matrix element of the $D_{s1}^+ \to f_0\pi^+$

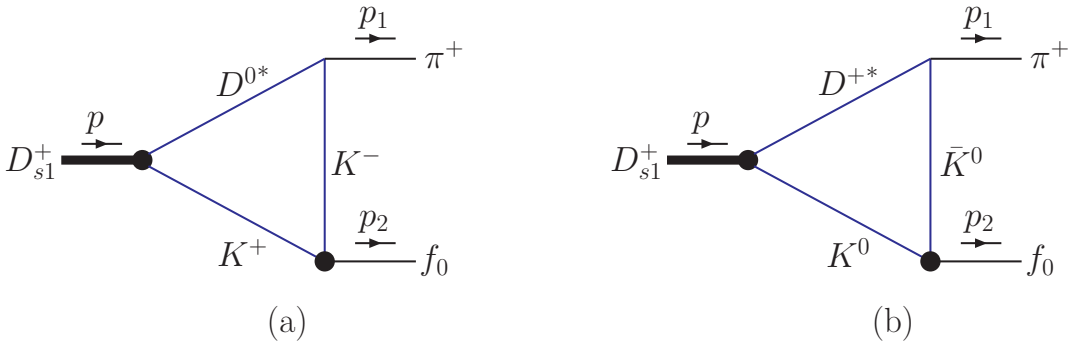

Figure 4.15.: $D_{s1}^*(2460)$ decay.

transition in terms of the form factors $F_\pm$ and $p_\pm = p_f \pm p_\pi$

$$\begin{aligned}\mathcal{M}^\mu &= \frac{g_f g_{D_{s1}} g_\pi}{(4\pi)^2}\big(I^\mu(m_{D^{*+}}^2, m_{K^0}^2) + I^\mu(m_{D^{*0}}^2, m_{K^+}^2)\big) \\ &= F_+(m_{D_{s1}}, m_\pi, m_{f_0})p_+^\mu + F_-(m_{D_{s1}}, m_\pi, m_{f_0})p_-^\mu\,,\end{aligned} \tag{4.93}$$

where p_f^μ and p_π^μ are the f_0 and π momenta, respectively.
The loop integral involving the constituent kaons and D^* meson is of the structure

$$\begin{aligned}I^\mu(m_{D^*}^2, m_K^2) = \int \frac{d^4k}{\pi^{2i}}\,\widetilde{\Phi}_f(-k^2)\widetilde{\Phi}_{D_s}\big(-\big(k - \frac{p}{2} + \omega p_{D^*}\big)^2\big)\,\big(p_\pi - k - \frac{p}{2}\big)_\nu \times \\ \times\ S_{D^*}^{\mu\nu}\big(k - \frac{p}{2} + p_{D_{s1}}\big)S_K\big(k - \frac{p}{2}\big)S_K\big(k + \frac{p}{2}\big)\,,\end{aligned} \tag{4.94}$$

where $g_\pi = 6.40 \cdot 10^{-5}$ was already determined in Eq. (4.91).
The form factor F_- defines the coupling $g_{D_{s1}f_0\pi} \equiv F_-$ which characterizes the decay

width given by the expression

$$\Gamma(D_{s1}^+ \to f_0\pi^+) \;=\; \frac{g^2_{D_{s1}f_0\pi}}{48\pi\, m^5_{D_{s1}^+}}\lambda^{\frac{3}{2}}(m^2_{D_{s1}^+}, m^2_{f_0}, m^2_{\pi^+})\,. \tag{4.95}$$

We compute the decay width $D_{s1}^+ \to f_0\pi^+$ for the size parameter Λ_f=1 GeV while Λ_D is varied between 1 GeV and 2 GeV. The results for the $D_{s1} \to f_0\pi$ decay width obtained within our hadronic molecule approach range from

$$\Gamma(D_{s1} \to f_0\pi) = 2.85 \cdot 10^{-2}\ \text{eV} \quad (\Lambda_D = 1\ \text{GeV}) \tag{4.96}$$

to

$$\Gamma(D_{s1} \to f_0\pi) = 4.35 \cdot 10^{-2}\ \text{eV} \quad (\Lambda_D = 2\ \text{GeV})\,. \tag{4.97}$$

By analogy, we also study the $B_{s1} \to f_0P$ decay, where P represents a pseudoscalar final state. However, since no data is available to determine the B^*f_0P coupling strength g_{B^*}, we quote the width and corresponding decay coupling in dependence on g_{B^*}. By varying Λ_D from 1.0 GeV to 2 GeV the width lies between

$$\Gamma(B_{s1} \to f_0\pi) = 8.82 \cdot 10^{-6} \cdot g_{B^*}\ \text{GeV} \quad (\Lambda_D = 1\ \text{GeV}) \tag{4.98}$$

and

$$\Gamma(B_{s1} \to f_0\pi) = 4.03 \cdot 10^{-5} \cdot g_{B^*}\ \text{GeV} \quad (\Lambda_D = 2\ \text{GeV})\,. \tag{4.99}$$

Summary

We focused on hadronic production processes of the scalar $f_0(980)$ in weak non–leptonic decays of the D_{s0}^*, B_{s0}^*, D_{s1} and B_{s1} considered as hadronic molecules. Since all coupling constants are either fixed self-consistently by the compositeness condition or are deduced from data, the only adaptive variables are the size parameters of the meson molecules which allow for their extended structure. Finite size effects are studied by varying the size parameters within a physically reasonable region between 1 and 2 GeV. Additionally, we also compare the results including finite size effects to the local case where point-like interactions are used. The molecular interpretation of both, the initial heavy mesons and the final decay product, the kaonic bound state f_0, offers a sensitive tool to study the structure issue in weak decays. In particular for the $D_{s0}^*(2317) \to f_0X$ transitions we give clear predictions for the decay pattern arising in the hadronic molecule picture. Similarly, the result for the process $D_{s1} \to f_0\pi$ is a straightforward consequence of the molecular interpretation. Presently no comparative calculations, as for example in the full or partial quark-antiquark interpretation, of the weak processes studied here exist and,

hence, the real sensitivity of the results on details of the meson structure remains to be seen. But judging from previous model calculations [171, 170] of for example the dominant observed decay modes of the D^*_{s0} and D_{s1} a strong dependence on the structure models can be expected. Therefore, upcoming experiments measuring the weak production processes involving the scalar meson $f_0(980)$ could lead to new insights into the structure issue of meson molecule candidates.

4.3. Heavy Charmonium–like Hadronic Molecules

In the previous section we applied our model to candidates for molecular structure namely the experimentally long established f_0 and a_0 mesons. It was found that the present hadronic molecule approach is well suited to describe the production and decay properties of these states. After these introductory cases of $f_0(980)$ and $a_0(980)$ we now turn to the case of the hidden–charm mesons. As it was already discussed in Chapter 3, the last 10 years were characterized by the discovery of charmonium–like resonances which are not easily explained by simple $c\bar{c}$ states. Hence, this observation lead to a lot of speculations about structure issues beyond the quark model in the heavy meson sector. In the following we study three charmonium–like resonances which all show common features like the proximity to thresholds and the unexpectedly large hidden–charm decay widths which clearly disfavor a charmonium–assignment of these states.

4.3.1. Y(3940) and Y(4140)

The discussion of the $Y(3940)$ and $Y(4140)$ mesons we combine since both states are very similar with respect to their properties and also to the way how decay modes are computed in the effective Lagrangian approach.
The first charmonium–like state is the well–established $Y(3940)$ which is known for several years. It was originally observed by the BELLE [68] and then confirmed by the BABAR collaboration [68, 69]. Nevertheless, the mass and width of the resonance are slightly different with $m_{Y(3940)} = 3943 \pm 11(\text{stat}) \pm 13(\text{syst})$ MeV, $\Gamma_{Y(3940)} = 87 \pm 22(\text{stat}) \pm 26(\text{syst})$ MeV measured by the BELLE collaboration [68] and $m_{Y(3940)} = 3914.6^{+3.8}_{-3.4}(\text{stat}) \pm 2.0(\text{syst})$ MeV, $\Gamma_{Y(3940)} = 34^{+12}_{-8}(\text{stat}) \pm 5(\text{syst})$ MeV published by BABAR [69].
The $Y(3940)$ was discovered in B decays with a subsequent decay to the hidden–charm mode $J/\psi\omega$. In particular, the large hidden–charm decay to $J/\psi\omega$ is a striking property which almost rules out a $c\bar{c}$ assignment. A conventional $c\bar{c}$ charmonium interpretation is disfavored since open charm decay modes would dominate while the $J/\psi\omega$ decay rate is essentially negligible. Note, current data deduce a lower bound for the $\Gamma(Y(3940) \to J/\psi\omega) > 1$ MeV [61] which is an order of magnitude higher than typical rates between known charmonium states and could therefore indicate

first evidence for a hadronic molecule structure of the $Y(3940)$.

The second property which suggests a meson molecule interpretation of the $Y(3940)$ is the proximity to the $D^*\bar{D}^*$ threshold. Already several years before the discovery of the $Y(3940)$ binding of the $D^*\bar{D}^*$ system was predicted in meson exchange models [70], although many other states not observed yet were also claimed to be bound.

Some of these properties allow a connection to the $Y(4140)$ [56] which was announced in 2009 by the CDF Collaboration at Fermilab as a narrow near–threshold structure with natural width $\Gamma_{Y(4140)} = 11.7^{+8.3}_{-5.0}(\text{stat}) \pm 3.7(\text{syst})$ MeV. The $Y(4140)$ is so far the latest discovery of charmonium-like X, Y and Z mesons which are not easily explained as quark-antiquark configurations.

Similar to the previously discussed $Y(3940)$ the $Y(4140)$ was found in the hidden–charm $J/\psi\phi$ mass spectrum in exclusive $B^+ \to J/\psi\phi K^+$ decays. Because of several common properties with the $Y(3949)$ the $Y(4140)$ is often considered as the heavier partner of the $Y(3940)$. Among them there is the closeness to open charm thresholds. The $Y(4140)$ mass $m_{Y(4140)} = 4130.0 \pm 2.9(\text{stat}) \pm 1.2(\text{syst})$ MeV lies close to the $\bar{D}_s^* D_s^*$ threshold. The $Y(4140)$ was found in the $J/\psi\phi$ mass spectrum with a unusually large hidden-charm decay width for a charmonium state. From experimental observations and from the upper limit for the branching fraction for B-decays to a charmonium state $\text{Br}(B \to K(c\bar{c})$ of about 10^{-3} we can estimate $\Gamma(Y(4140) \to J/\psi\phi) > 100$ keV. A detailed discussion of the $Y(4140)$ properties can be found in the overview on meson spectroscopy in section 2.2. For comparison, the $Y(3940)$ shows rather similar decay patterns since it was observed in $J/\psi\omega$ decays.

From the theoretical point of view the $Y(4140)$ is dominantly considered as a hadronic molecule. For instance in one of the first follow-ups to the CDF result the $Y(4140)$ is suggested to be composed of a ${D_s^*}^+ {D_s^*}^-$ system bound by strong interaction. For example the authors of Ref. [66] show that binding for above meson configurations can be achieved in the context of meson-exchange potentials generated by the Lagrangian of heavy hadron chiral perturbation theory (HHChPT) [177, 178]. As discussed in Section 2.2 different theoretical approaches based on meson exchange processes, QCD sum rules or lattice studies come to the conclusion that $J^{\text{PC}} = 0^{++}$ or 2^{++} are possible quantum numbers allowing for a binding of the ${\bar{D}_s^*}^- {D_s^*}^+$ system. In the following we adopt the idea of a meson molecule picture and study the $Y(3940)$ and $Y(4140)$ as pure hadronic molecules of the $D^*\bar{D}^*$ and ${D_s^*}^+ {D_s^*}^-$ systems with

$$\begin{aligned} |Y(3940)\rangle &= \frac{1}{\sqrt{2}}\left(|{D^*}^+ {D^*}^-\rangle + |{D^*}^0 \overline{D}^{*\,0}\rangle\right), \\ |Y(4140)\rangle &= |{D_s^*}^+ {D_s^*}^-\rangle\,. \end{aligned} \tag{4.100}$$

Since we deal with pure hadronic molecules all decay processes proceed via meson loops involving the constituents. The interactions between the hadronic molecule

and its constituents and couplings of the constituents to the final decay products are defined by effective Lagrangians. Besides the positive charge parity the quantum numbers of the $Y(4140)$ are unknown. However s-wave binding is most likely for molecular bound states. We consider both possible quantum numbers $J^{PC} = 0^{++}$ and 2^{++}. The bound system of the two charmed mesons which form the Y mesons $Y(3940)$ and $Y(4140)$ is given by

$$\mathcal{L}_{Y D^*_{(s)} D^*_{(s)}} = g_Y Y(x) \int d^4y \Phi(y^2) \overline{D}^*_{(s)\,\mu}(x - \frac{y}{2}) D^{*\,\mu}_{(s)}(x + \frac{y}{2}) \qquad (4.101)$$

for scalar quantum numbers and

$$\mathcal{L}_{Y D^*_{(s)} D^*_{(s)}} = g'_Y Y^{\mu\nu}(x) \int d^4y \Phi(y^2) \overline{D}^*_{(s)\,\mu}(x - \frac{y}{2}) D^*_{(s)\,\nu}(x + \frac{y}{2}) \qquad (4.102)$$

in the case of tensor-like $Y(3940)$ and $Y(4140)$ mesons, where we also consider finite size effects by including a Gaussian form factor $\Phi(y^2)$.

As already discussed we use the so-called compositeness or Weinberg condition to set up the bound structure of the state and to determine the couplings $g_Y^{(\prime)}$. When considering the tensor quantum numbers for the Y states, we neglect the longitudinal components of the vector meson propagators and obtain for the mass operator the following structure

$$\Pi(p^2)^{\mu\nu\alpha\beta} = \Pi_{(T)}(p^2) g^{\mu\nu} g^{\alpha\beta} \,. \qquad (4.103)$$

We obtain for the couplings

$$\begin{aligned} g_{Y(3940)} &= 14.08 \pm 0.30 \\ g_{Y(4140)} &= 13.20 \pm 0.26 \end{aligned} \qquad (4.104)$$

for $J^{PC} = 0^{++}$. When neglecting the longitudinal components of the constituent vector mesons (see Eq. (4.103)) the values of the couplings $g'_{Y(3940)}$ and $g'_{Y(4140)}$ for $J^P = 2^+$ are equal to those for $J^P = 0^+$ in Eq. (4.104). The numerical results for the couplings determined by the original Weinberg formula (4.6) of $g^W_{Y(3940)} = 9.16$ GeV and $g^W_{Y(4140)} = 8.91$ GeV are in good agreement with nonlocal results of $g_{Y(3940)} = 14.08$ GeV and $g_{Y(4140)} = 13.20$ GeV. The nonlocality is contained in the vertex function $\Phi(y^2)$ which allows for a spatially extended structure of the hadronic bound state. The Gaussian form $\Phi(p^2) = \exp(p^2/\Lambda_Y^2)$, which is the Fourier transform of the vertex function, contains the size parameter Λ with a value of about 2 GeV — a typical scale for the masses of the constituents of the Y states.

In the following we analyze the strong $Y(4140) \to J/\psi\phi$ and radiative $Y(4140) \to \gamma\gamma$ decay widths by using an effective Lagrangian approach. As in the case of the

previously discussed f_0 and a_0 mesons, decay processes are described by the coupling of the final state particles via one–loop meson diagrams to the constituents of the molecular state. The couplings of the molecular bound state to their hadronic constituents and of the constituents to other hadrons and photons are defined by effective Lagrangians. While the interaction between the hadronic molecule and the constituent mesons is already determined in the framework of the Weinberg condition, the remaining couplings have to be taken from data or other theoretical approaches.

Strong hidden-charm decay

We first investigate the $Y \to J/\psi\omega$ hidden-charm decay mode in which the $Y(3940)$ was discovered. The $J/\psi\omega$ decay proceeding from the $\bar{D}^* D^*$ interpretation is depicted in Fig. 4.16. The final vector mesons couple via an intermediate open charm meson loop to the molecular Y state. The interaction is characterized by the

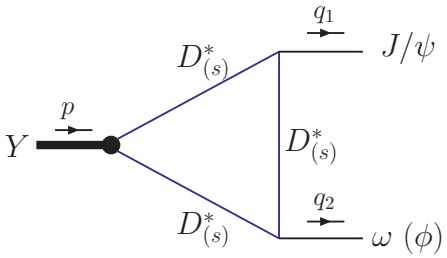

Figure 4.16.: Hidden-charm decay of the Y mesons.

HHChPT Lagrangian [177, 178]:

$$\begin{aligned}\mathcal{L}_{D^*D^*J_\psi} &= ig_{D^*D^*J_\psi} J^\mu_\psi \Big(D^{*\dagger}_{\mu i} \overset{\leftrightarrow}{\partial}_\nu D^{*\nu}_i + D^{*\dagger}_{\nu i} \overset{\leftrightarrow}{\partial}^\nu D^*_{\mu i} - D^{*\dagger\nu}_i \overset{\leftrightarrow}{\partial}_\mu D^*_{\nu i} \Big) , \\ \mathcal{L}_{D^*D^*V} &= ig_{D^*D^*V} V^\mu_{ij} D^{*\dagger}_{\nu i} \overset{\leftrightarrow}{\partial}_\mu D^{*\nu}_j + 4i f_{D^*D^*V} (\partial^\mu V^\nu_{ij} - \partial^\nu V^\mu_{ij}) D^*_{\mu i} D^{*\dagger\nu}_j \end{aligned} \tag{4.105}$$

where $A \overset{\leftrightarrow}{\partial} B \equiv A\partial B - B\partial A$; i, j are flavor indices; $V_{ij} = \mathrm{diag}\{\omega/\sqrt{2}, \omega/\sqrt{2}, \phi\}$ is the diagonal matrix containing ω and ϕ mesons (we omit the ρ and K^* mesons); $D^*_i = (D^{*0}, D^{*+}, D^{*+}_s)$ is the triplet of vector D^* mesons containing light antiquarks $\bar{u}$, $\bar{d}$ and $\bar{s}$, respectively. The chiral couplings $g_{D^*D^*J_\psi}$, $g_{D^*D^*V}$ and $f_{D^*D^*V}$ are taken from [177, 178]:

$$g_{D^*D^*V} = \beta g_V/\sqrt{2}\,, \quad f_{D^*D^*V} = m_{D^*}\lambda g_V/\sqrt{2}\,, \quad g_{D^*D^*J_\psi} = (m_D m_{J_\psi})/(m_{D^*} f_{J_\psi})\,,$$

where $f_{J_\psi} = 416.4$ MeV is the J/ψ leptonic decay constant. The parameters $g_V \approx 5.8$ and $\beta \approx 0.9$ are fixed using vector dominance and $\lambda = 0.56\ \mathrm{GeV}^{-1}$ is extracted by matching HHChPT to lattice QCD and light cone sum rules (see details in [179]).

The leading-order process relevant for the strong decays $Y(3940) \to J/\psi\omega$ and $Y(4140) \to J/\psi\phi$ is the diagram of Fig. 4.16 involving the vector mesons D^* or D_s^* in the loop.

The transition matrix element is given by

$$M_{\mu\nu}(Y \to J/\psi V) \;=\; g_{\mu\nu}\, g_{_{Y J_\psi V}} + v_{2\mu} v_{1\nu}\, f_{_{Y J_\psi V}}\,, \tag{4.106}$$

where $v_1(q_1)$ and $v_2(q_2)$ are the four–velocities (momenta) of J_ψ and V. The constants $g_{_{Y J_\psi V}}$ and $f_{_{Y J_\psi V}}$ are products of the coupling g_Y, the chiral couplings in Eq. (4.105) and the generic D^* meson loop structure integral (see Fig. 4.16). The coupling constant $g_{_{Y J_\psi V}}$ characterizes the decay properties, in particular the decay width, with

$$\Gamma(Y \to J/\psi V) \;=\; \frac{3P^*}{8\pi m_Y^2} g^2_{_{Y J_\psi V}} (1 + \beta + 2wr\beta + 3r^2\beta^2)\,,$$

where

$$r = \frac{f_{_{Y J_\psi V}}}{g_{_{Y J_\psi V}}}\,, \qquad \beta = \frac{1}{3}\left(\frac{P^* m_Y}{m_{J_\psi} m_V}\right)^2, \qquad w = v_1 v_2. \tag{4.107}$$

For the strong hidden–charm decay properties of the $Y(3940)$ we obtain

$$\begin{aligned}
g_{_{Y(3940) J_\psi \omega}} &= (1.72 \pm 0.03)\ \text{GeV, for } J^{PC} = 0^{++} \\
f_{_{Y(3940) J_\psi \omega}} &= (1.64 \pm 0.01)\ \text{GeV, for } J^{PC} = 0^{++} \\
\Gamma(Y(3940) \to J/\psi\omega) &= (5.47 \pm 0.34)\ \text{MeV, for } J^{PC} = 0^{++} \\
& \\
g_{_{Y(3940) J_\psi \omega}} &= (2.01 \pm 0.03)\ \text{GeV, for } J^{PC} = 2^{++} \\
f_{_{Y(3940) J_\psi \omega}} &= (1.92 \pm 0.01)\ \text{GeV, for } J^{PC} = 2^{++} \\
\Gamma(Y(3940) \to J/\psi\omega) &= (7.48 \pm 0.27)\ \text{MeV, for } J^{PC} = 2^{++}
\end{aligned} \tag{4.108}$$

The strong J/ψ decays of the $Y(3920)$ by assuming the quantum numbers 2^{++} are quite similar to the 0^{++} case. Therefore, from the large hidden–charm decay mode a 2^{++} scenario cannot be ruled out and is also consistent within a molecular interpretation of the Y states.

For the heavier $Y(4140)$ we obtain

$$\begin{aligned}
g_{Y(4140)J_\psi\phi} &= (1.46 \pm 0.03)\ \text{GeV, for } J^{PC} = 0^{++} \\
f_{Y(4140)J_\psi\phi} &= (1.84 \pm 0.01)\ \text{GeV, for } J^{PC} = 0^{++} \\
\Gamma(Y(4140) \to J/\psi\phi) &= (3.26 \pm 0.21)\ \text{MeV, for } J^{PC} = 0^{++} \\
& \qquad\qquad\qquad\qquad\qquad\qquad\qquad\qquad\qquad\qquad (4.109) \\
g_{Y(4140)J_\psi\phi} &= (1.70 \pm 0.03)\ \text{GeV, for } J^{PC} = 2^{++} \\
f_{Y(4140)J_\psi\phi} &= (2.14 \pm 0.01)\ \text{GeV, for } J^{PC} = 2^{++} \\
\Gamma(Y(4140) \to J/\psi\phi) &= (4.41 \pm 0.16)\ \text{MeV, for } J^{PC} = 2^{++}
\end{aligned}$$

In analogy with the $Y(3940)$ the strong decay properties of the $Y(4140)$ are not sensitive to the total spin since the decay width for $J^P = 2^+$ is similar to the case of $J^P = 0^+$.
The sizable strong decays widths are fully consistent with the upper limits set by present data on the total widths. The result for $\Gamma(Y(3940) \to J/\psi\omega)$ is also consistent with the lower limit of about 1 MeV [61]. Values of a few MeV for these decay widths naturally arise in the hadronic molecule interpretation of the $Y(3940)$ and $Y(4140)$, whereas in a conventional charmonium interpretation the $J/\psi V$ decays are strongly OZI suppressed [61]. In addition to the possibility of binding the $D^*\bar{D}^*$ and $D_s^{*+}D_s^{*-}$ systems [66], present results on the $J/\psi V$ decays give further strong support to the interpretation of the Y states as heavy hadron molecules.

Radiative decay

In order to study radiative decays we include the electromagnetic interaction by means of minimal substitution in the free meson Lagrangians of the charged vector mesons $D_{(s)}^{*\pm}$ which reads

$$\begin{aligned}
\mathcal{L}_{\rm em} &= eA_\alpha \Big(g^{\alpha\nu} D^{*-}_{(s)\,\mu} i\partial^\mu D^{*+}_{(s)\,\nu} - g^{\mu\nu} D^{*-}_{(s)\,\mu} i\partial^\alpha D^{*+}_{(s)\,\nu} + \text{H.c} \Big) \\
&+ e^2 D^{*-}_{(s)\,\mu} D^{*+}_{(s)\,\nu} \Big(A^\mu A^\nu - g^{\mu\nu} A^\alpha A_\alpha \Big) . \qquad (4.110)
\end{aligned}$$

The resulting diagrams connected with the two–photon decays of the $Y(3940)$ and $Y(4140)$ are illustrated in Fig. 4.17 (a) and (b). However, the non-local Lagrangians (4.101) and (4.102) need to be modified in order to fulfill electromagnetic gauge invariance. As already discussed in detail in Sec. 4.1 the inclusion of the gauge field exponential: $H^\pm(y) \to e^{\mp ieI(y,x,P)} H^\pm(y)$, where $I(x,y,P) = \int_y^x dz_\mu A^\mu(z)$ leads to further diagrams containing vertices where the photons couple directly to the $Y\bar{D}^*D^*$–vertex (see diagrams (c) and (d)). The contribution of these additional

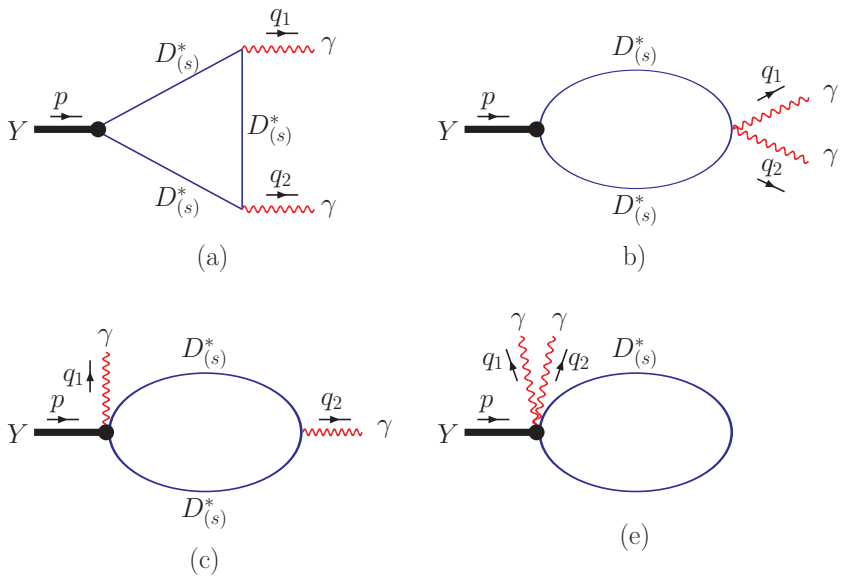

Figure 4.17.: Diagrams characterizing the radiative decay.

processes is significantly suppressed (of the order of a few percent of the total result) compared to the leading diagram of Fig. 4.17 (a). The matrix element of the two-photon transition can be expressed by the full gauge-invariant structure

$$M_{\mu\nu}(Y \to \gamma\gamma) \;=\; (g_{\mu\nu} q_1 q_2 - q_{2\mu} q_{1\nu})\, g_{_{Y\gamma\gamma}} \,. \tag{4.111}$$

From the coupling $g_{_{Y\gamma\gamma}}$ we can easily calculate the two-photon decay width

$$\Gamma(Y \to \gamma\gamma) \;=\; \frac{\pi}{4}\alpha^2 m_Y^3 g_{_{Y\gamma\gamma}}^2 \,, \tag{4.112}$$

where α is the fine structure constant.

Our results for the radiative decay properties are summarized in the box below.

$$\begin{aligned}
g_{_{Y(3940)\gamma\gamma}} &= (1.15 \pm 0.01) \times 10^{-2}\ \text{GeV}^{-1} \\
\Gamma(Y(3940) \to \gamma\gamma) &= (0.33 \pm 0.01)\ \text{keV, for } J^{PC} = 0^{++} \\
\Gamma(Y(3940) \to \gamma\gamma) &= (0.27 \pm 0.01)\ \text{keV, for } J^{PC} = 2^{++} \\
\\
g_{_{Y(4140)\gamma\gamma}} &= (1.46 \pm 0.01) \times 10^{-2}\ \text{GeV}^{-1} \\
\Gamma(Y(4140) \to \gamma\gamma) &= (0.63 \pm 0.01)\ \text{keV, for } J^{PC} = 0^{++} \\
\Gamma(Y(4140) \to \gamma\gamma) &= (0.50 \pm 0.01)\ \text{keV, for } J^{PC} = 2^{++}
\end{aligned} \tag{4.113}$$

The error bars refer to the experimental uncertainties of the Y masses. The decay properties for the quantum numbers $J^{PC} = 0^{++}$ and 2^{++} are very similar, so that even a precise measurement of the decay widths cannot be used to pin down the total spin of the two Y states.

For the ratio of the two–photon and strong decay widths of the $Y(3940)$ we obtain

$$R = \Gamma(Y(3940) \to \gamma\gamma)/\Gamma(Y(3940) \to J/\psi\omega) = 6.03 \times 10^{-5} \,. \tag{4.114}$$

In the case of the $Y(4140)$ the ratio

$$R = \frac{\Gamma(Y(4140) \to \gamma\gamma)}{\Gamma(Y(4140) \to J/\psi\phi)} = 1.93 \times 10^{-4} \tag{4.115}$$

is one order of magnitude larger than for the $Y(3940)$.

Present results should be compared to the ones obtained in the approach of Chapter 3 [23] which is based on the dynamically generation of the Y mesons. There we had a smaller decay width of the $Y(3940)$ with $\Gamma(Y(3940) \to \gamma\gamma) = 0.085$ keV ($J^P = 0^+$). Furthermore, we compare the $D_s^{*+}D_s^{*-}$ molecule $Y(4140)$ with the dynamically generated resonance $X(4190)$ of the previous model discussed in Chapter 3. The $X(4140)$ has the same molecular $D_s^{*+}D_s^{*-}$ structure and the spin–parity quantum numbers $J^P = 2^+$. In both theoretical approaches the two–photon decay widths of the respective $D_s^{*+}D_s^{*-}$ bound states are very similar. The hadronic molecule model leads to $\Gamma(Y(4140) \to \gamma\gamma) = 0.50$ keV for $J^{PC} = 2^{++}$ while the dynamical method of the previous chapter leads to 0.54 keV for the $X(4160) \to \gamma\gamma$ decay. Since the underlying molecular structure and the masses of the Y and X mesons are almost equal, it is not surprising that both theoretical frameworks lead to the same result.

Experimentally there is not too much known about the radiative decay modes of the two Y mesons. The only investigation of the two–photon production of the $Y(3940)$ and $Y(4140)$ was performed by the BELLE collaboration. The search for charmonium–like states in the process $\gamma\gamma \to J/\psi\omega$ [134] resulted in an enhancement with mass $M = 3915 \pm 3 \pm 2$ MeV termed $X(3915)$. According to its mass and width it is a good candidate for the $Y(3940)$ meson. The measured observable, which is the product of the two–photon width and the branching ratio of the strong decay, is given by [134]

$$\Gamma_{X(3915)\to\gamma\gamma}\, \mathrm{Br}(X(3915) \to J/\psi\omega) = \begin{cases} (61 \pm 17 \pm 8) \text{ eV for } J^P = 0^+ \\ (18 \pm 5 \pm 2) \text{ eV for } J^P = 2^+ \end{cases} . \tag{4.116}$$

If we compare above observations with the results in Eq. (4.113) and Eqs. (4.108)–

(4.109) of the present model calculation we obtain

$$\Gamma_{Y(3940)\to\gamma\gamma}\,\mathrm{Br}(Y(3940)\to J/\psi\omega) = \begin{cases} (21\pm 11)\ \mathrm{eV\ for}\ J^P = 0^+ \\ (23\pm 13)\ \mathrm{eV\ for}\ J^P = 2^+ \end{cases} \tag{4.117}$$

by using the BELLE data for the total width of $\Gamma_{Y(3940)} = 87 \pm 22 \pm 26$ MeV [68]. Given that we do not deal with a high–precision calculation, but rather an estimate, above results are in good agreement. As expected the values of (4.117) are independent of the total spin of the $Y(3940)$, where the result for $J^P = 2^+$ is even closer to experiment. If we perform the same analysis using the total width $\Gamma_{Y(3940)} = 4^{+12}_{-8} \pm 5$ MeV [69] deduced by BABAR we obtain

$$\Gamma(Y(3940)\to\gamma\gamma)\,\mathrm{Br}(Y(3940)\to J/\psi\omega) = (53\pm 20)\ \mathrm{eV} \tag{4.118}$$

for 0^{++} and 2^{++} which is also in agreement with the data in Eq. (4.116). Therefore, the observed two–photon decay properties also support the $D^*\bar{D}^*$ bound state interpretation of the $Y(3940)$ pursued in this theoretical analysis. For comparison, in the coupled channel analysis of Chapter 3 the $X(3915)$ was assigned to the $Z(3930)$ meson instead of the $Y(3940)$. The underlying structure is similar to the $Y(3940)$ since the $Z(3930)$ is interpreted as a dynamically generated $D^*\bar{D}^*$ state (see discussion in Chapter 3). The reason is that in the present approach, the strong hidden–charm and two–photon decay widths of the $Y(3940)$ are by a factor of about $3-4$ larger in comparison to the results in the dynamical picture. Therefore, a more precise study of the $X(3915)$ is required in order to clarify its identity with one of the nearby states $Y(3940)$ and $Z(3930)$.
At the same time the BELLE collaboration [71] also searched for the $Y(4140)$ in the two–photon process $\gamma\gamma \to J/\psi\phi$. In this framework they tested our prediction for the $Y(4140) \to \gamma\gamma$ decay width by experiment and obtained

$$\Gamma(Y(4140)\to\gamma\gamma)\,\mathrm{Br}(Y(4140)\to J/\psi\phi) < 40\ \mathrm{eV\ for}\ J^P = 0^+ \tag{4.119}$$

which results in a much smaller upper bound for the two-photon widths of about 0.2 keV. This finding is presently in conflict with a possible molecular interpretation of the $Y(4140)$ (see Eq. (4.113)).

Summary

A full interpretation of the $Y(3940)$ and $Y(4140)$ states requires:

1. an experimental determination of the J^{PC} quantum numbers, ii) a consistent and hopefully converging study of binding mechanisms in the $D^*_{(s)}\overline{D}^*_{(s)}$ systems

2. theory and experiment to consider the open charm decay modes, such as $D\bar{D}$, $D\bar{D}^*$, $D\bar{D}^*\gamma$, etc., which are also naturally fed in a charmonium picture.

Ultimately, only a full understanding of the decay patterns of the $Y(3940)$ and $Y(4140)$ can lead to a unique structure interpretation, yet present results clearly support the notion of the establishment of hadronic molecules in the meson spectrum.

4.3.2. Z(4430)

The experimental situation of the $Z^{\pm}$ was already discussed in Chapter 2 where one of the outstanding properties is the rather large hidden-charm decay width $Z^{\pm} \to \pi^{\pm}\psi'$ while the decay to the $\pi^{\pm}\psi$ channel is not observed. In the present work we reconsider and pursue a quantitative explanation of the hidden charm decay modes $Z^{\pm} \to \pi^{\pm}\psi$ and $\pi^{\pm}\psi'$ in the context of a molecular $D_1\bar{D}^*$ bound state interpretation [180]. In addition we determine the radiative decay width $Z^{\pm} \to \pi^{\pm}\gamma$ as a further key feature of the molecular idea. Since the $Z^{\pm}(4430)$ was observed in the $\psi'\pi^{\pm}$ final state, isospin and $G-$parity assignments are $I^G = 1^+$. If the $Z^{\pm}(4430)$ is a S-wave $D_1\overline{D}^*$ molecule the J^P quantum numbers are 0^-, 1^- or 2^-. Here we restrict the study to the 0^- and 1^- cases since $J^P = 2^-$ seems excluded by the small phase space in the $B \to Z^{\pm}K$ production process [90]. Two-body decays of the $Z^{\pm}$ were also analyzed in effective Lagrangian methods. The open charm decays $D^+\overline{D}^{*0}$, $D^{*+}\overline{D}^{0}$ and $D^{*+}\overline{D}^{*0}$ were studied in [72] and argued to be suppressed in the molecular interpretation while dominant for the tetraquark configuration. The hidden-charm decay modes was previously only investigated in the unpublished work of [76]. The results for the decay widths and in particular the possible suppression of J/ψ depends very much on form factors and the regularization in the loop diagrams. In the present study we assume the $Z^{\pm}$ to be a pure bound state of an axial $D_1^{(\prime)}$ and a vector D^* meson. In the charmed D meson spectrum two nearby P-wave excitations with $J^P = 1^{\pm}$ are expected. These two axial D_1 states can be identified with the $D_1(2420) \equiv D_1$ and the $D_1(2430) \equiv D_1'$. In the heavy quark limit the two degenerate 1^+ states are characterized by the angular momentum j_q of the light quark with $j_q = 3/2$ and $1/2$. While the strong decay $D_1(j_q = 3/2) \to D^*\pi$ proceeds by D-wave, the transition $D_1(j_q = 1/2) \to D^*\pi$ has a final S-wave. The state decaying via D-wave is narrow while the one decaying in an S-wave is expected to be broad. Since heavy-light mesons are not charge conjugation eigenstates the axial states can also be written as a superposition of the ${}^1P_1$ and ${}^3P_1$ configurations ($J = L$ and $S = 0$ or 1) with

$$\begin{aligned} \left|D_1\right\rangle &= \cos\phi \left|{}^1P_1\right\rangle + \sin\phi \left|{}^3P_1\right\rangle , \\ \left|D_1'\right\rangle &= -\sin\phi \left|{}^1P_1\right\rangle + \cos\phi \left|{}^3P_1\right\rangle . \end{aligned} \tag{4.120}$$

More detailed analyses [181, 182, 183] of the mixing scheme in terms of the total width indicate that the mixing angle has a value of about $\phi = \arctan\left(1/\sqrt{2}\right) \approx 35.3°$, the "magic" value expected from the heavy quark limit. With this phase

convention (alternatively one can use $\phi = -\arctan(\sqrt{2}) \approx -54.7°$) the D_1 state is identified with the narrow $D_1(2420)$ ($\Gamma \approx 20$ MeV [22]), while the broad $D_1(2430)$ ($\Gamma \approx 380$ MeV [22]) is connected to the D_1'. Since our aim is to study the $Z^\pm$ as a mesonic bound state containing a D_1 state the narrow $D_1(2420)$ with its long lifetime is more favorable than the broad $D_1(2430)$.

Following the convention discussed in [184, 90] the particle content of the isospin multiplet is given as:

$$\begin{aligned} \left|Z^+\right\rangle &= \frac{1}{\sqrt{2}}\left(\left|D_1^+ \overline{D}^{*\,0}\right\rangle + \left|\overline{D}_1^{\,0} D^{*\,+}\right\rangle\right), \\ \left|Z^0\right\rangle &= \frac{1}{2}\left(\left|D_1^+ D^{*\,-}\right\rangle - \left|D_1^0 \overline{D}^{*\,0}\right\rangle + \left|D_1^- D^{*\,+}\right\rangle - \left|\overline{D}_1^{\,0} D^{*\,0}\right\rangle\right), \\ \left|Z^-\right\rangle &= -\frac{1}{\sqrt{2}}\left(\left|D_1^0 D^{*\,-}\right\rangle + \left|D_1^- D^{*\,0}\right\rangle\right). \end{aligned} \tag{4.121}$$

In technical aspects we proceed in complete analogy to the previously discussed cases of $a_0/f_0(980)$, $Y(3940)$ and $Y(4140)$. First the meson bound state is set up by the effective interaction Lagrangian between the hadronic molecule and its constituent mesons. In case of $J^P = 0^-$ the Lagrangian reads

$$\begin{aligned} \mathcal{L}_{ZD_1D^*} =& \frac{g_{ZD_1D^*}}{\sqrt{2}} Z^-(x) \int dy\, \Phi(y^2) \times \\ & \times \left\{ D_1^{+\mu}(x_-) \overline{D}_\mu^{*\,0}(x_+) + \overline{D}_1^{\,0\mu}(x_-) D_\mu^{*\,+}(x_+) \right\} + \text{h.c.} \end{aligned} \tag{4.122}$$

with $x_\pm = x \pm \frac{y}{2}$. For $J^P = 1^-$ the respective Lagrangian $\mathcal{L}_{ZD_1D^*}$ is given by

$$\begin{aligned} \mathcal{L}_{ZD_1D^*} =& i\frac{g'_{ZD_1D^*}}{\sqrt{2}} \epsilon^{\alpha\beta\mu\nu} \partial_\mu Z_\nu^-(x) \int dy\, \Phi(y^2) \times \\ & \times \left\{ D_{1\,\alpha}^+(x_-) \overline{D}_\beta^{*\,0}(x_+) + \bar{D}_{1\,\alpha}^0(x_-) D_\beta^{*\,+}(x_+) \right\} + \text{h.c.} \end{aligned} \tag{4.123}$$

where the definitions of the parameters can be taken from Eq. (4.23). Again we deal with a Gaussian function in order to include the distribution of the constituents and we determine the size parameter Λ_Z in the physically meaningful region of a few GeV. In the present work we study finite size effects by varying Λ_Z in the range of $1.5 - 2.5$ GeV.

The coupling of Z to the virtual constituents, denoted by $g_{ZD_1D^*}$, is fixed by means of the compositeness condition [142, 185] (see also 4.4).

Values for the coupling constants in dependence on the binding energy ϵ are presented in Tab. 4.12. The binding energy is defined by the difference between the central value of the $Z^\pm$ mass and the lower threshold ($D_1^+ \overline{D}^{*\,0}$) with

$$m_{Z^+} = m_{D_1^+} + m_{\overline{D}^{*\,0}} - \epsilon\,. \tag{4.124}$$

Since the Z^+ mass lies close to the $(D_1^+\overline{D}^{*0})$ threshold at 4.43 GeV the values for ϵ are of a few MeV, we therefore vary ϵ between 1 and 10 MeV. The errors on the numerical results are due to variations of the model parameter Λ_Z from 1.5 to 2.5 GeV.

ϵ [MeV]	1	5	10
$g_{ZD_1D^*}$ $(J^P = 0^-)$	3.8 ± 0.1	5.6 ± 0.1	6.8 ± 0.2
$g'_{ZD_1D^*}$ $(J^P = 1^-)$	1.2 ± 0.1	1.8 ± 0.1	2.1 ± 0.1

Table 4.12.: Coupling constants $g_{ZD_1D^*}$ $(J^P = 0^-)$ and $g'_{ZD_1D^*}$ $(J^P = 1^-)$ in GeV for $\Lambda_Z = 1.5 - 2.5$ GeV and ϵ=1 − 10 MeV.

Radiative decay

Before we turn to the experimentally observed hidden–charm decay mode $Z^\pm \to J/\psi'\pi^\pm$ we concentrate on the radiative decay $Z^\pm \to \pi^\pm\gamma$ which can be more precisely determined than the strong decay modes since the couplings are well known. In analogy to the previously discussed hadronic molecules we include conventional vertices with photons coupling to the charged constituents. Additionally we also have to include the so-called contact vertices which arise due to the gauging of the nonlocal interaction Lagrangian $\mathcal{L}_{ZD_1D^*}$. The resulting diagrams contributing to the radiative decay are represented in Fig. 4.18. The interaction between the final pion

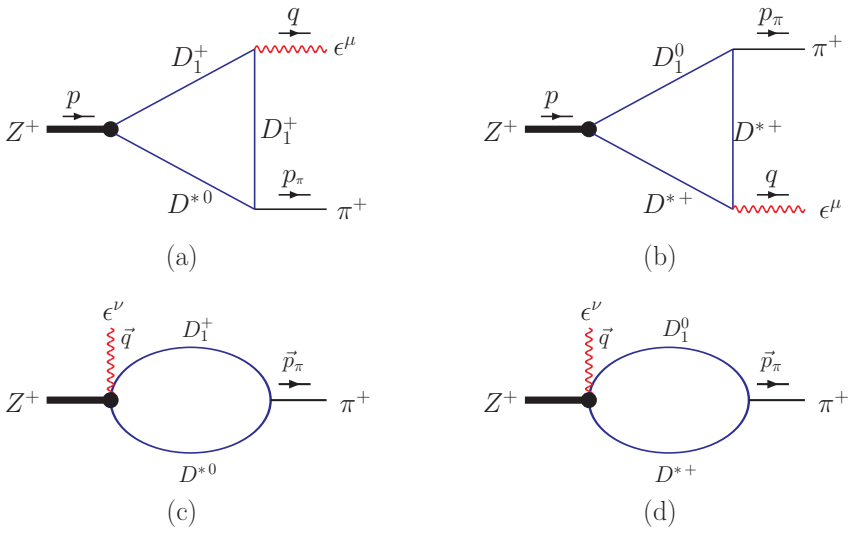

Figure 4.18.: Diagrams characterizing the radiative decay.

and the charmed mesons D_1, D^* in the loops is set up by the interaction Lagrangian

$$\mathcal{L}_{D_1 D^*\pi} = \frac{g_{D_1 D^*\pi}}{2\sqrt{2}} D_1^{\mu\nu}\, \vec{\pi}\cdot\vec{\tau}\, \overline{D}^*_{\mu\nu} + \text{h.c.}\,, \tag{4.125}$$

where $V^{\mu\nu} = \partial^\mu V^\nu - \partial^\nu V^\mu$ is the stress tensor of the vector mesons $V = \psi, D_1$ and D^*. The interaction vertex involving the $D_1(2420)$ meson should contain a dominant D-wave $D^*\pi$ coupling (see e.g. [181, 182, 186]) which leads to the two derivatives involved in the Lagrangian in Eq. (4.125). This dynamical selection rule, obtained in the heavy quark limit, also leads to the form of the Lagrangian (4.133) in case of the strong decays discussed in the next section. The coupling constant $g_{D_1 D^*\pi}$ is derived from the width of $D_1 \to D^*\pi$ which is the dominant decay mode of D_1. The partial decay width is expected to be around 20 MeV [183], where $\Gamma(D_1^0 \to D^{*+}\pi^-) = 2\,\Gamma(D_1^0 \to D^{*0}\pi^0)$. The decay width is set up as

$$\Gamma(D_1^0 \to D^{*+}\pi^-) = \frac{\lambda^{1/2}(m_{D_1}^2, m_{D^*}^2, m_\pi^2)}{16\pi\, m_{D_1}^3} \overline{\left|\mathcal{M}\right|^2}\,, \tag{4.126}$$

where $\lambda(a,b,c) = a^2 + b^2 + c^2 - 2ab - 2ac - 2bc$ denotes the Källen function and $\overline{\left|\mathcal{M}\right|^2} = 1/3 \sum_{\text{pol}} \left|\mathcal{M}\right|^2$ represents the spin-averaged transition amplitude squared. The effective D-wave interaction Lagrangian of Eq. (4.125) leads to the matrix element

$$\mathcal{M}^{\mu\nu}_{D_1^0 \to D^{*+}\pi^-} = g_{D_1 D^*\pi}\big(p_{D^*} p_{D_1} g^{\mu\nu} - p^\mu_{D^*} p^\nu_{D_1}\big)\,. \tag{4.127}$$

Hence, the decay width for a D-wave decay is of the form

$$\Gamma(D_1^0 \to D^{*+}\pi^-) = \frac{g^2_{D_1 D^*\pi}}{96\pi m^3_{D_1}} \lambda^{1/2}(m^2_{D_1}, m^2_{D^*}, m^2_\pi)\big(\lambda(m^2_{D_1}, m^2_{D^*}, m^2_\pi) + 6 m^2_{D_1} m^2_{D^*}\big)$$

with the resulting coupling $g_{D_1 D^*\pi} = 0.49$ GeV^{-1} for $\Gamma(D_1 \to D^*\pi) \approx$20 MeV.

An interesting feature is the fact that the radiative decay $Z^\pm \to \pi^\pm\gamma$ is forbidden in the case of $J^P = 0^-$ while allowed in case of the 1^- spin-parity of the $Z^\pm$. This selection rule becomes obvious when considering the matrix element with the general form

$$\mathcal{M}^\mu = F_1 q^\mu + F_2 p^\mu_\pi\,. \tag{4.128}$$

Terms proportional to the photon–momentum q^μ vanish because of the Lorentz gauge condition $\epsilon_\mu q^\mu = 0$. The remaining second part is not invariant under the substitution $p^\mu_\pi = p^\mu - q^\mu$ since again terms proportional to the photon four-momentum q^μ do not contribute to the transition.

The situation is different for the case of the vector quantum numbers 1^-. Now the

transition amplitude $\mathcal{M}^{\mu\nu}$ has the structure

$$\mathcal{M}^{\mu\nu} = e\, F_{Z\pi\gamma}(m_Z^2, m_\pi^2, 0)\, \epsilon^{\alpha\beta\mu\nu} p_\alpha q_\beta \,, \tag{4.129}$$

where $g_{Z\pi\gamma}$ is the effective coupling. It is related to the corresponding transition form factor $g_{Z\pi\gamma} \equiv F_{Z\pi\gamma}(m_Z^2, m_\pi^2, 0)$ evaluated via the loops of Fig. 4.18. Finally, in terms of the effective coupling $g_{Z\pi\gamma}$ the decay width $\Gamma(Z^\pm \to \pi^\pm\gamma)$ is given by

$$\Gamma(Z^\pm \to \pi^\pm\gamma) = \frac{\alpha}{24}\, g_{Z\pi\gamma}^2\, m_Z^3 \left(1 - \frac{m_\pi^2}{m_Z^2}\right)^3 \simeq \frac{\alpha}{24}\, g_{Z\pi\gamma}^2\, m_Z^3 \,. \tag{4.130}$$

We present the results for the decay properties in dependence on the binding energy ϵ to study the influence of the binding strength. Since the $Z^\pm$ mass is very close to threshold we vary the binding energy between 1-10 MeV. The results for the $\pi^\pm\gamma$ decay are indicated in Tab. 4.13. Here, the error bars refer to finite size effects since we vary Λ_Z from 1.5 to 2.5 GeV. The hadronic molecule model leads to rather sizable values for the radiative decay width of the order of 0.2 to 1.2 keV. In Tab. 4.13 the smaller value of each entry corresponds to $\Lambda_Z = 1.5$ GeV while the larger one is related to $\Lambda_Z = 2.5$ GeV (see also Ref. [180]).

ϵ [MeV]	1	5	10
$\Gamma_{Z^\pm\to\pi^\pm\gamma}$ [keV]	$0.3^{+0.2}_{-0.1}$	$0.6^{+0.3}_{-0.3}$	$0.8^{+0.4}_{-0.3}$

Table 4.13.: Decay widths $\Gamma_{Z^\pm\to\pi^\pm\gamma}$ in keV for $J^P = 1^-$ with $\epsilon = 1 - 10$ MeV and $\Lambda_Z = 1.5 - 2.5$ GeV.

Strong hidden-charm decays

The strong hidden-charm decays proceed in the meson molecule interpretation via open-charm meson loops which provides an opportunity to avoid the typical OZI suppression in the $c\bar{c}$ picture. Diagrammatically, the hidden-charm decay is represented by the two interfering diagrams of Fig. 4.19 which only differ in the D and D^* exchange and the corresponding couplings. To study the strong hidden-charm decays $Z^\pm \to \pi^\pm\psi^{(\prime)}$ we first set up the interaction between the final state and the constituent D_1 and D^* mesons. We use the effective Lagrangians

$$\mathcal{L}_{D^*D\pi} = \frac{g_{D^*D\pi}}{2\sqrt{2}}\, D_\mu^{*\dagger}\, \vec{\pi}\, \vec{\tau}\, i\overset{\leftrightarrow}{\partial^\mu} D + \text{h.c.}\,, \tag{4.131}$$

$$\mathcal{L}_{D^*D^*\psi} = i g_{D^*D^*\psi} \left(\psi^{\mu\nu} \overline{D}_\mu^* D_\nu^* + \psi^\mu \overline{D}^{*\nu} D_{\mu\nu}^* + \psi^\nu \overline{D}_{\mu\nu}^* D^{*\mu}\right), \tag{4.132}$$

$$\mathcal{L}_{D_1D\psi} = \frac{g_{D_1D\psi}}{2}\, D_1^{\mu\nu} \psi_{\mu\nu} D + \text{h.c.}\,. \tag{4.133}$$

While the coupling $g^{(\prime)}_{ZD_1D^*}$ to the initial hadronic molecule is determine by the compositeness condition of Eq. (4.4), the couplings to the final decay products have to be taken from other sources—data or theoretical predictions. The coupling $g_{D_1D^*\pi}$ was already determined from the D_1 decay width in the context of the radiative $Z^\pm \to \pi^\pm\gamma$ transition (4.125). Furthermore, the coupling strength $g_{D^*D\pi} = 17.9$ is also experimentally fixed by the $D^* \to D\pi$ decay. The couplings of the D^* mesons to the ψ and its radial excitation ψ' are estimated from heavy hadron chiral perturbation theory (HHChPT) [139, 171]. Within this framework the coupling to the ground state is given by $g_{D^*D^*J/\psi} \approx 8$ and the coupling constant $g_{D^*D^*\psi'}$ can be determined from the ratio $g_{\psi' D^*D^*}/g_{\psi D^*D^*} = m_{\psi'} f_\psi/(m_\psi f_{\psi'}) = 1.67$ [139, 171], where $f_{\psi^{(\prime)}}$ is the leptonic decay constant. The remaining couplings $g_{D_1D\psi}$ and $g_{D_1D\psi'}$

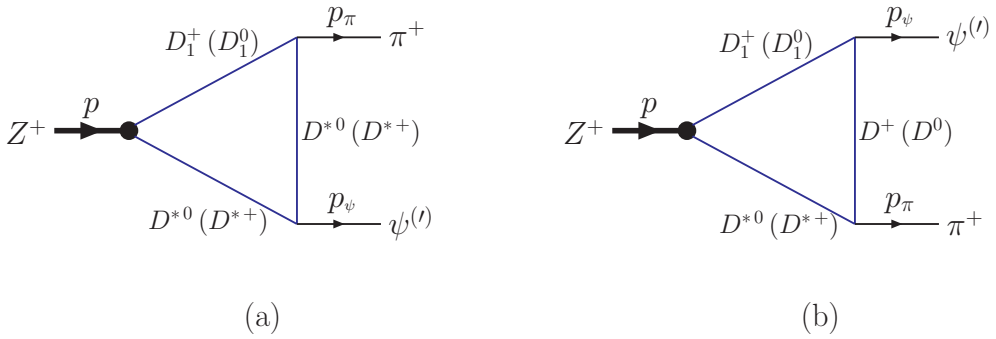

Figure 4.19.: The hidden-charm decay represented by Feynman diagrams.

of the diagram in Fig. 4.19 (b) are more difficult to estimate since neither data nor precise and reliable theoretical predictions are available. In a first step we relate the coupling between the final ψ and the intermediate D_1 and D mesons of the diagram on the right panel (Fig. 4.19 b) to the well-determined coupling $g_{D_1D^*\pi}$ of the left diagram. For this purpose we define the ratio $r_1 = g_{D_1D\psi}/g_{D_1D^*\pi} \approx 0.4 \pm 0.2$ which we estimate from the couplings $|g_{D_1D^*\pi}| \approx 72$ MeV and $|g_{D_1D\psi}| \approx 29$ MeV obtained by using the coupled channel model in [187]. We allow for the uncertainty of the model by including an error of 50%. By using the ratio r_1 and $g_{D_1D\pi} = 0.49$ GeV^{-1}, as defined above, we can give a rough estimate of $g_{D_1D\psi} \approx 0.2 \pm 0.1$ GeV^{-1}. The second task is the determination of the coupling of D_1D to the excited ψ'. We relate $g_{D_1D\psi'}$ to the previously estimated coupling $g_{D_1D\psi}$ by introducting the ratio $r_2 = g_{D_1D\psi'}/g_{D_1D\psi}$ which we esimate by using the $^3P_0$ model [188, 189]. Details of our calculation and a short introduction to the $^3P_0$ model can be found in the Appendix A.4. The advantage of computing $g_{D_1D\psi'}$ via the ratio r_2, in comparison to the direct calculation, is the reduced parameter dependence. In the $^3P_0$ model the couplings are proportional to the quark-antiquark-pair production strength α and are therefore rather sensitive to this parameter. Since in the $^3P_0$ model the $q\bar{q}$ creation parameter is assumed to be universal in for all transitions, this parameter cancels in case of ratios of couplings. We therefore only deal with the dependence on

the meson radii when computing the coupling ratio r_1. As a further positive aspect the ratio r_1 is characterized by very similar transitions $D_1 \to D\psi$ and $D_1 \to D\psi'$ where all particles involved remain the same except the replacement of ψ by ψ'. The ratio r_1 is therefore very stable with respect to variations of the meson radii. We find for the ratio of couplings $g_{D_1 D\psi'}/g_{D_1 D\psi}$ a value which is close to 2 and of the same order as the above mentioned ratio $g_{\psi' D^* D^*}/g_{\psi D^* D^*} = 1.67$. This hierarchy of couplings involving the ψ and ψ' charmonium states is consistent with the HHChPT scaling indicated above. Furthermore, we include uncertainties in the predictions of the $^3P_0$ model which for example might arise due to variations of the quark pair production amplitude (as e.g. discussed in [190]) which is usually fitted to data. In literature the quark-pair production strength ranges between 0.4 [181] to 0.5 [191]. We therefore consider an uncertainty of 50% in the ratio $r_2 = g_{D_1 D\psi'}/g_{D_1 D\psi} = 2 \pm 1$.

Provided that the $Z^\pm$ is a pseudoscalar with $J^P = 0^-$ the transition amplitude for the hidden charm decay mode can be expressed by two form factors $F_{1,2}$:

$$\mathcal{M}^\mu_{Z^\pm \to \pi^\pm \psi} = F_1(m_Z^2, m_\psi^2, m_\pi^2) p_\pi^\mu + F_2(m_Z^2, m_\psi^2, m_\pi^2) p_\psi^\mu \,. \tag{4.134}$$

Here only the first form factor contributes to the decay width $\Gamma(Z^\pm \to \pi^\pm \psi^{(\prime)})$:

$$\Gamma(Z^\pm \to \pi^\pm \psi^{(\prime)}) = \frac{\lambda^{1/2}}{16\pi m_Z^3} \overline{\left|\mathcal{M}\right|^2} = g_{Z_{\pi\psi}}^2 \frac{\lambda^{\frac{3}{2}}(m_Z^2, m_\psi^2, m_\pi^2)}{64\pi m_Z^3 m_\psi^2} \,, \tag{4.135}$$

where $g_{Z_{\pi\psi}} \equiv F_1(m_Z^2, m_\psi^2, m_\pi^2)$.

If we deal with a vector $Z^\pm$ the matrix element is given by

$$\mathcal{M}^{\mu\nu} \quad = \quad F_3(m_Z^2, m_\psi^2, m_\pi^2) \epsilon^{\alpha\beta\mu\nu} p_{\pi\,\alpha} p_\beta \tag{4.136}$$

and by analogy we use $g'_{Z\pi\psi} \equiv F_3(m_Z^2, m_\psi^2, m_\pi^2)$ in order to calculate the decay width

$$\Gamma(Z^\pm \to \pi^\pm \psi^{(\prime)}) = g'^2_{Z_{\pi\psi}} \frac{\lambda^{\frac{3}{2}}(m_Z^2, m_\psi^2, m_\pi^2)}{96\pi m_Z^3} \,. \tag{4.137}$$

Due to the the sizable $D^* D\pi$-coupling and the lighter D-meson mass (compared to D^* exchange) in the rescattering process, it becomes obvious that the diagram (b) of Fig. 4.19 dominates the transition amplitude. In fact, the ratio between diagram (a) and (b) can be about one order of magnitude depending on the size parameter and ratios r_1 and r_2. Therefore, in leading order the $Z^\pm \to \pi^\pm \psi^{(\prime)}$ transition can be regarded to be proportional to $g_{D_1 D\psi^{(\prime)}}$. As a consequence the decay widths are very sensitive to variations of the couplings $g_{D_1 D\psi^{(\prime)}}$ since it enters approximately quadratically in the decay widths.

In analogy to the radiative decay the results for the hidden-charm decays are presented in dependence on the binding energy of the hadronic molecule [180]. We have

to consider the relatively large uncertainties of the coupling constants. The decay properties of the $Z^{\pm}$ are studied for the full range of possible values of the couplings by indicating the decay properties in dependence on the ratios $r_1 = \frac{g_{D_1 D\psi}}{g_{D_1 D^*\pi}} = 0.4 \pm 0.2$ and $r_2 = \frac{g_{D_1 D\psi'}}{g_{D_1 D\psi}} = 2 \pm 1$. Under the assumption that we deal with a $J^P = 0^-$ state the decay widths for the hidden charm decay channels $Z \to \pi\psi$ and $Z \to \pi\psi'$ are given in Tab. 4.14. In case of the spin-parity quantum numbers 1^- the results are summarized in Tab. 4.15. In both tables the error bars indicate changes in the finite size with Λ_Z varied from 1.5 to 2.5 GeV.

	ϵ	$\Gamma_{Z\to\pi\psi}$	$\Gamma_{Z\to\pi\psi'}$			$R = \Gamma_{Z\to\pi\psi'}/\Gamma_{Z\to\pi\psi}$		
			$r_2 = 1$	$r_2 = 2$	$r_2 = 3$	$r_2 = 1$	$r_2 = 2$	$r_2 = 3$
$\frac{g_{D_1 D\psi}}{g_{D_1 D^*\pi}} = 0.2$	1	$0.2^{+0.1}_{-0.1}$	$0.1^{+0.0}_{-0.1}$	$0.3^{+0.1}_{-0.1}$	$0.8^{+0.2}_{-0.3}$	≈ 0.2	≈ 1.5	≈ 3.8
	5	$0.4^{+0.2}_{-0.2}$	$0.1^{+0.1}_{-0.0}$	0.6 ± 0.2	$1.5^{+0.4}_{-0.5}$	≈ 0.3	≈ 1.5	≈ 3.9
	10	$0.5^{+0.3}_{-0.2}$	$0.1^{+0.1}_{-0.0}$	$0.8^{+0.2}_{-0.3}$	$2.0^{+0.5}_{-0.6}$	≈ 0.3	≈ 1.5	≈ 3.7
$\frac{g_{D_1 D\psi}}{g_{D_1 D^*\pi}} = 0.4$	1	$0.9^{+0.3}_{-0.3}$	$0.3^{+0.1}_{-0.1}$	$1.5^{+0.4}_{-0.4}$	$3.5^{+0.9}_{-0.9}$	≈ 0.3	≈ 1.6	≈ 4.0
	5	$1.7^{+0.5}_{-0.6}$	$0.6^{+0.2}_{-0.2}$	$2.8^{+0.6}_{-0.8}$	$6.7^{+1.3}_{-1.7}$	≈ 0.3	≈ 1.7	≈ 4.0
	10	$2.3^{+0.7}_{-0.8}$	$0.8^{+0.2}_{-0.3}$	$3.7^{+0.8}_{-1.1}$	$8.7^{+1.8}_{-2.3}$	≈ 0.3	≈ 1.6	≈ 3.8
$\frac{g_{D_1 D\psi}}{g_{D_1 D^*\pi}} = 0.6$	1	$2.1^{+0.5}_{-0.7}$	$0.8^{+0.2}_{-0.3}$	$3.5^{+0.9}_{-0.9}$	$8.3^{+1.9}_{-2.0}$	≈ 0.4	≈ 1.7	≈ 4.0
	5	$3.9^{+1.2}_{-1.2}$	$1.5^{+0.4}_{-0.5}$	$6.7^{+1.3}_{-1.7}$	$15.6^{+2.8}_{-3.8}$	≈ 0.4	≈ 1.7	≈ 4.0
	10	$5.3^{+1.5}_{-1.7}$	$2.0^{+0.5}_{-0.6}$	$8.7^{+1.8}_{-2.3}$	$20.1^{+3.9}_{-4.9}$	≈ 0.4	≈ 1.6	≈ 3.8

Table 4.14.: Decay widths $\Gamma_{Z\to\psi^{(\prime)}\pi}$ in MeV for $J^P = 0^-$, $\Lambda_Z = 1.5 - 2.5$ GeV, $\epsilon = 1 - 10$ MeV and $r_2 = g_{D_1 D\psi'}/g_{D_1 D\psi} = 1 - 3$.

There are two experimental observations that limit the range of the coupling values, here represented by the ratios r_1 and r_2. First of all, the $Z^{\pm}$ is found in $\pi^{\pm}\psi'$ decay while there is no evidence for the kinematically favored $\pi^{\pm}\psi$ decay mode. This implies that the branching ratio $R = \Gamma_{Z\to\pi\psi'}/\Gamma_{Z\to\pi\psi}$ is expected to be much bigger than one. In the present meson molecule model the branching ratio R is given in the last three columns of Tabs. 4.14 and 4.15. R is obviously sensitive to the ratio r_2 relating the couplings of $D_1 D$ to ψ and ψ'. The lower limit $r_2 = 1$ can be immediately ruled out since in this case the ratio R is inverted compared to the experimental expectation.

The second condition is provided by the unexpectedly large $Z^{\pm} \to \pi^{\pm}\psi'$ hidden–charm decay width. In particular it is predicted to be bigger than 1 MeV [50] (see also discussion in Chapter 2.2.3). This fact disfavors values of r_1 smaller than 0.4.

	ϵ	$\Gamma_{Z\to\pi\psi}$	$\Gamma_{Z\to\pi\psi'}$			$R=\Gamma_{Z\to\pi\psi'}/\Gamma_{Z\to\pi\psi}$		
			$r_2=1$	$r_2=2$	$r_2=3$	$r_2=1$	$r_2=2$	$r_2=3$
$\frac{g_{D_1D\psi}}{g_{D_1D^*\pi}}=0.2$	1	0.1	0.1	$0.3^{+0.1}_{-0.1}$	$0.8^{+0.2}_{-0.1}$	≈ 0.8	≈ 5.5	≈ 14.0
	5	0.1	0.1	$0.6^{+0.0}_{-0.1}$	$1.5^{+0.2}_{-0.3}$	≈ 0.8	≈ 5.3	≈ 13.6
	10	0.1	0.1	$0.7^{+0.1}_{-0.1}$	$1.9^{+0.3}_{-0.4}$	≈ 0.8	≈ 5.2	≈ 13.6
$\frac{g_{D_1D\psi}}{g_{D_1D^*\pi}}=0.4$	1	$0.4^{+0.1}_{-0.1}$	$0.3-0.4$	$1.6^{+0.3}_{-0.4}$	$3.8^{+0.7}_{-0.8}$	≈ 0.7	≈ 3.5	≈ 8.3
	5	$0.8^{+0.2}_{-0.2}$	$0.6^{+0.1}_{-0.1}$	$2.9^{+0.4}_{-0.7}$	$6.9^{+1.0}_{-1.6}$	≈ 0.8	≈ 3.6	≈ 8.6
	10	$1.1^{+0.2}_{-0.3}$	$0.7^{+0.1}_{-0.1}$	$3.6^{+0.6}_{-0.7}$	$8.7^{+1.5}_{-1.9}$	≈ 0.6	≈ 3.3	≈ 7.9
$\frac{g_{D_1D\psi}}{g_{D_1D^*\pi}}=0.6$	1	$1.2^{+0.3}_{-0.3}$	$0.8^{+0.2}_{-0.1}$	$3.8^{+0.7}_{-0.8}$	$9.0^{+1.7}_{-2.1}$	≈ 0.7	≈ 3.1	≈ 7.4
	5	$2.3^{+0.4}_{-0.6}$	$1.5^{+0.2}_{-0.3}$	$6.9^{+1.0}_{-1.6}$	$16.2^{+2.6}_{-3.8}$	≈ 0.7	≈ 3.0	≈ 7.0
	10	$2.9^{+0.6}_{-0.8}$	$1.9^{+0.3}_{-0.4}$	$8.7^{+1.5}_{-1.9}$	$20.4^{+3.6}_{-4.5}$	≈ 0.7	≈ 3.0	≈ 7.0

Table 4.15.: Decay widths $\Gamma_{Z\to\psi^{(\prime)}\pi}$ in MeV for $J^P=1^-$, $\Lambda_Z=1.5-2.5$ GeV, $\epsilon=1-10$ MeV and $r_2=g_{D_1D\psi'}/g_{D_1D\psi}=1-3$.

If the ratio r_1 is relatively small as in the case of $r_1=0.2$ the decay width $\Gamma_{Z\to\pi\psi'}$ becomes smaller than one MeV, which seems excluded by observation.

In summary, the unusual decay pattern of the $Z^\pm$ meson can be explained by the meson molecule model in a certain window for the values of the couplings constants. For the quantum numbers $J^P=0^-$ the decay mode $Z\to\pi\psi$ is suppressed relative to $\pi\psi'$ by a factor ≈ 2 for $r_2=2$ and about 4 for $r_2=3$, respectively. In case of 1^- the ratio of decay rates $R=\Gamma(Z^\pm\to\pi^\pm\psi')/\Gamma(Z^\pm\to\pi^\pm\psi)$ is even larger with $R\approx 3$ for $r_2=2$ and $R\approx 8$ for $r_2=3$. This is at least qualitatively in line with the experimental observation that the $\pi^+\psi'$ decay mode dominates the $\pi^+\psi$ partial decay width. The ratio R is rather insensitive to variations of the model parameter Λ_Z and the binding energy ϵ as indicated in Tabs. 4.14 and 4.15 for $J^P=0^-$ and $J^P=1^-$. On the contrary, for equal couplings $g_{D_1D\psi'}$ and $g_{D_1D\psi}$, i.e. $r_2=1$, the branching ratio $R=\Gamma(Z^\pm\to\pi^\pm\psi')/\Gamma(Z^\pm\to\pi^\pm\psi)$ is smaller than one which presently is in contradiction with experimental observations.

Since the decay properties are not very sensitive to the choice of J^P, for $J^P=1^-$ the decay widths are only slightly smaller than for 0^-, the hidden-charm decay modes cannot be used to finally pin down the quantum numbers of the $Z^\pm$ without precise data.

The hidden-charm decays of the $Z^\pm$ are also discussed in the unpublished work of [76]. Here the $Z^\pm$ is studied within an effective model assuming a bound $D_1\bar{D}^*$ structure. There are two significant differences between this model and the present

approach. First of all, the kinematic background is different in Ref. [76] since the $Z^{\pm}$ is considered as a resonance above threshold while in the present work the $Z^{\pm}$ is bound (indicated by a positive binding energy ϵ) and is therefore below threshold. Second, in the present evaluation the contributions of the D^* and D rescattering processes represented in Fig. 4.19 are significantly different. In our case diagram 4.19 (b) is dominant because of the sizable coupling of the D^* meson to the $D\pi$ mode. On the contrary in [76] the diagram of Fig. 4.19 (b) is highly suppressed by a factor of about $15 - 30$ compared to the D^* exchange process, which was explained by the small $g_{D_1 D\psi}$ coupling. In this context it is important to remind that the prediction for $R = \Gamma(Z^{\pm} \to \pi^{\pm}\psi')/\Gamma(Z^{\pm} \to \pi^{\pm}\psi)$ primarily depends on the explicit values of the coupling $g_{D_1 D\psi^{(\prime)}}$ and therefore on the ratio $g_{D_1 D\psi'}/g_{D_1 D\psi}$, while variations of Λ_Z and ϵ only play a minor role. In comparison, in [76] sizable values for the ratio R are only obtained for small hidden charm decay widths.

Summary

In this section we studied hidden-charm and radiative decays of the $Z^{\pm}(4430)$ in a $D_1(2420)\overline{D}^*$+h.c. molecular structure interpretation. The peculiar decay properties of the meson bound state were analyzed in a effective model for hadronic bound systems by considering the influence of finite size effects and the dependence on the exact value of the binding energy. As guided by previous studies of possible binding mechanisms in this system we choose the preferred $J^P = 0^-$ and 1^- quantum numbers for the $Z^{\pm}$.

For the first time the radiative decay width $Z^+(4430) \to \pi^+\gamma$ is studied in the hadron molecule picture. This transition is forbidden for $J^P = 0^-$ and possibly can be used to determine the spin-parity quantum numbers of the $Z^{\pm}$. For a 1^- assignment of the $Z^{\pm}$ we obtain a radiative decay width of about 0.5 to 1 keV which should allow for a possible detection.

Besides the $Z^{\pm} \to \pi^{\pm}\gamma$ transition we also analyzed the hidden-charm decays which were the only transitions observed by experiment so far. As discussed previously, the hidden-charm decays are characterized by a number of strange properties which up to now are not fully explained by theoretical investigations. For example we analyzed the hidden charm decays $Z^{\pm} \to \pi^{\pm}\psi$, presently not observed, and $Z^{\pm} \to \pi^{\pm}\psi'$, the discovery mode of the $Z^{\pm}$. Both processes proceed in the meson molecule picture by loops containing open charm mesons, in particular by D^* or D rescattering processes. This formalism does not suffer from the typical OZI-suppression of hidden-charm modes as in the case of $c\bar{c}$ states and can reproduce the rather sizable $Z^{\pm} \to \pi^{\pm}\psi'$ decay width which according to experimental observations is expected to be above 1 MeV. The decay processes where analyzed for different values of the coupling constants. Since the D rescattering process is dominant, our predictions depend crucially on explicit values for the couplings $g_{D_1 D\psi^{(\prime)}}$. Concerning this issue we took guidance from a coupled channel analysis [94, 187] which essentially fixes $g_{D_1 D\psi}$ and

from the $^3P_0$ model estimating the ratio $r_2 = g_{D_1 D\psi'}/g_{D_1 D\psi}$. Finally we obtain a window for the coupling constants here expressed by the two ratios r_1 and r_2 for which we obtain a large branching ratio $R = \Gamma_{Z\to\pi\psi'}/\Gamma_{Z\to\pi\psi}$ which is in line with the non observation of the $\pi\psi$ mode. At the same time we can reproduce the $Z^\pm \to \pi^\pm\psi'$ decay width in the MeV range. For $J^P = 1^-$ the ratio R is slightly larger, but in general a sizable dependence of the predictions on the choice of J^P is not observed. Also, finite size effects are contained in the size parameter Λ_Z which was varied.
Present experimental observations suggest a $D_1\overline{D}^*$ bound state interpretation of the $Z^\pm(4430)$. From the theoretical side the present effective Lagrangian approach seems to confirm a dominant molecular structure of the $Z^\pm$ and is capable to explain at least the hidden charm decay properties. In addition we give predictions for the radiative decay mode $Z^\pm \to \pi^\pm\gamma$ which might offer a further test for the structure issue of the $Z^\pm$. A further evaluation of open charm decay modes does not seem to be decisive since predictions also depend crucially on principally unknown coupling constants [72]. In this respect the radiative mode $\pi^+\gamma$ offers a further test for the structure issue of the $Z^\pm$.
From the experimental side it is clear that the existence and, if possible, quantum numbers of the $Z^+(4430)$ still have to be firmly established. As long as the charged charmonium-like structures are not ruled out they remain an interesting object for future experiments e.g. the $Z^\pm$ could be studied in nucleon-antinucleon annihilation processes in the upcoming PANDA experiment [192].

4.4. Two–photon decay of heavy hadron molecules

The purpose of the present study is a more detailed discussion of the two-photon decays of heavy hadron molecules [193]. We want to work out the influence of the binding energy and the constituent meson masses on quantities like couplings (of the molecular state to its constituent mesons) and electromagnetic decay amplitudes. Under certain circumstances, as for a local theory, the results are analytical and the dependence on the above mentioned quantities can be shown explicitly. Especially ratios of two-photon decay rates of bound states, also in different flavor sectors, provide a simple and clear estimate whether a molecular structure is likely or not.
For the physical or nonlocal case, which effectively models finite size effects of hadronic molecules, results can deviate sizeably from the limiting case of a local theory. Here we find that the two-photon decay properties of heavy bound states are more sensitive to finite size effects than hadronic molecules of light mesons.
For the present study of two-photon decays of heavy meson molecules we concentrate on hadronic bound states in the meson sector. We further restrict to S-wave hadron molecules with quantum numbers $J^{PC} = 0^{++}$ whose constituents are pseudoscalar or scalar charmed/bottom mesons. The basis is again provided by the effective La-

grangian of Eq. (4.2) describing the interaction between the hadronic bound state and the constituents, where we again consider finite size effects by means of a Gaussian form factor $\Phi(k^2) = \exp(-k^2/\Lambda_{H_i}^2)$. Here, H_i denotes the hadronic molecule H composed of two equal mesons i. Further on we determine the coupling g_H by the compositeness condition.

In the following we first restrict to the case of a local coupling of the H state to its respective constituents. In case of a local interaction the vertex function is replaced by $\tilde{\Phi}_H(-k^2) = \exp(k^2/\Lambda_{H_i}^2) \equiv 1$. Then the coupling g_H can be expressed in the analytical form [26, 145]:

$$g_H^{-2} = \frac{1}{(8\pi m\zeta)^2}\left[\frac{\beta(\zeta)}{\sqrt{1-\zeta^2}} - 1\right], \tag{4.138}$$

where $\zeta = M/(2m)$, $\beta(\zeta) = \arcsin(\zeta)/\zeta$ and m is the mass of the constituent meson.

Inclusion of the electromagnetic interaction in a gauge invariant way is discussed in our previous works [26, 135]. In the local approximation we deal with the two diagrams (a) and (b) of Fig. 4.8 or 4.17. The extension to the nonlocal case leads to further diagrams, which need to be included in order to guarantee gauge invariance (see also Figs. 4.8 and 4.17).

The gauge invariant form of the matrix element for the radiative transition in case of real photons reads as:

$$M_{\mu\nu} = (g_{\mu\nu}q_1q_2 - q_{2\mu}q_{1\nu})\, g_{H\gamma\gamma}\,, \tag{4.139}$$

where q_1 and q_2 are the 4-momenta of the photons (see also Eq. (4.19)). For the local case the expression for the effective coupling constant $g_{H\gamma\gamma}$ is given by the simple form:

$$g_{H\gamma\gamma} = \frac{g_H}{(4\pi m\zeta)^2}\left[\beta^2(\zeta) - 1\right]. \tag{4.140}$$

However, this expression becomes more complicated and can only be solved numerically when including finite size effects (see e.g. Appendix of [26]). The radiative decay width of the 0^{++} molecule is calculated according to the formula

$$\Gamma(H \to \gamma\gamma) = \frac{\pi}{4}\alpha^2 M^3 g_{H\gamma\gamma}^2\,. \tag{4.141}$$

In the local limit we can write the decay width in terms of the quantity ζ by using Eq. (4.140)

$$\Gamma(H \to \gamma\gamma) = \frac{\alpha^2}{2\pi}\, m\, I(\zeta)\,, \tag{4.142}$$

with

$$I(\zeta) = \zeta\,\sqrt{1-\zeta^2}\,\frac{(\beta^2(\zeta)-1)^2}{\beta(\zeta)-\sqrt{1-\zeta^2}}\,. \tag{4.143}$$

Since in the case of hadronic bound states the binding energy ϵ is small in comparison to the masses of the constituent mesons m we can perform an expansion of g_H, $g_{H\gamma\gamma}$ and $\Gamma(H\to\gamma\gamma)$ in $x=\epsilon/(2m)$, where $\zeta = 1-x$. In order to guarantee an accurate approximation of the observables we need to include the leading (LO) and next-to-leading order (NLO) terms in the expansion of g_H and $g_{H\gamma\gamma}$. Therefore, the expansion of $\Gamma(H\to\gamma\gamma)$ includes three terms up to the next–to–next–to–leading order (NNLO) contribution.

The corresponding x–expansions of the quantities of interest are given by:

$$\begin{aligned} &g_H = m\,I_H(x)\,, \quad g_{H\gamma\gamma} = m^{-1}\,I_{H\gamma\gamma}(x)\,,\\ &\Gamma(H\to\gamma\gamma) = \left(\frac{\pi\alpha}{4}\right)^2 m\,J_{H\gamma\gamma}(x)\,, \end{aligned} \tag{4.144}$$

where

$$\begin{aligned} I_H(x) =& 8\sqrt{2\pi}\;(2x)^{1/4}\left(1+\frac{2}{\pi}\sqrt{2x}\right)+\mathcal{O}(x^{5/4})\,,\\ I_{H\gamma\gamma}(x) =& \frac{\sqrt{2\pi}}{8}\;(2x)^{1/4}\left(1-\frac{4}{\pi^2}-\frac{2}{\pi}\left(1+\frac{4}{\pi^2}\right)\sqrt{2x}\right)\\ &+\mathcal{O}(x^{5/4})\,,\\ J_{H\gamma\gamma}(x) =& \sqrt{2x}\left(\left(1-\frac{4}{\pi^2}\right)^2-\frac{4}{\pi}\left(1-\frac{16}{\pi^4}\right)\sqrt{2x}\right.\\ &\left.+2x\left(\frac{7}{8}+\frac{9}{\pi^2}-\frac{50}{\pi^4}+\frac{256}{\pi^6}\right)\right)+\mathcal{O}(x^2)\,. \end{aligned} \tag{4.145}$$

In the next step we consider bound states of the pseudoscalar D, D_s and B mesons which have the following structure

$$\begin{aligned} |H_D\rangle &= \frac{1}{\sqrt{2}}\big(|D^+D^-\rangle+|D^0\overline{D^0}\rangle\big)\,,\\ |H_{D_s}\rangle &= |D_s^+D_s^-\rangle\\ |H_B\rangle &= \frac{1}{\sqrt{2}}\big(|B^+B^-\rangle+|B^0\overline{B^0}\rangle\big)\,. \end{aligned} \tag{4.146}$$

Note, the existence of bound states of two heavy pseudoscalar mesons was proposed before in Ref. [95] where hadronic molecules are dynamically generated in a coupled channel formalism. Based on the identifications of Eq. (4.146) additional flavor

factors have to be considered in Eq. (4.144) which leads to:

$$\begin{aligned} g_{H_i} &= m_i\, I_H(x_i)\,, \quad g_{H_i\gamma\gamma} = \frac{c_{H_i\gamma\gamma}}{m_i}\, I_{H\gamma\gamma}(x_i)\,, \\ \Gamma(H_i \to \gamma\gamma) &= \left(\frac{\pi\alpha}{4}\right)^2 m_i\, c^2_{H_i\gamma\gamma}\, J_{H\gamma\gamma}(x_i)\,, \end{aligned} \tag{4.147}$$

where $x_i = \epsilon/(2m_i)$, $c_{H_i\gamma\gamma} = 1/\sqrt{2}$ for $i = D, B$ and 1 for $i = D_s$. From last equation follows the ratio of the two-photon widths of two different molecular states which is characterized by the respective constituent masses and binding energies. At leading order we deal with the simple expression:

$$\frac{\Gamma(H_B \to \gamma\gamma)}{\Gamma(H_D \to \gamma\gamma)} \sim \left(\frac{m_B\epsilon_B}{m_D\epsilon_D}\right)^{1/2}\,. \tag{4.148}$$

Varying the binding energy ϵ from 10 to 100 MeV which (besides the exception of the X(3872)) are typical values in the heavy meson sector, the two-photon decay widths are evaluated as

$$\begin{aligned} \Gamma(H_D \to \gamma\gamma) &= 0.25 - 1.19 \text{ keV}\,, \\ \Gamma(H_{D_s} \to \gamma\gamma) &= 1.31 - 2.58 \text{ keV}\,, \\ \Gamma(H_B \to \gamma\gamma) &= 1.19 - 2.78 \text{ keV}\,. \end{aligned} \tag{4.149}$$

Since $\Gamma(H_i \to \gamma\gamma) \propto \sqrt{m\epsilon}$ the smaller value of the binding energy also results in a smaller radiative decay width.

Up to now the results for the coupling and the two-photon decay widths were given in the local limit. For the physically appropriate description of an extended object, the hadronic molecule, finite size effects in terms of the vertex function have to be included. This will lead to a suppression of the couplings and the two-photon decay widths, hence the local case presents an upper limit for these quantities. In the following we study in addition to the influence of mass and binding energy the dependence on the size parameter Λ_{H_i}, which models the nonlocality.

The dependence of the couplings $g_{H_i\gamma\gamma}$ on the size parameter Λ_{H_i}, typically chosen in the range from 1 to 3 GeV, is illustrated in the logarithmic plots of Figs. 4.20 and 4.21 for different values of ϵ ranging from 10 to 100 MeV. For comparison we also include the coupling $g_{H_K\gamma\gamma}$ of $f_0(980)/a_0(980)$ to two photons with the well determined binding energy of $\epsilon = 7.35$ MeV. The local case, i.e. $\Lambda_{H_i} \to \infty$, characterizes the asymptotics of the curves. The convergence of the coupling $g_{H_i\gamma\gamma}$ towards the local or asymptotic value depends on the constituent meson masses. The coupling $g_{H_K\gamma\gamma}$ is almost stable with respect to variations of Λ_{H_i} near 1 GeV. The couplings of the heavy hadron molecules are more sensitive to finite size effects for values near $\Lambda_{H_i} \approx 1$ GeV, note that in Figs. 4.20 and 4.21 the dependence on

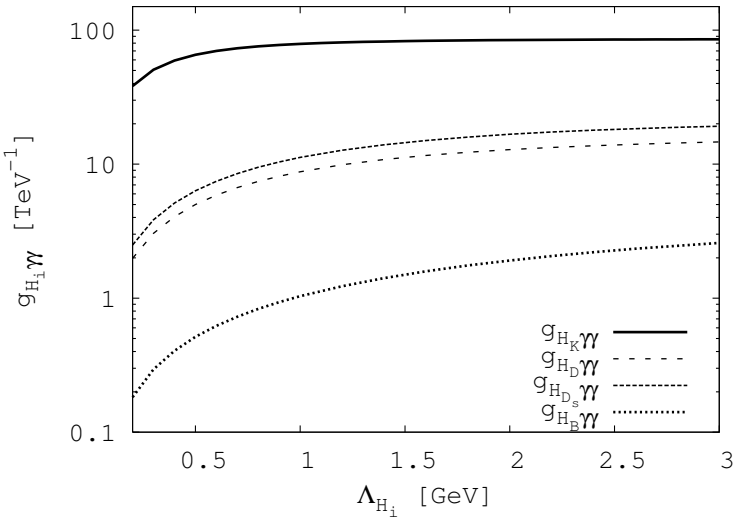

Figure 4.20.: Couplings $g_{H_K\gamma\gamma}$ and $g_{H_i\gamma\gamma}$ with $i = D, D_s, B$ in dependence on Λ_{H_i} for $\epsilon_K = 7.35$ MeV and $\epsilon_i = 10$ MeV.

Λ_{H_i} is displayed on a log scale. In fact, the coupling $g_{H_K\gamma\gamma}$ reaches 90% of the asymptotic value (local approximation) already at $\Lambda_{H_i} \approx 0.6$ GeV. In contrast, the couplings of heavy bound states approach 90% of the local value at around 4 GeV in case of the D and D_s–meson bound states and at about 9 GeV for the even heavier hidden-bottom molecule.

The behavior of the couplings $g_{H_i\gamma\gamma}$, which enter quadratically in the expression for the radiative decay width, shows that the suppression due to the size parameter Λ_{H_i} is larger in case of heavier constituents. Phenomenologically, the values for Λ_{H_i} tend to increase in case of heavy bound states. This behavior was already observed in earlier analyses in the framework of meson molecules [25, 171, 26] but also in case of baryons [138]. But still, for reasonable values of Λ_{H_i} heavier systems are strongly influenced by finite size effects as reflected in the two-photon coupling $g_{H_i\gamma\gamma}$.

In practice Λ_{H_i} should also depend in average on the binding energy. For instance, a small binding energy would lead to a loose bound state with a more extended structure than a strongly bound compact state. Therefore Λ_{H_i} should decrease with smaller binding energies, increasing the deviation from the local limit even more.

To quantify the inclusion of finite size effects for the two-photon decay widths we also give results for two values of Λ_{H_i}. For $\Lambda_{H_i} = 1$ GeV and $\epsilon = 10 - 100$ MeV we have [193]

$$\begin{aligned} \Gamma(H_D \to \gamma\gamma) &= 0.05 - 0.34 \text{ keV}\,, \\ \Gamma(H_{D_s} \to \gamma\gamma) &= 0.32 - 0.68 \text{ keV}\,, \\ \Gamma(H_B \to \gamma\gamma) &= 0.05 - 0.12 \text{ keV}\,. \end{aligned} \tag{4.150}$$

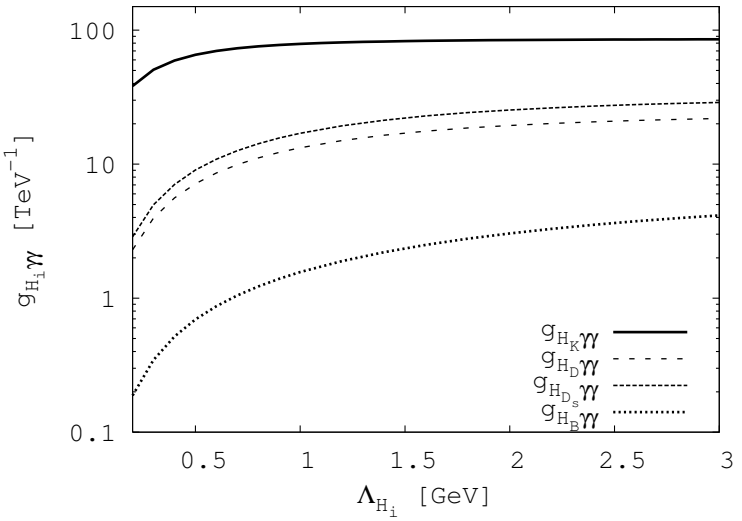

Figure 4.21.: Couplings $g_{H_K\gamma\gamma}$ and $g_{H_i\gamma\gamma}$ with $i = D, D_s, B$ in dependence on Λ_{H_i} for $\epsilon_K = 7.35$ MeV and $\epsilon_i = 100$ MeV.

When increasing Λ_{H_i} to 2 GeV the results are by a factor 2−3 larger

$$\begin{aligned} \Gamma(H_D \to \gamma\gamma) &= 0.13 - 0.73 \text{ keV}\,, \\ \Gamma(H_{D_s} \to \gamma\gamma) &= 0.71 - 1.52 \text{ keV}\,, \\ \Gamma(H_B \to \gamma\gamma) &= 0.18 - 0.44 \text{ keV}\,. \end{aligned} \tag{4.151}$$

These results should be compared to the local limits of Eq. (4.149).

From previous discussions it should be clear that finite-size effects are quite important for a quantitative determination of the radiative decay width of heavy hadron molecules. The same observation holds for molecular states composed of vector mesons [25], where we showed that for $\Lambda_{H_{D^*}} = \Lambda_{H_{D_s^*}} = 1 - 2$ GeV the radiative widths of the molecules $Y(3940) = \{D^* D^{*\dagger}\}$ and $Y(4140) = \{D_s^* D_s^{*\dagger}\}$ are of the order of 1 keV for $\Lambda_{H_i} = 2$ GeV.

For completeness, we compare the two-photon decays of the heavy systems to the one of the light scalars f_0/a_0. The stability of the coupling in case of a $K\bar{K}$ bound state already implies that the radiative decay width $\Gamma(f(980) \to \gamma\gamma)$ is not sensitive to the cutoff or finite-size effects provided Λ_{H_i} is above 0.5 GeV. Here we completely agree with the conclusions of Ref. [145]). In particular, in order to reproduce the current data on strong and radiative decays of $f(980)$ we fixed the cutoff parameter to the value $\Lambda_{H_K} \equiv \Lambda_f = 1$ GeV [26] with

$$\Gamma(f(980) \to \gamma\gamma) = 0.25 \text{ keV}\,, \tag{4.152}$$

a value which is very close to the result of the local approximation:

$$\Gamma(f(980) \to \gamma\gamma) = 0.29 \text{ keV} . \tag{4.153}$$

Similar results are obtained by the molecular approaches in [145] and [156]. However, for smaller values of $\Lambda_f < 0.6$ GeV the radiative decay width decreases which means that such small values of the cutoff parameter Λ_f are unlikely according to present data.

4.5. Quark–antiquark mesons

In the previous sections the effective Lagrangian approach was used to study bound states of mesons. In the following we apply this method to hadronic bound states on the quark level. In particular, we study mesons which are well established $q\bar{q}$ valence objects ranging from the light pseudoscalar and vector nonets to heavy–light and double–heavy quarkonia. In principle, we deal with the same problems as in the case of hadronic molecules. We simply replace the constituent meson fields by constituent quark fields. The resulting relativistic constituent quark model can be viewed as an effective quantum field approach to hadronic interactions which is based on an interaction Lagrangian of hadrons and their constituent quarks. For the description of the $q\bar{q}$ mesons we again use the compositeness condition where we set the field renormalization constant of the bound state (here the $q\bar{q}$ meson) to zero. The decays proceed via loops of the constituent quarks.
In analogy to bound states of mesons the present hadronic bound state approach includes finite size effects and full gauge invariance. However, we face one difficulty when dealing with quark–antiquark states. Except for the pion and sigma mesons all masses of the $q\bar{q}$ mesons are heavier than the masses of the two constituent quarks together. A problem arises if we deal with 'free' constituent quark propagators not containing confinement i.e. quark propagators with poles at the constituent quark mass. The evaluation of quark loops can lead to the appearance of threshold singularities corresponding to free quark production in the transition amplitudes. Therefore, the original application of the relativistic quark model is restricted to ground state mesons and baryons with masses less than the sum of the constituent quark masses and processes with relatively small energies.
The aim of the present work is to improve the relativistic approach and to extend its applicability to heavier mesons, i.e. to remove the above mentioned threshold restriction. Our ansatz to avoid the problem is contained in the description of the quark propagator. When dealing with excited hadron states the underlying quark propagators should reflect the confinement property. In quantum field theoretical approaches one can interpret confined quarks through the absence of quark poles and thresholds in Green's functions and matrix elements.
For example, in the Quark Confinement Model of Ref. [152] quark confinement was

implemented by assuming that, at low energies, the constituent quark interacts with some given nontrivial gluon configurations in the QCD vacuum. As a result quark Green's functions and matrix elements become free of quark poles. Models which are based on results obtained via QCD Dyson–Schwinger equations [194] possess the feature that quark propagation is described by fully dressed Schwinger functions. In summary dressing of the quarks removes the threshold problem which is somehow equivalent to working with confined quarks.

In the present work we propose a refinement of the model [135] by effectively implementing quark confinement into the model. Before we turn to the modifications of the model we introduce the basic method to study quark–antiquark mesons.

Similarly to the hadronic molecules the relativistic constituent quark model is based on an effective interaction Lagrangian describing the coupling of hadrons to their constituent quarks. Here we limit ourselves to the meson sector where mesons are described as quark–antiquark bound states. An extension of the model to baryons (three–quark states) and multiquark states is straightforward. The coupling of a meson $M(q_1\bar{q}_2)$ to its constituent quarks q_1 and $\bar{q}_2$ is described by the nonlocal Lagrangian

$$\mathcal{L}_{\rm int}^{\rm str}(x) = g_M M(x) \int dx_1 \int dx_2 \Phi(x, x_1, x_2)\, \bar{q}_1(x_1)\, \Gamma_M\, \lambda_M\, q_2(x_2) \,+\, \text{h.c.} \quad (4.154)$$

Here, λ_M and Γ_M are Gell–Mann and Dirac matrices chosen appropriately to describe the flavor and spin quantum numbers of the meson field $M(x)$. We set $\Gamma = \mathbb{1}$, γ^5, γ^μ, $\gamma^5\gamma^\mu$ when dealing with scalar, pseudoscalar, vector or axialvector mesons, respectively. In the case of pseudoscalar mesons we introduce singlet–octet mixing with a mixing angle of $\theta_P = -11^\circ$, while the vector mesons are assumed to be ideally mixed.

We include the vertex function Φ to allow for the distribution of the constituent quarks since mesons are not pointlike particles. For its Fourier transform $\widetilde{\Phi}(k^2) = \exp(-k^2/\Lambda^2)$ we choose a simple form in terms of a Gaussian function.

In previous works [135] for the quarks a free fermion propagator was taken

$$S_q(k) = \frac{1}{m_q - \not{k} - i\epsilon} \quad (4.155)$$

with an effective constituent quark mass m_q. Note that the fully dressed quark propagator takes the form

$$S_q(k) = \frac{Z(k^2)}{i\gamma_\mu k^\mu + M(k^2)} \quad (4.156)$$

in the framework of Dyson–Schwinger approaches (see e.g. Ref. [194]). As already mentioned the local form of the quark propagator leads to the appearance of thresh-

old singularities corresponding to free quark production which restricts the model to states which lie below the corresponding threshold of the constituents. Therefore, processes involving light vector mesons, e.g. the ρ and K^*, and excited states cannot be treated within the model. In the following we demonstrate how we implement confinement into our model in order to extend its application to the full range of $q\bar{q}$–mesons.
The implementation of confinement effects is demonstrated by means of the denominator of an arbitrary one–pole propagator. First of all, we represent the denominator by its Schwinger representation

$$\frac{1}{m^2 - p^2} = \int_0^\infty d\alpha \exp[-\alpha(m^2 - p^2)] \,. \tag{4.157}$$

The pole of this expression can be removed by introducing an upper integration limit $1/\lambda^2$. We call the parameter λ with mass dimension $[m]^{-1}$, the infrared confinement scale. By means of the cut–off one obtains an entire function which can be interpreted as a confined propagator

$$\int_0^{1/\lambda^2} d\alpha \exp[-\alpha(m^2 - p^2)] = \frac{1 - \exp[-(m^2 - p^2)/\lambda^2]}{m^2 - p^2} \,. \tag{4.158}$$

In general, singularities in the finite p^2–plane correspond to the mass of a free physical particle. Hence, the absence of poles indicates that one does not deal with a freely propagating particle and, therefore, it is confined.
Similar ideas have also been pursued in Refs. [195, 196] where an infrared cut–off has been introduced in the context of a Nambu–Jona–Lasinio model. Note that the propagator for a particle in a constant self–dual field has a form similar to Eq. (4.158). Such vacuum gluon configurations have been studied in [197] and were then employed e.g. in [198] to construct a model with confined constituent quarks. However, the use of confined propagators in the form of entire functions has its own difficulties. The convolution of entire functions leads to a rapid growth of physical matrix elements once the hadron masses and energies involved in the transition amplitude have been fixed. The numerical results become very sensitive to changes of the input parameters which requires extreme fine–tuning. For these reasons, we do not explicitly use confined propagators but we pursue an alternative approach which is introduced in the following.

4.5.1. Implementation of confinement

In the relativistic constituent quark model matrix elements are represented by a set of quark loop diagrams which are described by a convolution of the local quark

propagators and vertex functions. Using Schwinger's α–representation for each local quark propagator the loop momenta can be integrated out. One can write the resulting expression of the matrix element as an integral which includes integrations over the α–parameters and an integration over a scale variable t extending from zero to infinity. By introducing an infrared cutoff on the upper limit of the scale integration one can avoid the appearance of singularities in any matrix element. The new infrared cutoff parameter λ effectively introducing confinement will be taken to have a common value for all processes. We determine λ and the other parameters of the model by a fit to available experimental data.

First, we consider a general l–loop Feynman diagram with n propagators by using the Schwinger parameterization

$$\Pi(p_1,\ldots,p_n) = \int_0^\infty d^n\alpha \int [d^4k]^l \,\Phi\, \exp[-\sum_{i=1}^n \alpha_i(m_i^2 - p_i^2)] \tag{4.159}$$

where Φ stands for the numerator of the original product of propagators and vertex functions. After doing the loop integrations one obtains

$$\Pi = \int_0^\infty d^n\alpha\, F(\alpha_1,\ldots,\alpha_n)\,, \tag{4.160}$$

where F stands for the whole structure of a given diagram. The set of Schwinger parameters α_i can be expressed by an additional t–integration via the identity

$$1 = \int_0^\infty dt\, \delta(t - \sum_{i=1}^n \alpha_i) \tag{4.161}$$

leading to

$$\Pi = \int_0^\infty dt t^{n-1} \int_0^1 d^n\alpha\, \delta\Big(1 - \sum_{i=1}^n \alpha_i\Big)\, F(t\alpha_1,\ldots,t\alpha_n)\,. \tag{4.162}$$

As in Eq. (4.158) we set a cutoff for the upper limit of the integration at $1/\lambda^2$ and obtain

$$\Pi^c = \int_0^{1/\lambda^2} dt t^{n-1} \int_0^1 d^n\alpha\, \delta\Big(1 - \sum_{i=1}^n \alpha_i\Big)\, F(t\alpha_1,\ldots,t\alpha_n)\,. \tag{4.163}$$

By introducing the infrared cutoff all possible thresholds in the quark loop diagram

are removed, where the cutoff parameter λ is uniquely determined for all physical processes.

As a first application of the infrared confinement effect we consider the expression for the mass operator which we need for the compositeness condition:

$$\Pi_2(p^2) = \int \frac{d^4k}{\pi^2} \Phi^2(-k^2) \frac{N(p)}{[m^2 - (k + \frac{1}{2}p)^2][m^2 - (k - \frac{1}{2}p)^2]} \,. \tag{4.164}$$

Here p is the momentum of the meson and $N(p)$ is the numerator of the expression which we drop in the following for the sake of readability. By carrying out the loop integration one obtains

$$\Pi_2(p^2) = \int\limits_0^\infty dt \frac{t}{(s+t)^2} \int\limits_0^1 d\alpha \, \exp\Big\{ - t[m^2 - \alpha(1-\alpha)p^2] + \frac{st}{s+t}\Big(\alpha - \frac{1}{2}\Big)^2 p^2 \Big\} \,.$$

The integral $\Pi_2(p^2)$ can be seen to have a branch point at $p^2 = 4m^2$. By introducing a cutoff on the t–integration one obtains

$$\Pi_2^c(p^2) = \int\limits_0^{1/\lambda^2} dt \frac{t}{(s+t)^2} \int\limits_0^1 d\alpha \, \exp\Big\{ - t[m^2 - \alpha(1-\alpha)p^2] + \frac{st}{s+t}\Big(\alpha - \frac{1}{2}\Big)^2 p^2 \Big\} \,,$$

where the two–point function $\Pi_2^c(p^2)$ is free of singularities.

In our approach such a confinement scenario can be realized with only minor changes by shifting the upper t–integration limit from infinity to $1/\lambda^2$. The confinement scenario also allows to include all possible excited states in our calculations. The first calculations performed in this work show that the limited set of adjustable parameters of the model (size parameters, constituent quark masses and the confinement scale λ) leads to a consistent description of a large number of low–energy mesonic processes. We envisage a multitude of further applications as e.g. in the baryon sector.

The coupling constant g_M in Eq. (4.154) is, as in the case of hadronic molecules, determined by the compositeness condition:

$$Z_M = 1 - \Pi_M'(m_M^2) = 0 \,. \tag{4.165}$$

Here it is important to note that the alpha–parameterization including the introduction of the cutoff $1/\lambda^2$ does not commute with taking the derivative of the mass operator. Therefore, by determining the coupling constants via the compositeness condition, the derivative has to be carried out before doing the manipulations on the momentum integration. The meson–quark coupling constants are then determined from the compositeness condition Eq. (4.165). This requires the evaluation of the

derivative of the mass operator. For the pseudoscalar and vector mesons treated in this paper the derivatives of the mass operators read

$$\begin{aligned}
\Pi'_P(p^2) &= \frac{g_M^2}{2p^2} p^\alpha \frac{d}{dp^\alpha} N_c \int \frac{d^4k}{(2\pi)^4 i} \Phi_P^2(-k^2) \mathrm{tr}\Big[\gamma^5 S_1(k+w_1 p)\gamma^5 S_2(k-w_2 p)\Big] \\
&= g_M^2 \frac{N_c}{2p^2} \int \frac{d^4k}{(2\pi)^4 i} \Phi_P^2(-k^2) \qquad (4.166) \\
&\quad \times \mathrm{tr}\Big[\gamma^5 S_1(k+w_1 p)\, w_1 \not{p}\, S_1(k+w_1 p)\gamma^5 S_2(k-w_2 p)\Big] + (m_1 \leftrightarrow m_2), \\
\Pi'_V(p^2) &= g_M^2 \frac{1}{3}\Big[g^{\mu\nu} - \frac{p^\mu p^\nu}{p^2}\Big] \frac{1}{2p^2} p^\alpha \frac{d}{dp^\alpha} N_c \int \frac{d^4k}{(2\pi)^4 i} \Phi_V^2(-k^2) \\
&\quad \times \mathrm{tr}\Big[\gamma^\mu S_1(k+w_1 p)\gamma^\nu S_2(k-w_2 p)\Big] \qquad (4.167) \\
&= g_M^2 \frac{1}{3}\Big[g^{\mu\nu} - \frac{p^\mu p^\nu}{p^2}\Big] \frac{N_c}{2p^2} \int \frac{d^4k}{(2\pi)^4 i} \Phi_V^2(-k^2) \\
&\times \mathrm{tr}\Big[\gamma^\mu S_1(k+w_1 p)\, w_1 \not{p}\, S_1(k+w_1 p)\gamma^\nu S_2(k-w_2 p)\Big] + (m_1 \leftrightarrow m_2).
\end{aligned}$$

Because of the the p^μ–derivative Eqs.(4.166,4.168) contain three propagator factors.

4.5.2. Inclusion of the electromagnetic interaction

The interaction with the electromagnetic field is introduced in analogy to the previously discussed meson bound states in two stages. First, the free Lagrangian of quarks and charged hadrons $M^\pm$ is gauged in the standard manner by using minimal substitution:

$$\partial^\mu M^\pm \to (\partial^\mu \mp ieA^\mu)M^\pm, \quad \partial^\mu q \to (\partial^\mu - ie_q A^\mu)q, \quad \partial^\mu \bar{q} \to (\partial^\mu + ie_q A^\mu)\bar{q}, \quad (4.168)$$

where e is the positron (or proton) charge and e_q represents the quark charges ($e_u = \frac{2}{3}e$, $e_d = -\frac{1}{3}e$, etc.). Minimal substitution leads to the first part of the electromagnetic interaction Lagrangian

$$\begin{aligned}
\mathcal{L}_{\rm int}^{\rm em(1)}(x) &= \sum_q e_q\, A_\mu(x)\, J_q^\mu(x) + e\, A_\mu(x)\, J_M^\mu(x) + e^2 A^2(x) M^-(x) M^+(x)\,, \\
J_q^\mu(x) &= \bar{q}(x)\gamma^\mu q(x), \qquad (4.169) \\
J_M^\mu(x) &= i\Big(M^-(x)\partial^\mu M^+(x) - M^+(x)\partial^\mu M^-(x)\Big).
\end{aligned}$$

In the second step we also gauge the non–local strong interaction Lagrangian in

Eq. (4.2) and proceed in the same way as discussed in the previous sections (see also [143]) by multiplying each quark field $q(x_i)$ in $\mathcal{L}_{\rm int}^{\rm str}$ with a gauge field exponential according to

$$\begin{aligned}\mathcal{L}_{\rm int}^{\rm str}(x) =& g_M M(x) \int dx_1 \int dx_2 F_M(x, x_1, x_2) \\ & \times \bar{q}_1(x_1)\, e^{ie_{q_1} I(x_1,x,P)}\, \Gamma_M\, \lambda_M\, e^{-ie_{q_2} I(x_2,x,P)}\, q_2(x_1), \end{aligned} \tag{4.170}$$

where

$$I(x_i, x, P) = \int_x^{x_i} dz_\mu A^\mu(z). \tag{4.171}$$

In analogy to the meson molecules these interaction term lead to further interaction vertices with photon lines directly attached to the meson–quark–antiquark vertex. Due to this procedure the full Lagrangian is invariant under the local gauge transformations

$$q_i(x) \to e^{ie_{q_i} f(x)} q_i(x), \qquad \bar{q}_i(x) \to \bar{q}_i(x) e^{-ie_{q_i} f(x)}, \tag{4.172}$$

$$M(x) \to e^{ie_M f(x)} M(x)\,, \qquad A^\mu(x) \to A^\mu(x) + \partial^\mu f(x)\,, \tag{4.173}$$

where $e_M = e_{q_2} - e_{q_1}$ is the electric charge of the meson.
The second term of the electromagnetic interaction Lagrangian $\mathcal{L}_{\rm int;2}^{em}$ arises when one expands the gauge exponential in powers of A_μ up to the order of perturbation theory considered.
For example, expanding the Lagrangian Eq. (4.170) up to the first order in A^μ one obtains ($l = w_1 p_1 + w_2 p_2$)

$$\mathcal{L}_{\rm int}^{\rm em(2)}(x) = g_M M(x) \int dx_1 \int dx_2 \int dy\, E_M^\mu(x, x_1, x_2, y)\, A_\mu(y)\, \bar{q}_1(x_1) \Gamma_M \lambda_M q_2(x_2)\,,$$

$$E_M^\mu(x, x_1, x_2, y) = \int \frac{dp_1}{(2\pi)^4} \int \frac{dp_2}{(2\pi)^4} \int \frac{dq}{(2\pi)^4} e^{ip_1(x_1-x) - ip_2(x_2-x) + iq(y-x)} E_1^\mu(p_1, p_2, q)\,,$$

$$\begin{aligned} E_1^\mu(p_1, p_2, q) &= -e_{q_1} w_1 (w_1 q^\mu + 2l^\mu) \int_0^1 dt \Phi'_H \left(-t(w_1 q + l)^2 - (1-t) l^2\right) \\ &+ e_{q_2} w_2 (w_2 q^\mu - 2l^\mu) \int_0^1 dt \Phi'_M \left(-t(w_2 q - l)^2 - (1-t) l^2\right)\,, \end{aligned}$$

At this stage we are able to compute the electromagnetic form factor $\Lambda^\mu(p, p')$ described by the diagrams shown in Fig. 4.22, which is closely connected to the Ward

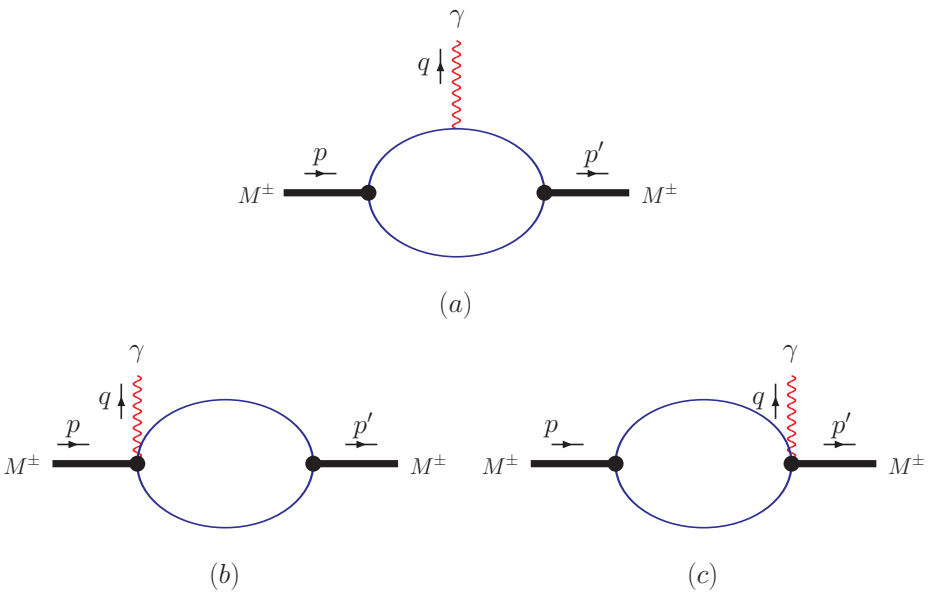

Figure 4.22.: Diagrams describing the electromagnetic meson vertex function.

identity. The Ward identity relates the electromagnetic vertex function at zero momentum transfer to the derivative of the mass operator for an on–mass–shell particle by

$$q^\mu \Lambda_\mu(p,p') = \Pi(p') - \Pi(p) \tag{4.174}$$

$$\Lambda^\mu(p,p) = \frac{d}{dp_\mu}\Pi(p^2) = 2p^\mu \frac{d}{dp^2}\Pi(p^2)\,. \tag{4.175}$$

4.6. Basic properties of π and ρ mesons

In a first step, we apply the relativistic constituent quark model including infrared confinement to the decays of the π and ρ mesons. The available data on the leptonic constants f_π, $g_{\rho\gamma}$ and the electromagnetic couplings $g_{\pi\gamma\gamma}$ and $g_{\rho\pi\gamma}$ allows us to fit the model parameters which are the constituent quark mass $m \equiv m_{u(d)}$, the size parameters Λ_π and Λ_ρ, and the scale parameter λ characterizing the infrared confinement.

The quark model diagrams for the leptonic decay constant and the vector–photon transition $g_{\rho\gamma}$ are illustrated in Fig. 4.23. The corresponding one-loop Feynman

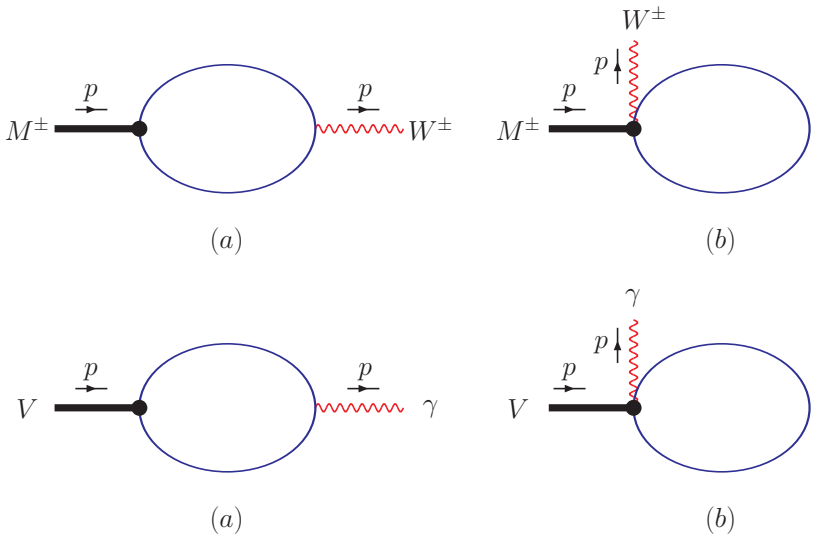

Figure 4.23.: Diagrams describing the $M^\pm \to W^\pm$ (upper panel) and $V \to \gamma$ (lower panel) transitions.

integrals read:

$$f_\pi\, p^\mu = N_c g_\pi \int \frac{d^4k}{(2\pi)^4 i} \Big\{ \Phi_\pi(-k^2)\, \mathrm{tr}\Big[O^\mu S(k+\tfrac{1}{2}\,p)\gamma^5 S(k-\tfrac{1}{2}\,p)\Big] + \int_0^1 d\alpha \Phi'_\pi(-z_\alpha)(2\,k+\tfrac{1}{2}\,p)^\mu \mathrm{tr}\Big[S(k)\Big]\Big\}, \tag{4.176}$$

$$g_{\rho\gamma}\left(g^{\mu\nu}p^2 - p^\mu p^\nu\right) = \frac{N_c g_\rho}{\sqrt{2}} \int \frac{d^4k}{(2\pi)^4 i} \Big\{ \Phi_\rho(-k^2)\, \mathrm{tr}\Big[\gamma^\mu S(k+\tfrac{1}{2}\,p)\gamma^\nu S(k-\tfrac{1}{2}\,p)\Big] - \int_0^1 d\alpha \Phi'_\rho(-z_\alpha)(2\,k+\tfrac{1}{2}\,p)^\mu \mathrm{tr}\Big[\gamma^\nu S(k)\Big]\Big\}, \tag{4.177}$$

with $z_\alpha = \alpha(k+\frac{1}{2}\,p)^2 + (1-\alpha)k^2$, $N_c = 3$ is the number of colors and $O^\mu = \gamma^\mu(\mathbb{1}-\gamma^5)$ is the left–chiral weak coupling matrix. In Appendix A.5 it is explicitly shown that the vector meson–photon transition fulfills gauge invariance.

The photon decays of pseudoscalar ($P \to \gamma\gamma$) and vector mesons ($V \to P\gamma$) are diagrammatically illustrated in Fig. 4.24. The respective expressions for the quark

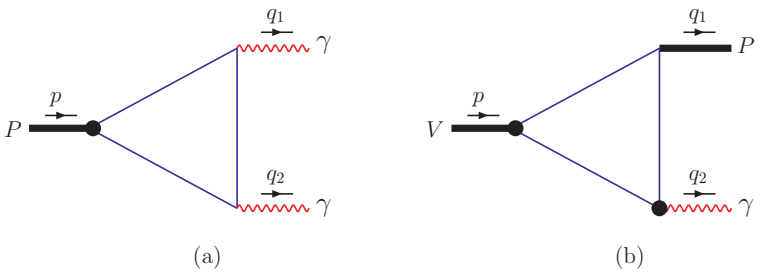

Figure 4.24.: Diagrams describing $P \to \gamma\gamma$ and $V \to P\gamma$ transitions.

loops are given by

$$g_{\pi\gamma\gamma}\,\epsilon^{\mu\nu} = \frac{\sqrt{2}N_c}{3}\int\frac{d^4k}{(2\pi)^4 i}\Phi_\pi(-k^2) \times \mathrm{tr}\left[i\gamma^5 S(k+\tfrac{1}{2}\,p)\gamma^\mu S(k-\tfrac{1}{2}\,p)\gamma^\nu S(k+\tfrac{1}{2}\,p-q_1)\right], \tag{4.178}$$

$$g_{\rho\pi\gamma}\,\epsilon^{\mu\nu} = \frac{N_c g_\rho g_\pi}{3}\int\frac{d^4k}{(2\pi)^4 i}\Phi_\rho(-k^2)\Phi_\pi\Big(-(k+\tfrac{1}{2}\,q_2)^2\Big) \times \mathrm{tr}\left[i\gamma^5 S(k+\tfrac{1}{2}\,p)\gamma^\mu S(k-\tfrac{1}{2}\,p)\gamma^\nu S(k+\tfrac{1}{2}\,p-q_1)\right]. \tag{4.179}$$

The evaluation of the one–loop integrals of Eqs.(4.176)–(4.179) and Eqs.(4.166) and (4.168) is described in Appendix A.6.
A least square fit to the observables yields the fit parameters:

m	Λ_π	Λ_ρ	λ	
0.217	0.711	0.295	0.181	GeV

. (4.180)

Here we deal with the constituent quark mass while the cutoff parameters Λ deviate from the natural scale around 1-2 GeV (see [135]) due to the introduction of the universal cutoff λ. The fitted value of the confinement scale parameter λ is very close to $\Lambda_{\rm QCD}$. In Tab. 4.16 we compare the results of the fit with available experimental data.
As a further application of our approach, now free of parameters, we calculate the pion electromagnetic form factor F_π generated by the diagrams in Fig. 4.22, and the pion transition form factor $F_{\pi\gamma\gamma^*}$ generated by the diagram in Fig. 4.24 (a). In the first case we are interested in the space–like region $q^2 = -Q^2$. In the second case one photon is on–mass–shell $q_1^2 = 0$ and the second photon has a space–like momentum squared $q_2^2 = -Q^2$. The electromagnetic radii are related to the slope of the form factors at the origin $r^2 = -6F'(0)$. Our result for the electromagnetic radius $r_\pi = 0.612$ fm is in good agreement with the present world average data of $r_\pi = (0.672 \pm 0.008)$ fm [174]. The result for the radius of the transition form factor

Quantity	Our	Data [174]
f_π, MeV	130.2	$130.4 \pm 0.04 \pm 0.2$
$g_{\pi\gamma\gamma}$, GeV^{-1}	0.23	0.276
$g_{\rho\gamma}$	0.2	0.2
$g_{\rho\pi\gamma}$, GeV^{-1}	0.75	0.723 ± 0.037

Table 4.16.: Basic properties of the π and ρ meson.

$r^2_{\pi\gamma} = 0.315$ fm^2 confirms the monopole–type approximation of the CLEO data [199] and is close to the CELLO measurement [200] of $r^2_{\pi\gamma} = 0.42 \pm 0.04$ fm^2.

The electromagnetic pion transition form factor is displayed in Fig. 4.25 and compared with data from the DESY [201], the Jefferson Lab F_π Collaboration [202] and the CERN NA7 Collaboration [203].

In Fig. 4.26 we display the $F_{\pi\gamma\gamma^*}(Q^2)$ form factor in the space–like region Q^2 up to 4 GeV^2. Here the slopes of the theoretical curves are quite sensitive to variations of the size parameter Λ_π. In order to exhibit the sensitivity to Λ_π we plot three curves for $\Lambda_\pi = 0.711, 1$ and 1.3 GeV.

One should mention that our $F_{\pi\gamma\gamma^*}(Q^2)$ form factor behaves as $1/Q^2$ at large Q^2 in accordance with perturbative QCD. The calculated form factor behavior disagrees with the new data above 4 GeV^2 presented by the BABAR Collaboration [204]. For a recent theoretical analysis of the BABAR data, see e.g. Ref. [205].

4.7. An extension to strange, charm and bottom flavors

In this subsection we extend our approach to mesons containing strange, charm and bottom quarks. We accordingly have to introduce further model parameters which are the values of constituent quark masses m_q ($q = s, c, b$) and the values of the size parameters Λ_M for the corresponding mesons indicated in Tab. 4.17. In contrast, the value of the confinement scale parameter λ remains the same for all physical processes. To determine the parameters we perform a least square fit to the weak and electromagnetic leptonic decay constants defined by $f_V = m_V g_{V\gamma}$ (see Tabs. 4.18 and 4.19). The dimensionless constant $g_{V\gamma}$ was previously introduced in

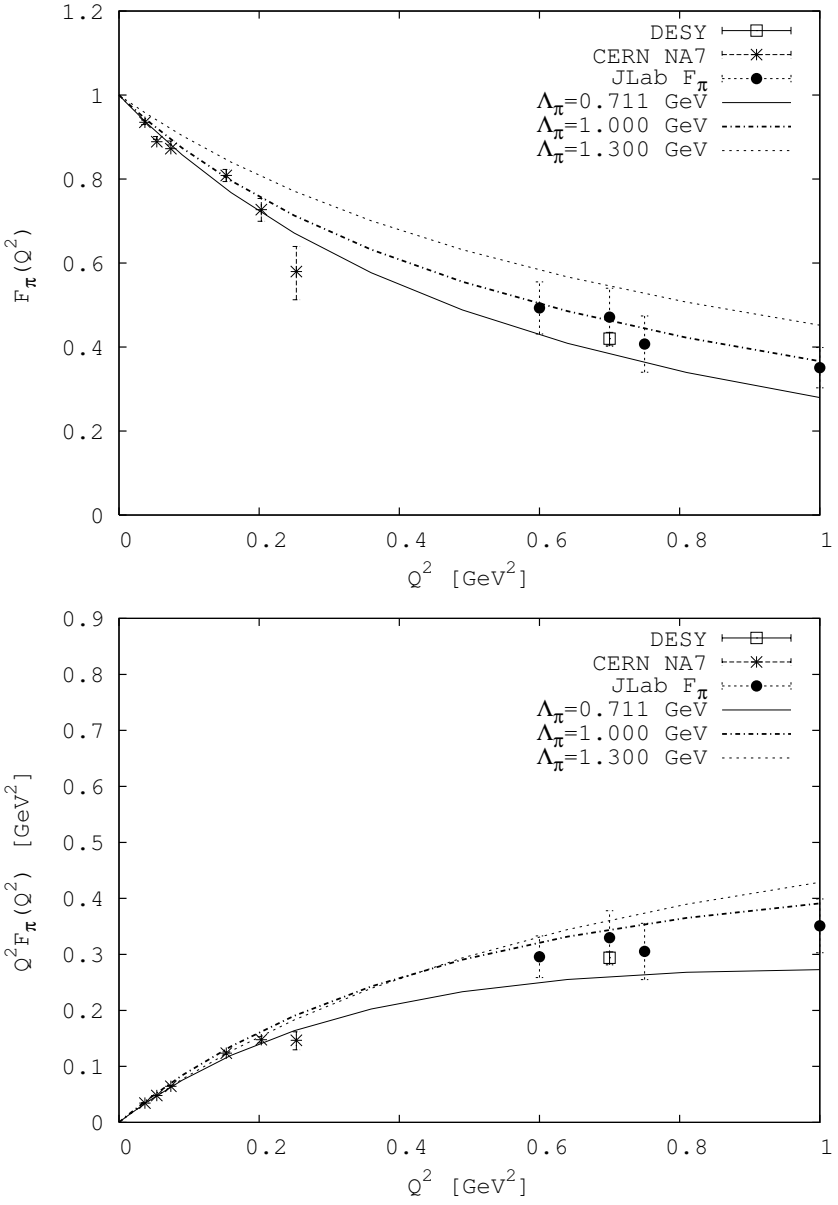

Figure 4.25.: Form factor $\pi^\pm \to \pi^\pm\gamma^*$ as a function of the space–like photon momentum Q^2. Data is taken from the JLAB F_π Collaboration [202], DESY [201] and CERN NA7 Collaboration [203].

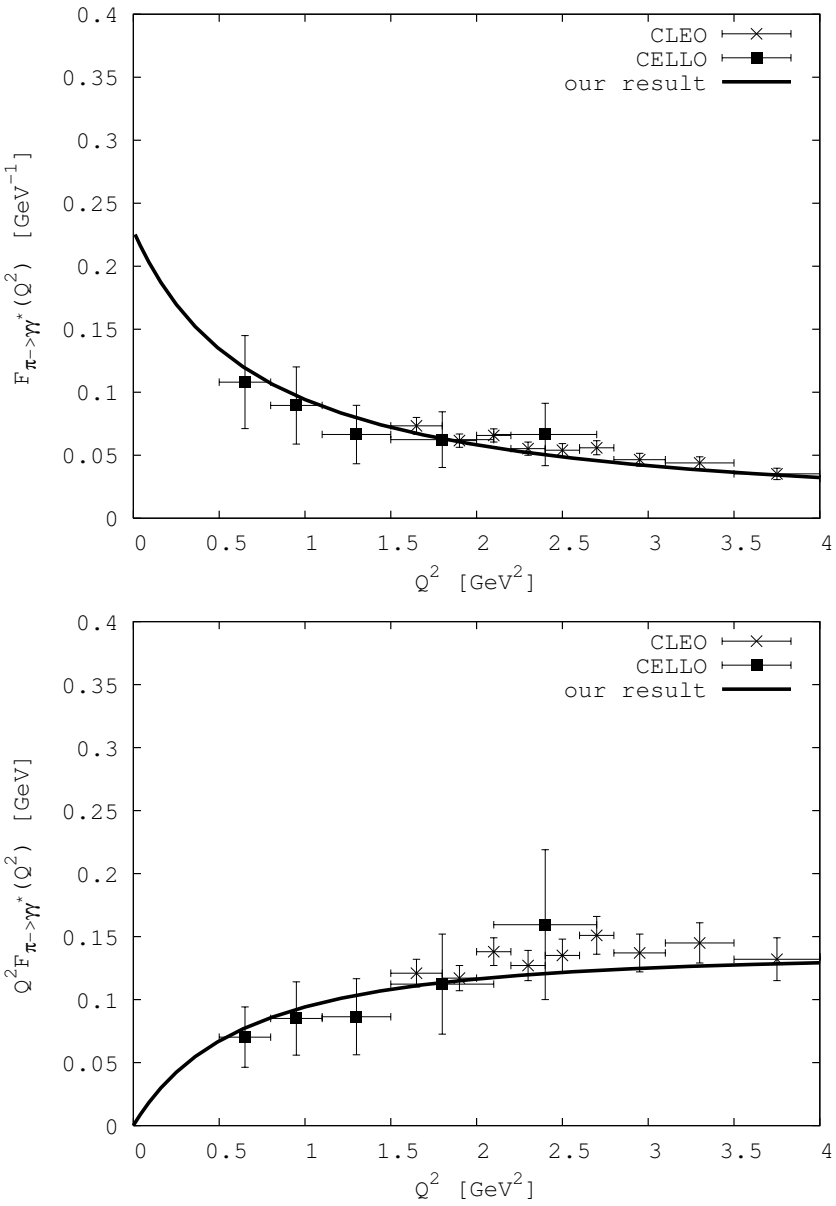

Figure 4.26.: Form factor $\gamma\gamma^* \to \pi^0$ as function of the space–like photon momentum Q^2. Data is taken from CLEO [199].

Eq. (4.177). The fit yields the quark masses

m_s	m_c	m_b	
0.360	1.6	4.8	GeV

(4.181)

which can be identified with the constituent quark masses. Due to the introduction of the cutoff λ the size parameters Λ_M in Tab. 4.17 are no longer correlated with the size of the meson. In Tabs. 4.18 and 4.19 we list the results of our numerical

$\Lambda_{\rho/\omega/\phi}$	Λ_η	$\Lambda_{\eta'}$	Λ_K	Λ_{K^*}	Λ_D	Λ_{D^*}	Λ_{D_s}	$\Lambda_{D_s^*}$
0.295	1.0	2.0	0.87	0.30	1.4	2.3	1.95	2.6
Λ_B	Λ_{B^*}	Λ_{B_s}	$\Lambda_{B_s^*}$	$\Lambda_{J/\psi}$	Λ_{η_c}	Λ_Υ	Λ_{η_b}	Λ_{B_c}
3.35	3.35	4.4	4.4	3.3	3.0	5.07	5.0	3.0

Table 4.17.: Size parameters

fit to the weak and electromagnetic leptonic decay constants together with their experimental values. Once the fit parameters are fixed one can use them to calculate a wide range of electromagnetic decay widths. The results of the calculation are presented in Tab. 4.20 which also includes experimental results whenever they are available.

4.8. Dalitz decays

As a final task we apply our approach to the Dalitz decays $P \to \gamma l^+ l^-$ and $V \to P l^+ l^-$ (for a theoretical review, see e.g. [209]). In particular, we analyze the transition form factors of the Dalitz decays $\eta \to \gamma\mu^+\mu^-$ and $\omega \to \pi^0\mu^+\mu^-$ which have recently been measured by the NA60 collaboration at the CERN SPS [210]. The $\omega \to \pi^0\mu^+\mu^-$ transition form factor has also been analyzed by the SND Collaboration at the BINP (Novosibirk) [211]. Here data is usually plotted as function of the dilepton mass $M = \sqrt{q^2}$, see e.g. [210].
The diagrams describing the Dalitz decays are shown in Fig. 4.27. They include both the diagrams with direct emission of the photon and resonance diagrams with an intermediate $V \to \gamma$ transition. The differential cross sections in dependence on the dilepton mass squared $q^2 = (p_{l^+} + p_{l^-})^2$ reads

$$\frac{d\Gamma(P \to \gamma l^+ l^-)}{dq^2} = \frac{2}{3}\frac{\alpha}{\pi}\frac{\Gamma(P \to \gamma\gamma)}{q^2}\left(1 + \frac{2m_l^2}{q^2}\right)\left(1 - \frac{4m_l^2}{q^2}\right)^{1/2}\left(1 - \frac{q^2}{m_P^2}\right)^3 \times \left|F_P(q^2)\right|^2 ,$$
$$4m_l^2 \le q^2 \le m_P^2 , \tag{4.182}$$

Meson	Our	Data [174]
π^-	130.2	$130.4 \pm 0.04 \pm 0.2$
K^-	155.4	$155.5 \pm 0.2 \pm 0.8$
D^+	206.2	205.8 ± 8.9
D_s^+	273.7	273 ± 10
B^-	216.4	216 ± 22
B_s^0	250.2	$253 \pm 8 \pm 7$
B_c	485.2	$489 \pm 5 \pm 3$ [206]
ρ^+	209.3	210.5 ± 0.6 [174]
D^{*+}	187.0	$245 \pm 20^{+3}_{-2}$ [207]
D_s^{*+}	273.6	$272 \pm 16^{+3}_{-20}$ [208]
B^{*+}	210.6	$196 \pm 24^{+39}_{-2}$ [207]
B_s^{*0}	264.6	$229 \pm 20^{+41}_{-16}$ [207]

Table 4.18.: Weak leptonic decay constants $f_{P(V)}$ in MeV.

Meson	Our	Data [174]
ρ^0	148.0	154.7 ± 0.7
ω	51.7	45.8 ± 0.8
ϕ	76.3	76 ± 1.2
J/ψ	277.4	277.6 ± 4
$\Upsilon(1s)$	238.4	238.5 ± 5.5

Table 4.19.: Electromagnetic leptonic decay constants f_V of hidden flavor vector mesons in MeV.

Process	Our	Data [174]
$\pi^0 \to \gamma\gamma$	6.03×10^{-3}	$7.7 \pm 0.6\ 10^{-3}$
$\eta \to \gamma\gamma$	0.44	0.510 ± 0.026
$\eta' \to \gamma\gamma$	7.21	4.28 ± 0.19
$\eta_c \to \gamma\gamma$	4.95	$7.2 \pm 0.7 \pm 2.0$
$\eta_b \to \gamma\gamma$	0.47	
$\rho^0 \to e^+e^-$	6.33	7.04 ± 0.06
$\omega \to e^+e^-$	0.76	0.60 ± 0.02
$\phi \to e^+e^-$	1.27	1.27 ± 0.04
$J/\psi \to e^+e^-$	5.54	$5.55 \pm 0.14 \pm 0.02$
$\Upsilon \to e^+e^-$	1.34	1.34 ± 0.018
$\rho^\pm \to \pi^\pm\gamma$	70.25	68 ± 7
$\rho^0 \to \eta\gamma$	42.48	62 ± 17
$\omega \to \pi^0\gamma$	677.80	$788 \pm 12 \pm 27$
$\omega \to \eta\gamma$	5.5	6.1 ± 2.5
$\eta' \to \omega\gamma$	4.5	9.06 ± 2.87
$\phi \to \eta\gamma$	57.0	$58.9 \pm 0.5 \pm 2.4$
$\phi \to \eta'\gamma$	0.12	0.27 ± 0.01
$K^{*\pm} \to K^\pm\gamma$	40.86	50 ± 5
$K^{*0} \to K^\pm\gamma$	122.85	116 ± 10
$D^{*\pm} \to D^\pm\gamma$	0.62	1.5 ± 0.8
$D^{*0} \to D^0\gamma$	22.02	$< 0.9 \times 10^3$
$D_s^{*\pm} \to D_s^\pm\gamma$	0.30	$< 1.8 \times 10^3$
$B^{*\pm} \to B^\pm\gamma$	0.36	
$B^{*0} \to B^0\gamma$	0.12	
$B_s^{*0} \to B_s^0\gamma$	0.12	
$J/\psi \to \eta_c\gamma$	1.89	1.58 ± 0.37
$\Upsilon \to \eta_b\gamma$	0.02	

Table 4.20.: Electromagnetic and leptonic decay widths in keV.

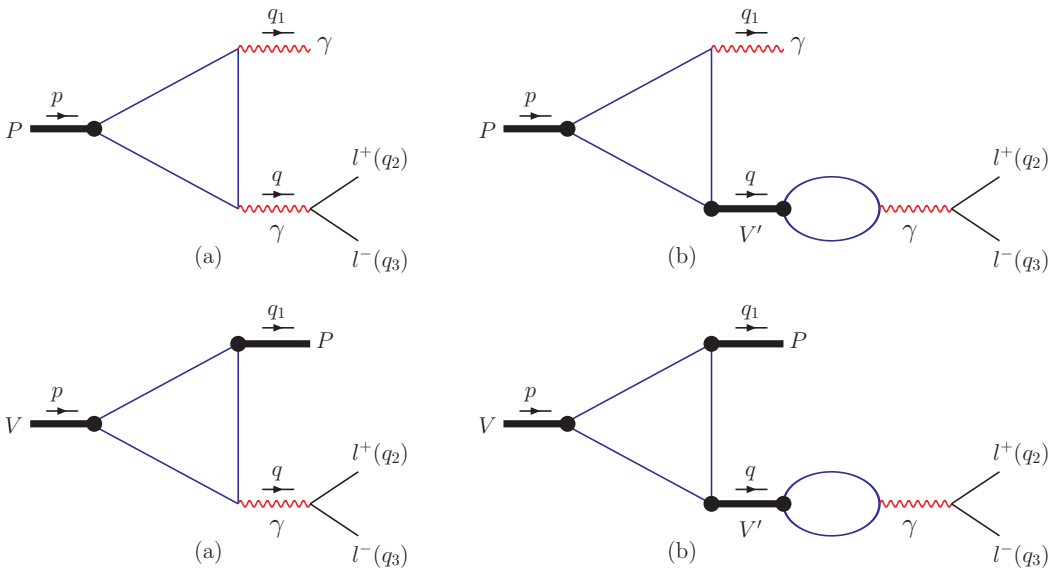

Figure 4.27.: Diagrams describing the Dalitz decays $P \to \gamma l^+ l^-$ (upper panel) and $V \to P l^+ l^-$ (lower panel).

$$\frac{d\Gamma(V \to P l^+ l^-)}{dq^2} = \frac{1}{3}\frac{\alpha}{\pi}\frac{\Gamma(V \to P\gamma)}{q^2}\left(1+\frac{2m_l^2}{q^2}\right)\left(1-\frac{4m_l^2}{q^2}\right)^{1/2}\left(1-\frac{q^2}{(m_V-m_P)^2}\right)^{3/2}$$
$$\times\left(1-\frac{q^2}{(m_V+m_P)^2}\right)^{3/2}\left|F_V(q^2)\right|^2,$$
$$4m_l^2 \le q^2 \le (m_V-m_P)^2\,. \tag{4.183}$$

In our approach the normalized transition form factors are calculated in terms of the diagrams Fig. 4.27. The form factors are given by

$$F_P(q^2) = \frac{1}{g_{P\gamma\gamma}} \times \left\{ g_{P\gamma\gamma}(q^2) + \sum_{V=\rho,\,\omega,\,\phi} g_{PV\gamma}(q^2)\, D_V(q^2)\, q^2 g_{V\gamma}(q^2) \right\}, \tag{4.184}$$

$$F_V(q^2) = \frac{1}{g_{VP\gamma}} \times \left\{ g_{VP\gamma}(q^2) + \sum_{V'=\rho,\,\omega,\,\phi} g_{VPV'}(q^2)\, D_{V'}(q^2)\, q^2 g_{V'\gamma}(q^2) \right\}. \tag{4.185}$$

The contributions of the intermediate vector meson resonances are described by a Breit–Wigner form where we have used a constant width in the imaginary part, i.e. we have used

$$D_V(q^2) = \frac{1}{m_V^2 - q^2 - i m_V \Gamma_V}\,. \tag{4.186}$$

In Figs. 4.28 and 4.29 we plot the transition form factors for the two Dalitz decays

$\eta \to \mu^+\mu^-\gamma$ and $\omega \to \pi^0\mu^+\mu^-$ measured by the CERN NA60 Collaboration [210] and the SND Collaboration BINP (Novosibirk) [211]. One can see that our approach gives a reasonable description of the experimental data. In Tab. 4.21 we present

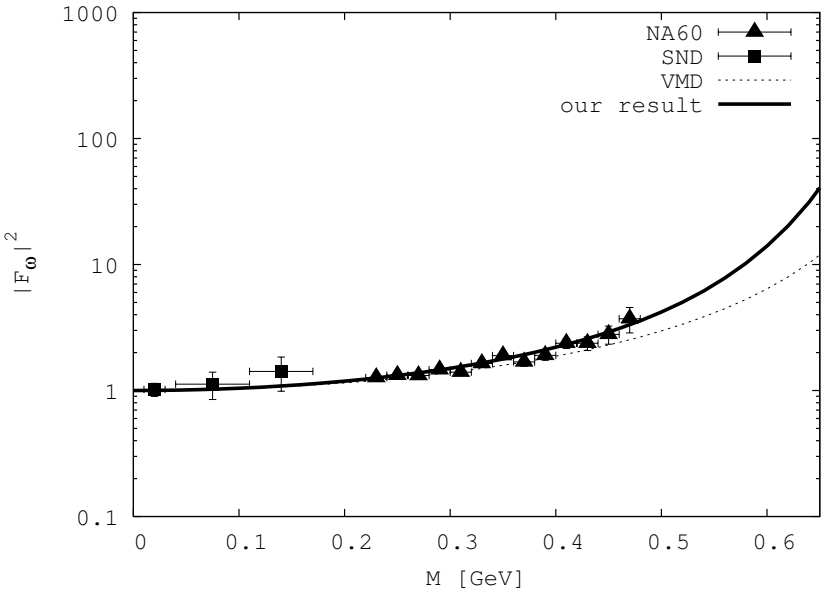

Figure 4.28.: The form factor of the Dalitz decay $\omega \to \pi^0 l^+ l^-$ as function of the dilepton mass $M = \sqrt{q^2}$. Experimental data is taken from [210]. For comparison we also show the VDM–curve with $\Lambda = 1.68\,\mathrm{GeV}^2$ taken from [209].

our results for the slope parameters defined by $F'_X(0)$. Finally, our predictions for the Dalitz decay widths are given in Tab. 4.22.

Summary

We have refined a relativistic constituent quark model [135] to include quark confinement effects. Quark confinement was implemented by introducing an upper cutoff on a scale integration which, in the original quark model, extends to infinity. The introduction of such an infrared cutoff removes all physical quark thresholds in the original quark transition diagrams. The cutoff parameter is taken to be the same for all physical processes. We adjust the model parameters by fitting the calculated quantities of the basic physical processes to available experimental data. As an application we calculate the electromagnetic form factors of the pion and the transition form factors of the Dalitz decays.

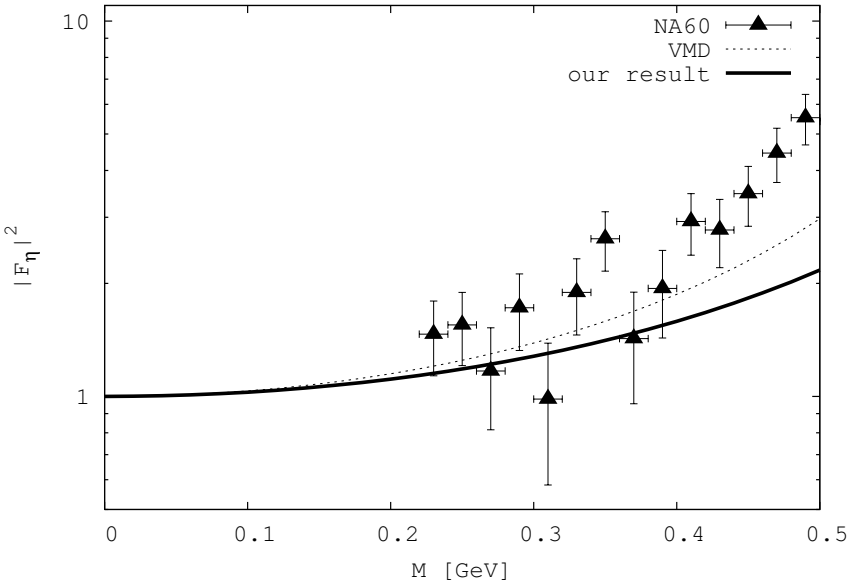

Figure 4.29.: Our result for the $\eta \to \gamma l^+ l^-$ Dalitz decay in dependence on the dilepton mass $M = \sqrt{q^2}$. Experimental data is taken from [210] and [211]. We also indicate the VDM–curve with $\Lambda = 1.8\,\mathrm{GeV}^2$ (see [209]).

Decay mode	Our	Data
$\pi^0 \to \gamma l^+ l^-$	1.4	5.5 ± 1.6 [212]
$\eta \to \gamma l^+ l^-$	1.5	3 ± 1 [213]
		$1.95 \pm 0.17 \pm 0.05$ [210]
$\eta' \to \gamma l^+ l^-$	1.2	1.68 [214]
$\rho^0 \to \pi^0 l^+ l^-$	1.8	
$\omega \to \pi^0 l^+ l^-$	1.8	$2.24 \pm 0.06 \pm 0.02$ [210]
$\rho^0 \to \eta l^+ l^-$	1.9	
$\omega \to \eta l^+ l^-$	1.1	
$\phi \to \eta l^+ l^-$	1.1	
$\phi \to \eta' l^+ l^-$	0.4	

Table 4.21.: Slope parameters of the Dalitz transition form factors in GeV^{-2}.

Decay mode	Our	Data [174]
$\pi^0 \to \gamma e^+ e^-$	7.2×10^{-5}	$(9.39 \pm 0.72) \times 10^{-5}$
$\eta \to \gamma e^+ e^-$	7.28×10^{-3}	$(8.84 \pm 1.14) \times10^{-3}$
$\eta \to \gamma \mu^+ \mu^-$	0.31×10^{-3}	$(4.03 \pm 0.56) \times10^{-3}$
$\eta' \to \gamma e^+ e^-$	0.1	< 0.2
$\eta' \to \gamma \mu^+ \mu^-$	1.8×10^{-2}	$(3.2 \pm 1.2) \times10^{-2}$
$\rho^0 \to \pi^0 e^+ e^-$	1.1	< 2.3
$\rho^0 \to \pi^0 \mu^+ \mu^-$	0.1	
$\omega \to \pi^0 e^+ e^-$	10.4	6.54 ± 0.77
$\omega \to \pi^0 \mu^+ \mu^-$	1.2	0.82 ± 0.20
$\rho^0 \to \eta e^+ e^-$	1.1	< 1
$\omega \to \eta e^+ e^-$	0.1	$< 9.3 \times 10^{-2}$
$\phi \to \eta e^+ e^-$	0.67	0.49 ± 0.04
$\phi \to \eta' e^+ e^-$	5.2×10^{-3}	
$\phi \to \eta \mu^+ \mu^-$	1.5×10^{-2}	$< 4 \times10^{-2}$

Table 4.22.: Dalitz decay widths in keV.

4.9. Conclusions

In this chapter we introduced a theoretical approach for the description of hadronic bound states. Despite that we deal with a rather simple model it is successfully applied to various kinds of hadron structures ranging from conventional $q\bar{q}$ mesons (and qqq baryons, not discussed in this thesis) to bound states on the hadron level, here meson–meson molecules. The method is obviously not restricted to particular flavor sectors as in the cases of ChPT or heavy quark effective theory. In the present work we studied meson molecules in the light sector, heavy charmonium–like hadronic molecules and finally discussed an extensive application to light, heavy–light and double–heavy $q\bar{q}$ mesons. The compositeness condition provides a self–consistent method to determine the coupling between the bound state and its constituents once the bound state mass is chosen. Thus the number of free parameters is reduced to the size parameters Λ of the respective hadrons. Here we do not fit Λ to each hadron (molecule) but rather determine its value for each hadron and flavor sector (e.g. 1–2 GeV for light and heavy meson molecules). Since we work in a fully covariant Lagrangian approach a further introduction of the electroweak interaction is rather straightforward. Especially the basic requirement of gauge invariance both in the Lagrangian and on the level of transition amplitudes can be shown to be fulfilled.

Our results confirm the assumption that the light scalars $a_0(980)$ and $f_0(980)$ can be interpreted by a dominant kaon and antikaon bound state configuration. In particular, the hadronic molecule interpretation is sufficient to describe both the electromagnetic and strong a_0 and f_0 decays based on the current status of experimental data. Furthermore, the f_0-a_0 mixing strength could deliver new insights into contributions being responsible for isospin–violating mixing and the meson structure issue.

We also applied this bound state method to the charmonium–like mesons $Y(3940)$ and $Y(4140)$, which are not simply explained as $c\bar{c}$ states due to the large hidden–charm decay widths, and to the $Z^{\pm}(4430)$ which cannot be assigned to a $c\bar{c}$ state because it is charged. Our results confirm the strong suspicion that the three candidates are possibly bound states of charmed mesons. The meson molecule approach allows to circumvent the OZI suppression of hidden charm decay modes and reproduces the experimental observations.

Finally, we applied the covariant method as a relativistic quark model. Color confinement is effectively modeled by introducing the infrared confinement parameter λ, which removes the threshold restriction that the mass of the bound state has to be smaller than the sum of the constituents. This modification allows e.g. for the application of the model to the full range of $q\bar{q}$ states including excited ones. First, we use the pion and ρ properties to fit the infrared cutoff which allows us to study for example the Dalitz decays of the π, ω and $\eta^{(\prime)}$ mesons.

In conclusion, the bound state model provides a very clear and straightforward approach to determine the decay properties of a whole kind of hadronic bound states.

5. Holographic model AdS/QCD

With the AdS/QCD model we present the last approach for the description of hadron structure. The present holographic model deviates from the more standard methods which were introduced in the previous chapters since now we deal with extra dimensions. In general, the AdS/QCD correspondence is probably one of the most significant results of string theory since it provides a connection between the physical world of hadron matter and string theory based on extra dimensions. Holographic approaches are a very contemporary research topic which attracted much interest in recent years. It offers an interesting and promising method to apply perturbative string theory calculations to nonperturbative QCD problems with the hope to make the theory of strong interactions analytically tractable. The aim of AdS/QCD is to provide a description of hadrons in terms of their QCD degrees of freedom—quarks and gluons—which allows for the computation of mass spectra and other observables. Holographic approaches find their application in more and more research fields like strong interaction, quantum gravity and astronomy.
In the present work based on Ref. [28] the AdS/QCD model is applied to mesons which are reduced to their $q\bar{q}$ valence quarks. We calculate the mass spectrum of light, heavy–light and double heavy mesons, where we include explicit quark masses, color Coulomb and hyperfine–splitting corrections. Finally, we also study the decay constants of the ground state mesons.

5.1. Basic approach

AdS/QCD is often also termed AdS/CFT correspondence which already indicates the two basic blocks of the theory. AdS/CFT approaches provide a relation between string theory, which is a quantum theory of gravity and other fields, and a quantum field theory with conformal invariance. The string theory part of the model is represented by the Anti–de–Sitter space (AdS) containing an extra dimension, in particular we deal with a five–dimensional AdS_5 space. The complementary part of the model represents the physical hadronic objects which are described in the framework of a conformal field theory (CFT).
In the following we will introduce the AdS/CFT approach in more detail. The starting point is a general overview of the model before we discuss the basic blocks of AdS/CFT separately. To simplify matters we start with the most simple case of AdS/CFT. Then we introduce successively breaking of the conformal invariance

(equivalent to confinement) and quark masses. We perform a refinement of the model by considering one–gluon exchange terms and hyperfine–splitting effects. Finally, we use the present holographic model to compute the mass spectra of mesons and decay constants, where the method is not restricted to light mesons, i.e. pions, as in the pioneering works (see e.g. [215]) but we consider light, heavy–light and double–heavy mesons.
The AdS/CFT formalism is schematically depicted in the following diagram which will be discussed below.

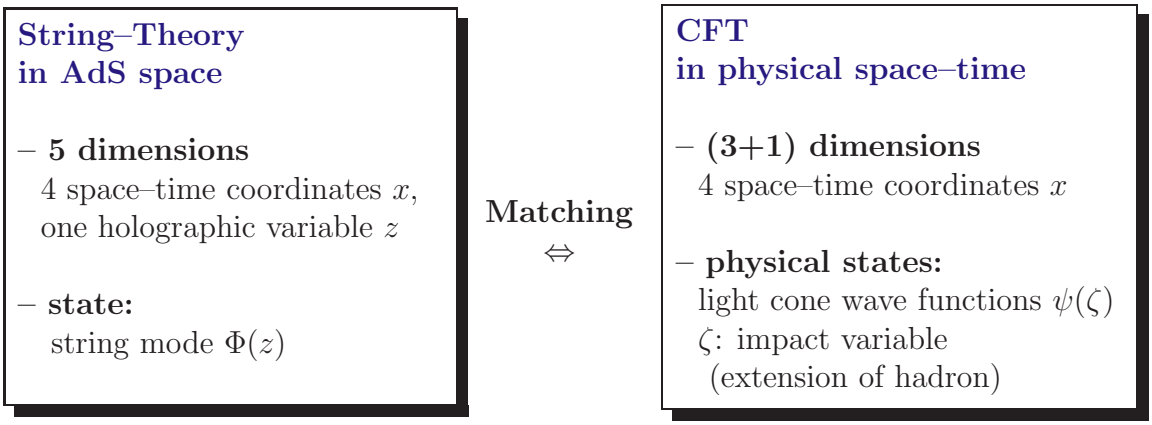

Figure 5.1.: Overview diagram of the AdS/CFT model.

The basis of the holographic model is provided by the additional fifth coordinate z which is included in the five–dimensional AdS_5 space (left box of Diagram 5.1). The scenario is schematically depicted in Fig. 5.2: The four–dimensional surface of the AdS_5 space represents the flat four–dimensional space we know containing three space coordinates plus a time dimension. The holographic variable z is perpendicular to the four space–time coordinates since we deal with a flat metric and it is in the interior of the AdS space. The string modes $\Phi(x, z)$ living on the extra dimensional holographic variable z included in the AdS_5 space are projected on our four–dimensional space–time as hadronic objects. For this reason AdS/CFT models are also called holographic approaches. Similar to a hologram, which encodes information of three dimensional objects in a two dimensional image, in holographic approaches string theory states of higher space–time dimensions are mapped on the four–dimensional space–time (boundary) which are identified with the hadron states in the conformal field theory. Of course the projection of the string states, corresponding to the size of the hadronic object or rather the impact variable ζ, cannot become arbitrary large because of confinement. Therefore we need to intro-

duce a cutoff along the z–coordinate at a value of about $z_0 = 1/\Lambda_{\mathrm{QCD}}$ which will be discussed later on.

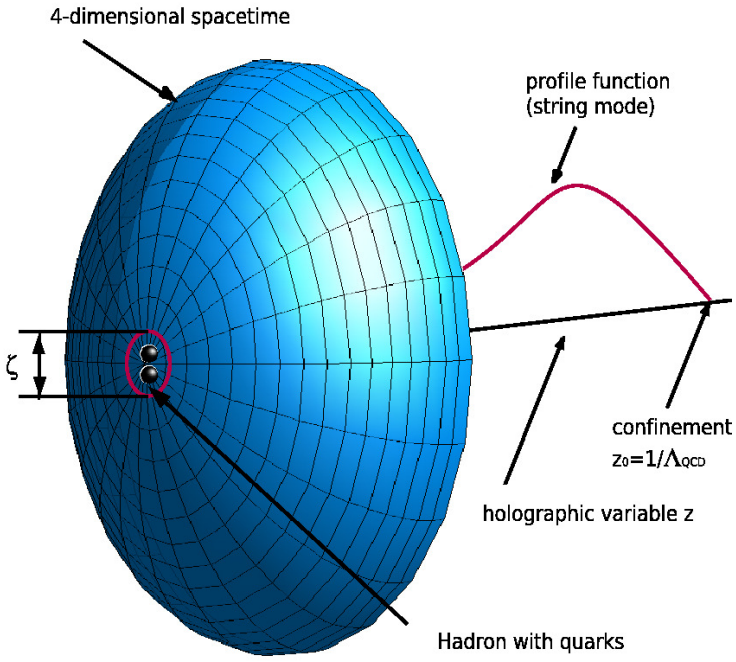

Figure 5.2.: Graphical representation of holographic models.

The counterpart of the AdS/CFT approach is the (hadronic) QCD–side of the theory which is addressed by means of a conformal field theory representing our four–dimensional space–time (see right box of Diagram 5.1). Hadronic states are expressed by its light front wave functions (LFWF) depending on the impact variable ζ which denotes the spatial extension of the hadron. The light front Fock expansion of the physical states is necessary in order to be able to perform the matching of the projection of the string mode on the AdS side and the hadronic object on the CFT side of the model. We will see that the holographic variable z can be identified with the impact variable ζ. In the following sections we shortly introduce the building blocks of the AdS/CFT approach.

5.1.1. Anti–de–Sitter space

Topologically the Anti–de–Sitter (AdS) space is a maximally symmetric Lorentzian manifold with constant negative curvature which leads to an effective attractive potential. The curvature leads to some special physical properties of the AdS–space: each object which is emitted from an observer returns after a constant time duration—only the distance changes with the initial velocity. Even when emitting a

light signal to infinity it comes back at the same time duration as a nonrelativistic object. The reason is a kind of a time dilatation which increases with the distance from the observer.

In physics the Anti–de–Sitter space is often mentioned in the context of General Relativity, where it provides the vacuum solution of Einstein's field equations. Furthermore the Anti–de–Sitter space also plays an important role in astronomy since in some theoretical models the universe is represented by a five–dimensional AdS_5 space. A well–known example is the Randall–Sundrum–Model [216, 217] considering the observable world to be a part of a higher dimensional space. More precisely the universe might consist of two branes which are connected by the fifth dimension. Here the notation 'brane' is derived from the word membrane which refers to the lower dimensional boundary of the respective space (here AdS_5). Our observable world is represented by one of the branes containing the Standard Model fields. Due to the curved space–time we do not have access to the other brane and in contrast to the electroweak and strong forces only the gravitational force can act along the fifth dimension. This ansatz yields an explanation for the weakness and special nature of gravity, i.e. to solve the hierarchy problem which was one reason for the development of the Randall–Sundrum–Model.

The metric in AdS_5 space is given by

$$ds^2 = \frac{R^2}{z^2}\left(\eta_{\mu\nu}dx^\mu dx^\nu - dz^2\right) = \left(g_{MN}dx^M dx^N\right). \tag{5.1}$$

Here R is the AdS radius, the x are the four–dimensional space–time coordinates and z is the fifth dimension (holographic variable). Therefore, the indices μ and ν run from 0 to 3 and the tensor $\eta_{\mu\nu}$ is the well known metric tensor $g_{\mu\nu}$ in Minkowski space. The metric can also be expressed by the metric tensor in $d+1$ dimensions

$$g_{MN} = \frac{R^2}{z^2}\begin{pmatrix} 1 & 0 & 0 & 0 & 0 \\ 0 & -1 & 0 & 0 & 0 \\ 0 & 0 & -1 & 0 & 0 \\ 0 & 0 & 0 & -1 & 0 \\ 0 & 0 & 0 & 0 & -1 \end{pmatrix}, \tag{5.2}$$

where $M, N = 0, ..., 4$. From Eq. (5.1) it is obvious that the AdS metric is invariant with respect to the scale transformations $x^\mu \to \lambda x^\mu$, $z \to \lambda z$. Therefore, scale transformations in the holographic variable z are mapped onto the four–dimensional space–time and vice versa (see also Fig. 5.2).

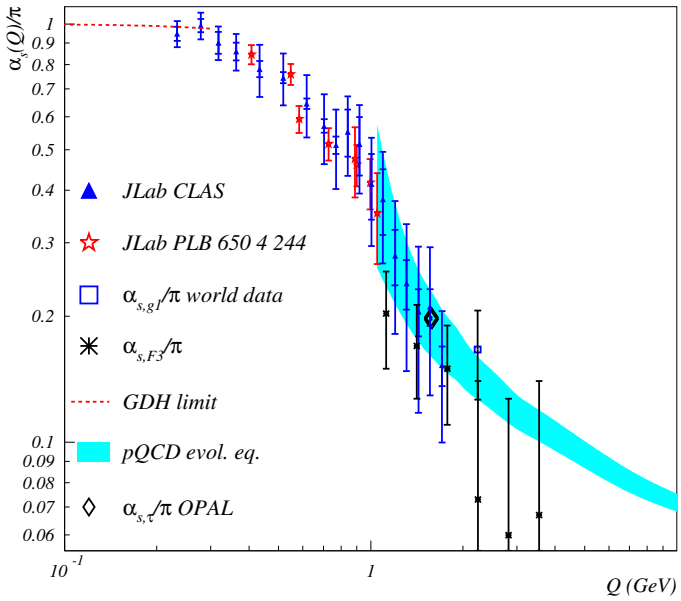

Figure 5.3.: Strong coupling constant $\alpha_s(Q^2)$ taken from [218].

5.1.2. Conformal field theory

The scale invariance of the AdS/CFT approach leads us to the next topic which is conformal field theory (CFT). As the name already says a CFT is invariant under conformal transformations which here is equivalent to scale invariance. One might ask how a scale invariant theory is capable to describe QCD which is rather known to be scale dependent. As depicted in Fig. 5.3 the strong coupling is very small at small scales, known as asymptotic freedom, while it becomes large in the strongly coupled region which makes QCD nonperturbative (see Fig.5.3). However, several theoretical investigations like the Dyson–Schwinger analyses for 3- and 4–gluon vertices [219, 220] or lattice gauge theory [221, 222] predict an infrared fixed point which is equivalent to a conformal window at large distances where the strong coupling α_s is almost stable (in Fig.5.3 between Q =0.1 and 0.4 GeV). Of course the conformal invariance has to be broken at some point since the issue of confinement needs to be implemented in the present model. Usually this problem is solved by introducing boundary conditions in the holographic variable z at the scale $z_0 = 1/\Lambda_{\rm QCD}$ which simulates confinement. In particular, we differentiate between hard–wall and soft–wall approaches. In the case of the hard–wall approach a hard cut–off is introduced in the holographic variable z while when dealing with soft–wall approaches a soft cut–off is realized e.g. by a introducing a dilaton field or by modifying the metric of the AdS space (introducing a warp factor in the metric). Since hard–wall approaches

fail to reproduce the Regge–like behavior $L \propto M^2$ of the mass spectrum of hadrons in the following we pursue the soft–wall method.

5.1.3. Light front Fock representation

To perform the matching between the string mode $\phi(z)$ and the hadron wave function $\psi(\zeta)$ as indicated in the diagram of Fig. 5.1 it is necessary to perform the analysis in the light front formalism. We will see later that matrix elements in light front representation are similar to the corresponding expressions derived in the AdS space which is a necessary condition to perform the matching. The light–cone coordinate system [223] was originally proposed by Dirac around 1950 to provide an effective method for treating the geometry of the Lorentz transformation in a rectangular coordinate system.
In order to switch from instant to light front representation we have to introduce new coordinates $x = (x^+, x^-, \vec{x}_\perp)$ which are related to the Minkowski coordinates $x^\mu = (x^0, x^1, x^2, x^3)$ by

$$\begin{aligned} x^\pm &= x^0 \pm x^3 \,, \\ \vec{x}_\perp &= \begin{pmatrix} x^1 \\ x^2 \end{pmatrix} . \end{aligned} \tag{5.3}$$

$x^\pm$ and $\vec{x}_\perp$ are called the longitudinal and transversal coordinates. For example, in the case of a parton with momentum p the coordinate p^+ denotes the forward while $\vec{p}_\perp$ is related to the transversal momentum component. In light front representation the scalar product is given by $x \cdot y = (x^+ y^- + x^- y^+)/2 - \vec{x}_\perp \cdot \vec{y}_\perp$.
To demonstrate the advantage of the light front representation we consider a Lorentz–boost in x^1–direction with velocity v in the instant and front form. In the instant form the Minkowski coordinates transform as

$$\begin{aligned} x^{0'} &= \cosh\eta\, x^0 - \sinh\eta\, x^1 \,, \\ x^{1'} &= -\sinh\eta\, x^0 + \cosh\eta\, x^1 \,, \\ x^{2'} &= x^2, \qquad x^{3'} = x^3 \,, \end{aligned} \tag{5.4}$$

where $\cosh\eta = 1/\sqrt{1 - v^2/c^2}$ and $\sinh\eta = \sqrt{\cosh^2\eta - 1}$. In the light front representation the Lorentz transformation takes the simple form

$$\begin{aligned} x^{+'} &= x^{0'} + x^{1'} = x^+ e^{-\eta} \,, \\ x^{-'} &= x^{0'} - x^{1'} = x^- e^{\eta} \,, \\ \vec{x}'_\perp &= \vec{x}_\perp \,. \end{aligned} \tag{5.5}$$

In contrast to the Minkowski coordinates in Eq. (5.4) the $x^\pm$ variables are not linearly

dependent under this transformation but they only undergo scale transformations, where the scalar product remains constant.

The difference between light front and instant (ordinary) time evolution is graphically illustrated by the conic sections in Fig. 5.4. For the instant time evolution, we are used to, a light signal expands spherically from a light source which is depicted in the left panel of Fig. 5.4: The intersection of the light cone (in blue) and the plane, which is moved in $x^0 \equiv ct$–direction to simulate the time evolution, represents the two–dimensional expansion of the light. While in the instant time evolution the time at which objects are illuminated increases linearly with the distance from the light source the situation is completely different in the front form. Here all objects that are placed in one particular direction are illuminated at the same time no matter at which distance from the light source they are placed. This property is graphically depicted in the right panel of Fig. 5.4: At time $t = 0$ when the flash is emitted the intersection of the plane with the light cone is represented by a line which is the x^-–axis. Therefore all objects that are placed in x^-–direction are illuminated at this time. Then the light expands parabolically from this line which is equivalent to moving the plane in direction of the x^+–axis (indicated by the red arrows).

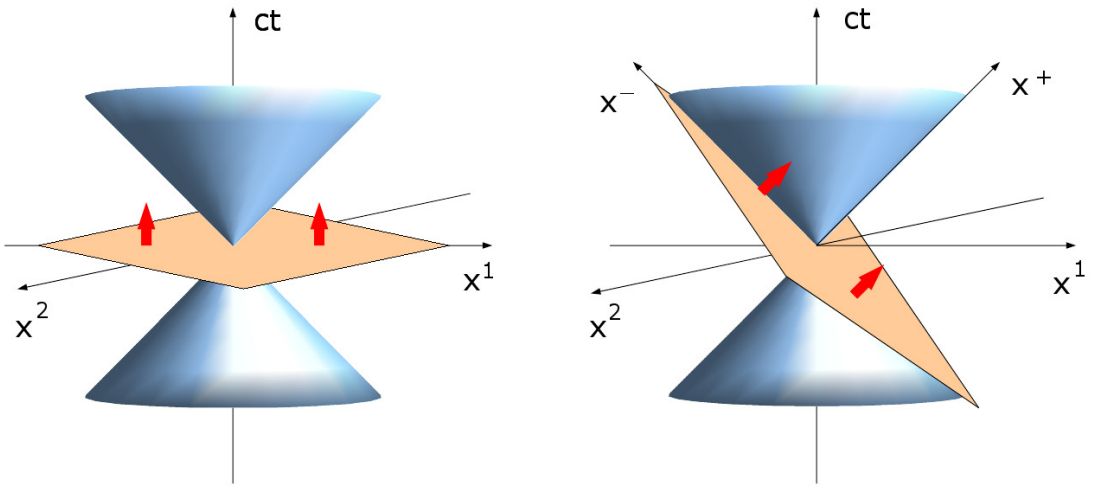

Figure 5.4.: Time evolution in instant and light front time.

The aim of the AdS/QCD approach is to derive hadron wave functions which allow for the computation of a large variety of hadron observables. For this purpose we write down the light–front Hamiltonian for the composite hadron system

$$H_{LF} = P^+P^- - \vec{p}_\perp^{\,2} \tag{5.6}$$

which has the eigenvalues M^2 of the hadron mass M:

$$H_{LF}\big|\psi_H\big\rangle = M^2\big|\psi_H\big\rangle\,. \tag{5.7}$$

Here $\big|\psi_H\big\rangle$ is the expansion of the hadron state in multi–particle Fock eigenstates $\big\{\big|n\big\rangle\big\}$ of the free light–front Hamiltonian

$$\big|\psi_H\big\rangle = \sum_n \psi_{n/h}\big|\psi_H\big\rangle\,. \tag{5.8}$$

At this stage it is required to introduce the light front Fock representation of hadrons in more detail. For this purpose we first express the hadron state $\big|\psi_H(P^+,\vec{P}_\perp,S)\big\rangle$ with momentum P and spin S by the sum over all possible configurations containing n constituents starting with the valence quark state. For example when dealing with mesons the minimal number of constituents is $n=2$, the valence quark–antiquark pair $q\bar{q}$. Further Fock states contain additional gluons and sea–quark–antiquark pairs. The full expansion of the hadron state $\big|\psi_H(P^+,\vec{P}_\perp,S)\big\rangle$ in n–parton Fock states reads

$$\begin{aligned}\big|\psi_H(P^+,\vec{P}_\perp,S)\big\rangle =& \sum_{n,\lambda_i}\prod_{i=1}^{n}\int\frac{dx_i}{\sqrt{x_i}}\frac{d^2k_{\perp i}}{2(2\pi)^3}(16\pi^3)\delta\big(1-\sum_{j=1}^{n}x_j\big)\delta^{(2)}\big(\sum_j k_{\perp j}\big)\\ &\times\psi_{n/H}(x_i,\vec{k}_{\perp i},\lambda_i)\big|n:x_iP^+,x_i\vec{P}_\perp+\vec{k}_{\perp i},\lambda_i\big\rangle\,.\end{aligned} \tag{5.9}$$

Here we denote the spin, longitudinal and relative transverse momentum of the respective constituent i by λ_i, k_i^+ and $\vec{k}_{\perp i}$. The variable $x_i=\frac{k_i^+}{P^+}$ represents the longitudinal momentum fraction of parton i. Momentum conservation leads to two simple conditions: The sum over all momentum fractions is one and all transverse momentum contributions of the partons cancel each other which leads to the following equations

$$\begin{aligned}\sum_i x_i &= 1\,,\\ \sum_i \vec{k}_{\perp i} &= 0\,.\end{aligned} \tag{5.10}$$

A special feature of the coefficients of the Fock expansion

$$\psi_{n/H}(x_i,\vec{k}_{\perp i},\lambda_i) = \big\langle n:x_iP^+,x_i\vec{P}_\perp+\vec{k}_{\perp i},\lambda_i\big|\psi_H\big\rangle \tag{5.11}$$

is the boost invariance with respect to the momentum P. This is fulfilled since the wave functions $\psi_{n/H}(x_i,\vec{k}_{\perp i},\lambda_i)$ only depend on the relative partonic coordinates x_i, $\vec{k}_{\perp i}$ and λ_i and not on the total momentum and spin of the hadron. The

normalization of the hadron state is as follows

$$\big\langle \psi_H(P'^+, \vec{P}'_\perp, S') \big| \psi_H(P^+, \vec{P}_\perp, S) \big\rangle = 2P^+(2\pi)^3 \delta(P^+ - P'^+) \delta^{(2)}(\vec{p}_\perp - \vec{p}'_{\perp i}) \delta_{S,S'} \,. \quad (5.12)$$

For our calculations we express the n–particle Fock state $\big|n : x_i P^+, x_i \vec{P}_\perp + \vec{k}_{\perp i}, \lambda_i\big\rangle$ with the help of creation and annihilation operators $b^\dagger_\lambda$, b_λ and $d^\dagger_\lambda$, d_λ of quarks and antiquarks, respectively, which fulfill the operator relations

$$\big\{ b_\lambda(p), b^\dagger_{\lambda'}(p') \big\} = \{ d_\lambda(p), d^\dagger_{\lambda'}(p') \} \quad = (2\pi)^3 \delta^{\lambda\lambda'} \delta(p^+ - p'^+) \delta^{(2)}(\vec{p}_\perp - \vec{p}'_\perp) \,. \quad (5.13)$$

A n particle Fock state is then defined by

$$\big|n : p_i^+, \vec{p}_{i\,\perp}, \lambda_i\big\rangle = \prod_i \sqrt{2p_i^+}\, b^\dagger_{\lambda_i}(p_i) \big|0\big\rangle \quad (5.14)$$

and has the normalization

$$\big\langle p_i^+, \vec{p}_{\perp i}, \lambda_i \big| p_i'^+, \vec{p'}_{\perp i}, \lambda'_i \big\rangle = 2p_i^+ (2\pi)^3 \delta(p_i^+ - p_i'^+) \delta^{(2)}(\vec{p}_{\perp i} - \vec{p'}_{\perp i}) \delta_{\lambda_i, \lambda'_i} \,. \quad (5.15)$$

Considering the normalizations of the hadron and Fock states of Eqs. (5.12) and (5.15) the norm of the coefficients $\psi_{n/H}(x_i, \vec{k}_{\perp i})$ can be easily derived as:

$$\sum_n \int dx_i d^2\vec{k}_{\perp i} \big| \psi_{n/H}(x_i, \vec{k}_{\perp i}) \big|^2 = 1 \,. \quad (5.16)$$

In the present thesis we apply the AdS/CFT approach to mesons where we restrict to the lowest Fock state ($n = 2$) which is the two–parton system of the valence quark–antiquark pair. The corresponding truncated Fock expansion of Eq. (5.9) reads

$$\begin{aligned} \big|\psi_H(P^+, \vec{P}_\perp, S)\big\rangle = \; & \sum_{\lambda_i} \prod_{i=1}^{2} \int \tfrac{dx_i}{\sqrt{x_i}} \tfrac{d^2k_{\perp i}}{2(2\pi)^3} (16\pi^3) \delta\big(1 - \sum_{j=1}^{2} x_j\big) \delta^{(2)}\big(\sum k_{\perp j}\big) \\ & \times \psi_{2/H}(x_i, \vec{k}_{\perp i}, \lambda_i) \big| 2 : x_i P^+, x_i \vec{P}_\perp + \vec{k}_{\perp i}, \lambda_i \big\rangle \,. \end{aligned} \quad (5.17)$$

Above expression can be simplified with the δ–function and by defining $x_1 \equiv x$, $x_2 \equiv 1 - x$, and $\vec{k}_{1\,\perp} = -\vec{k}_{2\,\perp} \equiv \vec{k}_\perp$ which leads to

$$\big|\psi_H(P^+, \vec{P}_\perp, S)\big\rangle = \sum_{\lambda_i} \int \frac{dx}{\sqrt{x(1-x)}} \frac{d^2k_\perp}{2(2\pi)^3} \psi_{2/H}(x, \vec{k}_\perp) \prod_{i=1}^{2} \big| 2 : x_i P^+, x_i \vec{P}_\perp + \vec{k}_{\perp i}, \lambda_i \big\rangle \,.$$

The operator representation (5.14) of the two–particle (quark–antiquark) Fock state

leads to

$$\prod_{i=1}^{2} \big|2 : x_i P^+, x_i \vec{P}_\perp + \vec{k}_{\perp i}, \lambda_i\big\rangle = 2\sqrt{p_1^+ p_2^+}\, b^\dagger_{\lambda_1} d^\dagger_{\lambda_2} \big|0\big\rangle\,, \tag{5.18}$$

with the quark momenta $p_1 = (xP^+, x\vec{P}_\perp + \vec{k}_\perp)$ and $p_2 = ((1-x)P^+, (1-x)\vec{P}_\perp - \vec{k}_\perp)$. Finally, we can express the meson state in the simple form

$$\big|\psi_H(P,S)\big\rangle = \frac{2P^+}{\sqrt{2N_c}} \int_0^1 dx \int \frac{d^2k_\perp}{16\pi^3} \psi(x, \vec{k}_\perp) \sum_{\lambda_1,\lambda_2} b^\dagger_{\lambda_1}(p_1) d^\dagger_{\lambda_2}(p_2) \big|0\big\rangle \tag{5.19}$$

where $N_c = 3$ is the number of colors.
Now we can easily generate the Fock states of pseudoscalar (P), scalar (S), vector (V) and axial (A) mesons, restricting again to the valence quark-antiquark contribution only. The corresponding mesonic eigenstates with momentum $P = (P^+, P^-, \vec{P}_\perp)$ are given by

$$\big|M_{P,S}(P)\big\rangle = \frac{2P^+}{\sqrt{2N_c}} \int_0^1 dx \int \frac{d^2\vec{k}_\perp}{16\pi^3} \psi_{q_1\bar{q}_2}(x, \vec{k}_\perp) \Big[d^{\dagger a}_{q_1\uparrow}(p_1)_{q_2\downarrow}(p_2) - d^{\dagger a}_{q_1\downarrow}(p_1) b^{\dagger a}_{q_2\uparrow}(p_2) \Big] |0\rangle \tag{5.20}$$

$$\begin{aligned} \big|M_{V,A}(P,\lambda)\big\rangle = \frac{2P^+}{\sqrt{2N_c}} \int_0^1 dx \int \frac{d^2\vec{k}_\perp}{16\pi^3} \psi_{q_1\bar{q}_2}(x, \vec{k}_\perp) \\ \times \begin{cases} d^{\dagger a}_{q\uparrow}(xP)\, b^{\dagger a}_{q\uparrow}((1-x)P)\big|0\big\rangle\sqrt{2}\,, & \lambda = +1 \\ d^{\dagger a}_{q\uparrow}(xP)\, b^{\dagger a}_{q\downarrow}((1-x)P) + d^{\dagger a}_{q\downarrow}(xP)\, b^{\dagger a}_{q\uparrow}((1-x)P)\big|0\big\rangle\,, & \lambda = 0 \\ d^{\dagger a}_{q\downarrow}(xP)\, b^{\dagger a}_{q\downarrow}((1-x)P)\big|0\big\rangle\sqrt{2}\,, & \lambda = -1 \end{cases} , \end{aligned} \tag{5.21}$$

where the polarization vectors $\epsilon^\mu(P,\lambda)$ in the light-cone representation read as

$$\epsilon^\mu(P,\lambda) = \begin{cases} \left(\frac{P^+}{M_V}, \frac{\vec{P}_\perp^{\,2} - M_V^2}{M_V P^+}, \frac{\vec{P}_\perp}{M_V} \right), & \lambda = 0 \\ \left(0, \frac{2\vec{e}_\perp(\pm 1)\vec{P}_\perp}{P^+}, \vec{e}_\perp(\pm 1) \right), & \lambda = \pm 1 \end{cases} \tag{5.22}$$

with $\vec{e}_\perp(\pm 1) = \mp \frac{(1, \pm i)}{\sqrt{2}}$.

5.2. AdS/QCD – the method

After we introduced the basic blocks of the AdS/QCD approach in the previous section we are now able to focus on the technical procedure of this method.
In the following we demonstrate the method where we start with the most simple case and step by step we include the basic requirements to be contained in the model as confinement and finite quark masses.

5.2.1. Action of a string

The starting point of the AdS/QCD approach is provided by the action of a string mode Φ in five–dimensional AdS_5 space. More precisely, we set up the action of a spin–J field Φ with momentum P and mass M:

$$S_\Phi = \frac{(-1)^J}{2} \int d^d x dz \sqrt{g} \left(\partial_N \Phi_J \partial^N \Phi^J - \mu_J^2 \, \Phi_J \Phi^J \right), \tag{5.23}$$

g denotes the metric of the AdS space given by $g = |detg_{MN}| = (R/z)^{2(d+1)}$ (see Eq. (5.2)). We separate the holographic variable z from the flat 4–dimensional coordinates x by choosing a plain wave ansatz along the Poincaré coordinates x while we assume a profile function $\Phi_{nJ}(z)$ in the holographic variable z

$$\Phi_{\nu_1 \cdots \nu_J}(x, z) \to e^{-iP_n x} \Phi_{nJ}(z) \,. \tag{5.24}$$

The equation of motion (EoM) of the string $\Phi_{nJ}(z)$ can be easily derived by means of variational calculus which leads to a Schrödinger–type equation

$$\big(- \frac{d^2}{dz^2} - \frac{1 - 4L^2}{4z^2} \big) \varphi_{nJ}(z) = \mathcal{M}^2 \varphi_{nJ}(z) \,, \tag{5.25}$$

where $\varphi_{nJ}(z)$ is defined by $\varphi_{nJ}(z) = e^{-\phi(z)/2} \big(\frac{R}{z}\big)^{-J+(d-1)/2} \Phi_{nJ}(z)$. Up to now we assumed a fully conformal behavior of the model which of course is not correct since we have to consider the effect of confinement. In the introduction of this chapter we already mentioned the different possibilities to implement confinement. The hard– and soft–wall approaches, which are compared in the following graphics, put limits on the z–values for example near $z_0 = 1/\Lambda_{\mathrm{QCD}}$ which leads to additional potentials $U(z)$ in the EoM. Both approaches are compared in the following graphic representation:

Two scenarios for AdS/QCD backgrounds

↙ ↘

Hard Wall Model

IR cutoff in the holographic variable

$$U(z) = \begin{cases} 0 & z \leq \frac{1}{\Lambda_{\rm QCD}} \\ \infty & z \geq \frac{1}{\Lambda_{\rm QCD}} \end{cases}$$

$\mathcal{M} \propto L$

Soft Wall Model

Soft cutoff by dilaton field
$\Rightarrow$ HO–Potential $\propto z^2$:

$U(z) = \kappa^4 z^2 + 2\kappa^2(J-1)$
κ: scale parameter.

Regge trajectory: $\mathcal{M}^2 \propto L$.

In the case of the hard–wall model the infrared cutoff leads to a step potential which is the cause for the major problem of the hard–wall scenario: The hadron masses of orbital excitations have linear dependence on the orbital angular momentum with $M \propto L$ instead of the experimentally favored quadratic behavior $M^2 \propto L$ known as Regge trajectory. This problem is circumvented in the soft–wall approach, where the introduction of a dilaton field (see below) leads to an effective harmonic oscillator potential. In fact, the soft–wall model was initiated in order to solve the problem of the hadronic mass spectrum.
For these reasons we restrict in the following to the soft–wall approach. Here we include an additional field which breaks the dilatation symmetry under $x \to \lambda x$, hence it is called dilaton field. The dilaton field $\phi(z) = \kappa^2 z^2$ is dependent on the scale parameter κ. The action of the string is modified by

$$S_\Phi = \frac{(-1)^J}{2} \int d^d x dz \, \sqrt{g}\, e^{-\phi(z)} \left(\partial_N \Phi_J \partial^N \Phi^J - \mu_J^2(z)\, \Phi_J \Phi^J \right). \tag{5.26}$$

In order to allow for the interaction of the dilaton field with the string mode $\Phi_{nJ}(z)$ we include a nontrivial z–dependence of the mass term which now is 'dressed' with $\mu_J^2 \to \mu_J^2(z) = \mu_J^2 + g_J \phi(z)$ which is an additional source for breaking of the conformal symmetry.
The equation of motion now reads as

$$\Big(-\frac{d^2}{dz^2} - \frac{1-4L^2}{4z^2} + U_J(z) \Big) \varphi_{nJ}(z) = M_{nJ}^2 \varphi_{nJ}(z) \tag{5.27}$$

where the additional potential $U_J(z) = \kappa^4 z^2 + 2\kappa^2(J-1)$ arises due to the dilaton field. By solving the differential equation (5.27) we can easily determine the

eigenfunctions

$$\varphi_{nL}(z) = \sqrt{\frac{2n!}{(n+L)!}}\ \kappa^{1+L}\ z^{1/2+L}\ e^{-\kappa^2 z^2/2} L_n^L(\kappa^2 z^2)\,, \tag{5.28}$$

where

$$L_n^m(x) = \frac{x^{-m}e^x}{n!}\frac{d^n}{dx^n}\Big(e^{-x}x^{m+n}\Big) \tag{5.29}$$

are the generalized Laguerre polynomial. The corresponding eigenvalues

$$M_{nJ}^2 = 4\kappa^2\Big(n + \frac{L+J}{2}\Big) \tag{5.30}$$

we will later identify with the meson masses.
Here we do not divide the total angular momentum J into the quantum numbers of the quark–antiquark pair – orbital angular momentum L and internal spin S. Such a model ansatz was done in Refs. [215]-[224]. Because of $J = L$ or $J = L \pm 1$ the present Soft-Wall model generates linear Regge trajectories in both quantum numbers n and J (or L): $M_{nJ}^2 \sim n + J$.

5.2.2. Matching procedure

So far we only dealt with the 'string side' of the model. In the next step we want to make contact with the hadronic world. In order to relate the AdS string mode $\Phi_{nJ}(z)$ to physical states we express for example the pion form factor F defined by

$$\big\langle P'\big|J^\mu(0)\big|P\big\rangle = 2(P+P')^\mu\, F(Q^2) \tag{5.31}$$

in the AdS and light front formalism. In AdS space the form factor is characterized by the transition amplitude between initial and final string mode $\Phi_{nJ}(z)$ [225]

$$F(Q^2) = \int_0^\infty dz \Phi_{nJ}(z) J(Q^2,z) \Phi_{nJ}(z) \tag{5.32}$$

and the current J is given by

$$J(Q^2,z) = \int_0^1 dx\, J_0\Big(zQ\sqrt{\frac{1-x}{x}}\Big)\,, \tag{5.33}$$

where J_0 are the Bessel functions.
Due to the use of light front coordinates and the introduction of the impact variable

ζ the corresponding expression for the electromagnetic form factor of the pion in the light front formalism can be written in a similar form as in Eq. (5.32)

$$F(Q^2) = 2\pi \int_0^1 dx \frac{1-x}{x} \int_0^\infty d\zeta \zeta J_0\big(\zeta Q \sqrt{\frac{1-x}{x}}\big) \widetilde{\rho}(x,\zeta)\,, \tag{5.34}$$

where $\widetilde{\rho}(x,\zeta)$ is the effective parton distribution (details see [225]).

By matching the expressions in Eqs. (5.32) and (5.34) we immediately see that the holographic and impact variables z and ζ have to be equal. Furthermore we obtain the relation

$$\widetilde{\rho}(x,\zeta) = \frac{x}{1-x} \frac{\big|\Phi_{nJ}(\zeta)\big|^2}{2\pi\zeta}\,. \tag{5.35}$$

Since we deal with $q\bar{q}$ mesons we can insert the density for a two–parton system which is proportional to the absolute value of the meson wave function squared

$$\widetilde{\rho}_{n=2}(x,\zeta) = \frac{\big|\widetilde{\psi}_{nJ}(x,\zeta)\big|^2}{(1-x)^2} \frac{1}{P_{q_1\bar{q}_2}}\,. \tag{5.36}$$

Here we also consider the the probability $P_{q_1\bar{q}_2}$ of finding the valence Fock state $\big|q_1\bar{q}_2\big\rangle$ in the meson M. By inserting the two–parton density in Eq. (5.35) we can express the meson wave function $\widetilde{\psi}(\zeta)$ by the string mode $\Phi_{nJ}(z)$:

$$\big|\widetilde{\psi}^{q_1\bar{q}_2}_{nJ}(x,\zeta)\big|^2 = P_{q_1\bar{q}_2}\, x(1-x) \frac{|\Phi_{nJ}(\zeta)|^2}{2\pi\zeta}\,. \tag{5.37}$$

Since the expression for the string mode $\Phi_{nJ}(z)$ is known (see Eq. (5.28)) we can write down the explicit form of the meson wave function

$$\widetilde{\psi}^{q_1\bar{q}_2}_{nL}(x,\zeta) = \sqrt{\frac{P_{q_1\bar{q}_2}}{\pi}} \sqrt{x(1-x)} \sqrt{\frac{n!}{(n+L)!}} \kappa^{1+L} \zeta^L \exp\Big(-\kappa^2\zeta^2/2\Big) L^L_n(\kappa^2\zeta^2)\,. \tag{5.38}$$

For the following calculations it is advantageous to express ζ by the transverse coordinate $\vec{b}_\perp$ which is the Fourier conjugate to the transverse momentum $\vec{k}_\perp$.

$$\zeta^2 = \vec{b}^{\,2}_\perp x(1-x)\,. \tag{5.39}$$

Therefore we obtain

$$\widetilde{\psi}_{nL}^{q_1\bar{q}_2}(x,\vec{b}_\perp) = \sqrt{\frac{P_{q_1\bar{q}_2}}{\pi}}\sqrt{x(1-x)}^{L+1}\sqrt{\frac{n!}{(n+L)!}}\kappa^{1+L}\big|\vec{b}_\perp\big|^L \exp\big(-\kappa^2\vec{b}_\perp^{\,2}x(1-x)/2\big) \times L_n^L(\kappa^2\vec{b}_\perp^{\,2}x(1-x)) \tag{5.40}$$

and the corresponding expression in momentum space $\widetilde{\psi}_{q_1\bar{q}_2}(x,\vec{k}_\perp)$ is derived by taking the Fourier transformation resulting in

$$\begin{aligned}&\psi_{nL}^{q_1\bar{q}_2}(x,\vec{k}_\perp)\\ &= \sqrt{4\pi}\int d^2\vec{b}_\perp^{\,2}e^{i\vec{k}_\perp\vec{b}_\perp}\widetilde{\psi}_{q_1\bar{q}_2}(x,\vec{b}_\perp) \qquad (5.41)\\ &= \frac{\sqrt{P_{q_1\bar{q}_2}}}{\sqrt{x(1-x)}^{L+1}}\sqrt{\frac{n!}{(n+L)!}}\kappa^{1+L}\big|\vec{k}_\perp\big|^L \exp\Big(-\frac{\vec{k}_\perp^{\,2}}{2\kappa^2x(1-x)}\Big)L_n^L\Big(\frac{\vec{k}_\perp^{\,2}}{\kappa^2x(1-x)}\Big)\,.\end{aligned}$$

With the representation (5.40) the probability for a two–parton state can be determined from

$$P_{q_1\bar{q}_2} = \int_0^1 dx\int d^2b|\widetilde{\psi}_{q_1\bar{q}_2}(x,\vec{b}_\perp)|^2 \le 1\,, \tag{5.42}$$

where we restrict in the following to the case of $P_{q_1\bar{q}_2} = 1$. The only exceptions are the pions and kaons with $P_{q_1\bar{q}_2} = 0.6$ and 0.8, respectively. Here the probabilities for the two–parton states were fitted to data.

In the next step we consider the quark masses which have been neglected so far. The inclusion of finite quark masses has been considered by Brodsky and de Téramond [226]. We illustrate this procedure by means of the ground state LFWFs in momentum space (5.41)

$$\psi_{n=0,L=0}^{q_1\bar{q}_2}(x,\vec{k}_\perp) = \frac{4\pi}{\kappa\sqrt{x(1-x)}}\exp\Big(-\frac{\vec{k}_\perp^{\,2}}{2\kappa^2x(1-x)}\Big)\,. \tag{5.43}$$

The quark masses are introduced by extending the kinetic energy of massless quarks by

$$\frac{\vec{k}_\perp^{\,2}}{x(1-x)} \to \frac{\vec{k}_\perp^{\,2}}{x(1-x)} + m_{12}^2\,, \quad m_{12}^2 = \frac{m_1^2}{x} + \frac{m_2^2}{1-x}\,. \tag{5.44}$$

which is equivalent to the following modification of the kinetic term in the Schrödinger

EoM (5.27)

$$-\frac{d^2}{d\zeta^2} \to -\frac{d^2}{d\zeta^2} + m_{12}^2 \,. \tag{5.45}$$

Finally, we obtain for the ground state wave function

$$\psi^{q_1\bar{q}_2}_{n=0,L=0}(x,\vec{k}_\perp) = \frac{4\pi N}{\kappa\sqrt{x(1-x)}} e^{-\frac{\vec{k}_\perp^2}{2\kappa^2 x(1-x)} - \frac{m_{12}^2}{2\kappa^2}} \,. \tag{5.46}$$

The quark mass term in the exponential of Eq. (5.46) can be absorbed in the longitudinal mode $f(x,m_1,m_2)$ (see [227])

$$f(x,m_1,m_2) \equiv N\, e^{-\frac{m_{12}^2}{2\kappa^2}} \,, \tag{5.47}$$

where N is the normalization constant determined from

$$1 = \int\limits_0^1 dx\, f^2(x,m_1,m_2) \,. \tag{5.48}$$

Hence, when dealing with meson LFWFs with massive quarks we only have to multiply the transversal wave function for massless quarks in Eq. (5.37) by the longitudinal mode [227]:

$$\widetilde{\psi}^{q_1\bar{q}_2}_{nJ}(x,\zeta,m_1,m_2) = \frac{\Phi_{nJ}(\zeta)}{\sqrt{2\pi\zeta}} f(x,m_1,m_2)\,\sqrt{x(1-x)} \,. \tag{5.49}$$

In this context we would like to mention that the way how massive quarks are introduced is not unique. In particular, the dimensional parameter entering in the longitudinal mode $f(x,m_1,m_2)$ should not necessarily be identified with the parameter κ characterizing the dilaton field. Later, in the analysis of the mass spectrum and the decay constants of heavy–light mesons, we will show that the dilaton parameter κ should scale as $\mathcal{O}(1)$ in the $1/m_Q$ expansion, where m_Q is the heavy quark mass, while the dimensional parameter in the longitudinal mode behaves like $\mathcal{O}(m_Q^{1/2})$. In the case of heavy quarkonia the dimensional parameter in the longitudinal mode should scale as $\mathcal{O}(m_Q)$. Hence, we will replace κ by an additional scale parameter parameter λ_{12} for the longitudinal mode of Eq. (5.46)

$$f(x,m_1,m_2) \equiv N\, e^{-\frac{m_{12}^2}{2\lambda_{12}^2}} \,. \tag{5.50}$$

The values for λ_{12} are determined for each meson flavor separately while the parameter κ in the transversal part of Eq. (5.46) is kept constant for all mesons.

Due to the inclusion of massive quarks the meson mass spectrum is modified which is now derived by computing the matrix element $\langle\phi|\mathcal{M}^2_{nJ}|\phi\rangle = \langle\phi|H_{LF}|\phi\rangle$ [227]:

$$M^2_{nJ} = \int_0^\infty d\zeta\, \Phi_{nJ}(\zeta)\left(-\frac{d^2}{d\zeta^2} - \frac{1-4L^2}{4\zeta^2} + \kappa^4\zeta^2 + 2\kappa^2(J-1)\right)\Phi_{nJ}(\zeta) + \int_0^1 dx\left(\frac{m_1^2}{x} + \frac{m_2^2}{1-x}\right) f^2(x, m_1, m_2)\,. \tag{5.51}$$

The inclusion of finite quark masses leads to an additional term in the mass spectrum which results in a shift of the meson masses. It is important to note that the potential in Eq. (5.51) is not complete since it includes confinement forces but does not consider all effects of chiral symmetry breaking, which are important for the infrared structure of QCD (see e.g. the discussion in Refs. [228, 229, 230, 125, 231, 232, 233, 224]). Moreover, it does not contain hyperfine splitting terms and the one–gluon exchange term, which is sufficient for the description of bottomia hadrons. In the following we will improve the AdS/CFT model accordingly by including hyperfine–splitting and one–gluon exchange.

5.2.3. One–gluon exchange and hyperfine–splitting contributions to the effective meson potential

In the following sections we discuss the phenomenological inclusion of one–gluon exchange and hyperfine–splitting terms by extending the effective potential by appropriate terms

$$U \to U + U_{\rm C} + U_{\rm HF}\,, \tag{5.52}$$

where $U_{\rm C}$ is the color Coulomb potential arising due to the one–gluon exchange and $U_{\rm HF}$ represents the hyperfine (HF) splitting contribution (see Ref. [28]).

From experiment it is known that the Regge–trajectories of bottomia states deviate from linearity [234, 235] since the one–gluon exchange term gives rise to an additional Coulomb–like interaction between quarks $V(r) = -4\alpha_s/3r$, where α_s is the strong coupling constant. The contribution of the effective meson potential $U_{\rm C}(\zeta)$to the mass spectrum M^2 is negative and proportional to the quark mass squared [235, 234]

$$U_{\rm C}(\zeta) = -\frac{\sigma}{\zeta}\,, \tag{5.53}$$

where the coupling constant σ is determined by

$$\sigma = \frac{64\alpha_s^2 m_1 m_2}{9\,(n+L+1)^2}\left\{\int\limits_0^\infty \frac{d\zeta}{\zeta}\,\Phi_{nJ}^2(\zeta)\right\}^{-1}. \tag{5.54}$$

The inclusion of the Color coulomb potential leads to the following shift of the mass spectrum

$$\Delta M_{\rm C}^2 = -\frac{64\alpha_s^2 m_1 m_2}{9\,(n+L+1)^2}\,, \tag{5.55}$$

where α_s is the QCD coupling considered as a free parameter. Since the quark masses enter linearly the one–gluon exchange term can be neglected for light mesons and charmonia while it becomes important for the bottomia states.

For the hyperfine–splitting potential $U_{\rm HF}(\zeta)$ one can use an effective operator containing a free parameter v (softening the original δ-functional form of the HF-potential) with dimension M^3 (see details in Refs. [236, 237]):

$$U_{\rm HF}(\zeta) = \frac{32\pi\alpha_s}{9}\,\frac{\vec{\sigma}_1\cdot\vec{\sigma}_2}{\mu_{12}}\,v\,, \tag{5.56}$$

where $\vec{\sigma}_1$ and $\vec{\sigma}_2$ are the spin operators of the quarks;

$$\mu_{12} = 2m_1m_2/(m_1+m_2)\,. \tag{5.57}$$

Projecting the operator $\vec{\sigma}_1\cdot\vec{\sigma}_2$ between meson states with $S=0$ and 1 gives

$$\beta_S = \langle M_S|\vec{\sigma}_1\cdot\vec{\sigma}_2|M_S\rangle = \left\{\begin{array}{ll} -3\,, & S=0 \\ 1\,, & S=1 \end{array}\right. . \tag{5.58}$$

Therefore, the mass shift due to the hyperfine–splitting potential is

$$\Delta M_{\rm HF}^2 = \frac{32\pi\alpha_s}{9}\,\frac{\beta_S\,v}{\mu_{12}}\,. \tag{5.59}$$

Finally, the master formula for meson masses including confinement, finite quark

masses, color Coulomb and hyperfine–splitting effects reads

$$M_{nJ}^2 = 4\kappa^2\Big(n+\frac{L+J}{2}\Big) + \int\limits_0^1 dx\Big(\frac{m_1^2}{x}+\frac{m_2^2}{1-x}\Big) f^2(x,m_1,m_2) - \frac{64\alpha_s^2 m_1 m_2}{9\,(n+L+1)^2} + \frac{32\pi\alpha_s}{9}\,\frac{\beta_S\, v}{\mu_{12}}\,. \tag{5.60}$$

There are two comments that should be made with respect to further modifications of the potential U:

1. In principle it is not excluded that the dilaton scale parameter might be different for distinct types of mesons – light and heavy ones (details see Ref. [238]). In particular, we observe that the use of a larger value for κ for heavy mesons helps to improve the description of the mass spectrum and the leptonic decay constants.

2. One could add a constant term c^2 to the effective potential which is independent on the parameter κ and controls the masses of the ground states as discussed in Ref. [239]. In our formalism such a constant term in the effective potential can be e.g. generated by an additional shift of the "dressed" mass term $\mu_J^2(z) \to \mu_J^2(z) + c^2 z^2/R^2$, which leads to the following modification of the mass spectrum: $M_{nJ}^2 \to M_{nJ}^2 + c^2$.

Although, both of these modifications can improve the description of meson properties, their appearance in the AdS action is not well justified. Therefore, in the present discussion we do not consider these options and postpone them for future study.

5.3. Properties of light and heavy mesons

In the following we compute the mass spectra and decay constants of light and heavy mesons within the framework of the AdS model introduced in the previous sections. There are several model parameters which need to be determined: quark masses, the dilaton parameter κ, the scale parameter λ_{12} of the longitudinal mass term, the strong coupling constant α_s and the parameter v entering in the HF splitting term. In particular we use the following constituent quark masses

$$m = 420\ \text{MeV}\,, \quad m_s = 570\ \text{MeV}\,, \quad m_c = 1.6\ \text{GeV}\,, \quad m_b = 4.8\ \text{GeV}\,, \tag{5.61}$$

where we restrict ourselves to the isospin limit, hence, we set $m_u = m_d = m$.

The parameters are determines from a least square fit to the mass spectrum and the decay constants of light and heavy mesons [28]. Here the unified value of the dilaton parameter $\kappa = 550$ MeV remains constant for all mesons while the dimensional parameters λ_{12} in the longitudinal wave functions are fitted as:

$$\begin{aligned}
&\lambda_{qq} = 0.63GeV\,, && \lambda_{us} = 1.2\text{GeV}\,, && \lambda_{ss} = 1.68\text{GeV}\,,\\
&\lambda_{qc} = 2.5\ \text{GeV}\,, && \lambda_{sc} = 3.0\ \text{GeV}\,, && \lambda_{qb} = 3.89\ \text{GeV}\,,\\
&\lambda_{sb} = 4.18\ \text{GeV}\,, && \lambda_{cc} = 4.04\ \text{GeV}\,, && \lambda_{cb} = 4.82\ \text{GeV}\,,\\
&\lambda_{bb} = 6.77\ \text{GeV}\,.
\end{aligned} \tag{5.62}$$

The strong coupling constant $\alpha_s \equiv \alpha_s(\mu_{12}^2)$ which enters in the additional Color coulomb and HF splitting potentials is consistently calculated using the parametrization of α_s with "freezing" [240]:

$$\alpha_s(\mu^2) = \frac{12\pi}{(33-2N_f)\ln\dfrac{\mu^2+M_B^2}{\Lambda^2}} \tag{5.63}$$

where N_f is the number of flavors, Λ is the QCD scale parameter and M_B is the background mass. Choosing $\Lambda = 420$ MeV and $M_B = 854$ MeV we obtain the following set of parameters α_s:

$$\begin{aligned}
&\alpha_s(\mu_{qq}^2) = 0.79\,, && \alpha_s(\mu_{qs}^2) = 0.77\,, && \alpha_s(\mu_{ss}^2) = 0.78\,,\\
&\alpha_s(\mu_{qc}^2) = 0.68\,, && \alpha_s(\mu_{sc}^2) = 0.67\,, && \alpha_s(\mu_{ub}^2) = 0.64\,,\\
&\alpha_s(\mu_{sb}^2) = 0.61\,, && \alpha_s(\mu_{cc}^2) = 0.52\,, && \alpha_s(\mu_{cb}^2) = 0.42\,,\\
&\alpha_s(\mu_{bb}^2) = 0.33\,,
\end{aligned} \tag{5.64}$$

where $q = u, d$.
Finally, the hyperfine–splitting parameter v has the value $v = 10^{-4}$ GeV^3.

5.3.1. Mass spectrum of light mesons

The mass spectrum of mesons can now be easily computed from the expression of Eq. (5.60). In the case of the light mesons we only need to consider the probabilities of the ground state pion and kaon, $P_\pi = 0.6$ and $P_K = 0.8$, which were fitted to data. For all other mesons the probabilities are supposed to be equal to one.
The predictions of our approach for the light meson spectrum according to the $n^{2S+1}L_J$ classification are given in Tab. 5.1. For the scalar mesons f_0 we present results for two limiting cases: with nonstrange flavor content $f_0[\bar{n}n] = (\bar{u}u + \bar{d}d)/\sqrt{2}$ and with a strange one $f_0[\bar{s}s] = \bar{s}s$. Provided data are available, the mass spectra are graphically depicted in Fig. 5.5. The mass spectrum obtained by the AdS model (solid line) slightly overestimates the meson masses determined from experiment

Meson	n	L	S	Mass [MeV]			
π	0	0,1,2,3	0	$M_{\pi(140)} = 140$	$M_{b_1(1235)} = 1355$	$M_{\pi_2(1670)} = 1777$	$M_{\pi_4} = 2099$
π	0,1,2,3	0	0	$M_{\pi(140)} = 140$	$M_{\pi(1300)} = 1355$	$M_{\pi(1800)} = 1777$	$M_{\pi(4s)} = 2099$
K	0	0,1,2,3	0	$M_K = 495$	$M_{K_1} = 1505$	$M_{K_2} = 1901$	$M_{K_3} = 2207$
η	0,1,2,3	0	0	$M_{\eta(1s)} = 544$	$M_{\eta(2s)} = 1552$	$M_{\eta(3s)} = 1946$	$M_{\eta(4s)} = 2248$
$f_0[\bar{n}n]$	0,1,2,3	1	1	$M_{f_0(1p)} = 1114$	$M_{f_0(2p)} = 1600$	$M_{f_0(3p)} = 1952$	$M_{f_0(4p)} = 2244$
$f_0[\bar{s}s]$	0,1,2,3	1	1	$M_{f_0(1p)} = 1304$	$M_{f_0(2p)} = 1762$	$M_{f_0(3p)} = 2093$	$M_{f_0(4p)} = 2372$
$a_0(980)$	0,1,2,3	1	1	$M_{a_0(1p)} = 1114$	$M_{a_0(2p)} = 1600$	$M_{a_0(3p)} = 1952$	$M_{a_0(4p)} = 2372$
$\rho(770)$	0,1,2,3	0	1	$M_{\rho(770)} = 804$	$M_{\rho(1450)} = 1565$	$M_{\rho(1700)} = 1942$	$M_{\rho(4s)} = 2240$
$\rho(770)$	0	0,1,2,3	1	$M_{\rho(770)} = 804$	$M_{a_2(1320)} = 1565$	$M_{\rho_3(1690)} = 1942$	$M_{a_4(2040)} = 2240$
$\omega(782)$	0,1,2,3	0	1	$M_{\omega(782)} = 804$	$M_{\omega(1420)} = 1565$	$M_{\omega(1650)} = 1942$	$M_{\omega(4s)} = 2240$
$\omega(782)$	0	0,1,2,3	1	$M_{\omega(782)} = 804$	$M_{f_2(1270)} = 1565$	$M_{\omega_3(1670)} = 1942$	$M_{f_4(2050)} = 2240$
$\phi(1020)$	0,1,2,3	0	1	$M_{\phi(1s)} = 1019$	$M_{\phi(2s)} = 1818$	$M_{\phi(3s)} = 2170$	$M_{\phi(4s)} = 2447$
$a_1(1260)$	0,1,2,3	1	1	$M_{a_1(1p)} = 1358$	$M_{a_1(2p)} = 1779$	$M_{a_1(3p)} = 2101$	$M_{a_1(4p)} = 2375$

Table 5.1.: Results for the light meson spectrum.

indicated by black dots.

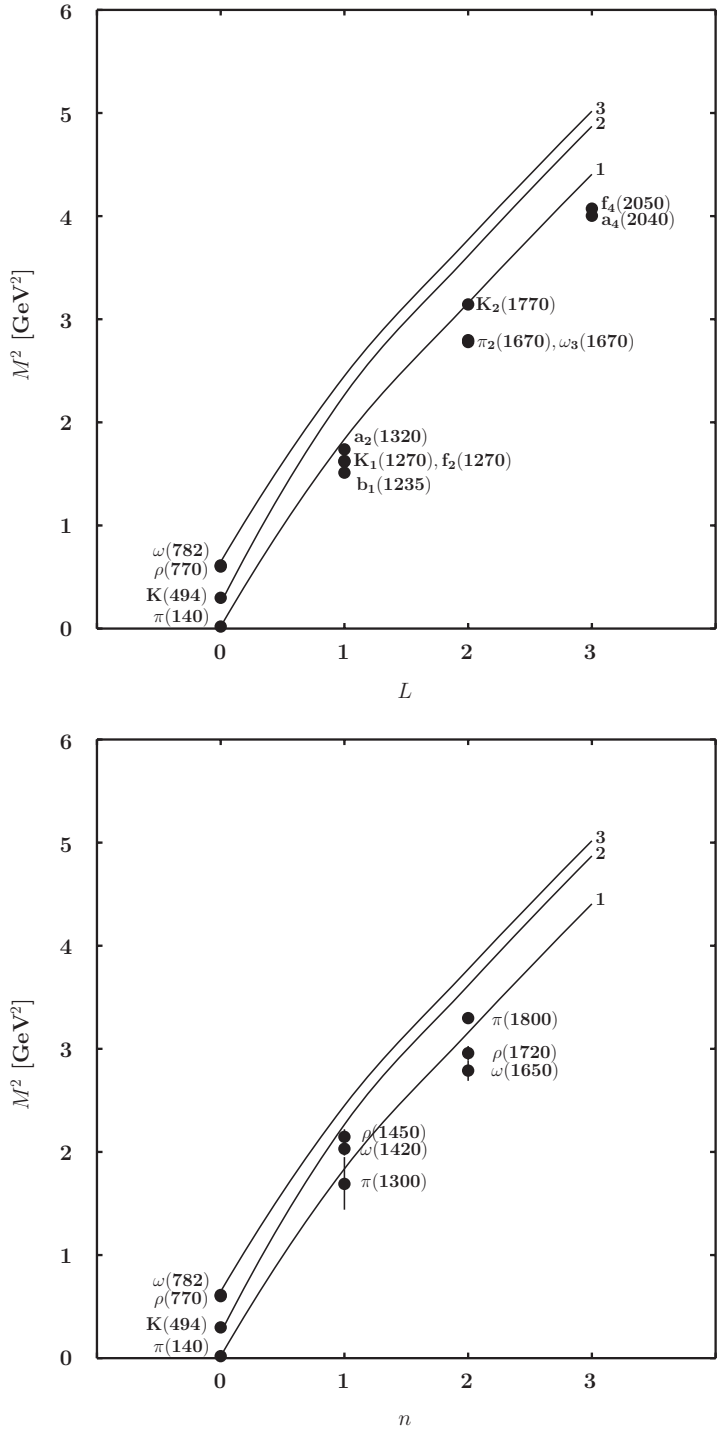

Figure 5.5.: Mass spectra of π, K, ρ and ω mesons in dependence on L and n. Experimental meson states are indicated by black dots where mass values in MeV are indicated in brackets.

In Fig. 5.6 we indicate the contributions of the one–gluon and HF splitting terms for the mass spectrum of the ρ mesons. The solid line represents the full potential including the one–gluon and HF splitting potentials U_{HF} and U_C, whereas the dotted line corresponds to the mass spectrum when neglecting both contributions. The difference between the two spectra arises almost completely from the color coulomb potential which is proportional to $1/(n+L+1)^2$. Therefore its contribution becomes larger for small values of n. In contrast, as it is expected hyperfine–splitting contributions only lead to a negligible offset by about $2 \cdot 10^{-3}$ GeV which cannot be displayed in Fig. 5.6.

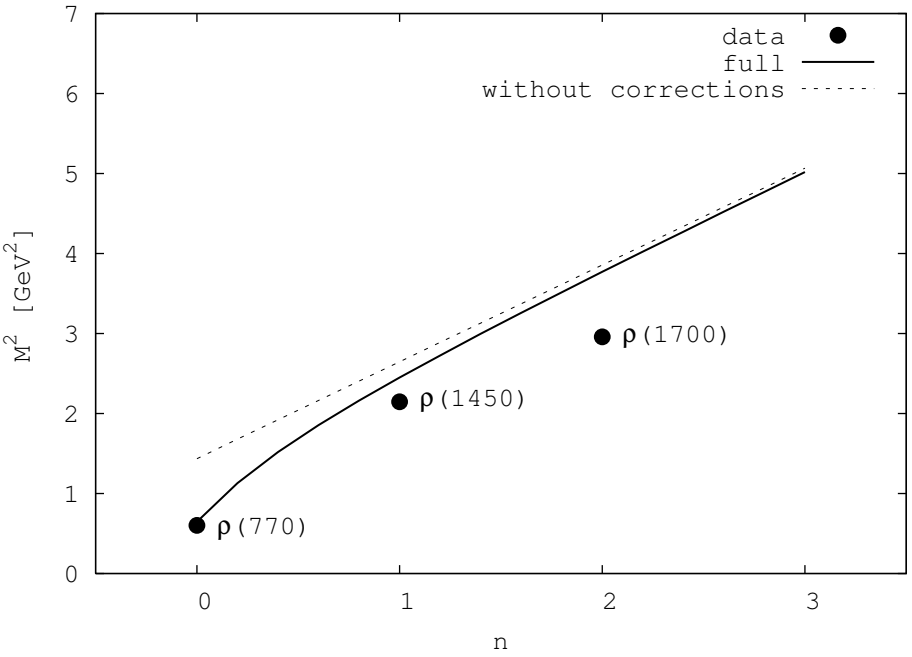

Figure 5.6.: Contributions of the color coulomb and HF potentials to the mass spectrum of the ρ mesons.

5.3.2. Mass spectrum of heavy–light mesons

Before we apply our approach to the properties of heavy–light mesons we need to check if our LFWFs are consistent with model–independent constraints imposed e.g. by heavy quark symmetry ($m_Q \to \infty$).
The mass spectrum of heavy-light mesons is also given by Eq. 5.60 and the longitudinal mode for heavy–light mesons is of the form

$$f(x, m_q, m_Q) \equiv N\, e^{-\dfrac{m_{qQ}^2}{2\lambda_{qQ}^2}}\,, \tag{5.65}$$

where λ_{qQ} is the dimensional parameter which scales as $\mathcal{O}(m_Q^{1/2})$. In the following we express λ_{qQ} as $\lambda_{qQ}^2 = m_q m_Q / r$, where r is a parameter of order $\mathcal{O}(1)$. The scaling of the parameter $\kappa \sim \mathcal{O}(1)$ is fixed by the scaling law of the leptonic constants of heavy–light mesons in the heavy quark limit (see discussion in section 5.3.4). This behavior of κ is also consistent with the mass spectrum of heavy–light mesons constrained by heavy quark effective theory (HQET) [9]. In particular, the $1/m_Q$ expansion of their masses should be

$$M_{qQ} = m_Q + \bar{\Lambda} + \mathcal{O}(1/m_Q)\,, \tag{5.66}$$

where the scale parameter $\bar{\Lambda}$ is of order $\mathcal{O}(1)$, and the mass splitting of vector and pseudoscalar states $\Delta M_{qQ} = M_{qQ}^V - M_{qQ}^P$ should be of order $1/m_Q$:

$$\Delta M_{qQ} = \frac{2}{M_{qQ}^V + M_{qQ}^P} \left(\kappa^2 + \frac{64\pi\alpha_s}{9} \frac{\beta_S\, v}{m_q} \right) \sim \frac{1}{m_Q}\,. \tag{5.67}$$

The mass splitting ΔM_{qQ} gets contributions from two sources — confinement and the hyperfine–splitting potential. Both contributions are of order $\mathcal{O}(1)$ in the heavy quark mass expansion. In Appendix B.1 we evaluate the r.h.s. of Eq. (5.60) and give an expression for the scale parameter $\bar{\Lambda}$.

Meson	$J^{\rm P}$	n	L	S	Mass [MeV]			
$D(1870)$	0^-	0	0,1,2,3	0	1857	2435	2696	2905
$D^*(2010)$	1^-	0	0,1,2,3	1	2015	2547	2797	3000
$D_s(1969)$	0^-	0	0,1,2,3	0	1963	2621	2883	3085
$D_s^*(2107)$	1^-	0	0,1,2,3	1	2113	2725	2977	3173
$B(5279)$	0^-	0	0,1,2,3	0	5279	5791	5964	6089
$B^*(5325)$	1^-	0	0,1,2,3	1	5336	5843	6015	6139
$B_s(5366)$	0^-	0	0,1,2,3	0	5360	5941	6124	6250
$B_s^*(5413)$	1^-	0	0,1,2,3	1	5416	5992	6173	6298

Table 5.2.: Masses of heavy–light mesons

Our results for the mass spectra of heavy–light mesons are indicated in Tab. 5.2 for different spin–parity quantum numbers ($n^{2S+1}L_J$), where the first column contains the ground state mesons.

5.3.3. Mass spectrum of heavy quarkonia

In analogy to the heavy–light mesons we first consider the heavy quark limit of our expressions before we turn to the numerical results. Here we follow the idea suggested in [227], and express the longitudinal momentum fractions through the z-component of the internal momentum $\vec{k} = (\vec{k}_\perp, k_z)$ as (see also [241]):

$$x = \frac{e_1 + k_z}{e_1 + e_2}\,, \quad 1 - x = \frac{e_2 - k_z}{e_1 + e_2}\,, \tag{5.68}$$

where $e_i = \sqrt{m_{Q_i}^2 + \vec{k}^{\,2}}$ and $\vec{k}^{\,2} = \vec{k}_\perp^{\,2} + k_z^2$. When considering the heavy quark limit $m_{Q_1}, m_{Q_2} \gg \vec{k}_\perp, k_z$ we get

$$x = \frac{m_{Q_1} + k_z}{m_{Q_1} + m_{Q_2}} + \mathcal{O}(1/m_Q^2)\,, \quad 1 - x = \frac{m_{Q_2} - k_z}{m_{Q_1} + m_{Q_2}} + \mathcal{O}(1/m_Q^2)\,. \tag{5.69}$$

Hence, we have

$$\frac{m_{Q_1}^2}{x} + \frac{m_{Q_2}^2}{1 - x} = (m_{Q_1} + m_{Q_2})^2 + \mathcal{O}(1)\,. \tag{5.70}$$

The leading term of the integral containing the longitudinal mode is simply given by $(m_{Q_1} + m_{Q_2})^2$ which is the leading contribution to the mass squared of the heavy quarkonia. This means that we correctly reproduce the expansion of the heavy quarkonia mass in the heavy quark limit:

$$M_{Q_1\bar{Q}_2} = m_{Q_1} + m_{Q_2} + E + \mathcal{O}(1/m_{Q_{1,2}})\,, \tag{5.71}$$

where E is the binding energy.

For the mass spectrum of heavy $(Q_1\bar{Q}_2)$ quarkonia, charmonium and bottomium mesons, we present our results in Tab. 5.3. The quality of our theoretical model can be judged from Figs. 5.7 and 5.8 where we graphically compare the mass spectrum of the AdS/CFT approach to data (central values by black circles and sizable error bars by vertical lines). Here we find that the calculated mass spectra are in agreement with predictions of other holographic models (see e.g. Refs. [242, 11, 228]). We clearly see that the masses of bottomia states, at least the low lying ones, strongly deviate from the Regge–like behavior. This fact can be reproduced by the present holographic model due to the consideration of the Color coulomb potential which bends down the lines for low values of L or n. Since the Color coulomb potential is proportional to $1/(n + L + 1)$ its influence is stronger for the fitted ground states J/ψ, $\eta_c(1S)$, $\Upsilon(1S)$ and $\eta_b(1S)$ than for the orbital excitations $\chi_{cn}(1P)$ and $\chi_{bn}(1P)$. This is the reason for the overestimate of the $\chi_{cn}(1P)$ and $\chi_{bn}(1P)$ meson masses in Figs. 5.7 and 5.8.

Meson	J^{P}	n	L	S	Mass [MeV]			
$\eta_c(2986)$	0^-	0,1,2,3	0	0	2997	3717	3962	4141
$\psi(3097))$	1^-	0,1,2,3	0	1	3097	3798	4038	4213
$\chi_{c0}(3414)$	0^+	0,1,2,3	1	1	3635	3885	4067	4226
$\chi_{c1}(3510)$	1^+	0,1,2,3	1	1	3718	3963	4141	4297
$\chi_{c2}(3555)$	2^+	0,1,2,3	1	1	3798	4038	4213	4367
$\eta_b(9300)$	0^-	0,1,2,3	0	0	9428	10190	10372	10473
$\Upsilon(9460)$	1^-	0,1,2,3	0	1	9460	10219	10401	10502
$\chi_{b0}(9860)$	0^+	0,1,2,3	1	1	10160	10343	10444	10521
$\chi_{b1}(9893)$	1^+	0,1,2,3	1	1	10190	10372	10473	10550
$\chi_{b2}(9912)$	2^+	0,1,2,3	1	1	10219	10401	10502	10579
$B_c(6276)$	0^-	0,1,2,3	0	0	6276	6911	7092	7209

Table 5.3.: Masses of heavy quarkonia $c\bar{c}$, $b\bar{b}$ and $c\bar{b}$

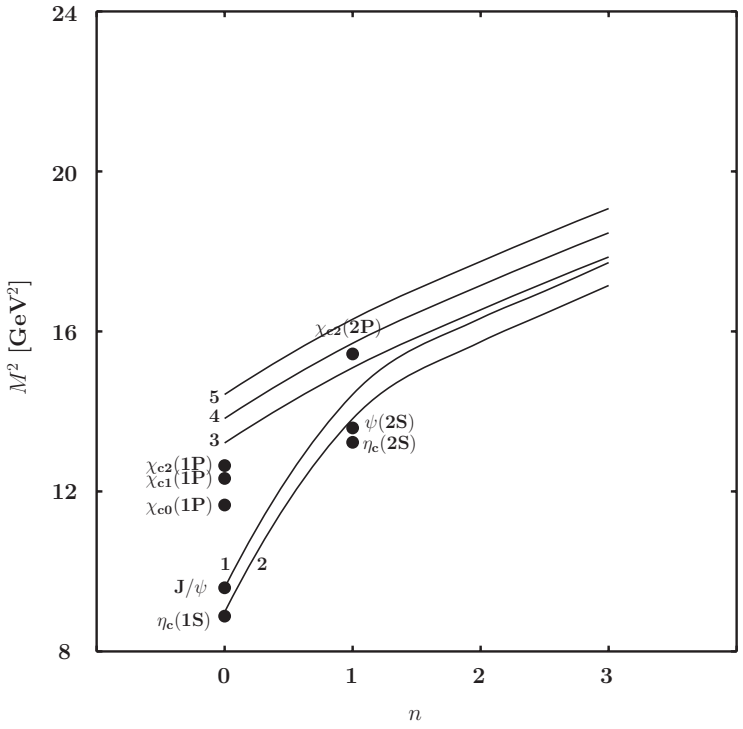

Figure 5.7.: Mass spectra of charmonium states.

The influence of the one–gluon exchange term can also be seen from Fig. 5.9, where we compare the mass spectra of the full potential (solid line) and when neglecting

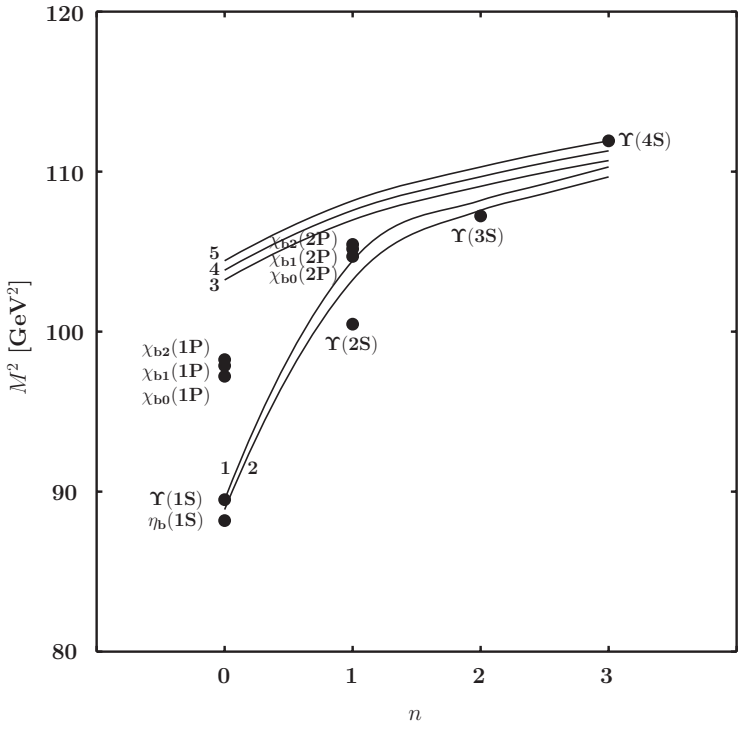

Figure 5.8.: Mass spectra of bottonium states.

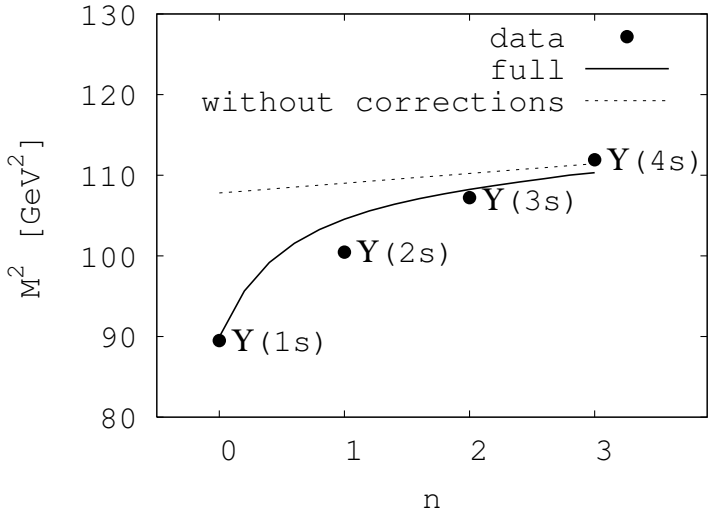

Figure 5.9.: Contribution of the color coulomb potential to the mass spectrum of the $\Upsilon(ns)$ mesons.

HF and Color coulomb terms are switched off (dotted line). In analogy to the mass spectrum of the ρ meson the hyperfine–splitting term leads to a negligible offset. Therefore the difference between both lines can be traced to the influence of the Color coulomb potential. When neglecting the one–gluon exchange term the lines show a linear Regge behavior which leads to a severe overestimate for the $n = 0$ and 1 states.

5.3.4. Leptonic and radiative meson decay constants

Besides the masses of the light and heavy mesons we also use the holographic approach to calculate the radiative and leptonic decay constants of the ground state mesons.
The decay constants are defined by

$$\langle 0|\bar{q}_2(0)\gamma^\mu\gamma^5 q_1(0)|M_P(P)\rangle = iP^\mu\, f_P \tag{5.72}$$

for pseudoscalar (f_P) mesons and

$$\langle 0|\bar{q}_2(0)\gamma^\mu q_1(0)|M_V(P,\lambda)\rangle = \epsilon^\mu(P,\lambda)\, M_V\, f_V \tag{5.73}$$

when dealing with vector (f_V) mesons. For the Fock states M_P and M_V we use the definitions of Eqs. (5.20) and (5.21).
For convenience we determine the decay constants by restricting to the $\mu = +$ component and spin projection $\lambda = 0$. In this case Eqs. (5.72) and (5.73) read

$$\left\langle 0\middle|\bar{q}_2(0)\gamma^+\gamma^5 q_1(0)\middle|P\right\rangle = P^+ f_P\,, \tag{5.74}$$
$$\left\langle 0\middle|\bar{q}_2(0)\gamma^+ q_1(0)\middle|V(P,\lambda=0)\right\rangle = P^+ f_V\,. \tag{5.75}$$

A detailed description of the calculational technique for determining these quantity can be found in Appendix B.2. Finally, we get for the decay constants of the ground state mesons:

$$f_P = f_V \;=\; 2\sqrt{6}\int_0^1 dx \int \frac{d^2\vec{k}_\perp}{16\pi^3}\psi_{q_1\bar{q}_2}(x,\vec{k}_\perp)\, f(x,m_1,m_2) \tag{5.76}$$

$$= \sqrt{\frac{6}{\pi}}\int_0^1 dx\, \tilde{\psi}_{q_1\bar{q}_2}(x,\vec{b}_\perp = 0)\, f(x,m_1,m_2)$$

$$= \kappa\frac{\sqrt{6}}{\pi}\int_0^1 dx \sqrt{x(1-x)}\, f(x,m_1,m_2)\,. \tag{5.77}$$

In the case of massless quarks f_P and f_V are proportional to the dilaton scale

parameter κ and the $f_{P(V)}$ are of the simple form:

$$f_P = f_V = \frac{\kappa\sqrt{6}}{8}\,. \tag{5.78}$$

In the other extreme of the heavy quark limit ($m_Q \to \infty$) the scaling of the leptonic decay constants of heavy–light mesons is in agreement with HQET:

$$f_P^{\rm HQL} = f_V^{\rm HQL} = \kappa\frac{\sqrt{6}}{\pi}\sqrt{\frac{m_q}{m_Q}}\,\frac{\int\limits_0^\infty dz\, e^{-\frac{r}{2}(z+\frac{1}{z})}}{\left[\int\limits_0^\infty dz\, e^{-r(z+\frac{1}{z})}\right]^{1/2}} \;\sim\; \frac{1}{\sqrt{m_Q}}\,. \tag{5.79}$$

Again, as in the case of the mass spectrum of heavy–light mesons, it is sufficient to propose the following scaling of dimensional parameters in our holographic approach: $\kappa \sim \mathcal{O}(1)$ and $\lambda_{qQ} \sim \mathcal{O}(\sqrt{m_Q})$.

When dealing with vector mesons with hidden flavor one additionally needs to consider the flavor factor c_V

$$c_V = \begin{cases} 1/\sqrt{2}\,, & V = \rho^0 \\ 2/3\,, & V = J/\psi \\ 1/3\,, & V = \phi, \Upsilon \\ 1/(3\sqrt{2})\,, & V = \omega \end{cases} \tag{5.80}$$

which arises from the flavor structure of the vector mesons

$$\rho^0 = \frac{1}{\sqrt{2}}\big(\bar{u}u - \bar{d}d\big),\quad \omega = \frac{1}{\sqrt{2}}\big(\bar{u}u + \bar{d}d\big),\quad \phi = -\bar{s}s,\quad J/\psi = \bar{c}c,\quad \Upsilon = -\bar{b}b \tag{5.81}$$

and the structure of the corresponding electromagnetic quark currents

$$V^\mu_{\rho,\omega} \;=\; e_u\bar{u}\gamma^\mu u + e_d\bar{d}\gamma^\mu d\,, \tag{5.82}$$

$$V^\mu_{\phi,J/\psi,\Upsilon} \;=\; e_q\bar{q}\gamma^\mu q,\ \text{with } q = s,c,b\,. \tag{5.83}$$

Our results for f_P and f_V are presented in Tabs. 5.4-5.6, where in particular the decay constants of the light mesons are in good agreement with data.

The decay constants for heavy–light and double–heavy mesons underestimate available data. The reason for this effect is the use of the universal dilaton scale parameter $\kappa = 550$ MeV which enters linearly in the leptonic decay constants (see Eq. (5.77)). Therefore we would need a slightly enhanced value for the parameter κ in the case of heavy–light mesons and an even larger value for κ in the case of the leptonic decay constants of heavy quarkonia states. In particular, it should be roughly 2, 3 and 4

times larger for $c\bar{c}$, $c\bar{b}$ and $b\bar{b}$ states, respectively, than the unified value of 550 MeV.

Meson	Data [174] [MeV]	f_P [MeV]
π^-	$130.4 \pm 0.04 \pm 0.2$	131
K^-	$155.5 \pm 0.2 \pm 0.8$	155
D^+	205.8 ± 8.9	167
D_s^+	273 ± 10	170
B^-	216 ± 22	139
B_s^0	$253 \pm 8 \pm 7$	144
B_c	$489 \pm 5 \pm 3$ [206]	159

Table 5.4.: Decay constants f_P of pseudoscalar mesons

Meson	Data [MeV]	f_V [MeV]
ρ^+	210.5 ± 0.6 [174]	170
D^*	$245 \pm 20^{+3}_{-2}$ [207]	167
D_s^*	$272 \pm 16^{+3}_{-20}$ [208]	170
B^*	$196 \pm 24^{+39}_{-2}$ [207]	139
B_s^*	$229 \pm 20^{+41}_{-16}$ [207]	144

Table 5.5.: Decay constants f_V of vector mesons with open flavor

Meson	Data [174] [MeV]	f_V [MeV]
ρ^0	154.7 ± 0.7	120
ω	45.8 ± 0.8	40
ϕ	76 ± 1.2	58
J/ψ	277.6 ± 4	116
$\Upsilon(1s)$	238.5 ± 5.5	56

Table 5.6.: Decay constants f_V of vector mesons with hidden flavor

5.4. Summary

In summary, we present an analysis of the mass spectrum and decay properties of light, heavy–light mesons and heavy quarkonia in an holographic soft-wall model using the conventional sign of the dilaton profile with $\phi(z) = \kappa^2 z^2$. In our calculations we consider in addition one-gluon exchange and hyperfine–splitting corrections phenomenologically by modifying the potential. The improvement of the present approach is that a consistent description of light, heavy-light and double-heavy mesons is achieved within the same holographic model. So far in the literature different values for the dilaton parameter κ have been used for mesons with different J^P and flavor quantum numbers. Furthermore we show that the obtained results for heavy–light mesons are consistent with constraints imposed by HQET.
As already mentioned, we use a universal value of κ which leads to mass spectra which are in quite good agreement with available data. The holographic approach reproduces the decay constants of the light mesons while the decay properties for the mesons containing heavy quarks are underestimated. Adjusted flavor dependent values for κ for different types of mesons lead of course to a better fit to the data. The present AdS/QCD approach can also be extended to baryons which is an interesting topic for future research projects.

6. Conclusions

The identification and description of the structure of hadrons is still one of the major challenges in particle physics. Especially recently discovered meson states in the heavy sector cannot be explained in the standard description of the constituent quark model extending the list of 'unusual' hadron resonances. It is very likely that this trend will continue with the running and upcoming experiments giving access to a higher mass range and, because of higher statistics, delivering more precise data. In this thesis we discussed different aspects of meson spectroscopy and the related problems in the light of the recent experimental advances. Since it is clear that the naive approach or the constituent quark model is not sufficient to explain the full features of the meson spectrum interest grew over the last years in the subject of hadron spectroscopy. Here, the discovery of numerous charmonium-like X, Y and Z states at the B factories (see Chapters 3 and 4) and of narrow D_{sJ} states (see $D^*_{s2}(2573)$ in Chapter 3) were among the highlights in the last decade and have fueled non–$q\bar{q}$ structure interpretations. These are some of the reasons why we focus on both structures—ordinary $q\bar{q}$ mesons but we also discussed exotic meson structures, in particular we studied bound states of mesons.

At the beginning, in Chapter 2, we shortly introduced the mesons discussed here including the present experimental status and the most common theoretical interpretations. The structure issues of mesons and their properties were analyzed with three different theoretical methods ranging from the dynamical generation of meson resonances to an holographic AdS/QCD model based on extra dimensions. The aim of this work was to cover several issues of meson spectroscopy and to discuss different theoretical methods for the description of meson structure.

The main part of this thesis was formed by the three theoretical methods each of them we introduced in a separate chapter. First we focused on unconventional meson structures namely bound states of two mesons which we looked at from two different viewpoints—as dynamically generated resonances and as bound states with small binding energies lying close to the corresponding thresholds.

In this context the first theoretical model introduced in Chapter 3 was very useful to study the possible existence of meson–meson states and their pole positions giving information on mass and decay width. In this model the interaction between mesons was studied in coupled channels of meson degrees of freedom. Provided the interaction is attractive enough one obtains dynamically generated meson–meson resonances. In the present case we studied coupled channels of vector mesons, where the interaction was given by the $SU(4)$ hidden gauge Lagrangian. More precisely

we studied channels with hidden– and open–charm flavors and additionally applied the coupled channel approach for the first time to flavor exotic states. In particular, the detection of flavor exotic quantum numbers, which cannot be built up by a $q\bar{q}$ state, would be a strong hint for a multiquark meson structure either realized as a tetraquark or a meson–meson bound state. In total, we obtained nine resonances, four in the charm–strange sector and five with exotic flavor quantum numbers. One charm–strange resonance which is dominantly formed by the D^*K^* system turned out to be a good candidate for the $D^*_{s2}(2573)$ meson. This molecular structure interpretation would be consistent with the results of earlier works assigning the $D^*_{s0}(2317)$ and $D^*_{s1}(2460)$ as DK and D^*K resonances. The flavor exotic structures could not be compared to experimental observations but to theoretical calculations for double–charmed tetraquarks $cc(\bar{q}\bar{q})$ with $J = 1$ where the result is in the same mass region (around 4 GeV) as the corresponding dynamically generated state. In summary, the flavor exotic states provide a interesting research topic for future experiments.

In the second part of Chapter 3 we discussed the radiative decays of dynamically generated states. First we applied the method to the dynamically generated resonances from coupled vector meson channels containing three flavors ($SU(3)$). Some of the resonances showed similar properties as the well–established $q\bar{q}$ mesons $f_2(1270)$, $f_0(1370)$, $f_2'(1525)$, $f_0(1710)$ and $K_2^*(1420)$. Despite that a possible molecular structure of these states is not the mainstream interpretation, the coupled channel approach can be considered as a complementary or alternative interpretation of the scalar and tensor mesons. The radiative decay properties of these states were in good agreement with available data. Furthermore, our results for the two–photon and $V\gamma$ decay properties could give further insight into the substructure of this states when corresponding experiments will be available in the future.

Then we turned to the more interesting case of the recently discovered hidden–charm mesons $Y(3940)$, $Z(3930)$ and $X(4160)$ which are most likely not $c\bar{c}$ states but good candidates for molecular meson structures. The radiative decay properties were compared to data from BELLE and to the results obtained within the second model for hadronic bound states discussed in the following Chapter 4. We found that the results in both approaches are consistent within one order of magnitude which was expected since the underlying structures were the same.

The second theoretical model for hadron structure was introduced in Chapter 4. It is based on effective Lagrangians describing the interaction between the bound state and its constituents. Since we dealt with a clear and straightforward method, the compositeness condition, it has a wide range of applications. For example, in previous works [135] it was successfully used to study ordinary $q\bar{q}$ mesons and baryons as qqq states in the light and heavy sector. But it could also be applied to bound states of hadrons as for example the meson molecules discussed here. Further important features of the model are gauge invariance concerning the electroweak interaction and the consideration of finite size effects arising due to the spatially

extended structure of hadronic bound states by a minimal amount of free parameters.
In the first part of Chapter 4 we continued the study of meson molecules. First we applied the model to the light scalar $a_0(980)$ and $f_0(980)$ mesons which are prime candidates for a $K\overline{K}$ bound state structure. Since both mesons are experimentally intensively studied there is much data available which provides an excellent reference for our results. Therefore, the $a_0(980)$ and $f_0(980)$ served as ideal test cases for this model. We did a comprehensive study of the radiative $\gamma\gamma$ and $V\gamma$ decay modes, computed the $\phi \to f_0(a_0)\gamma$ production rate and also considered the strong $\pi\pi$ and $\pi\eta$ decay widths. Furthermore, in our calculations we included the isospin violating $f_0 - a_0$ mixing. The results were found in very good agreement with data and clearly support the $K\overline{K}$ hadronic molecule structure. Finally, we also studied the f_0 production in weak $D^*_{s0}(B^*_{s0})$ and $D_{s1}(B_{s1})$ meson decays.
After this introductory examples we applied the effective Lagrangian approach to the more interesting cases of the charmonium–like resonances $Y(3940)$, $Y(4140)$ and $Z^{\pm}(4430)$. The unusually large hidden–charm decay widths of these states are in disagreement with the $c\bar{c}$ expectations since the hidden–charm modes are OZI suppressed. In the case of the $Z^{\pm}$ we additionally dealt with a charged state, hence, a standard $c\bar{c}$ assignment can be ruled out. Provided the $Z^{\pm}$ is confirmed by a second experiment it would be a clear signal for a $q^2\bar{q}^2$ state or a hadronic molecule. We studied the hidden charm and radiative decay modes within the meson molecule interpretation assigning the $Y(3940)$, $Y(4140)$ and $Z^{\pm}(4430)$ to the following meson bound states: $D^*\overline{D}^*$, $D_s^{*+}D_s^{*-}$ and $\overline{D}_1 D^*$. The results for the decay widths of the hidden–charm modes were in all cases larger than 1 MeV and could therefore reproduce the experimental observations. Our results for the radiative decays $Y \to \gamma\gamma$ were found in agreement with data for the $Y(3940)$ which supports the $D^*\overline{D}^*$ interpretation while the result for the two–photon decay of the $Y(4140)$ overestimated the upper limit set by experiment. Hence, the molecular interpretation of the $Y(4140)$ needs further consideration.
Along the same lines, the $D^*\overline{D}_1$ interpretation of the $Z^{\pm}$ could reproduce the unusual properties of this charmonium–like state. For example, in analogy to the Y states the hadronic molecule model could explain the large $\pi^{\pm}\psi'$ hidden–charm decay widths and furthermore the suppression of the kinematically favored $\pi^{\pm}\psi$ channel. Our results for the $Z^{\pm} \to \pi^{\pm}\gamma$ decay widths could be useful to determine the quantum numbers of the $Z^{\pm}$ since this mode is forbidden for $J^P = 0^-$.
In the second part of Chapter 4 we also applied the effective Lagrangian framework to $q\bar{q}$ states. Since our aim was to study excited states as well we faced the difficulty that the quark loops became divergent as soon as the mass of the bound states exceeded the threshold of the respective constituents. To circumvent the problem we improved the phenomenological model by introducing a confinement scale parameter which enlarged the application range of the model to the whole $q\bar{q}$ spectrum. We first applied the approach to the pion and rho mesons to determine the scale parameter then we calculated the radiative and strong decay properties of light and heavy

mesons. We also studied the Dalitz decays of the ω, η and η' mesons. Altogether we found that our results are in good agreement with data.
The last of the three models introduced in this thesis was very different from the previously discussed coupled channel and effective Lagrangian approaches. The holographic AdS/QCD method is based on extra dimensions and contains elements of string theory. More precisely, we dealt with a mapping between string modes existing in an extra dimension and meson wave functions in four–dimensional space time. We implemented the effect of confinement by using a soft–wall approach which allowed for the Regge–behavior of the meson masses. This method was used to compute the mass spectrum of light and heavy $q\bar{q}$ mesons. After the inclusion of one–gluon exchange terms we obtained good agreement with the meson mass spectra for light, heavy–light and heavy quarkonia states. Furthermore, we studied the decay constants of the ground state mesons. The present discussion of two parton states provided only the first step for further investigations of the AdS/CFT approach as for example its extension to baryon states.
Since at present the situation and understanding of the meson spectrum is far from clear future experimental investigations are necessary to get a comprehensive view. In particular, precise data and more information on decay and production channels in the charmonium sector are essential to pin down the structure of the puzzling X, Y and Z states. Hopes are placed on the new generation of experiments as for instance the LHC which is the leading facility at present. The LHCb detector designed for precision measurements of CP violating and rare B–decays is expected to be an excellent environment for charmonium observation as known from other B–factories. Furthermore, the GSI future project PANDA in Darmstadt and the upgrade of BES, the BES–III experiment, will certainly lead to interesting and, as usual, unexpected new observations which again give a new momentum to the field of meson spectroscopy.

A. Appendix: Effective Model for hadronic bound states

A.1. Loop Integrals

Here we give a short presentation of the structure integrals and its evaluation relevant for the derivation of the transition form factors.

A.1.1. Radiative transitions

For simplicity we restrict to the diagrams of Figs. 4.8 (a,b), 4.9 (a,b) and 4.10 (a) to (c), which do not contain contact vertices. The additional diagrams generated due to nonlocal effects are discussed in detail in [26, 135]. The full structure integrals characterizing the electromagnetic decays are given by

$$I^{\mu\nu}_{S\gamma V}(m_S^2,0,m_V^2) = \int \frac{d^4k}{\pi^2 i}\,\widetilde{\Phi}(-k^2)\Big((2k+p-q)^\mu(2k-q)^\nu S_K\big(k+\frac{p}{2}\big)S_K\big(k-\frac{p}{2}\big) \times S_K\big(k+\frac{p}{2}-q\big)+g^{\mu\nu}S_K\big(k+\frac{p}{2}\big)S_K\big(k-\frac{p}{2}\big)\Big)\,, \tag{A.1}$$

$$I^{\mu\nu}_{\phi S\gamma}(m_\phi^2,m_S^2,0) = \int \frac{d^4k}{\pi^2 i}\,\widetilde{\Phi}(-k^2)\Big(\frac{(2k-q-p)^\nu(2k-q)^\mu}{S_K\big(k+\frac{p}{2}\big)S_K\big(k-\frac{p}{2}\big)S_K\big(k-\frac{p}{2}-q\big)} \times +\frac{g^{\mu\nu}}{S_K\big(k+\frac{p}{2}\big)S_K\big(k-\frac{p}{2}\big)}\Big)\,, \tag{A.2}$$

where q is the photon momentum and p of the scalar. In the case of the two-photon decay the expressions corresponding to all the diagrams of Fig. 4.8 are quoted in [26]. We use the expression for the $S \to V\gamma$ decay (Eq. A.1) as an example to demonstrate the technique for the derivation of the loop integral $I_{S\gamma V}(m_S^2,0,m_V^2)$. In the first step we separate the gauge invariant part of the full expression $I^{\mu\nu}$ by writing

$$I^{\mu\nu}_{S\gamma V}(m_S^2,0,m_V^2) = I_{S\gamma V}(m_S^2,0,m_V^2)b^{\mu\nu} + I^{(2)}_{S\gamma V}(m_S^2,0,m_V^2)c^{\mu\nu} + \delta I_{S\gamma V}\,, \tag{A.3}$$

where the remainder term $\delta I_{S\gamma V}$ contains the non-invariant terms. The tensor structures $b^{\mu\nu}$ and $c^{\mu\nu}$ have already been defined in (4.18). Since we deal with

real photons only the first term of (A.3), proportional to $b^{\mu\nu}$, is relevant. In the second step Feynman-parameterization is introduced and the integration over the four-momentum k is performed. For instance, in the local limit we obtain

$$I_{S\gamma V}(m_S^2, 0, m_V) = \int_0^1 d^3\alpha\, \delta(1 - \sum_i \alpha_i)\, \frac{4\alpha_1\alpha_3}{m_K^2 - m_S^2\alpha_1\alpha_3 - m_V^2\alpha_2\alpha_3}\,. \quad \text{(A.4)}$$

The mathematical treatment of the diagrams including contact vertices is straightforward and in complete analogy with above example.

A.1.2. Strong decays

The loop integrals of the diagrams contributing to the strong decays (Fig. 4.11 (a) and (b)) read as

$$\begin{aligned} I^{(a)}(m_K^2, p^2, q_1^2, q_2^2) =& \frac{g_\pi g_{\pi(\eta)}}{(4\pi)^2} \int \frac{d^4k}{\pi^2 i}\, \widetilde{\Phi}(-k^2)\big(k - \frac{p}{2} - q_2\big)_\mu (k + \frac{p}{2} + q_1)_\nu \times \\ & \times S_K\big(k + \frac{p}{2}\big) S_K\big(k - \frac{p}{2}\big) S_{K^*}^{\mu\nu}\big(k + \frac{p}{2} - q_1\big)\,, \quad \text{(A.5)} \\ I^{(b)}(m_K^2, p^2, q_1^2, q_2^2) =& -\frac{1}{m_{K^*}^2} \frac{g_\pi g_{\pi(\eta)}}{(4\pi)^2} \int \frac{d^4k}{\pi^2 i}\, \widetilde{\Phi}(-k^2)\big(k - \frac{p}{2} - q_2\big)(k + \frac{p}{2} + q_1) \times \\ & \times S_K\big(k + \frac{p}{2}\big) S_K\big(k - \frac{p}{2}\big)\,. \quad \text{(A.6)} \end{aligned}$$

Again, we evaluate above expressions by introducing Feynman parameters and integrating over the loop-momentum k. The full structure integral $G(p^2, p_1^2, p_2^2)$ is obtained when multiplying above expression by the couplings $g_{f_0K\bar{K}}/\sqrt{2}$ or $g_{a_0K\bar{K}}/\sqrt{2}$.

A.2. Gauge invariance

In this Appendix gauge invariance is demonstrated by means of the charged a_0 meson decays. The kaon loop integral corresponding to the diagrams (a) and (b) of Fig. 4.9 is given by

$$\begin{aligned} I_\triangle^{\mu\nu} = \int \frac{d^4k}{\pi^2 i} \widetilde{\Phi}(-k^2) \Big\{ & S\Big(k + \frac{p}{2}\Big) S\Big(k - \frac{q}{2}\Big) S\Big(k - \frac{p}{2}\Big) (2k + q_2)^\mu (2k - q_1)^\nu \\ & + g^{\mu\nu} S\Big(k + \frac{p}{2}\Big) S\Big(k - \frac{p}{2}\Big) \Big\}\,, \quad \text{(A.7)} \end{aligned}$$

where $q = q_1 - q_2$. The part $I^{\mu\nu}_{\triangle_\perp}$ being gauge invariant with respect to the photon momentum q_1^μ is separated from the so-called remainder term $\delta I^{\mu\nu}_\triangle$ by using

$$\begin{aligned}(2k+q_2)^\mu &= (2k+q_2)^\mu_{\perp q_1} + q_1(2k+q_2)\frac{q_1^\mu}{q_1^2}\\ g^{\mu\nu} &= g^{\mu\nu}_{\perp q_1} + \frac{q_1^\mu q_1^\nu}{q_1^2}\,.\end{aligned} \tag{A.8}$$

Therefore, the non-invariant term is given by

$$\begin{aligned}\delta I^{\mu\nu}_\triangle &= \int \frac{d^4k}{\pi^2 i}\widetilde{\Phi}(-k^2)\Big\{\Big[S\Big(k+\frac{p}{2}\Big)S\Big(k-\frac{p}{2}\Big) - S\Big(k-\frac{p}{2}\Big)S\Big(k-\frac{q}{2}\Big)\Big]\frac{q_1^\mu}{q_1^2}(2k-q_1)^\nu\\ &\quad + S\Big(k+\frac{p}{2}\Big)S\Big(k-\frac{p}{2}\Big)\frac{q_1^\mu q_1^\nu}{q_1^2}\Big\}\\ &= -\int \frac{d^4k}{\pi^2 i}\widetilde{\Phi}(-k^2)S\Big(k-\frac{p}{2}\Big)S\Big(k-\frac{q}{2}\Big)\Big]\frac{q_1^\mu}{q_1^2}(2k-q_1)^\nu\,.\end{aligned} \tag{A.9}$$

For the bubble diagram (c) of Fig. 4.10 the loop integral reads as (see [135])

$$I^{\mu\nu}_{bub} = -\int \frac{d^4k}{\pi^2 i}\big(2k+\frac{q_1}{2}\big)^\mu k^\nu \int_0^1 dt\widetilde{\Phi}'\big[-\big(k+\frac{q_1}{2}\big)^2 t - k^2(1-t)\big]\,. \tag{A.10}$$

This leads to the remainder

$$\delta I^{\mu\nu}_{bub} = \int \frac{d^4k}{\pi^2 i}\widetilde{\Phi}(-k^2)\frac{q_1^\mu}{q_1^2}(2k-q_1)^\nu S\Big(k-\frac{p}{2}\Big)S\Big(k-\frac{q}{2}\Big) \tag{A.11}$$

which cancels with $\delta I^{\mu\nu}_\triangle$ and therefore

$$\delta I^{\mu\nu} = \delta I^{\mu\nu}_\triangle + \delta I^{\mu\nu}_{bub} = 0\,. \tag{A.12}$$

A.3. Coupling constants for the weak nonleptonic decays

In Tab. A.1 we indicate the results for the coupling constants at the secondary interaction vertex involving charged (c) and neutral (n) B and D mesons. The coupling strengths are deduced from the decays $B/D \to KX$ ($X = \pi,\, K, \eta', \eta, \omega, \rho$) and the branching ratios are taken from [173, 174].

Channel	Branching Ratio	g_X^n	Channel	Branching Ratio	g_X^c
$D^0 \to K^-\pi^+$	$(3.89 \pm 0.05)\,\%$	$2.88 \cdot 10^{-6}$ GeV	$D^+ \to \pi^+\bar{K}^0$	$(2.83 \pm 0.18)\,\%$	$0.14 \cdot 10^{-5}$ GeV
$D^0 \to K^+K^-$	$(3.93 \pm 0.08) \cdot 10^{-3}$	$0.83 \cdot 10^{-6}$ GeV	$D^+ \to K^+\bar{K}^0$	$(5.7 \pm 0.5) \cdot 10^{-3}$	$0.63 \cdot 10^{-6}$ GeV
$D^0 \to \rho^+K^-$	$(10.8 \pm 0.7)\,\%$	$2.92 \cdot 10^{-6}$	$D^+ \to \rho^+\bar{K}^0$	$(7.3 \pm 2.5)\,\%$	$0.15 \cdot 10^{-5}$
$B^0 \to K^0\pi^0$	$(9.8 \pm 0.6) \cdot 10^{-6}$	$3.36 \cdot 10^{-8}$ GeV	$B^+ \to K^+\pi^0$	$(1.29 \pm 0.06) \cdot 10^{-5}$	$3.73 \cdot 10^{-8}$ GeV
$B^0 \to K^0\eta'$	$(6.5 \pm 0.4) \cdot 10^{-5}$	$0.91 \cdot 10^{-7}$ GeV	$B^+ \to K^+\eta'$	$(7.02 \pm 0.25) \cdot 10^{-5}$	$8.84 \cdot 10^{-8}$ GeV
$B^0 \to K^0\eta$	$< 1.9 \cdot 10^{-6}$	$< 0.15 \cdot 10^{-7}$ GeV	$B^+ \to K^+\eta$	$(2.7 \pm 0.9) \cdot 10^{-6}$	$0.17 \cdot 10^{-7}$ GeV
$B^0 \to K^0\bar{K}^0$	$(9.6^{+2.0}_{-1.8}) \cdot 10^{-7}$	$1.06 \cdot 10^{-8}$ GeV	$B^+ \to K^+\bar{K}^0$	$(1.36 \pm 0.27) \cdot 10^{-6}$	$1.22 \cdot 10^{-8}$ GeV
$B^0 \to K^0\omega$	$(5.0 \pm 0.6) \cdot 10^{-6}$	$1.41 \cdot 10^{-9}$	$B^+ \to K^+\omega$	$(6.7 \pm 0.8) \cdot 10^{-6}$	$1.57 \cdot 10^{-9}$
$B^0 \to K^0\rho^0$	$(5.4 \pm 0.9) \cdot 10^{-6}$	$0.14 \cdot 10^{-8}$	$B^+ \to K^+\rho^0$	$(4.2 \pm 0.5) \cdot 10^{-6}$	$1.23 \cdot 10^{-9}$

Table A.1.: Coupling constants deduced from the decays $B/D \to KX$, $(X = \pi,\ K,\ \eta',\ \eta,\ \omega,\ \rho)$. Branching ratios are taken from [173, 174].

A.4. Coupling ratio $g_{D_1D\psi'}/g_{D_1D\psi}$

Here we give an estimate for the ratio of couplings for the D_1DJ/ψ and $D_1D\psi'$ vertices by using the $^3P_0$ model [188, 189, 243, 181, 191]. The $^3P_0$ model is a standard phenomenological tool to analyze hadron decays. Thereby a $q\bar{q}$ pair is created from the vacuum with quantum numbers $I^G(J^{PC}) = 0^+(0^{++})$, hence $^3P_0$ in spin-orbit coupling. The $^3P_0$ model is rather sensitive to variations of the parameters i.e. the elementary pair creation strength and the radii of the hadron wave functions involved. The model can deliver meaningful results for strong hadronic decay rates when evaluated in the center of mass frame and provided that all initial or final state particles are on-shell. Further extensions of the $^3P_0$ model concern for example nucleon-antinucleon annihilation processes [244, 33] and the determination of baryon meson coupling constants [245, 181] where the emitted meson is not necessarily on-shell anymore. Since in the present work we deal with transitions between off-shell mesons, the $D_1 \to D\psi$ and $D_1 \to D\psi'$ decays are kinematically forbidden. Also, since the ratio of transition matrix elements has a less pronounced parameter dependence, we use the $^3P_0$ model to determine the ratio of the couplings $r_2 = g_{D_1D\psi'}/g_{D_1D\psi}$.
In the $^3P_0$ model the transition amplitude for the process $A \to BC$ is given by

$$T_{A\to BC} = \left\langle \Psi^B_{n_B,l_B,m_B}(1,3)\Psi^C_{n_C,l_C,m_C}(2,4)\middle|\hat{\mathcal{O}}_{^3P_0}(3,4)\middle|\Psi^A_{n_A,l_A,m_A}(1,2)\right\rangle , \tag{A.13}$$

where the indices $i = 1, 2, 3, 4$ refer to the respective quarks (see Fig. A.1).

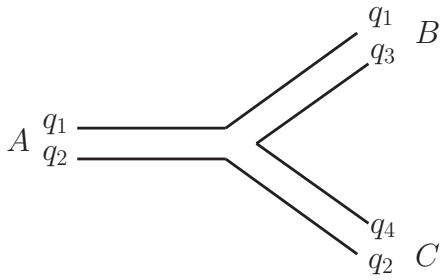

Figure A.1.: The decay process $A \to BC$ in the $^3P_0$ model.

For the initial and final mesons we use, as usual, simple harmonic oscillator wave functions

$$\begin{aligned}\psi_{n,l,m}(\vec{p}) =& N_{n,l}L_n^{l+1/2}(R^2p^2)\exp\big(-\frac{R^2}{2}\vec{p}^{\,2}\big)(Rp)^l\big[\big|(s_1s_2)sm_s\big\rangle \otimes Y_{lm}(\hat{p})\big]_{J,m_J} \\ &\times \delta^{(3)}(\vec{P}-\vec{p}_1-\vec{p}_2)\chi^s_m(12)\chi^{f+c}(q_1q_2)\,,\end{aligned} \tag{A.14}$$

with the normalization $N_{n,l} = (-i)^{2n+l}\sqrt{\frac{2n!R^3}{\Gamma(n+l+3/2)}}$, the radius R and the relative momentum $\vec{p} = \frac{m_1\vec{p}_2-m_2\vec{p}_1}{m_1+m_2}$. Quark q_i is characterized by its mass m_i and spin

s_i. L_n^l and Y_{lm} represent the Legendre polynomials and the spherical harmonics, respectively. χ^s and χ^{f+c} denote the spin and flavor-color wave functions.

The additional quark-antiquark pair required for the decay of a meson into a two-body final state is generated by the $^3P_0$ operator

$$\hat{\mathcal{O}}_{^3P_0} = \lambda V_{^3P_0}^{34\,\dagger} \underbrace{\delta^{(3)}(\vec{p}_1 - \vec{p}_1\,')\delta^{(3)}(\vec{p}_2 - \vec{p}_2\,')}_{\text{spectator quarks}} \tag{A.15}$$

where λ is the creation strength assumed to be independent of the scale set by the total energy and

$$V_{^3P_0}^{34\,\dagger} = \sum_{\mu}(-)^{1+\mu}\langle 1\,1\,-\mu\,\mu\,|00\rangle \mathcal{Y}_{1\mu}^*(\vec{p}_3 - \vec{p}_4)\delta^{(3)}(\vec{p}_3 - \vec{p}_4)\sigma_{-\mu}^{(34)\dagger} \tag{A.16}$$

with the Pauli matrix σ and $\mathcal{Y}_{lm}(\vec{p}) = |p|Y_{lm}(\hat{p})$.

In the following we give the final result for the amplitudes characterizing the $\psi^{(\prime)} \to D_1 D$ transitions $(2)1^3S_1 \to^1 P_1(^3P_1) +^1 S_0$, where only the D-wave contribution $(L = 2)$ is relevant

$$T_{L=2} = \lambda\delta^{(3)}(\vec{P}_A - \vec{P}_B - \vec{P}_C)\sum_{L,m_L} Y_{Lm_L}(\hat{P})T_L^{\text{space}} f_L(\mu, m_{l_B}, m_L) \tag{A.17}$$

with

$$T_{L=2}^{\text{space,n=0}} = i\frac{\sqrt{R}2^3}{\pi^{\frac{3}{4}}3^2}\sqrt{\frac{1}{5}}\alpha\big(1 - \frac{2}{3}\alpha\big)R^2P^2\exp\big(-\frac{R^2}{3}P^2\alpha^2\big), \tag{A.18}$$

$$T_{L=2}^{\text{space,n=1}} = -3i\frac{\sqrt{R}2^{\frac{9}{2}}}{3^{\frac{9}{2}}\pi^{\frac{3}{4}}}\sqrt{\frac{1}{5}}\Big(\frac{11}{4}\alpha - \frac{7}{6}\alpha^2 - \frac{2}{3}\alpha^3R^2P^2 + \frac{4}{9}\alpha^4R^2P^2\Big)R^2P^2 \times \exp\big(-\frac{R^2}{3}P^2\alpha^2\big) \tag{A.19}$$

and

$$f_L(\mu, m_{l_B}, m_L) = \langle 1\,1\,0\,0|2\,0\rangle\langle 1\,1\,-\mu\,-m_{l_B}|L\,m_L\rangle(-)^{m_L}\delta_{L,2} \tag{A.20}$$

(see also in e.g. [243]). Here L is the relative angular momentum between the final mesons and J_{BC} is the total spin of the two final states B and C. The different quark masses of the charm mesons are accounted for by the factor $\alpha = \frac{m_c}{m_q+m_c}$. The last expression (A.20) represents the spin part of the amplitude for a $^1P_1$ and $^3P_1$

state, respectively

$$T^{\text{spin}}_{^1P_1} = \sqrt{\frac{2}{3}}\frac{\sqrt{10}}{6}\big\langle J_{BC}\, 2\, m_{BC}\, m_L \big| 1\, m_A\big\rangle \delta_{L,2}\,,$$
$$T^{\text{spin}}_{^3P_1} = \sqrt{\frac{1}{3}}\frac{\sqrt{10}}{6}\big\langle J_{BC}\, 2\, m_{BC}\, m_L \big| 1\, m_A\big\rangle \delta_{L,2}\,. \tag{A.21}$$

Finally we consider the mixing $|D_1\rangle = \sqrt{\frac{2}{3}}|^1P_1\rangle + \sqrt{\frac{1}{3}}|^3P_1\rangle$ which leads to

$$T^{\text{space,n=0(1)+spin}}_{\psi\to D_1 D} = \sqrt{\frac{3}{2}} T^{\text{space,n=0(1)}}_{L=2}\, T^{\text{spin}}_{^1P_1}\,. \tag{A.22}$$

Due to this mixing pattern the D_1 couples via D-wave only.
We find that the ratio $g_{D_1 D\psi'}/g_{D_1 D\psi} = T^{\text{space,n=1}}_{L=2}/T^{\text{space,n=0}}_{L=2} = 2.15$ is independent of the radii R and the coupling strength λ. The amplitudes are evaluated at threshold, i.e. P=0, which is in analogy to the determination of the nucleon-meson couplings in [190]. The quark masses $m_q = 0.33$ GeV and $m_c = 1.6$ GeV are taken from [181].

A.5. Gauge invariance of the $\rho^0 \to \gamma$ transition amplitude

In this Appendix we want to demonstrate in an explicit calculation that the transition amplitude $\rho^0 \to \gamma$ written down in Eq. (4.177) satisfies gauge invariance, i.e. that e.g. the on–shell photon has only two transverse degrees of freedom. According to the formalism developed in Sec. 4.9 there are the two contributions to the transition $\rho^0 \to \gamma$. The first contribution results from the minimal substitution in the free quark Lagrangian and is depicted in Fig. 4.23(a). In Fig. 4.23(b) we consider in addition the point interaction resulting from gauging the nonlocal Lagrangian.
We begin by looking at the transition of an on–shell ρ to an off–shell photon with invariant mass p^2. The corresponding transition amplitude $M^{\mu\nu}(p)$ must satisfy the gauge invariance condition $p_\nu M^{\mu\nu}(p) = 0$ as has already been assumed in writing down Eq. (4.177). Now we shall show by explicit calculation that the non–gauge invariant pieces in the two contributions cancel each other resulting in an overall gauge invariant contribution. First we isolate the non–gauge invariant pieces in the two respective contributions by writing

$$M_a^{\mu\nu}(p) = \int \frac{d^4k}{4\pi^2 i}\Phi_\rho(-k^2)\,\text{tr}\Big(\gamma^\mu S(k+\tfrac{1}{2}\,p)\gamma^\nu S(k-\tfrac{1}{2}\,p)\Big)$$
$$= g^{\mu\nu}\Big[I_a^{(1)}(p^2) + I_a^{(2)}(p^2)\Big] + (g^{\mu\nu}p^2 - p^\mu p^\nu)\, I_a^\perp(p^2)\,. \tag{A.23}$$

The non–gauge invariant contributions are given by

$$I_a^{(1)}(p^2) = \int\limits_0^\infty \frac{dt}{(s+t)^2} e^{-z_1}\,, \qquad z_1 = tm^2 - \frac{s\,t}{s+t}\frac{p^2}{4}\,, \tag{A.24}$$

$$I_a^{(2)}(p^2) = \int\limits_0^\infty \frac{dt\,t}{(s+t)^2} \int\limits_0^1 d\alpha e^{-z_2}\left[-\frac{1}{s+t} + \frac{2\,t^2}{(s+t)^2}\left(\alpha - \frac{1}{2}\right)^2 p^2\right],$$
$$z_2 = t\left(m^2 - \alpha(1-\alpha)p^2\right) - \frac{s\,t}{s+t}\left(\alpha - \frac{1}{2}\right)^2 p^2\,, \tag{A.25}$$

whereas the gauge invariant term is given by

$$I_a^{\perp}(p^2) = \int\limits_0^\infty \frac{dt\,t}{(s+t)^2} \int\limits_0^1 d\alpha e^{-z_2}\left[\frac{1}{2} - \frac{2\,t^2}{(s+t)^2}\left(\alpha - \frac{1}{2}\right)^2\right]. \tag{A.26}$$

Similarly we have

$$M_b^{\mu\nu}(p) = -\int \frac{d^4k}{4\pi^2 i}\,(2k + \tfrac{1}{2}\,p)^\mu \int\limits_0^1 d\alpha\,\Phi_\pi'\Big(-\alpha\,(k+\tfrac{1}{2}\,p)^2 - (1-\alpha)\,k^2\Big)\mathrm{tr}\Big(\gamma^\nu S(k)\Big)$$
$$= g^{\mu\nu}\,I_b^{(3)}(p^2) + (g^{\mu\nu}p^2 - p^\mu p^\nu)\,I_b^{\perp}(p^2)\,, \tag{A.27}$$

$$I_b^{(3)}(p^2) = \int\limits_0^\infty \frac{dt\,s}{(s+t)^2} \int\limits_0^1 d\alpha\,e^{-z_3}\left[-\frac{1}{s+t} - \left(1 - \frac{2\,s\,\alpha}{s+t}\right)\frac{s\,\alpha}{s+t}\frac{p^2}{4}\right], \tag{A.28}$$

$$I_b^{\perp}(p^2) = \int\limits_0^\infty \frac{dt\,s}{(s+t)^2} \int\limits_0^1 d\alpha\,e^{-z_3}\frac{1}{4}\left(1 - \frac{2\,s\,\alpha}{s+t}\right)\frac{s\,\alpha}{s+t}\,, \tag{A.29}$$
$$z_3 = tm^2 - \left(1 - \frac{s\,\alpha}{s+t}\right)\frac{s\,\alpha}{4}p^2\,,$$

where $s = 1/\Lambda_\rho^2$. The non–gauge invariant pieces $I_a^{(1,2)}$ and $I_b^{(3)}$ cancel each other as can be seen after the following transformations. First we note that the integrands of the integrals $I_a^{(2)}(p^2)$ and $I_b^{(3)}(p^2)$ may be expressed via the derivatives of z_2 and

z_3, respectively:

$$I_a^{(2)}(p^2) \to -\frac{1}{s+t} + \frac{2\,t^2}{(s+t)^2}\left(\alpha - \frac{1}{2}\right)^2 p^2 \quad = -\frac{1}{s+t}\left[1 - \left(\alpha - \frac{1}{2}\right)\frac{\partial z_2}{\partial \alpha}\right], \quad \text{(A.30)}$$

$$I_b^{(3)}(p^2) \to -\frac{1}{s+t} - \frac{p^2}{4}\left(1 - \frac{2\,\alpha\,s}{s+t}\right)\frac{\alpha\,s}{s+t} \qquad = -\frac{1}{s+t}\left[1 - \alpha\frac{\partial z_3}{\partial \alpha}\right]. \quad \text{(A.31)}$$

The α–integration can be done by using the bound–state conditions $z_2(\alpha = 1) = z_2(\alpha = 0) = z_3(\alpha = 1) = z_1$. One obtains

$$I_a^{(2)}(p^2) = -\int_0^\infty \frac{dt\,t}{(s+t)^3}\int_0^1 d\left[\left(\alpha - \frac{1}{2}\right)e^{-z_2}\right] = -\int_0^\infty \frac{dtt}{(s+t)^3}e^{-z_1}\,,$$

$$I_b^{(3)}(p^2) = -\int_0^\infty \frac{dt\,s}{(s+t)^3}\int_0^1 d\left[\alpha\,e^{-z_3}\right] = -\int_0^\infty \frac{dt}{(s+t)^3}e^{-z_1}$$

Finally, one has

$$I_a^{(1)}(p^2) + I_a^{(2)}(p^2) + I_b^{(3)}(p^2) = \int_0^\infty \frac{dt}{(s+t)^2}e^{-z_1}\left[1 - \frac{t}{s+t} - \frac{s}{s+t}\right] \equiv 0\,. \quad \text{(A.32)}$$

The gauge invariance condition $p_\nu M^{\mu\nu}(p) = 0$ also guarantees that the longitudinal component of the photon decouples as $p^2 \to 0$.

A.6. Loop integration techniques

In order to demonstrate how the loop integrations are performed we consider a n–point one–loop diagram with n local propagators $S_i(k + v_i)$ and n Gaussian vertex functions $\Phi_i\left(-(k + v_{i+n})^2\right)$. In Minkowski space the one–loop diagram can be written as

$$I_n(p_1, ..., p_n) = \int \frac{d^4k}{\pi^2 i}\,\mathrm{tr}\,\prod_{i=1}^{n}\Phi_i\left(-(k + v_{i+n})^2\right)\,\Gamma_i\,S_i(k + v_i) \quad \text{(A.33)}$$

where the vectors v_i are linear combinations of the external momenta p_i to be specified in the following, k is the loop momentum, and the Γ_i are Dirac matrices (or strings of Dirac matrices) for the ith meson. The external momenta p_i are all chosen as for an initial state such that $\sum_{i=1}^{n} p_i = 0$. Due to translational invariance the integral Eq. (A.33) is invariant under a shift of the loop momentum $k \to k + l$ by

any four–vector l. The four–vector l may be any linear combination of the external momenta p_i.

Using the Schwinger representation of the local quark propagator one has

$$S_i(k+v_i) \;=\; (m_i + \not{k} + \not{v}_i) \times \int_0^\infty d\beta_i \, \exp\left[-\beta_i \, (m_i^2 - (k+v_i)^2)\right] \, . \quad \text{(A.34)}$$

For the vertex functions one takes the Gaussian form. One has

$$\Phi_i\left(-(k+v_{i+n})^2\right) \;=\; \exp\left[\beta_{i+n}\,(k+v_{i+n})^2\right] \qquad i = 1, ..., n \, , \quad \text{(A.35)}$$

where the $\beta_{i+n} = s_i = 1/\Lambda_i^2$ are related to the size parameters Λ_i. The factors $m_i + \not{k} + \not{v}_i$ in the numerator can be replaced by a differential operator in the following manner:

$$\begin{aligned} I_n(p_1, ..., p_n) &= \int \frac{d^4k}{\pi^2 i} \, \mathrm{tr} \prod_{i=1}^n \int_0^\infty d\beta_i \, e^{-\beta_i m_i^2} (m_i + \not{k} + \not{v}_i) \, \exp\left(\sum_{i=1}^{2\,n} \beta_i \, (k+v_i)^2\right) \\ &= \int \frac{d^4k}{\pi^2 i} \, \mathrm{tr} \prod_{i=1}^n \int_0^\infty d\beta_i \, e^{-\beta_i m_i^2} \left(m_i + \not{v}_i + \frac{1}{2} \, \not{\partial}_r\right) \\ &\quad \times \exp\left(\beta k^2 + 2kr + \sum_{i=1}^{2\,n} \beta_i \, v_i^2\right) \end{aligned} \quad \text{(A.36)}$$

where $\beta = \sum\limits_{i=1}^{2\,n} \beta_i$ and $r = \sum\limits_{i=1}^{2\,n} \beta_i \, v_i$. Next we perform the loop integration and move the Gaussian $\exp\Big(-r^2/\beta\Big)$ to the left of the differential operator. By using the identity

$$-\frac{r^2}{\beta} + \sum_{i=1}^{2\,n} \beta_i \, v_i^2 = \frac{1}{\beta} \sum_{1 \le i < j \le 2\,n} \beta_i \, \beta_j \, (v_i - v_j)^2 \quad \text{(A.37)}$$

one obtains

$$\begin{aligned} I_n(p_1, ..., p_n) = &\prod_{i=1}^n \int_0^\infty \frac{d\beta_i}{\beta^2} \times \exp\left\{-\sum_{i=1}^n \beta_i m_i^2 + \frac{1}{\beta} \sum_{1 \le i < j \le 2\,n} \beta_i \, \beta_j \, (v_i - v_j)^2\right\} \\ &\times \mathrm{tr} \prod_{i=1}^n \Gamma_i \left(m_i + \not{v}_i - \frac{1}{\beta} \, \not{r} + \frac{1}{2} \, \not{\partial}_r\right) \, . \end{aligned} \quad \text{(A.38)}$$

As described in the main text the set of Schwinger parameters β_i $(i = 1, ..., n)$ can

complemented by an additional parameter t by writing

$$\int_0^\infty d^n\beta F(\beta_1,...,\beta_n) = \int_0^\infty dt\, t^{n-1} \int d^n\alpha\, \delta\left(1-\sum_{i=1}^n \alpha_i\right) F(t\,\alpha_1,...,t\,\alpha_n)\,. \tag{A.39}$$

One then arrives at the final representation of the one–loop n–point diagram in the form

$$I_n(p_1,...,p_n) = \int_0^\infty dt \frac{t^{n-1}}{(s+t)^2} \int d^n\alpha\, \delta\Big(1-\sum_{i=1}^n \alpha_i\Big) \exp\Big\{ -t\, z_{\rm loc} + \frac{s\,t}{s+t}\, z_1 + \frac{s^2}{s+t}\, z_2\Big\}$$
$$\times \,{\rm tr} \prod_{i=1}^n \Gamma_i \left(m_i + \not{p}_i - \frac{1}{s+t}\, \not{r} + \frac{1}{2}\, \not{\partial}_r \right)\,, \tag{A.40}$$

where

$$z_{\rm loc} = \sum_{i=1}^n \alpha_i\, m_i^2 - \sum_{1\le i<j\le n} \alpha_i\, \alpha_j\, A_{ij}\,,$$
$$z_1 = \sum_{i=1}^n \alpha_i \sum_{j=n+1}^{2\,n} \bar\beta_j\, A_{ij} - \sum_{1\le i<j\le n} \alpha_i\, \alpha_j\, A_{ij}\,,$$
$$z_2 = \sum_{n+1\le i<j\le 2\,n} \bar\beta_i\, \bar\beta_j\, A_{ij}\,,$$
$$r = t \sum_{i=1}^n \alpha_i\, v_i + s \sum_{i=n+1}^{2\,n} \bar\beta_i\, v_i\,.$$

Here, $\bar\beta_{i+n} = s_i/s,\ s = \sum_{i=1}^n s_i$. The matrix $A_{ij} = (v_i - v_j)^2 \quad (1 \le i,j \le 2n)$ depends on the invariant variables of the process.

Altogether there are n numerical integrations, $n-1$ α–parameter integrations and the integration over the scale parameter t. For the derivative of the (two–point function) mass operator one has to do one more α–parameter integration due to the extra propagator which enters after the differentiation. The integration of the derivative of the mass operator proceeds in analogy to the case of the n point function described in this Appendix. We mention that the correctness of the numerical integration procedure can be checked very conveniently by shifting the momentum of the loop integration by a fixed four–momentum.

Some further remarks are in order. The convergence of the loop integral Eq. (A.40) is defined by the local α form $z_{\rm loc}$. If $z_{\rm loc} \le 0$ the t–integration becomes divergent due to contributions from the large t–region. The large t–region corresponds to

the regime where the singularities of the diagram with its local quark propagators appear. However, as described before, if one introduces an infrared cutoff on the upper limit of the t–integration, all singularities vanish because now the integral is convergent for any value of the set of kinematical variables. Note that the one–loop integration techniques described in this Appendix can be extended to an arbitrary number of loops in a straightforward manner. Of particular interest is the extension to the two–loop case needed for the description of baryon transitions.

B. Appendix: AdS/QCD

B.1. Evaluation of integrals in the heavy quark limit

We evaluate the integral in the r.h.s. of Eq. (5.60) with

$$J = \int_0^1 dx \left(\frac{m_q^2}{x} + \frac{m_Q^2}{1-x} \right) f^2(x, m_q, m_Q) = \frac{\int_0^1 dx \left(\frac{m_q^2}{x} + \frac{m_Q^2}{1-x} \right) \exp\left(-\frac{m_q^2}{\lambda_{qQ}^2 x} + \frac{m_Q^2}{\lambda_{qQ}^2 (1-x)} \right)}{\int_0^1 dx \exp\left(-\frac{m_q^2}{\lambda_{qQ}^2 x} + \frac{m_Q^2}{\lambda_{qQ}^2 (1-x)} \right)} \tag{B.1}$$

Scaling the variable $x = z m_q/m_Q$ and then performing an expansion in powers of $1/m_Q$ we get:

$$J = m_Q^2 + m_Q m_q \frac{\int_0^\infty dz \left(z + \frac{1}{z} \right) \exp\left(-\frac{m_q m_Q}{\lambda_{qQ}^2} \left(z + \frac{1}{z} \right) \right)}{\int_0^\infty dz \exp\left(-\frac{m_q m_Q}{\lambda_{qQ}^2} \left(z + \frac{1}{z} \right) \right)} + \mathcal{O}(1) \tag{B.2}$$

where the parameter λ_{qQ} scales as $\sqrt{m_Q}$. Such a scaling of λ_{qQ} is consistent with the scaling of the leptonic coupling constants of heavy–light mesons (see Sec. 5.3.4). For convenience we introduce the parameter $r = m_q m_Q/\lambda_{qQ}^2$. Finally, the expansion of the heavy–light meson mass reads

$$M_{qQ} = m_Q + \bar{\Lambda} + \mathcal{O}(1/m_Q) \tag{B.3}$$

where

$$\bar{\Lambda} = m_q I \tag{B.4}$$

and

$$I = \frac{1}{2} \frac{\int_0^\infty dz \left(z + \frac{1}{z} \right) e^{-r(z+\frac{1}{z})}}{\int_0^\infty dz\, e^{-r(z+\frac{1}{z})}} \,. \tag{B.5}$$

B.2. Decay constants

The leptonic decay constant f_π of the pion is taken as an example to demonstrate the computation of matrix elements in our approach. We start with the expression

$$\left\langle 0\middle|\bar{u}_{\lambda_1}(q_1)\gamma^+ d_{\lambda_2}(q_2)\middle|\pi^-(P)\right\rangle = P^+ f_\pi \tag{B.6}$$

The current is given by

$$\begin{aligned}\bar{u}_{\lambda_1}(q_1)\gamma^+ d_{\lambda_2}(q_2) = \sum_{\lambda_1,\lambda_2}\int \frac{dq_1^+}{\sqrt{2q_1^+}}\frac{dq_2^+}{\sqrt{2q_2^+}}\frac{d^2\vec{q}_{1\perp}}{(2\pi)^3}\frac{d^2\vec{q}_{2\perp}}{(2\pi)^3}\\ \times\left[\bar{u}(q_1,\lambda_1)b^\dagger_{d\lambda_1}(q_1)+\bar{v}(q_1,\lambda_1)d_{u\lambda_1}(q_1)\right]\\ \times\gamma^+\left[b_{d\lambda_2}(q_2)u(q_2,\lambda_2)+d^\dagger_{u\lambda_2}(q_2)v(q_2,\lambda_2)\right]\end{aligned} \tag{B.7}$$

and the state $\left|\pi^-\right\rangle$ is set up as

$$\left|\pi^-(P^+)\right\rangle = \frac{2P^+}{\sqrt{2N_c}}\int_0^1 dx\int\frac{d^2\vec{k}_\perp}{(2\pi)^3}\psi^{\bar{u}d}_{nL}(x,\vec{k}_\perp)\left[b^{\dagger a}_{d\downarrow}(p_1)d^{\dagger a}_{u\uparrow}(p_2)-b^{\dagger a}_{d\uparrow}(p_1)d^{\dagger a}_{u\downarrow}(p_2)\right]\left|0\right\rangle$$

with $p_1=(xP^+,x\vec{P}_\perp+\vec{k}_\perp)$ and $p_2=((1-x)P^+,(1-x)\vec{P}_\perp-\vec{k}_\perp)$. By using the anticommutator relations (5.13) one easily derives

$$\begin{aligned}f_\pi =&2\sqrt{6}\int_0^1 dx\int\frac{d^2\vec{k}_\perp}{(2\pi)^3}\psi^{\bar{u}d}_{nL}(x,\vec{k}_\perp)\int dq_1^+dq_2^+d^2\vec{q}_{1\perp}d^2\vec{q}_{2\perp}\delta(q_2^+-p_1^+)\delta(q_1^+-p_2^+)\\ &\times\delta^{(2)}(\vec{q}_{2\perp}-\vec{p}_{1\perp})\delta^{(2)}(\vec{q}_{1\perp}-\vec{p}_{2\perp}) = 2\sqrt{6}\int_0^1 dx\int\frac{d^2\vec{k}_\perp}{(2\pi)^3}\widetilde{\psi}^{\bar{u}d}_{nL}(x,\vec{k}_\perp)\\ =&2\sqrt{6}\int_0^1 dx\frac{\widetilde{\psi}^{\bar{q}_1q_2}_{nL}(x,\vec{b}_\perp=0)}{\sqrt{4\pi}}\,.\end{aligned} \tag{B.8}$$

Bibliography

[1] H. Yukawa, Proc. Phys. Math. Soc. Jap. **17**, 48 (1935).

[2] M. Creutz, L. Jacobs, and C. Rebbi, Phys. Rept. **95**, 201 (1983).

[3] C. J. Morningstar and M. J. Peardon, Phys. Rev. **D60**, 034509 (1999), arXiv:hep-lat/9901004.

[4] J. Gasser and H. Leutwyler, Ann. Phys. **158**, 142 (1984).

[5] J. Gasser, Nucl.Phys.Proc.Suppl. **86**, 257 (2000), arXiv:hep-ph/9912548.

[6] S. Weinberg, Physica **A96**, 327 (1979).

[7] S. Scherer, Adv.Nucl.Phys. **27**, 277 (2003), arXiv:hep-ph/0210398, To be edited by J.W. Negele and E. Vogt.

[8] A. F. Falk and M. Neubert, Phys.Rev. **D47**, 2965 (1993), arXiv:hep-ph/9209268.

[9] M. Neubert, Phys. Rept. **245**, 259 (1994), arXiv:hep-ph/9306320.

[10] A. J. Buras, (ed.) and M. Lindner, (ed.), Singapore, Singapore: World Scientific (1998) 828 p.

[11] L. Da Rold and A. Pomarol, Nucl. Phys. **B721**, 79 (2005), arXiv:hep-ph/0501218.

[12] C. Amsler, Rev. Mod. Phys. **70**, 1293 (1998), arXiv:hep-ex/9708025.

[13] E. Klempt and A. Zaitsev, Phys. Rept. **454**, 1 (2007), arXiv:0708.4016.

[14] S. Godfrey and J. Napolitano, Rev. Mod. Phys. **71**, 1411 (1999), arXiv:hep-ph/9811410.

[15] M. Gell-Mann, Phys. Lett. **8**, 214 (1964).

[16] E. D. Bloom *et al.*, Phys. Rev. Lett. **23**, 930 (1969).

[17] R. L. Jaffe, Phys. Rev. **D15**, 267 (1977).

[18] J. D. Weinstein and N. Isgur, Phys. Rev. Lett. **48**, 659 (1982).

[19] J. D. Weinstein and N. Isgur, Phys. Rev. **D27**, 588 (1983).

[20] J. D. Weinstein and N. Isgur, Phys. Rev. **D41**, 2236 (1990).

[21] T. Barnes, Phys. Lett. **B165**, 434 (1985).

[22] Particle Data Group, K. Nakamura *et al.*, J. Phys. **G37**, 075021 (2010).

[23] T. Branz, R. Molina, and E. Oset, (2010), arXiv:1010.0587.

[24] T. Branz, L. S. Geng, and E. Oset, Phys. Rev. **D81**, 054037 (2010), arXiv:0911.0206.

[25] T. Branz, T. Gutsche, and V. E. Lyubovitskij, (2009), arXiv:0903.5424.

[26] T. Branz, T. Gutsche, and V. E. Lyubovitskij, Eur. Phys. J. **A37**, 303 (2008), arXiv:0712.0354.

[27] T. Branz, T. Gutsche, and V. E. Lyubovitskij, Phys. Rev. **D78**, 114004 (2008), arXiv:0808.0705.

[28] T. Branz, T. Gutsche, V. E. Lyubovitskij, I. Schmidt, and A. Vega, Phys. Rev. **D82**, 074022 (2010), arXiv:1008.0268.

[29] R. L. Jaffe, K. Johnson, and Z. Ryzak, Ann. Phys. **168**, 344 (1986).

[30] M. Strohmeier-Presicek, T. Gutsche, R. Vinh Mau, and A. Faessler, Phys. Rev. **D60**, 054010 (1999), arXiv:hep-ph/9904461.

[31] Crystal Barrel, C. Amsler *et al.*, Phys. Lett. **B291**, 347 (1992).

[32] WA102, D. Barberis *et al.*, Phys. Lett. **B474**, 423 (2000), arXiv:hep-ex/0001017.

[33] C. B. Dover, T. Gutsche, A. Faessler, and R. Vinh Mau, Phys. Lett. **B277**, 23 (1992).

[34] S. Godfrey, (2002), arXiv:hep-ph/0211464.

[35] S. Godfrey and N. Isgur, Phys. Rev. **D32**, 189 (1985).

[36] Y. Kalashnikova, A. E. Kudryavtsev, A. V. Nefediev, J. Haidenbauer, and C. Hanhart, Phys. Rev. **C73**, 045203 (2006), arXiv:nucl-th/0512028.

[37] A. V. Anisovich, V. V. Anisovich, and V. A. Nikonov, Eur. Phys. J. **A12**, 103 (2001), arXiv:hep-ph/0108186.

[38] R. Delbourgo, D.-s. Liu, and M. D. Scadron, Phys. Lett. **B446**, 332 (1999), arXiv:hep-ph/9811474.

[39] for the Belle, S. Uehara *et al.*, Phys. Rev. **D78**, 052004 (2008), arXiv:0810.0655.

[40] M. N. Achasov *et al.*, Phys. Lett. **B485**, 349 (2000), arXiv:hep-ex/0005017.

[41] CMD-2, R. R. Akhmetshin *et al.*, Phys. Lett. **B462**, 380 (1999), arXiv:hep-ex/9907006.

[42] KLOE, F. Ambrosino *et al.*, Phys. Lett. **B648**, 267 (2007), arXiv:hep-ex/0612029.

[43] KLOE, F. Ambrosino *et al.*, Eur. Phys. J. **C49**, 473 (2007), arXiv:hep-ex/0609009.

[44] G. Isidori, L. Maiani, M. Nicolaci, and S. Pacetti, JHEP **05**, 049 (2006), arXiv:hep-ph/0603241.

[45] F. E. Close, N. Isgur, and S. Kumano, Nucl. Phys. **B389**, 513 (1993), arXiv:hep-ph/9301253.

[46] CLEO, J. Yelton *et al.*, Phys. Rev. **D80**, 052007 (2009), arXiv:0903.0601.

[47] CLEO, K. M. Ecklund *et al.*, Phys. Rev. **D80**, 052009 (2009), arXiv:0907.3201.

[48] BABAR, B. Aubert *et al.*, Phys. Rev. **D78**, 051101 (2008), arXiv:0807.1599.

[49] T. V. Brito, F. S. Navarra, M. Nielsen, and M. E. Bracco, Phys. Lett. **B608**, 69 (2005), arXiv:hep-ph/0411233.

[50] S. Godfrey and S. L. Olsen, Ann. Rev. Nucl. Part. Sci. **58**, 51 (2008), arXiv:0801.3867.

[51] S. L. Olsen, (2009), arXiv:0909.2713.

[52] Belle, S. Cheng-Ping, (2009), arXiv:0912.2386.

[53] Belle, M. Kreps, (2009), arXiv:0912.0111.

[54] BaBar, W. Dunwoodie, Nucl. Phys. **A827**, 291c (2009).

[55] BaBar, A. Palano, Int. J. Mod. Phys. **A24**, 343 (2009).

[56] CDF, T. Aaltonen *et al.*, Phys. Rev. Lett. **102**, 242002 (2009), arXiv:0903.2229.

[57] CDF and D0, K. Yi, (2010), arXiv:1004.0343.

[58] CLEO, R. E. Mitchell, (2007), arXiv:0705.2899.

[59] BaBar, A. Zghiche, (2007), arXiv:0710.0314.

[60] E. S. Swanson, Phys. Rept. **429**, 243 (2006), arXiv:hep-ph/0601110.

[61] E. Eichten, S. Godfrey, H. Mahlke, and J. L. Rosner, Rev. Mod. Phys. **80**, 1161 (2008), arXiv:hep-ph/0701208.

[62] F. E. Close and P. R. Page, Phys. Lett. **B366**, 323 (1996), arXiv:hep-ph/9507407.

[63] X.-Q. Luo and Y. Liu, Phys. Rev. **D74**, 034502 (2006), arXiv:hep-lat/0512044.

[64] X.-H. Liu, Q. Zhao, and F. E. Close, Phys. Rev. **D77**, 094005 (2008), arXiv:0802.2648.

[65] R. Molina and E. Oset, Phys. Rev. **D80**, 114013 (2009), arXiv:0907.3043.

[66] X. Liu and S.-L. Zhu, Phys. Rev. **D80**, 017502 (2009), arXiv:0903.2529.

[67] Belle Collaboration, S. K. Choi *et al.*, Phys. Rev. Lett. **100**, 142001 (2008), arXiv:0708.1790.

[68] Belle, K. Abe *et al.*, Phys. Rev. Lett. **94**, 182002 (2005), arXiv:hep-ex/0408126.

[69] BaBar, B. Aubert *et al.*, Phys. Rev. Lett. **101**, 082001 (2008), arXiv:0711.2047.

[70] N. A. Tornqvist, Z. Phys. **C61**, 525 (1994), arXiv:hep-ph/9310247.

[71] Belle, C. P. Shen *et al.*, Phys. Rev. Lett. **104**, 112004 (2010), arXiv:0912.2383.

[72] X. Liu, B. Zhang, and S.-L. Zhu, Phys. Rev. **D77**, 114021 (2008), arXiv:0803.4270.

[73] R. M. Albuquerque, M. E. Bracco, and M. Nielsen, Phys. Lett. **B678**, 186 (2009), arXiv:0903.5540.

[74] L. Maiani, A. D. Polosa, and V. Riquer, New J. Phys. **10**, 073004 (2008).

[75] L. Maiani, A. D. Polosa, and V. Riquer, (2007), arXiv:0708.3997.

[76] C. Meng and K.-T. Chao, (2007), arXiv:0708.4222.

[77] J. L. Rosner, Phys. Rev. **D76**, 114002 (2007), arXiv:0708.3496.

[78] Belle Collaboration, R. Mizuk *et al.*, Phys. Rev. **D80**, 031104 (2009), arXiv:0905.2869.

[79] Belle Collaboration, R. Mizuk *et al.*, Phys. Rev. **D78**, 072004 (2008), arXiv:0806.4098.

[80] Y. Li, C.-D. Lu, and W. Wang, Phys. Rev. **D77**, 054001 (2008), arXiv:0711.0497.

[81] G.-J. Ding, (2007), arXiv:0711.1485.

[82] K.-M. Cheung, W.-Y. Keung, and T.-C. Yuan, Phys. Rev. **D76**, 117501 (2007), arXiv:0709.1312.

[83] D. V. Bugg, J. Phys. **G35**, 075005 (2008), arXiv:0802.0934.

[84] T. Matsuki, T. Morii, and K. Sudoh, Phys. Lett. **B669**, 156 (2008), arXiv:0805.2442.

[85] C.-F. Qiao, J. Phys. **G35**, 075008 (2008), arXiv:0709.4066.

[86] M. B. Voloshin, Prog. Part. Nucl. Phys. **61**, 455 (2008), arXiv:0711.4556.

[87] F. Close, C. Downum, and C. E. Thomas, Phys. Rev. **D81**, 074033 (2010), arXiv:1001.2553.

[88] X. Liu, Y.-R. Liu, W.-Z. Deng, and S.-L. Zhu, Phys. Rev. **D77**, 094015 (2008), arXiv:0803.1295.

[89] S. H. Lee, A. Mihara, F. S. Navarra, and M. Nielsen, Phys. Lett. **B661**, 28 (2008), arXiv:0710.1029.

[90] M. Nielsen, F. S. Navarra, and S. H. Lee, (2009), arXiv:0911.1958.

[91] CLQCD Collaboration, G.-Z. Meng *et al.*, Phys. Rev. **D80**, 034503 (2009), arXiv:0905.0752.

[92] T. Barnes and E. S. Swanson, Phys. Rev. **D46**, 131 (1992).

[93] J. A. Oller and E. Oset, Nucl. Phys. **A620**, 438 (1997), arXiv:hep-ph/9702314.

[94] D. Gamermann and E. Oset, Eur. Phys. J. **A33**, 119 (2007), arXiv:0704.2314.

[95] D. Gamermann, E. Oset, D. Strottman, and M. J. Vicente Vacas, Phys. Rev. **D76**, 074016 (2007), arXiv:hep-ph/0612179.

[96] M. Bando, T. Kugo, and K. Yamawaki, Phys. Rept. **164**, 217 (1988).

[97] U. G. Meissner, Phys. Rept. **161**, 213 (1988).

[98] R. Molina, D. Nicmorus, and E. Oset, Phys. Rev. **D78**, 114018 (2008), arXiv:0809.2233.

[99] L. S. Geng and E. Oset, Phys. Rev. **D79**, 074009 (2009), arXiv:0812.1199.

[100] H. Nagahiro, L. Roca, A. Hosaka, and E. Oset, Phys. Rev. **D79**, 014015 (2009), arXiv:0809.0943.

[101] A. I. Titov, B. Kampfer, and B. L. Reznik, Eur. Phys. J. **A7**, 543 (2000), arXiv:nucl-th/0001027.

[102] F. S. Navarra, M. Nielsen, and M. E. Bracco, Phys. Rev. **D65**, 037502 (2002), arXiv:hep-ph/0109188.

[103] R. Molina, T. Branz, and E. Oset, Phys. Rev. **D82**, 014010 (2010), arXiv:1005.0335.

[104] CLEO, Y. Kubota *et al.*, Phys. Rev. Lett. **72**, 1972 (1994), arXiv:hep-ph/9403325.

[105] S. Godfrey and R. Kokoski, Phys. Rev. **D43**, 1679 (1991).

[106] CLEO, D. Besson *et al.*, Phys. Rev. **D68**, 032002 (2003), arXiv:hep-ex/0305100.

[107] BABAR, B. Aubert *et al.*, Phys. Rev. Lett. **90**, 242001 (2003), arXiv:hep-ex/0304021.

[108] F. S. Navarra, M. Nielsen, and S. H. Lee, Phys. Lett. **B649**, 166 (2007), arXiv:hep-ph/0703071.

[109] B. Silvestre-Brac and C. Semay, Z. Phys. **C57**, 273 (1993).

[110] D. Janc and M. Rosina, Few Body Syst. **35**, 175 (2004), arXiv:hep-ph/0405208.

[111] CLEO, S. Ahmed *et al.*, Phys. Rev. Lett. **87**, 251801 (2001), arXiv:hep-ex/0108013.

[112] V. M. Belyaev, V. M. Braun, A. Khodjamirian, and R. Ruckl, Phys. Rev. **D51**, 6177 (1995), arXiv:hep-ph/9410280.

[113] P. Colangelo *et al.*, Phys. Lett. **B339**, 151 (1994), arXiv:hep-ph/9406295.

[114] R. Molina, H. Nagahiro, A. Hosaka, and E. Oset, Phys. Rev. **D80**, 014025 (2009), arXiv:0903.3823.

[115] J. J. Sakurai, *Currents and Mesons* (University of Chicago Press, 1969).

[116] J.-F. Sun, D.-S. Du, and Y.-L. Yang, Eur. Phys. J. **C60**, 107 (2009), arXiv:0808.3619.

[117] W. H. Liang, R. Molina, and E. Oset, Eur. Phys. J. **A44**, 479 (2010), arXiv:0912.4359.

[118] L. S. Geng *et al.*, Eur. Phys. J. **A44**, 305 (2010), arXiv:0910.5192.

[119] H. Nagahiro, J. Yamagata-Sekihara, E. Oset, S. Hirenzaki, and R. Molina, Phys. Rev. **D79**, 114023 (2009), arXiv:0809.3717.

[120] TOPAZ, I. Adachi *et al.*, Phys. Lett. **B234**, 185 (1990).

[121] D. Morgan and M. R. Pennington, Z. Phys. **C48**, 623 (1990).

[122] S. Ishida, K. Yamada, and M. Oda, Phys. Rev. **D40**, 1497 (1989).

[123] M. Suzuki, Phys. Rev. **D47**, 1043 (1993).

[124] J. Boyer *et al.*, Phys. Rev. **D42**, 1350 (1990).

[125] E. Katz, A. Lewandowski, and M. D. Schwartz, Phys. Rev. **D74**, 086004 (2006), arXiv:hep-ph/0510388.

[126] Y.-s. Oh and T. S. H. Lee, Phys. Rev. **C69**, 025201 (2004), arXiv:nucl-th/0306033.

[127] F. E. Close, A. Donnachie, and Y. S. Kalashnikova, Phys. Rev. **D67**, 074031 (2003), arXiv:hep-ph/0210293.

[128] F. Giacosa, T. Gutsche, V. E. Lyubovitskij, and A. Faessler, Phys. Rev. **D72**, 114021 (2005), arXiv:hep-ph/0511171.

[129] D.-M. Li, H. Yu, and Q.-X. Shen, J. Phys. **G27**, 807 (2001), arXiv:hep-ph/0010342.

[130] M. A. DeWitt, H.-M. Choi, and C.-R. Ji, Phys. Rev. **D68**, 054026 (2003), arXiv:hep-ph/0306060.

[131] H. Nagahiro, L. Roca, E. Oset, and B. S. Zou, Phys. Rev. **D78**, 014012 (2008), arXiv:0803.4460.

[132] F. Giacosa, T. Gutsche, V. E. Lyubovitskij, and A. Faessler, Phys. Rev. **D72**, 094006 (2005), arXiv:hep-ph/0509247.

[133] L. S. Geng, E. Oset, R. Molina, and D. Nicmorus, PoS **EFT09**, 040 (2009), arXiv:0905.0419.

[134] Belle, S. Uehara *et al.*, Phys. Rev. Lett. **104**, 092001 (2010), arXiv:0912.4451.

[135] A. Faessler, T. Gutsche, M. A. Ivanov, V. E. Lyubovitskij, and P. Wang, Phys. Rev. **D68**, 014011 (2003), arXiv:hep-ph/0304031.

[136] T. Branz *et al.*, Phys. Rev. **D81**, 034010 (2010), arXiv:0912.3710.

[137] A. Faessler *et al.*, Phys. Rev. **D78**, 094005 (2008), arXiv:0809.4159.

[138] T. Branz *et al.*, Phys. Rev. **D81**, 114036 (2010), arXiv:1005.1850.

[139] Y. Dong, A. Faessler, T. Gutsche, and V. E. Lyubovitskij, (2009), arXiv:0909.0380.

[140] I. Anikin, M. A. Ivanov, N. Kulimanova, and V. E. Lyubovitskij, Phys. Atom. Nucl. **57**, 1021 (1994).

[141] I. V. Anikin, M. A. Ivanov, N. B. Kulimanova, and V. E. Lyubovitskij, Z. Phys. **C65**, 681 (1995).

[142] S. Weinberg, Phys. Rev. **130**, 776 (1963).

[143] J. Terning, Phys. Rev. **D44**, 887 (1991).

[144] N. A. Tornqvist, Z. Phys. **C68**, 647 (1995), arXiv:hep-ph/9504372.

[145] C. Hanhart, Y. S. Kalashnikova, A. E. Kudryavtsev, and A. V. Nefediev, Phys. Rev. **D75**, 074015 (2007), arXiv:hep-ph/0701214.

[146] N. N. Achasov, S. A. Devyanin, and G. N. Shestakov, Phys. Lett. **B88**, 367 (1979).

[147] F. E. Close and A. Kirk, Phys. Lett. **B489**, 24 (2000), arXiv:hep-ph/0008066.

[148] N. N. Achasov and A. V. Kiselev, Phys. Lett. **B534**, 83 (2002), arXiv:hep-ph/0203042.

[149] C. Hanhart, B. Kubis, and J. R. Pelaez, Phys. Rev. **D76**, 074028 (2007), arXiv:0707.0262.

[150] Belle, T. Mori *et al.*, Phys. Rev. **D75**, 051101 (2007), arXiv:hep-ex/0610038.

[151] Crystal Ball, H. Marsiske *et al.*, Phys. Rev. **D41**, 3324 (1990).

[152] G. V. Efimov and M. A. Ivanov, *The Quark confinement model of hadrons* (Bristol, UK: IOP, 1993).

[153] M. D. Scadron, G. Rupp, F. Kleefeld, and E. van Beveren, Phys. Rev. **D69**, 014010 (2004), arXiv:hep-ph/0309109.

[154] M. Schumacher, Eur. Phys. J. **A30**, 413 (2006), arXiv:hep-ph/0609040.

[155] N. N. Achasov, S. A. Devyanin, and G. N. Shestakov, Phys. Lett. **B108**, 134 (1982).

[156] J. A. Oller and E. Oset, Nucl. Phys. **A629**, 739 (1998), arXiv:hep-ph/9706487.

[157] H. Nagahiro, L. Roca, and E. Oset, Eur. Phys. J. **A36**, 73 (2008), arXiv:0802.0455.

[158] Particle Data Group, W. M. Yao *et al.*, J. Phys. **G33**, 1 (2006).

[159] M. N. Achasov *et al.*, Phys. Lett. **B479**, 53 (2000), arXiv:hep-ex/0003031.

[160] G. Ecker, J. Gasser, A. Pich, and E. de Rafael, Nucl. Phys. **B321**, 311 (1989).

[161] G. Ecker, J. Gasser, H. Leutwyler, A. Pich, and E. de Rafael, Phys. Lett. **B223**, 425 (1989).

[162] WA102, D. Barberis *et al.*, Phys. Lett. **B453**, 316 (1999), arXiv:hep-ex/9903043.

[163] L3, P. Achard *et al.*, Phys. Lett. **B526**, 269 (2002), arXiv:hep-ex/0110073.

[164] WA102, D. Barberis *et al.*, Phys. Lett. **B488**, 225 (2000), arXiv:hep-ex/0007019.

[165] M. K. Volkov and V. L. Yudichev, Phys. Atom. Nucl. **64**, 2006 (2001), arXiv:hep-ph/0011326.

[166] V. V. Anisovich and A. V. Sarantsev, Eur. Phys. J. **A16**, 229 (2003), arXiv:hep-ph/0204328.

[167] L. S. Celenza, S.-f. Gao, B. Huang, H. Wang, and C. M. Shakin, Phys. Rev. **C61**, 035201 (2000).

[168] J. A. Oller, E. Oset, and J. R. Pelaez, Phys. Rev. **D59**, 074001 (1999), arXiv:hep-ph/9804209.

[169] A. Faessler, T. Gutsche, V. E. Lyubovitskij, and Y.-L. Ma, Phys. Rev. **D76**, 114008 (2007), arXiv:0709.3946.

[170] A. Faessler, T. Gutsche, S. Kovalenko, and V. E. Lyubovitskij, Phys. Rev. **D76**, 014003 (2007), arXiv:0705.0892.

[171] A. Faessler, T. Gutsche, V. E. Lyubovitskij, and Y.-L. Ma, Phys. Rev. **D76**, 014005 (2007), arXiv:0705.0254.

[172] A. Faessler, T. Gutsche, V. E. Lyubovitskij, and Y.-L. Ma, Phys. Rev. **D77**, 114013 (2008), arXiv:0801.2232.

[173] Particle Data Group, S. Eidelman *et al.*, Phys. Lett. **B592**, 1 (2004).

[174] C. Amsler and A. Masoni.

[175] Z. G. Wang and S. L. Wan, Phys. Rev. **D74**, 014017 (2006), arXiv:hep-ph/0606002.

[176] M. E. Bracco, A. Cerqueira, Jr., M. Chiapparini, A. Lozea, and M. Nielsen, Phys. Lett. **B641**, 286 (2006), arXiv:hep-ph/0604167.

[177] M. B. Wise, Phys. Rev. **D45**, 2188 (1992).

[178] P. Colangelo, F. De Fazio, and T. N. Pham, Phys. Rev. **D69**, 054023 (2004), arXiv:hep-ph/0310084.

[179] C. Isola, M. Ladisa, G. Nardulli, and P. Santorelli, Phys. Rev. **D68**, 114001 (2003), arXiv:hep-ph/0307367.

[180] T. Branz, T. Gutsche, and V. E. Lyubovitskij, Phys. Rev. **D82**, 054025 (2010), arXiv:1005.3168.

[181] T. Barnes, S. Godfrey, and E. S. Swanson, Phys. Rev. **D72**, 054026 (2005), arXiv:hep-ph/0505002.

[182] E. van Beveren and G. Rupp, Eur. Phys. J. **C32**, 493 (2004), arXiv:hep-ph/0306051.

[183] X. Zhong and Q. Zhao, Phys. Rev. **D78**, 014029 (2008), arXiv:0803.2102.

[184] X. Liu, Y.-R. Liu, W.-Z. Deng, and S.-L. Zhu, Phys. Rev. **D77**, 034003 (2008), arXiv:0711.0494.

[185] A. Salam, Nuovo Cim. **25**, 224 (1962).

[186] S. Godfrey, AIP Conf. Proc. **432**, 231 (1998), arXiv:hep-ph/9712545.

[187] D. Gamermann, private communication .

[188] A. Le Yaouanc, L. Oliver, O. Pene, and J. C. Raynal, Phys. Rev. **D8**, 2223 (1973).

[189] A. Le Yaouanc, L. Oliver, O. Pene, and J. C. Raynal, Phys. Rev. **D9**, 1415 (1974).

[190] C. Downum, T. Barnes, J. R. Stone, and E. S. Swanson, Phys. Lett. **B638**, 455 (2006), arXiv:nucl-th/0603020.

[191] E. S. Ackleh, T. Barnes, and E. S. Swanson, Phys. Rev. **D54**, 6811 (1996), arXiv:hep-ph/9604355.

[192] H.-W. Ke and X. Liu, Eur. Phys. J. **C58**, 217 (2008), arXiv:0806.0998.

[193] T. Branz, T. Gutsche, and V. E. Lyubovitskij, Phys. Rev. **D82**, 054010 (2010), arXiv:1007.4311.

[194] C. D. Roberts and S. M. Schmidt, Prog. Part. Nucl. Phys. **45**, S1 (2000), arXiv:nucl-th/0005064.

[195] D. Ebert, T. Feldmann, and H. Reinhardt, Phys. Lett. **B388**, 154 (1996), arXiv:hep-ph/9608223.

[196] M. K. Volkov and V. L. Yudichev, Phys. Atom. Nucl. **63**, 464 (2000).

[197] H. Leutwyler, Phys. Lett. **B96**, 154 (1980).

[198] G. V. Efimov and S. N. Nedelko, Phys. Rev. **D51**, 176 (1995).

[199] CLEO, J. Gronberg *et al.*, Phys. Rev. **D57**, 33 (1998), arXiv:hep-ex/9707031.

[200] CELLO, H. J. Behrend *et al.*, Z. Phys. **C49**, 401 (1991).

[201] P. Brauel *et al.*, Zeit. Phys. **C3**, 101 (1979).

[202] The Jefferson Lab F(pi), J. Volmer *et al.*, Phys. Rev. Lett. **86**, 1713 (2001), arXiv:nucl-ex/0010009.

[203] NA70, S. R. Amendolia *et al.*, Nucl. Phys. **B277**, 168 (1986).

[204] The BABAR, B. Aubert *et al.*, Phys. Rev. **D80**, 052002 (2009), arXiv:0905.4778.

[205] A. E. Dorokhov, Phys. Part. Nucl. Lett. **7**, 229 (2010), arXiv:0905.4577.

[206] TWQCD, T.-W. Chiu and T.-H. Hsieh, PoS **LAT2006**, 180 (2007), arXiv:0704.3495.

[207] D. Becirevic *et al.*, Phys. Rev. **D60**, 074501 (1999), arXiv:hep-lat/9811003.

[208] C. Aubin *et al.*, Phys. Rev. Lett. **95**, 122002 (2005), arXiv:hep-lat/0506030.

[209] L. G. Landsberg, Phys. Rept. **128**, 301 (1985).

[210] NA60, R. Arnaldi *et al.*, Phys. Lett. **B677**, 260 (2009), arXiv:0902.2547.

[211] M. N. Achasov *et al.*, J. Exp. Theor. Phys. **107**, 61 (2008).

[212] J. Fischer *et al.*, Phys. Lett. **B73**, 359 (1978).

[213] Y. B. Bushnin *et al.*, Phys. Lett. **B79**, 147 (1978).

[214] R. I. Dzhelyadin *et al.*, Phys. Lett. **B88**, 379 (1979).

[215] S. J. Brodsky and G. F. de Teramond, Phys. Lett. **B582**, 211 (2004), arXiv:hep-th/0310227.

[216] L. Randall and R. Sundrum, Phys. Rev. Lett. **83**, 4690 (1999), arXiv:hep-th/9906064.

[217] L. Randall and R. Sundrum, Phys. Rev. Lett. **83**, 3370 (1999), arXiv:hep-ph/9905221.

[218] A. Deur, V. Burkert, J. P. Chen, and W. Korsch, Phys. Lett. **B665**, 349 (2008), arXiv:0803.4119.

[219] R. Alkofer, C. S. Fischer, and F. J. Llanes-Estrada, Phys. Lett. **B611**, 279 (2005), arXiv:hep-th/0412330.

[220] C. S. Fischer and D. Zwanziger, Phys. Rev. **D72**, 054005 (2005), arXiv:hep-ph/0504244.

[221] S. Furui, (2009), arXiv:0912.5397.

[222] E. T. Neil, T. Appelquist, and G. T. Fleming, PoS **LATTICE2008**, 057 (2008).

[223] P. A. M. Dirac, Rev. Mod. Phys. **21**, 392 (1949).

[224] S. J. Brodsky, Invited Talk at the JTI Workshop on Dynamics of Symmetry Breaking, ANL, IL http://www.slac.stanford.edu/grp/th/recentlectures.html , arXiv:/grp/th/recentlectures.html.

[225] S. J. Brodsky and G. F. de Teramond, Phys. Rev. **D77**, 056007 (2008), arXiv:0707.3859.

[226] S. J. Brodsky and G. F. de Teramond, (2008), arXiv:0802.0514.

[227] G. de Teramond, Invited Talk at the Third Workshop of the APS Topical Group in Hadron Physics **GHP2009**, http://www.fz.

[228] A. Karch, E. Katz, D. T. Son, and M. A. Stephanov, Phys. Rev. **D74**, 015005 (2006), arXiv:hep-ph/0602229.

[229] P. Colangelo, F. De Fazio, F. Jugeau, and S. Nicotri, Phys. Lett. **B652**, 73 (2007), arXiv:hep-ph/0703316.

[230] J. Babington, J. Erdmenger, N. J. Evans, Z. Guralnik, and I. Kirsch, Phys. Rev. **D69**, 066007 (2004), arXiv:hep-th/0306018.

[231] H. J. Kwee and R. F. Lebed, Phys. Rev. **D77**, 115007 (2008), arXiv:0712.1811.

[232] T. Gherghetta, J. I. Kapusta, and T. M. Kelley, Phys. Rev. **D79**, 076003 (2009), arXiv:0902.1998.

[233] S. J. Brodsky and R. Shrock, (2009), arXiv:0905.1151.

[234] M. N. Sergeenko, Phys. Atom. Nucl. **56**, 365 (1993).

[235] S. S. Gershtein, A. K. Likhoded, and A. V. Luchinsky, Phys. Rev. **D74**, 016002 (2006), arXiv:hep-ph/0602048.

[236] S.-G. Zhou and H.-C. Pauli, J. Phys. **G30**, 983 (2004), arXiv:hep-ph/0311305.

[237] M. Karliner and H. J. Lipkin, Phys. Lett. **B650**, 185 (2007), arXiv:hep-ph/0608004.

[238] M. Fujita, K. Fukushima, T. Misumi, and M. Murata, Phys. Rev. **D80**, 035001 (2009), arXiv:0903.2316.

[239] H. R. Grigoryan, P. M. Hohler, and M. A. Stephanov, Phys. Rev. **D82**, 026005 (2010), arXiv:1003.1138.

[240] A. M. Badalian, A. I. Veselov, and B. L. G. Bakker, Phys. Rev. **D70**, 016007 (2004).

[241] W. Jaus, Phys. Rev. **D41**, 3394 (1990).

[242] J. Erlich, E. Katz, D. T. Son, and M. A. Stephanov, Phys. Rev. Lett. **95**, 261602 (2005), arXiv:hep-ph/0501128.

[243] T. Barnes, F. E. Close, P. R. Page, and E. S. Swanson, Phys. Rev. **D55**, 4157 (1997), arXiv:hep-ph/9609339.

[244] C. B. Dover, T. Gutsche, M. Maruyama, and A. Faessler, Prog. Part. Nucl. Phys. **29**, 87 (1992).

[245] T. Gutsche, R. D. Viollier, and A. Faessler, Phys. Lett. **B331**, 8 (1994).

List of Figures

List of Tables

Acknowledgments

At this place, I would like to express my gratitude to all people who supported me during my PhD and who have made this dissertation possible.

Mein besonderer Dank geht dabei an Herrn Prof. Dr. Thomas Gutsche, der mir die Möglichkeit zur Promotion gegeben hat. Er hat mich stets mit außergewöhnlichem Engagement unterstützt und gefördert. Durch seinen Einsatz hat er mir auch die Teilnahme an verschiedenen Konferenzen und die Forschungsaufhalte am CERN und an der Universität Valencia ermöglicht. Dadurch ist mir während meiner Promotion die Möglichkeit gegeben worden, mich nicht nur fachlich, sondern auch persönlich weiterzuentwickeln, was mindestens genauso wichtig ist, wie die Veröffentlichung von Publikationen. Über das mir hier entgegengebrachte Vertrauen habe ich mich sehr gefreut.

I also would like to thank Dr. Valery E. Lyubovitskij for his guidance and intense and fruitful discussions. He was always pushing our work forward which allowed for numerous publications.

Furthermore, I would like to acknowledge Professor Eulogio Oset who was my advisor during my stay at the University of Valencia. In particular, I am grateful for his warm welcome in his research group and his support concerning our work.

Thanks to my collaborators in Valencia and Chile: Raquel Molina, Lisheng Geng and Afredo Vega for the pleasant and productive collaboration.

Ich bedanke mich beim Sprecher des Tübinger Graduiertenkollegs Herrn Prof. Dr. Josef Jochum für die Unterstützung durch das Internationale Graduiertenkolleg, von dem ich sehr profitiert habe. Neben meinem Promotionsstipendium konnte dadurch auch die Teilnahme an Konferenzen und der Forschungsaufenthalt in Spanien ermöglicht werden.

Außerdem möchte ich mich noch bei meiner Bürokollegin Bettina Oexl für die angenehme Arbeitsatmosphäre und die hilfreichen Gespräche bedanken.

Schließlich danke ich noch meiner Familie, insbesondere meiner Schwester Katrin für ihre Unterstützung.

Publications

1. T. Branz, T. Gutsche, V. E. Lyubovitskij, I. Schmidt, A. Vega
   "Light and heavy mesons in a soft-wall holographic approach"
   Phys. Rev. D **82**, 074022 (2010)

2. T. Branz, T. Gutsche and V. E. Lyubovitskij
   "Two-photon decay of heavy hadron molecules"
   Phys. Rev. D **82**, 054010 (2010)

3. T. Branz, T. Gutsche and V. E. Lyubovitskij
   "Hidden-charm and radiative decays of the Z(4430) as a hadronic $D_1\overline{D^*}$ bound state"
   Phys. Rev. D **82**, 054025 (2010)

4. T. Branz, A. Faessler, T. Gutsche, M. A. Ivanov, J. G. Korner, V. E. Lyubovitskij and B. Oexl
   "Radiative decays of double heavy baryons in a relativistic constituent three–quark model including hyperfine mixing"
   Phys. Rev. D **81**, 114036 (2010)

5. R. Molina, T. Branz, E. Oset
   "A new interpretation for the $D^*_{s2}(2573)$ and the prediction of novel exotic charmed mesons"
   Phys. Rev. D **82**, 014010 (2010)

6. T. Branz, A. Faessler, T. Gutsche, M. A. Ivanov, J. G. Korner, V. E. Lyubovitskij
   "Relativistic Constituent Quark Model With Infrared Confinement"
   Phys. Rev. D **81**, 034010 (2010)

7. T. Branz, L. S. Geng and E. Oset
   "Two-photon and one photon-one vector meson decay widths of the $f_0(1370)$, $f_2(1270)$, $f_0(1710)$, $f'_2(1525)$, and $K^*_2(1430)$"
   Phys. Rev. D **81**, 054037 (2010)

8. A. Vega, I. Schmidt, T. Branz, T. Gutsche and V. E. Lyubovitskij
"Meson wave function from holographic models"
Phys. Rev. D **80**, 055014 (2009)

9. T. Branz, T. Gutsche and V. E. Lyubovitskij
"Hadronic molecule structure of the $Y(3940)$ and $Y(4140)$"
Phys. Rev. D **80**, 054019 (2009)

10. T. Branz, T. Gutsche and V. E. Lyubovitskij
"Weak decays of heavy hadron molecules involving the $f_0(980)$"
Phys. Rev. D **79**, 014035 (2009)

11. T. Branz, T. Gutsche and V. E. Lyubovitskij
"Strong and radiative decays of the scalars $f_0(980)$ and $a_0(980)$ in a hadronic molecule approach"
Phys. Rev. D **78**, 114004 (2008)

12. T. Branz, T. Gutsche and V. E. Lyubovitskij
"$f_0(980)$ meson as a $K\bar{K}$ molecule in a phenomenological Lagrangian approach"
Eur. Phys. J. A **37**, 303 (2008)